# University of Alberta

Physicochemical Properties and Microencapsulation Process Development for Fish Oil using Supercritical Carbon Dioxide

by

Bernhard Seifried

A thesis submitted to the Faculty of Graduate Studies and Research
in partial fulfillment of the requirements for the degree of

Doctor of Philosophy

in

Bioresource and Food Engineering

Department of Agricultural, Food and Nutritional Science



Spring 2010
Edmonton, Alberta

## Examining Committee

Dr. Feral Temelli, Department of Agricultural, Food and Nutritional Science

Dr. Thava Vasanthan, Department of Agricultural, Food and Nutritional Science

Dr. David Bressler, Department of Agricultural, Food and Nutritional Science

Dr. Anthony Yeung, Department of Chemical and Materials Engineering

Dr. Philip G. Jessop, Department of Chemistry, Queen's University

This thesis is dedicated to my parents Hans and Theresia Seifried…

# Abstract

Fish oil is an excellent source of long chain polyunsaturated fatty acids (LC-PUFA), which can reduce the risk of cardiovascular disease in addition to other health benefits. However, the average intake of LC-PUFA in the Western diet is much lower than the recommended levels. Fish oil is prone to oxidative deterioration when exposed to oxygen and thus must be protected in order to be used in food products. Microencapsulation is one possibility that is already applied by the industry to protect fish oil. However, most of the conventional microencapsulation techniques suffer from shortcomings such as harsh processing conditions or the use of numerous chemicals. The main objective of this thesis was to develop a novel spray process to microencapsulate fish oil based on supercritical fluid (SCF) technology using supercritical carbon dioxide (SC-$CO_2$) and $CO_2$-expanded ethanol (CX EtOH).

Fundamental physicochemical properties essential for optimal process design were lacking in the literature; therefore, density, interfacial tension (IFT) and viscosity of fish oil in the form of triglycerides and fatty acid ethyl esters were determined at different temperatures and pressures. Fish oil when equilibrated with SC-$CO_2$ at elevated pressure expanded by up to about 40% in volume and increased in density by up to about 5%. Furthermore, IFT of fish oil in contact with SC-$CO_2$ decreased substantially by an order of magnitude with an increase in $CO_2$ pressure. When fish oil was in contact with CX EtOH, IFT decreased to ultra low levels at pressures of less than 10 MPa. Viscosity of fish oil

equilibrated with SC-$CO_2$ decreased substantially with pressure but increased with shear rate.

Based on the physicochemical properties determined in this research, a novel process to produce micro- and nano-sized particles containing fish oil was developed based on a SCF spray-drying method. Key processing parameters have been evaluated and can be further optimized to improve encapsulation efficiency.

Determination of physicochemical properties contributed to the fundamental understanding of the behavior of the fish oil+$CO_2$ system with and without ethanol under high pressure conditions. The new microencapsulation process shows great potential for the delivery of bioactives in various product applications.

# Acknowledgements

This research and thesis would not have been possible without the great support of my supervisor Dr. Feral Temelli, whose brilliance, encouragement, guidance and support from the beginning to the final level enabled me to complete this work. Thank you Dr. Temelli, I think that you are an excellent supervisor, mentor and coach, who helped me to go far in my research and development.

Thank you to Dr. Thava Vasanthan and Dr. David Bressler for being in my supervisory committee and excellent mentors giving great support, valuable guidance and feedback making this work a success. Many thanks to Dr. Anthony Yeung, from the Department of Chemical and Materials Engineering for being on my examining committee and providing great support. Thanks to Dr. Jonathan Curtis for providing helpful feedback and valuable guidance in my research.

Special thanks to Dr. Philip G. Jessop, from the Department of Chemistry at the Queen's University for being my external examiner.

Furthermore, I am grateful to NSERC (Natural Sciences and Engineering Research Council of Canada) and Alberta Ingenuity Fund for their financial support.

Thanks to Jody Forslund and Francine Hodder, who assisted me with administrative work throughout my PhD program. I would also like to thank my labmates and friends, Paul Moquin, Lauren Comin, Ehsan Jenab and Oguz Akin for their fruitful discussions and help in many aspects throughout the past years. Thanks a lot to Mei Sun and Jean Bourgois who often assisted me in the lab and gave me a helping hand. As well, I am grateful to Dr. Selma Guigard for providing equipment for my viscosity study. Thanks to the fabulous technicians in the glass shop and in the SEM lab who contributed important parts to my work.

Finally, I would like to thank Susan, my family and all my friends for giving me support, good energies and love.

# Table of Contents

# List of Tables

# List of Figures

# List of Abbreviations

| | |
|---|---|
| AcN | acetonitrile |
| ADSA | axisymmetrical drop shape analysis |
| ALA | alpha-linolenic acid |
| ASES | aerosol solvent extraction system |
| AV | anisidine value |
| BG | β-Glucan |
| BHA | butylated hydroxyanisole |
| BHT | butylated hydroxytoluene |
| $C_p$ | critical point |
| CCD | charge-coupled device |
| CMOS | complementary metal oxide semiconductor |
| $CO_2$ | carbon dioxide |
| CPF | concentrated powder form |
| CVD | cardiovascular disease |
| CX | $CO_2$-expanded |
| CXL | $CO_2$-expanded liquid |
| DAQ | data acquisition |
| DELOS | depressurization of an expanded liquid organic solution |
| DHA | docosahexaenoic acid |
| DMSO | dimethyl sulfoxide |
| EDTA | ethylene diamine tetraacetate |
| EMD | emulsifying device |
| EPA | eicosapentaenoic acid |
| EtOH | ethanol |
| FAEE | fatty acid ethyl ester |
| FFA | free fatty acids |
| FID | flame ionization detector |
| FO | fish oil |
| GA | gum arabic |
| GAME | gas-assisted mechanical extrusion |
| GAS | gas antisolvent process |
| GC-O | gas chromatography-olfactometry |
| GRAS | generally regarded as safe |
| GXL | gas-expanded liquid |
| HMC | high molecular-weight components |
| HPLC | high performance liquid chromatography |
| HS-SPME | headspace solid phase microextraction |
| ID | inner diameter |
| IFT | interfacial tension |
| $K_F$ | film number |
| LC-PUFA | long chain polyunsaturated fatty acid |
| LMC | low molecular-weight components |
| LUV | large unilamellar vesicles |
| MCP | mixture critical point |

| | |
|---|---|
| MLV | multilamellar vesicles |
| MMP | minimum miscibility pressure |
| MS | mass spectrometry |
| n-OSA starch | n-octenylsuccinate-derivatised starch |
| OD | outer diameter |
| Oh | Ohnesorge number |
| P | pressure |
| $P_c$ | critical pressure |
| PAV | p-anisidine value |
| PCA | precipitation with a compressed fluid antisolvent |
| PGSS | particles from gas saturated solutions |
| PI | pressure indicator |
| PID controller | proportional integral derivative controller |
| PLA | polylactic acid |
| PLLA | poly(l-lactide) |
| PUFA | polyunsaturated fatty acid |
| PV | peroxide value |
| QCM | quartz crystal microbalance |
| Re | Reynolds number |
| Ref. | reference |
| RESOLV | rapid expansion of a supercritical solution into a liquid solvent |
| RESS | rapid expansion of supercritical solutions |
| RH | relative humidity |
| RQCM | research quartz crystal microbalance |
| SAFT | supercritical antisolvent fractionation |
| SAS | supercritical fluid antisolvent |
| SC-$CO_2$ | supercritical carbon dioxide |
| SCF | supercritical fluid |
| SEDS | solution-enhanced dispersion by supercritical fluids |
| SFEE | supercritical fluid extraction of emulsions |
| SUV | small unilamellar vesicles |
| T | temperature |
| $T_c$ | critical temperature |
| TBARS | thiobarbituric acid reactive substances |
| TG | triglyceride |
| TIC | temperature indicator and controller |
| $v_{CO2}$ | molar volume of $CO_2$ |
| We | Weber number |
| $x_{CO2}$ | molar fraction of $CO_2$ in the liquid phase |

Greek symbols:

| | |
|---|---|
| $\gamma$ | interfacial tension |
| $\Gamma_{CO2}$ | surface excess concentration |
| $\eta$ | viscosity |
| $\rho$ | density |

# 1 Introduction and Objectives

According to the World Health Organization [1], one third of all deaths worldwide are caused by cardiovascular diseases (CVD), which are not limited to stressed, middle aged, overweight men living in developed countries anymore but can also affect women and children all over the world. Epidemiological studies indicate that long chain polyunsaturated fatty acids (LC-PUFA) derived from marine fish have a protective effect with respect to CVD [2, 3]. Furthermore, LC-PUFA have an anti-inflammatory effect, exhibit beneficial effects on patients with diabetes, arthritis, inflammatory and autoimmune diseases [4], and they play an important role for bone growth and repair, as well as brain function and development [5].

Numerous scientific and expert committees all over the world recommend minimum dietary intake levels for LC-PUFA to benefit from their positive health effects of around 0.2 g/d, which is higher than what is currently consumed by most people (0.15 g/d) [6]. The American Heart Association recommends a daily intake of about 1 g LC-PUFA or 0.5% of the daily total nutritional energy consumption [7].

A major source of LC-PUFA is marine fish, which contains relatively high levels of eicosapentaenoic acid (C20:5 ω-3, EPA) and docosahexaenoic acid (C22:6 ω-3, DHA) [8]. Fish oil can be incorporated into common food products to provide EPA and DHA in the diet of those people who habitually consume little or no fish. However, the susceptibility of EPA and DHA to oxidative deterioration, resulting in the formation of oxidation products potentially hazardous to health and causing organoleptic problems, has presented obstacles to the more widespread use of fish oils by the food industry.

Microencapsulation is a technology that can effectively isolate sensitive materials from the oxidative environment. The encapsulated ‘core’ material is covered by a polymer matrix forming a ‘shell’, as a result, the entrapped material is protected against adverse reactions such as lipid oxidation or nutritional

deterioration. A large variety of microencapsulation techniques have been developed for food ingredients based on physical, chemical, and physicochemical methods [9].

Several methods have been applied in research labs and industry to encapsulate fish oil in diverse materials in an attempt to extend shelf life, such as spray drying or freeze drying [10, 11] and complex coacervation [12]. To date, the main microencapsulating agents used are gum arabic, modified starches or milk proteins [13]. However, at present there are several shortcomings in the existing technologies for microencapsulation of fish oil. The level of LC-PUFA in such dried encapsulated powders is low. Furthermore, current spray-drying technologies operate at elevated temperatures, which are necessary for drying. High temperatures and the presence of oxygen lead to increased oxidation of LC-PUFA [11]. The inclusion of air in particles containing fish oil is another disadvantage of these freeze- and spray-drying techniques, which leads to decreased shelf life.

Supercritical fluids (SCF) could potentially aid in minimizing the degradation of PUFA during processing of fish oil into a microencapsulated product. A pure component when heated above its critical temperature and pressurized to a level above its critical pressure but below the pressure needed for solidification is called a supercritical fluid [14]. In the supercritical state, density and subsequently solvent strength are highly adjustable by modest changes in temperature and pressure. SCF are tunable solvents, which exhibit liquid-like densities, gas-like diffusivity and viscosity, and low surface tension. These properties combined with the pressure dependent solvent power of SCF and enhanced mass transfer have provided the impetus for development of a wide variety of processes in many segments of the industry [15]. SC-$CO_2$ is the most widely used SCF due to its moderate critical temperature and pressure (31.1°C and 7.4 MPa), which is environmentally benign compared to conventional solvents, generally regarded as safe (GRAS), easily removable upon depressurization, recyclable and readily available.

Particle formation of biopolymers is of great interest for the food and pharmaceutical industries. Particle formation techniques utilizing SC-$CO_2$ have been developed over the past decades to generate nano- and micrometer sized particles [16] mainly for pharmaceutical components and to a limited extent for food components. However, to date, no process has been developed to microencapsulate fish oil using SCF technology.

Therefore, the aim of this PhD research was to develop a novel process for microencapsulation of fish oil using SCF technology to overcome the shortcomings of conventional techniques. Such a process capable of encapsulating fish oil into micron-sized particles should ideally use a water-soluble shell material, only food-grade solvents and SC-$CO_2$, thereby avoiding contact with air and high temperatures.

The proposed water-soluble shell materials to encapsulate fish oil in the scope of this research were gum arabic (GA), which is commonly used for microencapsulation of food ingredients in spray-drying techniques, and a polysaccharide found in barley, namely β-glucan (BG), which is a soluble dietary fibre component, that has demonstrated health benefits [17, 18], including lowering of blood cholesterol to reduce the risk of heart disease, regulation of blood glucose levels for diabetes management [19, 20], and promotion of the growth of beneficial gut microflora (i.e. as a prebiotic) [21, 22]. In 2006, the US Food and Drug Administration (FDA) authorized a health claim for the role of β -glucan soluble fibre from barley in reducing the risk of coronary heart disease [23].

The process envisioned for the encapsulation of fish oil was a modified 'precipitation with a compressed fluid antisolvent' (PCA) process (see Section 2.3.3.3 for more details). The basic idea of this modified PCA process is to spray an aqueous emulsion containing the dissolved shell material and dispersed fish oil into a precipitation chamber together with a mixture of ethanol+$CO_2$ at elevated pressure, which acts as an antisolvent for the shell material and as a solvent for water leading to precipitation into fine solid particles encapsulating the fish oil. The design of this process required the knowledge of physicochemical properties

potentially affecting the emulsification and spraying into the high pressure chamber, such as density, interfacial tension and viscosity. However, such data for fish oil+$CO_2$ and fish oil+$CO_2$-expanded ethanol systems were not available in the literature. Thus, an emphasis was placed on studying the physical properties of fish oil under high pressure $CO_2$. Therefore, this thesis research is divided into two major sections, namely 'Fundamental Data' and 'Process Development'.

The main objective of the 'Fundamental Data' section was the determination of density, interfacial tension and viscosity of fish oil in the form of triglycerides (TG) and fatty acid ethyl esters (FAEE) in contact and equilibrium with high pressure $CO_2$ and $CO_2$-expanded ethanol. The specific objectives were:

- to measure the density of fish oil TG and FAEE in equilibrium with $CO_2$ at 40, 55 and 70°C and pressures ranging from 0.1 to 25 MPa as well as to determine the volumetric expansion of fish oil TG and FAEE in equilibrium with $CO_2$ at 40°C with pressure (Chapter 3),

- to determine the interfacial tension (IFT) of fish oil in the form of TG and FAEE in contact with high pressure $CO_2$ at 40, 55 and 70°C and pressures of up to about 25 MPa and to develop a correlation to describe the data (Chapter 4),

- to determine the density of saturated $CO_2$-expanded ethanol at 40, 55 and 70°C and pressures of up to about 12 MPa, which is close to the mixture critical point and to develop a correlation to describe the density data (Chapter 5),

- to measure the IFT of fish oil TG in contact with $CO_2$-expanded ethanol at 40, 55, and 70°C using the pendant drop method at pressures of up to about 6 MPa and to correlate the data to pressure and temperature (Chapter 6),

- to review the mechanisms involved and to investigate interfacial phenomena, including interfacial turbulence, occurrence of an oscillating drop with convective patterns inside and outside of the drop, gas bubble formation inside a drop, and jet formation at atmospheric and elevated pressures including a whipping jet at pressures of up to 10.3 MPa at 40°C (Chapter 7),

- to determine the viscosity and rheological behavior of fish oil TG in equilibrium with $CO_2$ at 40, 55 and 70°C and pressures of up to about 12 MPa using a rotational viscometer equipped with a high pressure cell (Chapter 8), and

- to determine the viscosity and rheological behavior of fish oil FAEE in equilibrium with $CO_2$ at 40, 55 and 70°C and pressures of up to about 12 MPa using a rotational viscometer equipped with a high pressure cell and to assess the potential of a quartz crystal microbalance to determine the viscosity of $CO_2$-expanded liquids at elevated pressures (Chapter 9).

In the 'Process Development' section the results and observations of the previous studies for density, interfacial tension and viscosity were applied to design the process for particle formation and microencapsulation of fish oil.

- The objectives of this study were: (a) to design a process capable of continuously atomizing an aqueous solution of BG and GA together with a mixture of $CO_2$+ethanol into a high pressure chamber, thereby causing precipitation and particle formation, and (b) to design a process, to continuously disperse the fish oil TG into that solution prior to being atomized in the high pressure chamber, so that the fish oil would be encapsulated by the shell material forming micrometer-sized particles (Chapter 10).

## 1.1 References


1. J. McKay, G.A. Mensah, S. Mendis, K. Greenlund, The Atlas of Heart Disease and Stroke. 2004, Geneva: World Health Organization. 112.

2. J. Dyerberg, D. Eskesen, P. Andersen, A. Astrup, B. Buemann, J. Christensen, P. Clausen, B. Rasmussen, E. Schmidt, T. Tholstrup, E. Toft, S. Toubro, S. Stender, Effects of trans- and n-3 unsaturated fatty acids on cardiovascular risk markers in healthy males. An 8 weeks dietary intervention study. Eur. J. Clin. Nutr. 58 (2004) 1062-1070.

3. E.B. Schmidt, J. Dyerberg, Omega-3-fatty-acids - current status in cardiovascular medicine. Drugs 47 (1994) 405-424.

4. F. Sahena, I.S.M. Zaidul, S. Jinap, N. Saari, H.A. Jahurul, K.A. Abbas, N.A. Norulaini, PUFAs in fish: Extraction, fractionation, importance in health. Compr. Rev. Food Sci. Food Safety 8 (2009) 59-74.

5. P. Benatti, G. Peluso, R. Nicolai, M. Calvani, Polyunsaturated fatty acids: biochemical, nutritional and epigenetic properties. J. Am. Coll. Nutr. 23 (2004) 281-302.

6. W. Kolanowski, G. Laufenberg, Enrichment of food products with polyunsaturated fatty acids by fish oil addition. Eur. Food Res. Technol. 222 (2006) 472-477.

7. P.M. Kris-Etherton, W.S. Harris, L.J. Appel, Fish consumption, fish oil, omega-3 fatty acids, and cardiovascular disease. Circulation 106 (2002) 2747-2757.

8. A. Simopoulos, Summary of the conference on the health-effects of polyunsaturated fatty-acids in seafoods. J. Nutr. 116 (1986) 2350-2354.

9. A. Kamyshny, S. Magdassi, Microencapsulation. in 2nd ed. Encyclopedia of Surface and Colloid Science, ed. P. Somasundaran and A. Hubbard. 2006, Boca Raton, FL, Taylor & Francis. 3957 - 3969.

10. S. Hogan, E. O'Riordan, M. O'Sullivan, Microencapsulation and oxidative stability of spray-dried fish oil emulsions. J. Microencapsulation 20 (2003) 675-688.

11. K. Heinzelmann, K. Franke, J. Velasco, G. Marquez-Ruiz, Microencapsulation of fish oil by freeze-drying techniques and influence of process parameters on oxidative stability during storage. Eur. Food Res. Technol. 211 (2000) 234-239.

12. N. Yan, Y. Jin, S. Moulton, T.-C. Perrie, Ocean Nutrition Canada Ltd., Microcapsules having multiple shells and method for the preparation thereof. Patent #: WO2004041251, 2004.

13. M. Keogh, B. O'Kennedy, J. Kelly, M. Auty, P. Kelly, A. Fureby, A. Haahr, Stability to oxidation of spray-dried fish oil powder microencapsulated using milk ingredients. J. Food Sci. 66 (2001) 217-224.

14. G. Brunner, Gas Extraction: An Introduction to Fundamentals of Supercritical Fluids and the Application to Separation Processes. Topics in Physical Chemistry. Vol. 4. 1994, Darmstadt: Springer.

15. M.A. McHugh, V.J. Krukonis, Supercritical Fluid Extraction: Principles and Practice. 2nd ed. Butterworth-Heinemann Series in Chemical Engineering. 1994, Boston: Butterworth-Heinemann.

16. J. Jung, M. Perrut, Particle design using supercritical fluids: Literature and patent survey. J. Supercrit. Fluids 20 (2001) 179-219.

17. A. Lazaridou, C.G. Biliaderis, Molecular aspects of cereal beta-glucan functionality: Physical properties, technological applications and physiological effects. J. Cereal Sci. 46 (2007) 101-118.

18. C.S. Brennan, L.J. Cleary, The potential use of cereal (1-3,1-4)-beta-D-glucans as functional food ingredients. J. Cereal Sci. 42 (2005) 1-13.

19. J. Hallfrisch, D.J. Scholfield, K.M. Behall, Physiological responses of men and women to barley and oat extracts (Nu-trimX). II. Comparison of glucose and insulin responses. Cereal Chem. 80 (2003) 80-83.

20. J. Li, T. Kaneko, L.Q. Qin, J. Wang, Y. Wang, Effects of barley intake on glucose tolerance, lipid metabolism, and bowel function in women. Nutrition 19 (2003) 926-929.

21. R. Crittenden, S. Karppinen, S. Ojanen, M. Tenkanen, R. Fagerstrom, J. Matto, M. Saarela, T. Mattila-Sandholm, K. Poutanen, In vitro fermentation of cereal dietary fibre carbohydrates by probiotic and intestinal bacteria. J. Sci. Food Agric. 82 (2002) 781-789.

22. B. Tungland, Fructooligosaccharides and other fructans: Structures and occurrence, production, regulatory aspects, food applications, and nutritional health significance. Oligosaccharides in food and agriculture. Vol. 849 ACS Symp. Ser. 2003. 135-152.

23. US Food and Drug Administration, Food labeling: health claims; soluble dietary fiber from certain foods and coronary heart disease. Final rule. Federal Register. 71 (2006) 29248-29250.

# 2 Literature Review[1]

## 2.1 Fish oil

Fish oil is considered a by-product of the fishing industry, which aims to produce protein-rich fish meal for animal feeds besides catching fish for human consumption. The main source of fish oil is fish caught in the open sea, where the fish species used in commercial production of fish meal and oil depend on the region. For example, anchovy, jack mackerel, Pacific mackerel, and sardine are the main species for the South American fishing nations, while capelin, Atlantic horse mackerel, sand eel, Norway pout, sprat and herring are caught by the European fisheries, whereas menhaden and pollack are popular for the US fish industry [1]. The Canadian fisheries process mainly salmon, herring and mackerel [2]. World fish production by catch and aquaculture from both marine and inland sources in 2006 amounted to about 102 and 42 million tons, respectively [3]. About 15% of the world fish production from both aquaculture and commercial catch are processed into fish oil and fish meal, with about 85% of the produced fish oil being used by the aquaculture industry, mostly for salmonids [3]. However, the demand for fish oil for human consumption is growing, accounting for about 10% of the global crude fish oil production [4].

Crude fish oil is produced mainly by the wet-rendering process in which hot steam is used to heat the fish thereby rupturing the oil-rich cells [1]. The resulting slurry is mechanically pressed yielding the press liquor containing the bulk of the oil, while the press cake contains 40-50% solids and a small quantity of oil. The press liquor containing 5-10% solids is further treated by a centrifugal desludging process followed by another centrifugal separation resulting in crude fish oil, which is further refined into a suitable end product, depending on the use of the oil [1]. On average, approximately 10 kg of fish oil and 20 kg of dried fish meal can be produced from 100 kg of wet fish depending on the oil content of the fish, which should not be less than about 3 wt% of the raw fish in order to be

[1] Sections 2.2.1 to 2.2.3 of this chapter are to be published as part of a book chapter; "Bioseparations of Nutraceuticals using Supercritical Carbon Dioxide" (chapter 8) in "Food Engineering at Interfaces", (eds.) J.M. Aguilera, G.V. Barbosa-Canovas, R. Simpson and J. Weltri-Chanes, copyright 2010 Springer. Reprinted with kind permission of Springer Science+Business Media, Germany.

economically viable [1]. About 75% of the fish harvested are classified as oily fish, which contains between 5 to 25% lipids [1].

Fish oil used in aquaculture is usually not highly refined, since the maximum retention of the original constituents present in the natural fish oil is desirable [1]. However, removal of industrial pollutants such as dioxins by treating the oil with silica or activated carbon is required.

In order to be suitable for human consumption, crude fish oil needs to be purified. This requires additional refining steps, which mainly aim at removing undesirable compounds such as free fatty acids, off aromas and peroxides [5]. Additionally, high value compounds such as squalene, and vitamins A and D are targets of refining processes as well. The refining steps include clarification to remove solid matter and degumming using phosphoric acid to precipitate phospholipids and proteinaceous matter as well as neutralisation of free fatty acids using aqueous alkali [1]. Additionally, bleaching is done with bleaching earth to remove carotenoids and absorb residual amounts of soap, and deodorization using steam at elevated temperatures under vacuum removes volatile materials [1]. Finally, additional treatments with activated carbon, molecular short-path distillation and vacuum distillation can be applied to purify the fish oil to highest standards for various nutraceutical applications [1, 5].

Fish oils containing up to 300 mg/g of eicosapentaenoic acid (EPA) and docosahexaenoic acid (DHA), which are highly polyunsaturated fatty acids (PUFA), can be obtained by winterization, blending, solvent crystallization and/or vacuum distillation [6]. For applications requiring higher EPA and DHA levels, the fish oil triglyerides (TG) are hydrolyzed to liberate the fatty acids, which can then be converted into fatty acid ethyl esters (FAEE) or methyl esters (FAME). The esters are subsequently fractionated by various methods to obtain higher concentrates of EPA and DHA [7]. Conventional methods to fractionate fish oil esters include vacuum or short path distillation [8-12], solvent crystallization [13-15] or urea complexation [16-21]. These methods often require the use of flammable and toxic organic solvents or elevated process temperatures, which can lead to polymerization and degradation of thermally labile PUFA [7, 14, 22].

Furthermore, selective enzymatic hydrolysis of fish oil TGs using fatty acid specific lipases facilitates separation and concentration of EPA and DHA [23-30]. Finally, supercritical fluids offer great potential for processing of fish oils [31, 32], as discussed later (Section 2.2.4).

The global fish oil production is estimated at about 1000 kilotons (kt) per year [33]. The leading countries for fish oil production are Peru and Chile, producing about 262 and 170 kt in the years 2005 and 2006, respectively [1]. The Scandinavian countries account for about 21% of the global fish oil production [4]. According to recent reports from the Food and Agriculture Organization of the United Nations, the production of fish oil reached 627 kt in 2007 [34], while fish production from capture fisheries and aquaculture amounted for 90 and 50 million tons per year [35], respectively.

The major uses for fish oil in the year 2000 were production of hydrogenated fats (36%), aquaculture feed (55%), industrial use (6%) and pharmaceutical use (2-3%) [1]. In 2003, it was estimated that the total consumption of fish oil was distributed between aquaculture (72%), direct human consumption (19%), technical uses (5%) and other uses (4%) [1]. The total amount of fish oil used in 2003 for human consumption was about 190 kt, with about 150 kt used as hydrogenated fat mainly in South America and the rest consumed as refined fish oil often in encapsulated form [1]. However, since then the percentages changed substantially, with 10 and 85% of the fish oil being used for hydrogenation and aquaculture, respectively [4]. Human consumption of refined fish oil is growing at about 15% annually, fuelled by increasing consumer demand and interest by the food industry to develop foods rich in PUFA derived from fish oil [36].

The price for crude fish oil on the world market spiked in 2008 reaching prices of up to US$1,800 per metric ton [33, 37], as illustrated in Fig. 2-1. However, since 2008 the price for crude fish oil went back to a level of US$925 per metric ton in January 2010 [37]. The reason for the price spike in 2008 was apparently the occurrence of the El Niño event, which reduced the global fish oil production during that time to about 50% [33].

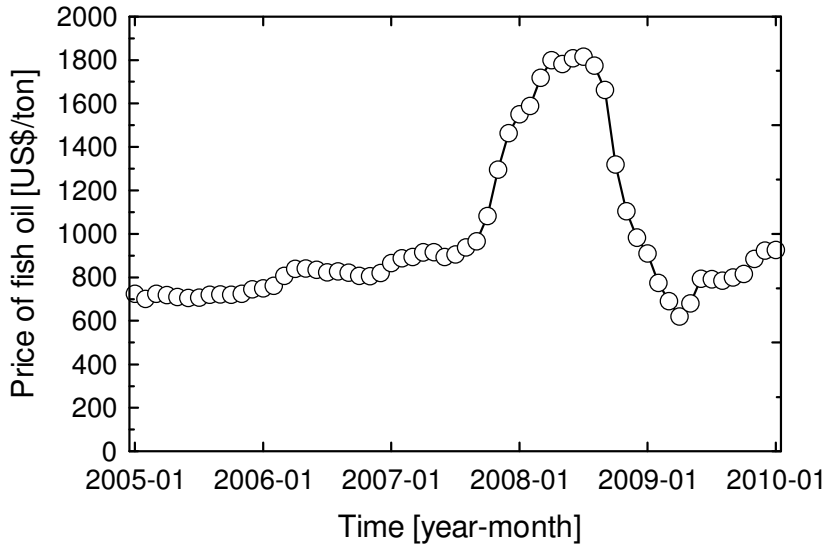


**Figure 2-1.** Commodity price of crude fish oil from 2005 until 2010. Data from Ref. [37].

### 2.1.1 Composition

The fatty acid composition of fish oil is variable and complex, with fatty acid chain lengths ranging from 14 to 24 carbons and degrees of unsaturation ranging from saturated to highly unsaturated molecules having five or six double bonds [1]. The abbreviations used in this thesis for fatty acids are in the format C*m*:*n*, where *m* and *n* refer to the number of carbon atoms in the fatty acid chain and the number of double bonds, respectively. Fish oil is the main source of long-chain polyunsaturated fatty acids (LC-PUFA), with the two most important LC-PUFA in fish oil being EPA (C20:5 ω-3) and DHA (C22:6 ω-3), which belong to the family of ω-3 fatty acids, where the first double bond begins with the third carbon atom from the methyl end of the molecule, as illustrated in Fig. 2-2.

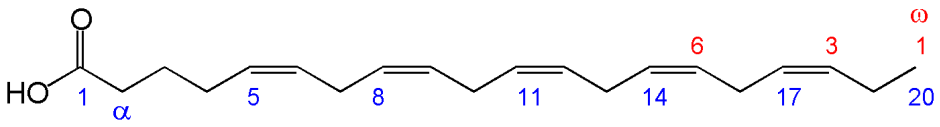


EPA, cis-5,8,11,14,17-eicosapentaenoic acid

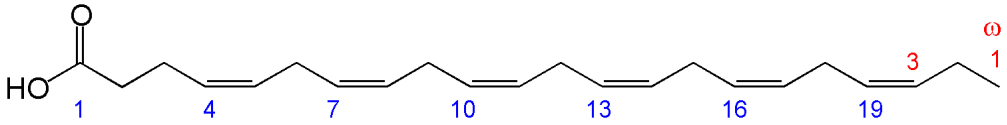


DHA, cis-4,7,10,13,16,19-docosahexaenoic acid

**Figure 2-2.** Chemical structure of EPA and DHA.

The contents of EPA and DHA in marine fish oil depend on numerous factors, such as species, origin, catch season and feed of the fish. It must be emphasized that unicellular phytoplankton and seaweed are the primary source of PUFA in marine fish, which accumulate PUFA by ingestion [38]. Therefore, the amount and composition of fish oil present in a given species can fluctuate depending on the availability of phytoplanktons to the fish [39]. In the 1960s, Gruger *et al.* [40] assessed the fatty acid composition of oils obtained from various Pacific and Atlantic saltwater fish and found a range of 5.0-21.5 wt% and 5.9-26.2 wt% of total fatty acids for EPA and DHA, respectively. EPA and DHA levels of up to 16 and 36 wt% of total fatty acids, respectively, were found in marine fish from the southeast Brazilian coast and Mediterranean Sea [39, 41]. The fatty acid composition for various common fish oils is given in Table 2-1 [42].

**Table 2-1.** Fatty acid composition of various fish oils.

| | Industrially produced fish oils | | | Natural fish oils | | |
|---|---|---|---|---|---|---|
| **Fatty acid** | **Menhaden fish oil [%][a]** | **Chilean fish oil [%][a]** | **Russian fish oil [%][a]** | **Mackerel body oil [%][a]** | **Capelin oil [%][a]** | **Herring body oil [%][a]** |
| C14:0 | 7.9 | 6.4 | 7.6 | 8.2 | 6.8 | 7.4 |
| C15:0 | 0.6 | 0.8 | Tr | 0.6 | Tr | Tr |
| C16:0 | 19.8 | 20.1 | 18.2 | 12.6 | 10.6 | 13.8 |
| C16:1 | 9.8 | 5.8 | 6.9 | 3.4 | 9.5 | 7.5 |
| C16:2 | 1.3 | 0.5 | 0.6 | Tr | 0.5 | 0.8 |
| C16:3 | 1.4 | Tr | Tr | Tr | Tr | 0.6 |
| C16:4 | 0.8 | 0.7 | 1.5 | Tr | 0.9 | 1.1 |
| C18:0 | 3.4 | 4.2 | 2.1 | 1.5 | 0.8 | 1.2 |
| C18:1 | 12.6 | 17.7 | 13.6 | 9.6 | 11.2 | 9.9 |
| C18:2 | 1.3 | 1.4 | 1.2 | 2.2 | 1.1 | 0.9 |
| C18:3 | 1.2 | 0.8 | 0.7 | 2.3 | 0.5 | 0.6 |
| C18:4 | 3.9 | 2.1 | 3 | 6.1 | 2.1 | 2.2 |
| C20:0 | Tr | -- | -- | -- | -- | Tr |
| C20:1 | 1.3 | 1.3 | 5.7 | 10.6 | 19.1 | 10.3 |
| C20:4 | 2 | 1.7 | 1.7 | 1.9 | Tr | 0.5 |
| **C20:5** | **12.7** | **13.4** | **17.4** | **6.6** | **7.8** | **10.1** |
| C22:1 | 1.4 | Tr | 6 | 15.8 | 22.7 | 20.7 |
| C21:5 | 0.6 | Tr | 0.5 | Tr | Tr | 0.5 |
| C22:5 | 2 | 3.1 | 2.2 | 1.1 | 0.5 | 0.9 |
| **C22:6** | **11.2** | **18.4** | **10.2** | **12.8** | **3.9** | **10** |

[a]Data adapted from Ref. [42] showing % area of total detected area for all fatty acids using $Ag^+$-HPLC.

Since the fatty acid composition of fish oil depends to a great extent on the species used to produce the oil, it is possible to obtain oils rich in either EPA or DHA depending on the fish processed. A brief overview of composition of fish

oils from various fish species rich in EPA and DHA is presented in Table 2-2 [43].

**Table 2-2.** EPA and DHA contents of fish oils from various fish species.

| Fish species | EPA [%][a] | DHA [%][a] |
|---|---|---|
| Tuna | 6 | 22 |
| Sardine | 16 | 9 |
| Anchovy | 22 | 9 |
| Menhaden | 14 | 8 |
| Farmed salmon | 7 | 11 |

[a]Data from Ref. [43].

An alternative source for EPA and DHA besides fish oil is microbial or single cell oil (SCO), which is oil produced by microorganisms, including marine algae and bacteria, fungi or yeasts [44-46]. The global production of SCO in 2003 was about 700 tons [45] and since then has increased to about 1000 tons in 2009 [33]. The production of PUFA from SCO offers several advantages over that from fish oil, since the microbial cells can be grown in controlled fermenters or bioreactors, thereby avoiding issues with environmental contaminants, such as polychlorinated biphenyls (PCB), heavy metals and dioxins [44]. Furthermore, microbes can synthesize oils with a simple fatty acid profile and a high content of a specific fatty acid. The disadvantages are mainly the limited production capacity and relatively high production costs. Nevertheless, a very promising microbial strain already used commercially is *Crypthecodinium cohnii*, a heterotrophic marine dinoflagellate, which is capable of producing over 40% of its biomass as oil [45], containing about 50% DHA while no other PUFA are produced in any significant amount [47].

Squalene (Fig. 2-3) is another valuable dietary constituent found in marine fish, especially in shark liver oil where it can reach levels of more than 40% [48]. Squalene is a terpenoid, which acts as an antioxidant, inhibits the development of

various tumors, protects the skin against bacterial and fungal infections for patients suffering from atopic dermatitis and has many more health benefits [48].

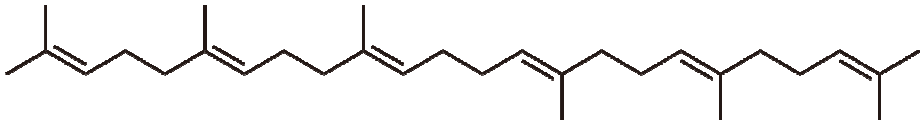

**Figure 2-3.** Chemical structure of squalene.

Vitamin A (retinol) and D levels in fish oil and especially fish liver oils are relatively high, with retinol reaching levels of about 287 and $3x10^6$ μg/100 g fat in herring and cod liver oil, respectively, while vitamin D in the same oils can reach about 100 and 210 μg/100 g fat. Therefore, fish oil and fish liver oils have been previously considered to be an important source of those vitamins. However, since synthetic forms of vitamins are readily available in most parts of the world, the main interest in fish oil today is associated to their high content in LC-PUFA.

### 2.1.2 Health benefits of LC-PUFA

Fish has been considered to be an essential part of a healthy diet ever since it was suggested by the ancient Greek philosopher Plato in the $5^{th}$ to $4^{th}$ century BC [49]. The use of marine lipids for medical purposes in the form of cod liver oil as a treatment for arthritis has been documented in the scientific literature in the 1780s [50]. In the $20^{th}$ century, marine lipids have gained attention in the early 1950s when Strøm and Jensen [51] examined the diet of Norwegian families during the war years and revealed that a higher consumption of fish during World War II correlated to a decrease in fatal heart attacks. In the early 1970s, Dyerberg *et al.* [52-54] analysed the fatty acid composition of the plasma lipids in Greenland Eskimos and found a strong correlation between their diet rich in fish and the low incidence of heart diseases. Since the 1970s numerous studies have shown that the LC-PUFA found in fish oil exhibit many health benefits [55, 56], especially suggesting that EPA and DHA have beneficial effects on heart health and may

lower the risk of cardiovascular disease (CVD) [57, 58]. Noteworthy, ω-3 fatty acids such as EPA and DHA obtained from fish oils seem to be superior in reducing the rates of all-cause mortality, cardiac and sudden death, and possibly stroke compared to those found in vegetable oils, such as α-linolenic acid ( C18:3 ω-3, ALA) [59, 60].

EPA and DHA may also have beneficial effects on patients with type-2 diabetes [61-63], arthritis as well as other inflammatory and autoimmune diseases, including rheumatoid arthritis, Crohn's disease, ulcerative colitis, psoriasis, lupus erythematosus, multiple sclerosis and migraine headaches [64]. Furthermore, consumption of DHA has beneficial effects on brain development and function and may alleviate cognitive decline and dementia, age-related macular degeneration and depression [65-71].

PUFA obtained from marine sources are mainly consumed in the form of either TG or FAEE. However, there are controversial results concerning the absorption of PUFA in the form of TG and FAEE. Studies conducted in the 1980s have shown that absorption of EPA and DHA was lower when ingested as FAEE compared to TG [72, 73]. However, in later studies the absorption of PUFA in TG and FAEE forms by the human body were found to be similar [74, 75]. In the case of TG ingestion, EPA and DHA are more readily absorbed when located in the middle (*sn*-2) position of the triacylglycerol [76].

Due to the demonstrated health benefits of EPA and DHA the American Heart Association recommends at least two servings of fatty fish per week [77, 78]. Many expert committees in other countries recommend a minimum EPA and DHA intake of about 0.2 g/day, while the US Food and Drug Administration (FDA) suggested in 2000 that the daily intake of EPA and DHA in the form of fish oil should not exceed 3 g/day [36]. Since the average intake of ω-3 fatty acids in the Western diet is about 0.15 g/day, which is below the recommended levels, there is a great potential for the enrichment of food products with PUFA [36]. The increased awareness of consumers about the numerous health benefits of ω-3 PUFA has led to a growing demand for food products and supplements containing EPA and DHA [36]. One approach for increasing the level of PUFA in our diet is

to increase the ω-3 content of meat and eggs by mixing fish meal and oil into animal feed. However, fish oil and PUFA can also be used in food formulations in microencapsulated form, as discussed in Section 2.3.2.

Functional foods enriched with PUFA available on the market include bread, bakery products, pasta, yogurts, spreads, juices and others [36]. Furthermore, infant formula rich in EPA and DHA derived from both fish oil and SCO have gained great attention in many parts of the world because they seem to aid in the proper development of the brain and eyes of the infant [69]. However, controversial studies indicating that elevated intakes of ω-3 PUFA could lead to detrimental health effects in infants suggest that only modest amounts of ω-3 PUFA should be administered to infants or consumed by pregnant or breastfeeding women [38].

### 2.1.3 Stability of fish oil

Fish oil rich in PUFA is prone to deterioration due to autooxidation, polymerisation and hydrolysis. When fish oil is exposed to oxygen, it appears that for some duration of time no oxidation occurs. This period is called the induction period after which a rapid uptake of oxygen and autooxidation of the oil takes place. The sequence of reaction steps involved in autooxidation are called the initiation, propagation, branching and termination [1, 79], which are illustrated in Fig. 2-4.

Initiation:

$RH \Rightarrow R\bullet + H\bullet$ free radicals

Propagation:

$R\bullet + O_2 \Rightarrow ROO\bullet$ peroxy free radical

$ROO\bullet + R'H \Rightarrow ROOH + R'\bullet$ hydroperoxide + free radical

Branching:

$ROOH \Rightarrow ROO\bullet + H\bullet$

$ROOH \Rightarrow RO\bullet + OH\bullet$

$2\ ROOH \Rightarrow RO\bullet + H_2O + ROO\bullet$

Termination:

$ROO\bullet + ROO\bullet \Rightarrow$ stable products

$ROO\bullet + R\bullet \Rightarrow$ stable products

$R\bullet + R\bullet \Rightarrow$ stable products

**Figure 2-4.** Reaction steps involved in autooxidation.

The first reaction step in autooxidation is called initiation, where a C-H bond of a lipid molecule (RH) is broken to form the first free radical (R•). This initiation step is more likely to happen if the oil is exposed to heat, light, metal ions and enzymes such as lipoxygenase [1]. In the propagation step, the free radical reacts with oxygen ($O_2$) to form peroxy free radicals (ROO•), which can then further react with a lipid molecule (RH) to give another free radical (R'•) and hydroperoxide (ROOH). In the branching steps of autooxidation, this hydroperoxide (ROOH) can breakdown to produce more free radicals. Therefore, a rapid increase in the number of free radicals and peroxy free radicals leads to the acceleration of the reaction mechanism.

Autooxidation can also happen in the dark and at low temperatures due to the very low activation energies required for the first step [1]. If no antioxidants are present, fish oil would be rapidly oxidised and completely deteriorate. However, there are some reactions that may lead to a reduction in free radicals, which are summarized under the termination step in Fig. 2-4. Catalyzed by metal ions the hydroperoxides can react further, releasing hydrocarbons, aldehydes,

ketones and alcohols, thereby generating undesirable flavors and aromas, including rancid off-flavors, such as short chain molecules with very low odour threshold levels [1].

The addition of antioxidants and metal chelating agents can substantially reduce the amount of free radicals. Among the numerous antioxidants and chelating agents used for fish oil are butylated hydroxyanisole (BHA), butylated hydroxytoluene (BHT), tocopherols, rosemary extract, boldo extract, ascorbic acid, ascorbyl palmitate, propyl gallate, gallic acid, lactoferrines, ethylene diamine tetraacetate (EDTA), citric acid, and others [79].

Polymerisation usually takes place when oils containing unsaturated fatty acids are heated to elevated temperatures of around 180°C. However, in the case of fish oil, polymerisation can occur even at room temperature due to the very high levels of PUFA. Free radicals (R•) formed during oxidation further react to form polymers and even cyclic compounds, which can influence the viscosity and flavor of the oil [1].

Hydrolysis of fish oil due to the reaction of TG with water is usually very slow at room temperature. However, enzymes or catalysts can greatly enhance the reaction rate and accelerate the formation of free fatty acids, monoacylglycerols and diacylglycerols. The moisture level of refined fish oil is usually very low (< 0.1%). Nevertheless, water can reach levels of up to 0.5% in fish oil. The enzyme lipase can be introduced by microorganisms (yeast or mould) or during processing of the fish since the enzyme is present in the flesh and liver of the fish [1]. Free fatty acids can then be broken down by the enzyme lipoxygenase to volatile off-flavors [1]. However, during refining of the fish oil the moisture level should be greatly reduced and the enzymes introduced by the fish are usually inactivated during the high temperature treatments [1].

## 2.2 Supercritical fluids

### 2.2.1 Introduction

A pure component when heated above its critical temperature and pressurized to a level above its critical pressure but below the pressure needed for solidification is called a supercritical fluid. In the supercritical fluid region the phase boundary between the liquid and vapor phases disappears, thus, both phases having identical density become indistinguishable and form what is often referred to as 'dense gas' [80]. Above the critical temperature a pure gas cannot be liquefied even at very high pressures, as illustrated in Fig. 2-5 for $CO_2$.

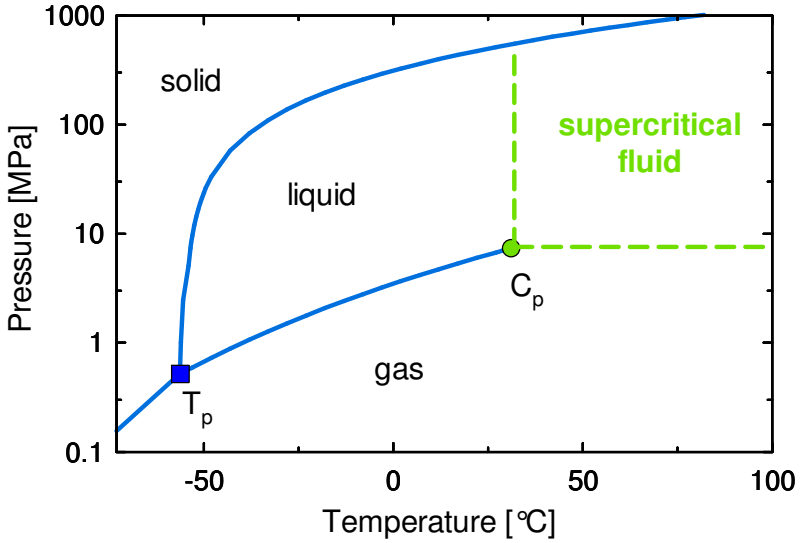


**Figure 2-5.** Phase diagram for pure $CO_2$ showing the critical point ($C_p$) and triple point ($T_p$).

Depending on molecular size, polarity and intermolecular hydrogen bonding, the critical temperatures of pure substances vary over a wide range, with water having a particularly high critical temperature ($T_c$=374.2°C) and pressure ($P_c$=22 MPa), while that for carbon dioxide ($CO_2$) is considered to be moderate ($T_c$=31.1°C, $P_c$=7.4 MPa) [81]. Supercritical carbon dioxide (SC-$CO_2$) is the most widely used supercritical fluid (SCF) due to its moderate critical pressure and temperature, which allows processing at nearly ambient temperatures thereby

minimizing degradation of thermally labile substances. As well, SC-$CO_2$ is a solvent with physical properties in between those of a gas and liquid that is environmentally benign, is generally regarded as safe (GRAS), easily removable upon depressurization, recyclable and readily available.

### 2.2.2 Physical and transport properties

In Fig. 2-5, there is no sudden change of component properties when crossing the 'dashed lines' from the liquid or gas region into the supercritical fluid region. With the exception of the critical point, the variation in fluid properties is monotonous. The values for density, viscosity and diffusivity of supercritical fluids are between those of gases and liquids (Table 2-3).

**Table 2-3.** Physical properties of supercritical fluids (SCF).

| **Physical property** | **Gas** | **SCF** | **Liquid** |
|---|---|---|---|
| Density [g/cm$^3$] | 0.001 | 0.2-1.0 | 0.6-1.6 |
| Viscosity [mPa.s] | 0.0001 | 0.001 | 0.01 |
| Diffusivity [cm$^2$/s] | 0.1 | 0.001 | 0.00001 |

However, at the critical point, some physical properties such as heat capacity and thermal conductivity exhibit a maximum. Gas-like diffusivity and viscosity, low surface tension, and liquid-like density, together with the tunable solvent power of supercritical fluids, are particularly advantageous for processes involving mass transfer, such as extraction and fractionation. Transport properties of supercritical fluids, such as viscosity, diffusivity and thermal conductivity are influenced by pressure, temperature and concentrations of solute or co-solvent. Data on transport and physical properties of supercritical fluid systems are essential for designing processing equipment. However, they are challenging to measure and quantify accurately to reflect real processing situations, where often multicomponent mixtures at considerable concentrations are encountered rather than dilute binary mixtures. Numerous attempts have been made to develop

models and correlations to accurately predict transport properties. However, the accuracy of experimental data still outperforms most correlations and models, which indicates that more research is needed to fully understand all factors impacting transport properties.

#### 2.2.2.1 Density

Close to the critical point the density of supercritical fluids is highly dependent on pressure and temperature, where the isothermal compressibility of $CO_2$ tends to infinity, whereas at higher pressures the influence of temperature is less pronounced. The pressure dependence of density is illustrated in Fig. 2-6, where the slope of the isotherms close to the critical point located in the supercritical region is steeper than at higher pressures and temperatures.

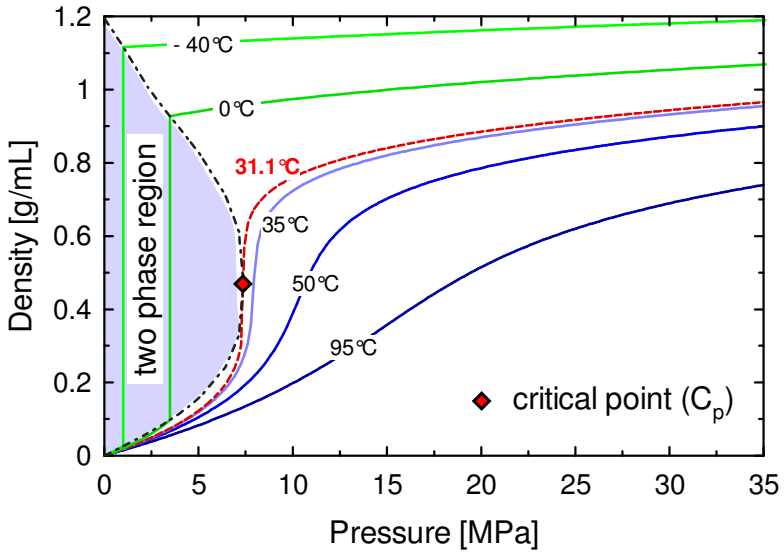


**Figure 2-6.** Density of pure $CO_2$ as a function of pressure at various temperatures. Data from Ref. [82].

The density and subsequently the solvent strength of a supercritical fluid are adjustable by modest changes in pressure and temperature, which is utilized in solubility-based separation processes.

#### 2.2.2.2 Viscosity

The dynamic viscosity of neat $CO_2$ increases with pressure and decreases with temperature, as illustrated in Fig. 2-7 [82, 83].

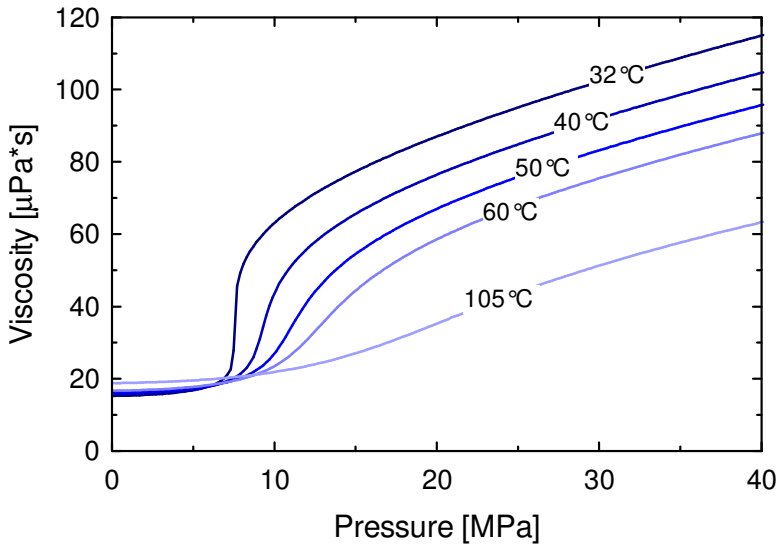


**Figure 2-7.** Viscosity of pure $CO_2$ as a function of pressure at various temperatures. Data from Ref. [82].

It is challenging to measure the viscosity of supercritical fluids close to the critical point due to the highly compressible nature of the fluid phase. Therefore, there are discrepancies between results obtained by different experimental methods [83]. For example, experimental data for the dynamic viscosity of SC-$CO_2$ determined using a capillary instrument, suggesting that the viscosity increased substantially along isotherms in the vicinity of the critical point [84], were found to be inaccurate when compared to other methods [85]. It has been shown in later measurements carried out using an oscillating disc viscometer that there is only a mild divergence (<1%) of the viscosity isotherms in the vicinity of the critical point [85]. The oscillating disc viscometer is better suited for measurements close to the critical point, whereas compressibility of SC-$CO_2$ with capillary instruments can lead to errors because such instruments require an appreciable pressure drop across the capillary. The viscosity of binary or multi-component mixtures of SC-$CO_2$ involving solute and co-solvent mixtures is even

more complex to measure and only limited data are available in the literature [86, 87]. Using a capillary viscometer, Yener *et al.* [87] found that the viscosity of SC-$CO_2$ saturated with methyl oleate at maximum concentrations of 4-5 wt% increased by 15-20%, compared to neat SC-$CO_2$ at 13.7 MPa and 50$^{o}$C. The viscosity increase for SC-$CO_2$ mixed with lipids was found to be linear with increasing lipid concentration. The mixture viscosity of SC-$CO_2$ with various co-solvents at concentrations ranging from 1 to 5 mol% was measured using a falling weight viscometer, indicating that the fluid viscosity was increased by the co-solvent addition, depending on the size, polarity and concentration of co-solvent molecules [88]. Therefore, during separation processes, changes in the concentration of solutes or co-solvent can have a pronounced effect on the viscosity of the supercritical phase, thereby impacting fluid flow, diffusivity, thickness of boundary layer and, finally, the mass transfer rate.

#### 2.2.2.3 Diffusion coefficient

The diffusion coefficient being influenced by viscosity is equally important for separation processes involving mass transfer. Diffusion in supercritical fluids was reviewed by Liong *et al.* [89], including a description of experimental methods and a discussion of various factors influencing diffusion coefficients. Diffusion coefficients of solutes in supercritical fluids are affected by numerous factors, such as temperature, pressure, solute and co-solvent concentrations, density, viscosity, as well as molar volume, molecular weight, structure and polarity of the solute. Similar to viscosity, interactions between solute, solvent and co-solvent can affect the diffusion coefficient. An excellent review of binary diffusion coefficients at infinite dilution in supercritical fluids, as well as graphical correlations and trends, are given by Suárez *et al.* [90]. The following general trends can be observed: diffusion coefficients in supercritical fluids increase with increasing temperature and decreasing pressure, due to reduced density and viscosity, leading to decreased collisions and increased mean free paths of the solute. Additionally, smaller molecules diffuse faster than larger ones and diffusion coefficients of polar solutes seem to be more affected by temperature

changes than those of non-polar or low polarity substances, indicating that interactions between solute and solvent need to be considered.

Most data available in the literature regarding diffusion coefficients of solutes in SC-$CO_2$ have been reported for infinite dilution. However, the reality in some separation processes is far from that, and thus diffusion coefficients determined at infinite dilution have limited applicability and the concentration dependence of diffusion coefficients has to be taken into account [91]. Likewise, since most experimental data have been determined for infinite dilution, most of the subsequent correlations and models developed to predict diffusion coefficients are also valid for infinite dilution. For some nutraceutical solutes of very low solubility, such as β-carotene, the diffusion coefficient at infinite dilution may be applicable. However, for cases where solubility is high the influence of concentration should not be overlooked. This can be accomplished by using a modified form of the Darken equation [92], which takes into account the solute concentration and a thermodynamic factor that can be predicted by an equation of state approach [93].

Diffusion coefficients of unsaturated fatty acid methyl esters with carbon chain lengths ranging from $C_{16}$ to $C_{24}$ in SC-$CO_2$ were reported by Funazukuri *et al.* [94]. Additionally, the authors tested several correlations for calculating the binary diffusion coefficient and proposed a new correlation based on the Schmidt number. Diffusion coefficients of lipids, including oleic, linoleic and linolenic acids, methyl and ethyl oleate and di- and trilinolein, were determined by Rezaei and Temelli [95] based on the peak broadening technique using supercritical fluid chromatography; the diffusion coefficients decreased in the following order: fatty acid esters > fatty acid > triglycerides, indicating that both size and polarity play a role. The effects of molecular weight and degree of unsaturation of lipids on infinite dilution binary diffusion coefficients in SC-$CO_2$ were assessed by Funazukuri *et al.* [96], showing that for $C_{18}$ fatty acids with increasing number of double bonds, the diffusion coefficient decreased moderately in the case of methyl and ethyl esters as well as triglycerides. However, for free fatty acids ($C_{18}$ and $C_{20}$) the trend was the opposite, which may be explained by a stronger effect of

the carboxyl group on diffusivity than that of double bonds. A relatively simple hydrodynamic equation relating the binary diffusion coefficient at infinite dilution to viscosity and temperature of the supercritical fluid, together with two solute dependant parameters fitted to experimental data, was successfully applied to lipids and other solutes, including EPA, DHA, α-tocopherol, and β-carotene [97]. Under conditions away from the binary mixture critical point, where diffusion coefficients tend to zero, a correlation for calculating the binary diffusion coefficients of various biomaterials, such as tocopherols and triglycerides, can be used with average deviations of ±10% compared to literature data [98]. The correlation requires the solvent molecular weight, reduced temperature, density, solute molecular weight and an estimate of the solute critical volume as input data.

#### 2.2.2.4 Thermal conductivity

Knowledge of thermal conductivity of the supercritical fluid phase is important for separation processes involving heat transfer, where separation is brought about by a change in temperature, thereby affecting density and solubility. Thermal conductivity for pure $CO_2$ as a function of pressure and temperature is illustrated in Fig. 2-8 [82, 99].

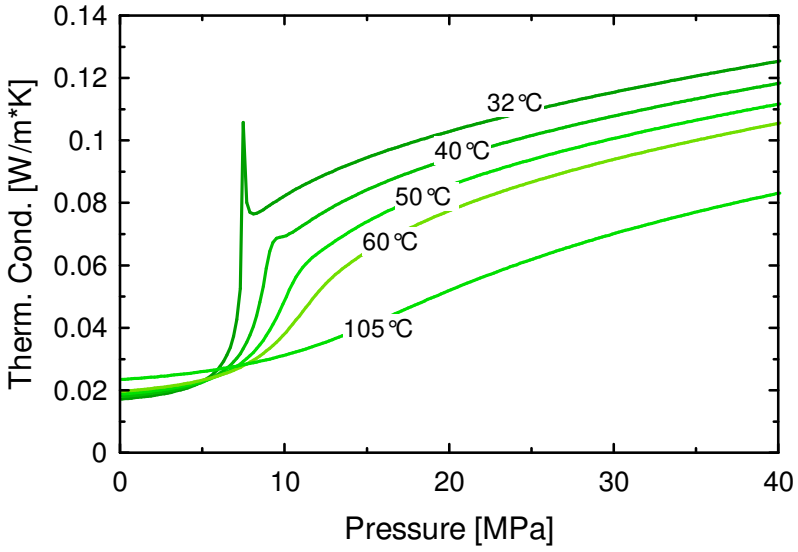


**Figure 2-8.** Thermal conductivity of pure $CO_2$ as a function of pressure at various temperatures. Data from Ref. [82].

#### 2.2.2.5 Interfacial tension

Interfacial tension (IFT) is related to the amount of energy required to create a new interface. In most systems consisting of a liquid in contact with a compressed dense gas such as $CO_2$, the IFT usually decreases with increasing pressure. However, for water in contact with pressurized helium an increase in IFT was reported due to the hydrostatic pressure effect on IFT and the low solubility of helium in water [100]. The IFT of triglycerides, fatty acids and their methyl and ethyl esters decreased when in contact with pressurized $CO_2$ [101, 102]. The IFT of liquids in dense gas systems affects the stability of falling films, jet formation and wetting behavior [103, 104]. A more detailed literature review and discussion of IFT in dense gas systems is provided in Chapters 4, 6, and 7.

### 2.2.3 Solubility in supercritical fluids

Solubility describes the equilibrium between a solute and a solvent and is a key aspect of separations involving supercritical fluids, similar to conventional solvent processing. Solubility is the maximum amount of a solute that can be solubilized in a solvent at a given temperature and pressure, and is typically reported in terms of mole fraction (i.e., moles of solute per mole of solvent).

#### 2.2.3.1 Factors affecting solubility in supercritical fluids

Solubility of a solute in SC-$CO_2$ is highly dependent on temperature and pressure, which influence $CO_2$ density and subsequently solvent power. The solubility of a substance in a supercritical fluid depends on the interactions between the solute and solvent. Increasing the pressure leads to liquid-like density of the supercritical fluid, thus increasing the probability of interactions between the solute and solvent, including dispersion, hydrogen-bonding and polar interactions, such as the dipole-quadrupole interactions in the case of $CO_2$ [81]. Consequently, solubility increases dramatically with pressure. Increasing temperature leads to a decrease in density, which is more pronounced at pressure levels close to the critical point. However, temperature not only affects density of the solvent but it also leads to an increase in the vapor or sublimation pressure of the solute. Therefore, the impact of temperature on solubility depends on both effects. A

temperature increase usually leads to a decrease in solubility at low pressures due to the stronger effect on density, whereas at higher pressures an increase in temperature leads to increased solubility. This results in the well-known crossover phenomenon for solubility isotherms. The pressure, above which the effect of temperature on vapor or sublimation pressure prevails, is called crossover pressure. The solubility isotherms converge with increasing pressure and intersect at the crossover pressure, as illustrated in Fig. 2-9 for caffeine [105], which is a key ingredient of energy drinks, a product of increasing popularity. Separation of solutes can be realized in processes taking advantage of the crossover pressure, which in most cases is a pressure region rather than a specific pressure [106]. Below the crossover pressure, a solute can be precipitated by increasing the temperature at isobaric conditions. This behavior, where solubility decreases with increasing temperature is also referred to as retrograde condensation, which can be of advantage for certain separation processes. In terms of nutraceuticals, heat sensitivity of the target compound would dictate how much temperature can be increased to achieve retrograde condensation.

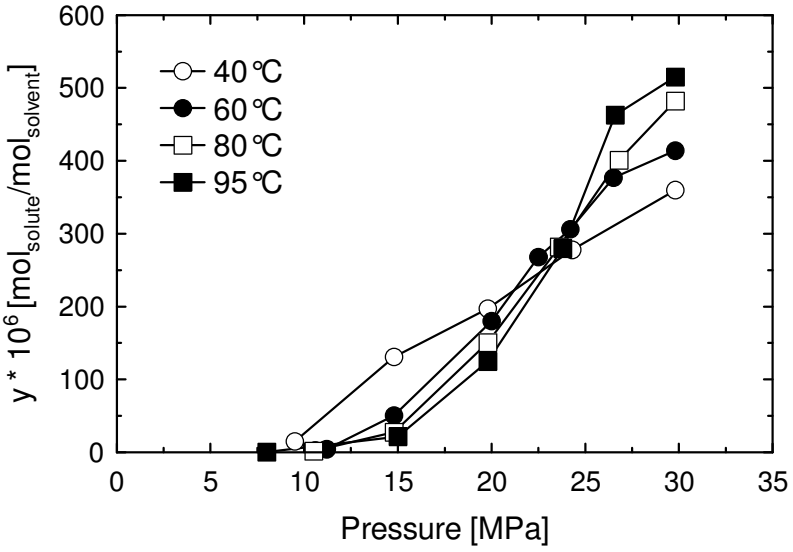


**Figure 2-9.** Solubility of caffeine in SC-$CO_2$ showing the crossover point. Data from Ref. [105].

Solute properties, especially molecular weight, polarity and vapor (or sublimation) pressure, also influence solubility in SC-$CO_2$. The solubility of substances in SC-$CO_2$ is affected by solute-solvent as well as solute-solute interactions, such as hydrogen bonding. Due to the non-polar nature of $CO_2$, the solubility of non-polar components is usually higher than that for polar components with a similar molecular weight. An increase in the molecular size of a solute decreases the solubility in the supercritical fluid. Therefore, non-polar solutes of low molecular weight and high vapor pressure are preferentially solubilized in SC-$CO_2$ at relatively low density conditions, and higher density conditions are needed for larger, slightly polar and less volatile solutes. Thus, a few rules of thumb were established for extractability of natural substances by Stahl and coworkers [107, 108]:

> "1) hydrocarbons and other lipophilic organic compounds of relatively low molecular mass and polarity are easily extractable;
>
> 2) the introduction of polar functional groups, hydroxyl or carboxyl groups render the extraction more difficult or impossible;
>
> 3) sugars and amino acids cannot be extracted up to 500 bar [50 MPa];
>
> 4) fractionation effects are possible if there are marked differences in mass, vapor pressure or polarity of the constituents of a mixture."

Besides temperature and pressure, the solvent power of a supercritical fluid can be adjusted by adding a co-solvent exhibiting interactions, such as hydrogen bonding, charge transfer complex formation, and dipole-dipole coupling between solute and co-solvent molecules [109]. A co-solvent can also interact with the supercritical solvent, which can in turn affect the solubility of a solute [109]. Density of a supercritical fluid solution is increased by the addition of a co-solvent, thereby affecting the solubility of a solute beneficially. In this context, it is noteworthy to mention the so-called co-solvent effect (also referred to as the entrainer effect) [110], which refers to the dramatic increase in both solubility and selectivity when certain co-solvents are added to a supercritical fluid [111-115]. The co-solvent effect can lead to an increase in the solubility of a solute in a supercritical fluid by up to several hundred percent [116], which for some systems

is more than what can be achieved by a pressure increase of several tens of MPa [117]. However, interactions between different solutes in a mixture can also cause a decrease in solubility, as observed for the solubility of capsaicin, which was lower in the presence of β-carotene [118]. Recently, Nobre *et al.* [119] reported the solubility of a mixture of bixin and β-carotene (1:1, w:w) in SC-$CO_2$ at 40 and 60°C and pressures of up to 35 MPa and showed a substantial solubility enhancement of up to about 265% for bixin in the presence of β-carotene. Solubilities of solid mixtures in SC-$CO_2$, including a discussion of the observed increase and decrease of solubility, are reviewed by Lucien and Foster [120]. A beneficial co-solvent effect can be exploited for improving separation processes.

The proper selection of a co-solvent can aid in separation processes by improving selectivity and solubility. For example, the addition of up to 10% (volume %) ethanol increased the solubility of gallic acid from 0.005 mg/$kg_{CO2}$ in pure $CO_2$ to 7.48 mg/$kg_{CO2}$ at 20 MPa and 40°C [121]. Furthermore, the solubility behavior of ternary systems of lipids, co-solvents and SC-$CO_2$ is affected by co-solvent addition [122, 123]. The addition of co-solvents can increase as well as decrease selectivity in fractionation processes of lipids using SC-$CO_2$, if there are specific interactions between the solutes of interest and co-solvent. For example, the addition of ethanol can improve the deacidification of oils, as demonstrated for the separation of free fatty acids (FFA) from palm oil [124] or FFA and peroxides from orange roughy fish oil [125]. However, there are cases where selectivity decreases upon the addition of a co-solvent, such as in the fractionation of shark liver oil, where the separation of squalene from di- and triglycerides decreased with increasing ethanol content [125].

#### 2.2.3.2 Solubility determination and correlation

Methods to determine the phase equilibrium or solubility of a solute in a supercritical fluid can be divided into two classes depending on how the concentration in the phases is determined, namely analytical (direct sampling methods) and synthetic (indirect methods) [126]. Several reviews discussing the pros and cons of the various experimental methods can be found elsewhere [126-

128]. However, some challenges that can be encountered when measuring solubilities are highlighted here and discussed briefly, using the case of β-carotene as an example. The literature data for the solubility of β-carotene in SC-$CO_2$ are very scattered with differences ranging over more than an order of magnitude [129, 130]. These discrepancies can be attributed to differences in the purity of the solutes as well as the limitations of the experimental techniques used. Impurities in the sample can enhance or reduce the solubility of a solute [131], due to impurities acting like a co-solvent. Furthermore, β-carotene can oxidize and isomerize easily during experiments or when exposed to air, which requires special precautions during sample preparation and measurements [132]. The crystalline nature of β-carotene affects solubility; as shown by Sakaki [133], the solubility of crystalline β-carotene was lower compared to that of amorphous β-carotene, which may be expected due to the higher heat of fusion for crystalline β-carotene. In addition to issues related to purity or cystallinity of β-carotene, the different experimental methods applied for solubility determination come with certain limitations and can lead to errors as well. For example, in systems using a dynamic method reaching true equilibrium may be challenging. In static systems or recirculation systems, attainment of equilibrium may be monitored by adequate sensors to ascertain changes in the solute-SC-$CO_2$ mixture over time.

After ensuring proper equilibration one has to watch out for another source of error caused by the sampling/quantification of the solute in the supercritical phase. During off-line sampling from a static equilibrium cell a small volume of equilibrated fluid phase is removed, which can lead to changes in pressure and/or temperature, thereby disturbing equilibrium. Furthermore, loss of solute by precipitation in the valves or sampling lines can occur. To minimize disturbance of the equilibrium inside a static equilibrium cell, variable volume cells have been developed, which compensate for the sample volume removed. On-line sampling allows solute quantification prior to the depressurization step by means of chromatographic or spectrophotometric systems attached to the extraction cell. However, the use of UV detectors can lead to errors due to the potential saturation of the sensor [134]. Another method based on a quartz crystal

microbalance (QCM) was used by Saldaña *et al.* [135] to measure the solubility of β-carotene *in situ*, which eliminates the need for sampling. However, the QCM technique is very sensitive to environmental factors and loading the crystal uniformly can be challenging. In summary, solubility measurements of unstable substances having a relatively low solubility, such as carotenoids, in SC-$CO_2$ are challenging and great care must be taken to avoid the above-mentioned errors and pitfalls.

There are also numerous studies where solubility for a component is reported based on dynamic extraction of a complex plant matrix. In this case, the 'apparent solubility' is not only based on thermodynamic solubility but also on the interactions of the solute with the solid matrix, as well as the potential co-solvent effects of the other components present. This approach may be more representative of the complex multicomponent systems under consideration for process development purposes; however, care must be taken to ensure equilibrium criteria are met. These include having sufficient solute present to saturate the $CO_2$, using low enough flow rates to allow sufficient residence time, and evaluating the slope of the initial linear portion of the extraction curve, which corresponds to the solubility-controlled region, rather than reporting the yield obtained on a single point on the extraction curve. Comparison of β-carotene solubility in the binary system of pure β-carotene+SC-$CO_2$ to the apparent solubility obtained in the multicomponent carrot system revealed a 5-10 fold reduction in the multicomponent system under similar temperature and pressure conditions mainly due to interactions of β-carotene with the solid matrix [135].

Bibliographic summaries covering high pressure phase equilibrium data published from 1900 to 2004 are available in the literature [126, 136-140]. Furthermore, solubility data as well as correlations for numerous less volatile substances and high boiling substances can be found [141, 142]. An excellent collection of solubility data for more than 780 solutes including liquids, solids, polymers, foods, drugs, nutraceuticals, dyes, pesticides and metal complexes has been compiled by Gupta and Shim [143]. Solubility of numerous nutraceutical compounds in SC-$CO_2$ has been investigated using pure components and mostly

employing static methods. Diaz-Reinoso *et al.* [144] compiled a list of pure phenolic components with antioxidant activity for which solubility has been reported.

Accuracy and precision of measured solubility data are believed to be superior to data predicted by correlations or models based on group contribution methods or equations of state (EoS) in many cases. For example, the performance of six different cubic EoS to predict the solubility of cholesterol and β-carotene in SC-$CO_2$ and ethane was assessed by Hartono *et al*. [145]. The study revealed deviations by several orders of magnitude between the experimental data and predicted solubility values in cases of the Van der Waals and Redlich Kwong EoS, whereas the Mohsen-Nia–Moddaress–Mansoori EoS delivered acceptable results [145]. However, the use of EoS requires the knowledge of parameters, which in many cases are not experimentally accessible, such as critical pressure and temperature. Since those parameters cannot be measured experimentally due to decomposition of the solute, as in the case of cholesterol and β-carotene, the critical parameters need to be estimated by group contribution methods, which add uncertainty to the calculations [146]. Furthermore, experimental data are needed to adjust interaction parameters in those EoS models. The solubility of a mixture of bixin and β-carotene in SC-$CO_2$ taking into account the interaction between the solutes was described reasonably well with a model based on the Peng-Robinson EoS, with deviations from experimental data of about 18.2 and 44.6% for β-carotene and bixin, respectively [119].

Empirical, semi-empirical and theoretical correlations to model solubility data for binary supercritical fluid systems [147-149] can be used in certain cases to predict solubility data based on available experimental data. Unlike approaches utilizing EoS, which require properties of solutes, such as critical properties, that are often difficult or impossible to determine experimentally, these empirical, semi-empirical and theoretical correlations are mostly based on accessible density and solubility data. If properties required for modeling are not available, the application of property estimation methods is required, leading to uncertainties in the prediction of solubility data. A well known density-based correlation for

solubility data was developed by Chrastil [147] that relates the solubility $S$ [g/L] of a solute to the solvent density $\rho$ [g/L] and temperature T [K]:

$$S = \rho^k e^{(a/T+b)} \tag{2-1}$$

where $k$ is the association constant, and $a$ and $b$ are defined as

$$a = \frac{\Delta H}{R} \tag{2-2}$$

$$b = -\ln\left(\frac{M_G^k}{M_A + k * M_G}\right) + q \tag{2-3}$$

with the ideal gas constant $R$, the sum of heat of solvation and vaporization $\Delta H$, a constant $q$, and the molecular weights of solute $M_A$, and solvent $M_G$. Chrastil's model is based on the assumption that a solute molecule (A) associates with $k$ molecules of the supercritical solvent (G) forming a solvate complex ($AG_k$), which is in equilibrium with the supercritical fluid. Plotting ln($S$) versus ln(ρ) results in a straight line with a slope of $k$ and intercept of $(a/T+b)$. For solutes with a low solubility, the solubility $S$ can be converted from [g/L] into a mol fraction $y$ in [$mol_{solute}$/$mol_{solvent}$] by multiplying Eq (2-1) with $\rho * M_A/M_G$, which leads to:

$$y = \rho^{k+1} \frac{M_A}{M_G} e^{(a/T+b)} \tag{2-4}$$

Plotting ln($y$) versus ln($\rho$) also results in a straight line, now with a slope of (k+1), as illustrated in Fig. 2-10 for the solubility of caffeine in SC-$CO_2$ [105].

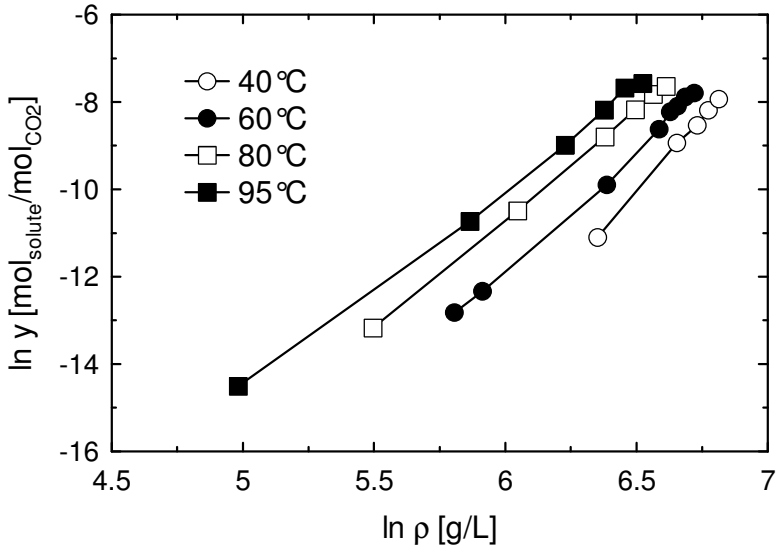


**Figure 2-10.** Chrastil plot for solubility of caffeine in $CO_2$. Data from Ref. [105].

The density-based correlation methods for solubility data work reasonably well for non-polar solutes and to a lesser extent for polar solutes at pressure levels corresponding to high supercritical fluid densities [150]. However, when applied over the entire supercritical fluid density range to systems with higher concentrations or polar solutes, simple relationships between the solute solubility and solvent density exhibit a weakness, because the complex nature of solute-solvent and solute-solute interactions cannot be described by these correlations. Chrastil's model was applied to correlate literature data for solubility of lipids, such as fatty acids, mono-, di-, and triglycerides, and fatty acid esters as well as minor lipid components, such as β-carotene, α-tocopherol, stigmasterol, and squalene in SC-$CO_2$ [130, 131]. Solubility data of oleic acid, β-carotene, and capsaicin in SC-$CO_2$ were also correlated using Chrastil's model [151], resulting in deviations between experimental and correlated solubility values of up to about 30% for both oleic acid and β-carotene. Furthermore, Skerget *et al.* [151] found that the association constant *k* differs for liquid $CO_2$ and SC-$CO_2$, which indicates that the same model constants cannot be used for both cases.

Phase equilibria and solubility of fish oil TG and FAEE in SC-$CO_2$ have been studied extensively over the past decades [22, 152-160]. Staby *et al.* [155]

measured the phase equilibria for fish oil FAEE in sub- and supercritical $CO_2$ up to 22 MPa at 10, 40 and 70°C in order to determine the molar composition ratio (i.e. partition coefficient or K values) between the vapor and liquid phase. The K values depended strongly on pressure and carbon chain length of the esters and to a lesser extent on the degree of unsaturation and position of the double bonds [155]. Borch-Jensen and Mollerup [153] determined the phase equilibria of fish oil in sub- and supercritical $CO_2$ up to 65 MPa at 20, 40, 80 and 120°C, reporting that fish oil and $CO_2$ were not completely miscible at any of the temperatures investigated. Riha and Brunner [157] determined the phase equilibria of 13 different fish oil FAEE mixtures up to 25 MPa and correlated the data using the Peng-Robinson EoS.

### 2.2.4 Applications of supercritical fluids related to fish oil

Due to the drawbacks of conventional techniques requiring harsh processing conditions such as steam at elevated temperatures, processing of heat sensitive materials containing PUFA using SC-$CO_2$ offers numerous advantages [161]. Fractionation of fish oil FAEE using SC-$CO_2$ has been investigated by numerous research groups. In an attempt to fractionate fish oil FAEE in a semi-continuous system, Eisenbach [162] used a packed column equipped at the top with a "hot finger" held at 90ºC to generate a reflux to take advantage of retrograde condensation. This method was suitable for separating fractions of different carbon lengths but showed limited ability in separating EPA and DHA from other $C_{20}$ and $C_{22}$ fatty acids, respectively. Nilsson [163] used a packed column equipped with individually controlled heaters to create temperature zones, ranging from room temperature at the bottom of the column up to 100ºC at the top. By applying incremental pressure programming to the column, it was possible to reduce the required temperature gradient for fractionation [164].

More recently research activities focused mostly on continuous fractionation of fish oil esters using countercurrent columns. Continuous fractionation of fish oil FAEE was studied in a pilot plant countercurrent packed column [165, 166] to separate low molecular-weight components (LMC; C14 to

C18) from high molecular-weight components (HMC; C20 to C22), obtaining concentrations for HMC in the raffinate of greater than 95 wt% at a recovery of HMC of greater than 95%. Continuous fractionation of squalene from shark liver oil in a countercurrent packed column resulted in squalene with up to 99% purity [167]. Semi-continuous separation of a commercial mixture of fish oil FAEE containing 64% EPA+DHA was investigated by Perretti *et al.* [168] in a column filled with Raschig rings, employing three temperature zones along the column held at constant temperatures of 40, 50, and 60°C, respectively, from bottom to top. In this study [168], 450 g of FAEE mixture were loaded onto the column (L = 3 m, ID = 3 cm) at three different column heights and subsequently fractionated at pressures ranging from 10-30 MPa and $CO_2$ flow rates ranging from 2.5-10 kg/h over a duration of 2 h. By fractionating the FAEE mixture at 15 MPa with a $CO_2$ flow rate of 5 kg/h the total content of EPA and DHA esters was increased from 64% in the feed mixture to about 82% in the raffinate (fractions collected from the bottom of the column). However, the yield of raffinate was less than 10% and the EPA/DHA ratio changed from 1.61 for the initial mixture to 0.65 for the raffinate due to EPA being extracted preferentially over DHA from the column.

Simulation of a countercurrent column was carried out by Gironi and Maschietti [169] after studying the fractionation of a natural mixture of fish oil FAEE by means of a semi-continuous single stage process. The results obtained by the single-stage process showed that in order to achieve the best compromise between selectivity and solubility, the operating conditions resulting in a SC-$CO_2$ density between 570-595 kg/m$^3$ should be selected at relatively high temperatures. For example, at 70°C and 16.7 MPa, an oil with more than 80% of EPA and DHA ethyl esters was obtained in the process, with a recovery of about 40% in the raffinate. With the results obtained in their semi-continuous fractionation experiments as well as available pilot plant data [166], Gironi and Maschietti [169] satisfactorily modeled a continuous fractionation process, which enabled them to study various process parameters, including the number of theoretical stages, reflux ratio and solvent-to-feed ratio. Based on the simulation of the continuous countercurrent process, it seems feasible to obtain a raffinate with

95% (wt. %) of $C_{20}$+$C_{22}$ FAEE, together with 95% recovery of these valuable compounds, by operating a multistage column (from 11 to 30 stages) with a reflux ratio of 2.5-5.2 and a solvent-to-feed ratio in the range of 90-150. The results of such simulations based on mass balances and equilibrium calculations are useful to better understand the influence of various parameters on the theoretical performance of a column. However, in order to calculate the required height and diameter of a packed countercurrent column, mass transfer, fluid flow and flooding behavior considerations should be taken into account, thus requiring more sophisticated calculations, involving properties such as density, viscosity, and diffusivity of both the liquid and gaseous phases as well as interfacial tension, which are often challenging to measure or accurately predict [170-174]. Therefore, more research is needed evaluating both the experimental and theoretical aspects in order to obtain reliable data and to develop further the correlations and models used for calculating such complex fractionation processes.

Another novel approach different from the ones described above in order to concentrate EPA and DHA in the form of FFA or FAEE is the combination of urea fractionation and supercritical processing. The first steps in the development of the process include the use of urea dissolved in hot ethanol and mixing it with FFA or FAEE, thereby forming a complex with their long hydrocarbon chain, which depends on temperature and degree of unsaturation [31]. Then, separation is achieved by cooling until precipitation of urea complexes occurs. However, a potentially better way was suggested, where SC-$CO_2$ containing fatty acids or esters is passed through a bed of urea, which leads to complexation of the monounsaturated and saturated fatty acids, thereby separating them from the polyunsaturates [175]. Furthermore, the fractionation process was improved by combining urea fractionation as described above using ethanol with supercritical antisolvent fractionation (SAFT) [176]. In the combined process, urea complex formation takes place in ethanol, followed by separation of the urea complex using a filter and feeding the filtrate containing fatty acids or ethyl esters, solvent (ethanol and water), and dissolved urea into a pressurized apparatus together with

$CO_2$. By mixing the solution with $CO_2$, the antisolvent effect of $CO_2$ leads to precipitation of urea and water, which is recovered in the first separator, while fatty acids and ethanol can be obtained separately in subsequent separators through sequential pressure reduction steps. With this patented method, it seems possible to obtain PUFA concentrates containing over 90% ω-3 fatty acids.

Jakobsson *et al.* [177, 178] demonstrated that SC-$CO_2$ can also be applied to remove dioxins from deacidified fish oil in a counter-current extraction process. Catchpole *et al.* [125] used a counter-current fractionation column to remove peroxides, fatty acids and odour components from different crude fish oils showing that by the use of ethanol as co-solvent (5 wt%) the purification process could be improved.

The enrichment of LC-PUFA by concentration of fish oil in its natural form instead of FAEE using SC-$CO_2$ has been evaluated by Antunes-Corrêa *et al.* [179] who measured phase equilibrium data from 28 to 50°C and pressures from 7.8 to 29.4 MPa using the dynamic method determining the separation factors for EPA and DHA. The authors [179] reported that enrichment of EPA from fish oil in the form of TG using SC-$CO_2$ seemed ineffective, since EPA had a separation factor close to unity at all conditions studied, while that of DHA was 0.67 at a pressure of 7.8 MPa and 28°C, which makes fractionation possible.

### 2.2.5 Gas-expanded liquids

Gas-expanded liquids (GXL) have gained great attention in the past two decades. A GXL consists of a liquid with a compressed gas dissolved in it, which can cause the liquid phase to expand up to several times its original volume at pressures below 10 MPa [180]. The most common GXL are $CO_2$-expanded liquids (CXL) due to the advantages of $CO_2$, including its moderate critical temperature and pressure, safety, non-toxicity and economics. According to Jessop and Subramaniam [180], CXL can be classified according to the solubility of $CO_2$ in the liquid phase into three classes:

- Class 1 liquids, such as water do not dissolve great amounts of $CO_2$ even at elevated pressures and therefore do not expand to a great extent.

However, addition of co-solvents such as methanol could lead to the formation of ternary systems that can be expanded.

- Class 2 liquids are mostly organic solvents such as short chain alcohols, hexane, acetonitrile, ethyl acetate, which upon dissolution of large amounts of $CO_2$ at moderate pressures (< 10 MPa) can expand by several hundred percent along with a pronounced change in almost every physical property, including density, viscosity, polarity, interfacial tension and others.
- Class 3 liquids include liquids, such as ionic liquids, liquid polymers, and mineral oil that can dissolve only moderate amounts of $CO_2$ and consequently expand less. Due to the limited expansion of Class 3 liquids, the effect of expansion may only change some physical properties noticeably, such as the viscosity but not polarity.

By tuning the pressure and temperature as well as $CO_2$ content of CXL the solvent properties, such as polarity, can span from that of pure $CO_2$ to that of an organic solvent. Therefore, CXL have been applied as solvents for catalytic reactions, separations, particle precipitation, polymer processing and others [180]. Furthermore, CXL offer several advantages compared to pure organic solvents or SC-$CO_2$, because processes can be designed at relatively low pressures compared to SC-$CO_2$, while substantial amounts of conventional solvents can be replaced by $CO_2$, which is non-toxic, non-flammable and fairly easy to recycle. As well, gas solubility in CXL can be enhanced up to 2 orders of magnitude compared to the neat organic solvent, which can be of importance for hydrogenation or oxidation reactions.

#### 2.2.5.1 Properties of gas-expanded liquids

As indicated above, Class 2 CXL expand substantially with pressure up to several hundred percent of the original volume, as illustrated for ethanol, acetonitrile and dimethyl sulfoxide at 25°C in Fig. 2-11.

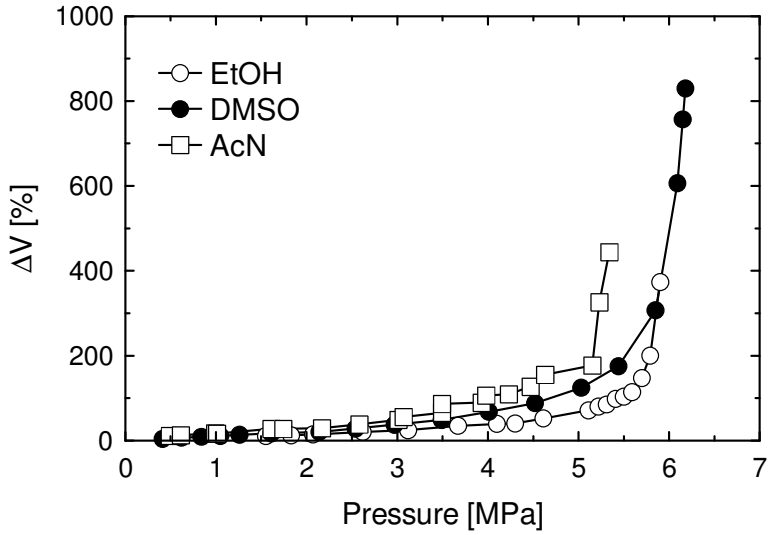


**Figure 2-11.** Volumetric expansion of ethanol (EtOH), dimethyl sulfoxide (DMSO), and acetonitrile (AcN) equilibrated with $CO_2$ at 25°C up to 6.5 MPa. Data from Ref. [181].

Due to that large expansion, several physical properties are affected and change substantially depending on the level of expansion. For example, viscosity of CXL decreases with pressure as a function of $CO_2$ content, which has been measured for various solvents, such as ethanol, methanol and acetone, demonstrating that the viscosity of those CXL decreased fairly linearly with temperature and with $CO_2$ mole fraction in the liquid phase [182-184]. Lipids when saturated and expanded with $CO_2$ exhibit a pronounced decrease in viscosity with pressure as well [185, 186], which is discussed in more detail in Chapters 8 and 9.

The pronounced expansion of polar organic solvents with $CO_2$ can be accompanied with a change in solvent polarity [180], which can be quantified by the Kamlett-Taft $\pi^*$ parameter, that characterizes the local polarity and polarizability of a solvent or by the dielectric constant $\varepsilon$ relating to the bulk solvent polarity. For example, depending on the mole fraction of $CO_2$ in the system $CO_2$+EtOH, the static dielectric constant can be tuned between that of pure $CO_2$ and ethanol ranging from around 1 (non-polar) to about 23 (polar) [187]. By changing the polarity of the solvent system, the solubility of

components in that system can be affected or mechanisms of reactions can be tuned. Besides the aforementioned properties, the expansion of liquids or polymers also affects the density, melting point, conductivity, interfacial tension, and diffusivity of the expanded material [180].

#### 2.2.5.2 Applications of $CO_2$-expanded liquids

The applications for CXL are numerous, including particle formation, enhanced oil recovery, polymer processing, separations and crystallizations, post-reaction separations, switchable solvents and various options to tune catalysed or non-catalysed reactions [180]. The application of expansion with $CO_2$ is of advantage in enhanced oil recovery, where the viscosity of crude oil [188] and interfacial tension decrease substantially with $CO_2$ pressure [189]. As well, the effect of dissolved $CO_2$ on volumetric expansion and reduction in viscosity of lipids contained in oilseeds are factors contributing to the enhanced yield in gas-assisted mechanical oilseed pressing [190, 191]. The versatility of CXL was used for the fractionation of propolis applying a modified gas antisolvent process to obtain a concentrated flavonoid fraction as the primary product, and an essential oil/ethanol fraction as a secondary product [192]. Particle formation processes using gas-expanded liquids and supercritical fluid technology are further discussed in Section 2.3.3.

## 2.3 Particle formation and microencapsulation

Microencapsulation is a process in which a core material is entrapped or coated by a shell material. The core material can be a solid, a liquid or a gas. The core material is also referred to as actives, internal phase or payload. The shell or coating material is also called the wall material, membrane or carrier. Microcapsules consist of one core enveloped by the shell, whereas microspheres carry multiple core particles in a carrier matrix. Microcapsules can fulfill a multitude of functions depending on the encapsulated active ingredient, the shell material, the surrounding environment and the desired release mechanism. Some of the major reasons for food ingredient encapsulation are [193]:

- to protect the core material from the outside environment (light, oxygen, heat, hostile pH conditions),
- to control the release or transfer rate of the core material into surrounding environment, such as the food matrix or the digestive tract (controlled release mechanism),
- to protect the surrounding food matrix from potential deterioration caused by the active core material (iron fortification of dairy products),
- to facilitate easier handling by transforming liquid ingredients into powder form (flavor oils, fish oil),
- to improve food processing (heat stable encapsulated flavors, sweeteners), and
- to mask the core taste and aroma (fish oil).

The first commercial application of microcapsules developed by the National Cash Register Corporation [194] was carbonless copy paper. The key compound of carbonless copy paper is micro-encapsulated dye or ink, which is released upon rupture of the capsule when subjected to pressure caused by the point of the writing instrument. In this non-food application, the release of the core material is caused by an external mechanical force, which is just one of many mechanisms also applied for controlled release of food ingredients.

Release mechanisms play an important role in food systems for the processor as well as for the consumer. A controlled flavor release profile is desirable for the consumer and crucial for satisfactory sensory characteristics especially for low-fat products, which can be achieved by the use of encapsulated flavors in food products [195]. The release rate of the core material into the environment is affected by numerous parameters, such as the coating properties of the shell material and its interactions with the surrounding environment [193]. Physicochemical properties of the coating material, such as density, solubility, orientation, plasticizer level and cross linking are factors influencing the release rate of the core material. The surrounding environment is equally important for

controlled release. The release can be triggered by changing the temperature, pH, moisture, solvent, pressure changes or by mechanical or enzymatic action.

Several mechanisms may be involved in the release of the core material. The most straightforward release mechanism is through fracture of the shell material by internal or external forces. Internal forces can be caused by expansion of the core material or through selective permeation. External forces basically crack open the shell by mechanical forces, such as pressure, shearing, grinding or ultrasonics. Mechanical release mechanisms usually release the core material in a short period of time under controlled conditions. More sophisticated release mechanisms involve the melting of the shell material at a defined temperature or moisture to set free the core active ingredient, such as leavening agents or sweeteners in bakery products or flavors in chewing gums [196]. Another way to set the core free is to remove the shell by dissolution into a surrounding solvent or by biodegradation involving enzymatic action [196]. Diffusion mechanisms are driven by concentration gradients and can be controlled by temperature and the choice of shell material. Crystallinity, cross linking and thickness of the capsule wall play an important role in the diffusion process next to size, shape and polarity of the penetrating molecules [197]. The physicochemical properties of the encapsulated compound as well as the enveloping matrix are crucial to understand the retention or release of encapsulated ingredients. Carbohydrates are common matrices used to encapsulate flavor and aroma compounds by extrusion, spray drying or freeze drying techniques. The retention and release of such aroma compounds greatly depend on the physicochemical characteristics of both the aroma compound and the carbohydrate matrix, which influence the interaction between the encapsulating matrix and the aroma compound. Molecular weight, steric hindrance, polarity and chemical groups of the entrapped aroma compound as well as the molecular weight, conformation and physical state of the shell material influence the diffusion and release mechanism [198]. The physical state of the carbohydrate can be either crystalline or amorphous, depending on the moisture content and temperature. The amorphous state usually found in spray dried microcapsules after rapid dehydration is preferred over the crystalline state

for retention of volatile compounds due to reduced mobility of the molecules [199-201].

### 2.3.1 Conventional technologies

There are numerous methods available to prepare encapsulated ingredients in a wide range of particle sizes using a variety of encapsulation materials. Excellent review papers have been published in the last 20 years describing and discussing available technologies for encapsulation of ingredients [193, 196, 202]. Depending on the mechanism of microcapsule formation, three general groups can be distinguished for encapsulation methods, such as physical, chemical and physicochemical methods [193]. The following is a brief overview of encapsulation methods and the basic principles involved.

#### 2.3.1.1 Physical methods

Physical methods encompass spray drying, spray chilling, spray cooling, fluidized bed coating, extrusion, multiorifice centrifugal extrusion, co-crystallization and freeze drying. The basic idea of spray drying and freeze drying is to disperse the core material in a solution of coating material and to remove the solvent afterwards causing the shell material to precipitate around the core to form the capsule. Spray chilling and spray cooling usually involve the use of coating materials with a moderate melting point, such as fats or fatty acid esters. In the spray chilling process, the core material is first dispersed in the molten coating material and the formed dispersion is then sprayed into a cold fluid solidifying the shell. Fluidized bed coating, also known as air suspension coating, is used to encapsulate solid core particles. In this process, the core particles are suspended in a fluidized bed by an upward stream of hot or cold air. The shell is formed by spraying the coating material in a molten or dissolved form onto the dissipated turbulently moving particles [203]. Encapsulation by extrusion can be carried out by extruding a dispersion of core material in a molten carbohydrate matrix through a die into a cooling fluid which causes the matrix to solidify. After extrusion the strands are dried, ground to a desired particle size and washed to remove excess core material from the surface of the particles [193, 202].

Rotational suspension separation, also known as spinning disk, and multiorifice centrifugal coextrusion both take advantage of centrifugal forces to atomize a suspension of core material dispersed in a molten or dissolved coating matrix. In the spinning disk method, the core particles and coating liquid are simultaneously fed onto a fast rotating disk causing the core to be coated by a thin film. For the centrifugal coextrusion, the core and shell liquids are simultaneously pumped in coaxial tubes with the core material flowing in the inner tube and the coating liquid in the outer tube. Both liquids are then sprayed into a spray tower at the end of the tube through multiple coaxial nozzles by rotational forces and atomized into droplets. Co-crystallization has been applied for encapsulation of flavors such as orange peel oil in sucrose [204, 205]. In this process, supersaturated sucrose syrup is heated and mixed with the flavor oil initiating the co-crystallization, which causes rapid precipitation of sucrose entrapping the flavor compound in a crystalline sucrose aggregate. Applying this method, orange peel oil can be transformed into a granular, easy to handle, good flowing powder. However, due to the porosity of the agglomerate the encapsulated oil is not well protected from oxygen, which makes the addition of antioxidants necessary [204].

#### 2.3.1.2 Chemical methods

Chemical methods for encapsulating ingredients such as flavors are inclusion complexation and interfacial polymerization. Inclusion complexation is used to encapsulate sensitive molecules like flavor compounds in a cyclic glucose oligomer, such as β-cyclodextrin [206-209]. This encapsulation method takes place on a molecular level, where molecules rather than droplets or particles are trapped within the cyclic structure of cyclodextrin. Depending on the number of glucose units linked together to a ring structure by α-1-4-glycosidic linkages one can distinguish between α-, β-, or γ-cyclodextrin with six, seven, or eight glucose units, respectively. The mechanism of encapsulation in cyclodextrins is based on intermolecular forces in a manner that single molecules are held inside the slightly non-polar cavity of the bottomless bucket-shaped molecule [193, 206, 209]. Formation of inclusion complexes using cyclodextrins is limited to molecules

with a suitable size and polarity to fit into the cavity. Cyclodextrins exhibit a variable affinity for different compounds, which can be advantageous to selectively remove unwanted goaty flavors in milk or disadvantageous in the case of retention of flavor compounds in heat treated food products [210, 211]. Besides the size, polarity, and affinity, release of the guest compound depends on the moisture and temperature of the food matrix, which can for example cause a more intensive flavor sensation in hot tea than in iced tea [207]. A major drawback of cyclodextrin complexes is their relatively low payload, which has been found to be in the range between 6 to 15% (w/w) for aromas and flavors corresponding to a molar ratio of 1:1 (host:guest molecule) [208].

Another chemical encapsulation method, namely interfacial polymerization, takes advantage of the formation of an interface that is formed when a liquid is dispersed in another immiscible liquid. Furthermore, a polymer film can be formed around the dispersed droplets by polymerization of two reactive bifunctional monomers, each solubilized in one of the two immiscible liquids. However, the application of interfacial polymerization is very limited in the food industry due to the fact that most monomers, such as alkyl diamines and acid dichlorides are not food grade [193].

#### 2.3.1.3 Physicochemical methods

Physicochemical methods combining chemical and mechanical means to form the capsule are coacervation, organic phase separation and liposome entrapment.

Coacervation is used to encapsulate flavor oils [212-214], fish oil [215-217], nutrients, vitamins [218] and enzymes [219-221]. Complex coacervation exploits the phenomenon which occurs when oppositely charged polyelectrolytes, such as gelatin and gum acacia, with a relatively low charge density are mixed at an appropriate temperature, pH, and concentration forming a polyelectrolyte complex. This polyelectrolyte complex causes a separate phase of hydrocolloids to be created, which can then form a coating around an insoluble active ingredient [222-225].

Organic phase separation used for encapsulation purposes takes place when two different incompatible polymers are dissolved in a common solvent. Thus, two phases are formed with one phase being rich in one polymer and the other phase rich in the other polymer. If one of these phases has an affinity to the dispersed core particles it can form the so-called embryo microcapsules, which can be separated and dried [226].

Liposome entrapment has been studied in many fields from food science and agriculture to cosmetic and pharmaceutical applications [227, 228]. Liposomes are spherical bilayer vesicles made from polar lipids, mainly phospholipids like lecithin, which tend to form lipid bilayers in aqueous solvents. The formation of liposomes requires energy to be introduced into the aqueous dispersion of lipid-bilayer structures by mechanical methods, such as high intensity ultrasonication, high pressure homogenization, microfluidization, colloid milling or membrane homogenizing [193, 228]. Non-mechanical methods to form or refine liposomes include reverse phase evaporation or freeze-drying rehydration and freeze thawing [228]. Liposomes can be produced as large and small unilamellar vesicles (LUV, SUV) or multilamellar vesicles (MLV) having one or several bilayers around the aqueous core, respectively. Liposomes are used for dairy product applications, such as liposome-encapsulated proteinase to improve cheese ripening [229], or liposome-encapsulated nisin to extend shelf life and improve sensory qualities of processed Cheddar cheese by suppressing spoilage and pathogenic bacteria [230, 231]. Other applications of liposomes include ferrous sulfate liposomes to fortify milk [232] and encapsulation of vitamins [233, 234].

### 2.3.2 Encapsulation of fish oil

The susceptibility of EPA and DHA to oxidative deterioration, resulting in the formation of oxidation products potentially hazardous to health and organoleptic problems, has presented obstacles to the more widespread use of fish oils in the food industry. Microencapsulation is a technology that can effectively isolate sensitive materials from the oxidative environment. The following discussion

aims at describing current methods for the microencapsulation of fish oil using various techniques, highlighting the potential and challenges. Most studies published on fish oil encapsulation report on oxidative stability of fish oil powders, which is of paramount importance in order to avoid lipid oxidation and the development of off-flavors causing organoleptic disadvantages.

The bioavailability of microencapsulated fish oil incorporated into foods has been shown to be equal to fish oil capsule supplements when consumed by humans [235-237]. Another study on bioavailability conducted with laboratory rats using fish oil encapsulated with marine phospholipid-based liposomes indicated an increased fatty acid absorption using liposomes (98 ± 1%) compared to pure fish oil (73 ± 6%) [238]. Moreover, the DHA proportion in lymph was higher after liposome ingestion (78%) than after fish oil ingestion (47%). However, a disadvantage of those liposomes was the need to incorporate cholesterol (27%) in order to stabilize the liposomes, which was reflected in the results of this study revealing a three-fold increase in cholesterol levels in the lymph when liposomes were fed to rats as compared to pure fish oil [237]. An increase in cholesterol levels could outweigh the health benefits gained by increased absorption of DHA. In that context, Hsieh *et al.* [239] successfully replaced cholesterol in the liposomes by stearic acid for stabilization purposes of liposomes to encapsulate bovine serum albumin (BSA).

Heinzelmann *et al.* [240, 241] applied a freeze-drying technique using a mix of sodium caseinate and lactose or maltodextrin to encapsulate fish oil. Prior to freeze drying, the emulsion of fish oil with caseinate and carbohydrate was frozen at a fast, medium or slow freezing rate by using a bath of liquid nitrogen, a freezing extruder or a freezing room, respectively [240, 241]. Furthermore, the authors [240, 241] investigated the effect of process parameters such as the addition of antioxidants, variations in homogenization procedure and initial temperature in the freeze-drying process on encapsulation efficiency and oxidative stability. The freezing-extruder process had a detrimental effect on the shelf life of encapsulated fish oil because the shear stress in the extruder might have damaged the protein structure of the caseinate, leading to a decreased

protection [240, 241]. Furthermore, the addition of antioxidants was crucial to obtain fish oil capsules with a reasonable oxidative stability. Scanning electron micrographs revealed a rather porous structure of freeze-dried microcapsules, which can potentially lead to a short shelf life. However, the freeze dryer was flushed with nitrogen after processing which could have filled the pores of the powder with nitrogen and thus improved the stability by simply removing oxygen [240, 241].

Márquez-Ruiz *et al.* [242] prepared microencapsulated fish oil by freeze drying emulsions containing fish oil, sodium caseinate and lactose, where they used fish oil with and without an added antioxidant mixture (ALT), consisting of ascorbic acid (0.03% w/w), lecithin (0.5% w/w) and δ-tocopherol (0.02% w/w). After homogenization, the emulsion was frozen at –50ºC for 24 h and then freeze dried for 48 h to obtain freeze-dried samples, which were milled and dry fish oil powder obtained [242]. It is noteworthy that the authors [242] determined the free oil on the surface of the powder to be about 9% of the total powder weight and microencapsulation efficiency was 71%. Surface oil could be the explanation for their finding that the evolution of total oxidation compounds in freeze-dried fish oil powders developed much faster than in bulk fish oils with and without ALT during storage at 30ºC. Oil ending up on the surface of microcapsules is highly detrimental to stability and leads to the development of oxidative products through lipid oxidation due to a larger surface area exposed to oxygen. Therefore, great emphasis must be directed towards avoiding surface oil in order to obtain desirable oxidative stability of fish oil powders.

Keogh *et al.* [243] applied a spray-drying technique to encapsulate fish oil with reconstituted sodium caseinate, calcium caseinate or skim milk powder with lactose as filler. Besides surface oil, the amount of entrapped air, which is correlated to vacuole volume in the fish oil powder was analyzed in this study. The best results in terms of shelf life were achieved using skimmed milk powder (SMP) containing a mixture of micellar casein and whey proteins in a 76:24 ratio. However, since the use of SMP also yielded the lowest vacuole volume there was confounding of these factors and thus more research is required to find out if the

improved oxidative stability can be attributed to SMP only. Furthermore, homogenization pressure and passes had a great influence on vacuole volume and surface oil. However, the influence of vacuole volume or occluded air in the powders had a much greater impact on shelf life and development of off-flavors than surface oil. The authors [243] mention that the auto-oxidation process of fish lipids can be triggered by very small amounts of oxygen trapped in the capsules. This finding leads to the conclusion that not only surface oil but also entrapped oxygen in the microcapsules are very important factors influencing the shelf life of fish oil powder.

Cho *et al*. [244] presented a novel approach for encapsulating fish oil in soy protein isolate by means of double emulsification and subsequent enzymatic gelation method. This study evaluated the possibility of using microbial transglutaminase (MTGase) to achieve cross-linking of the protein wall material to improve the stability of the protein capsules rather than using chemical cross-linking agents such as glutaraldehyde, which may be toxic for food applications. MTGase treatment (incubation at 37ºC for 4 h) was compared to a heat-induced gelation (incubation at 85ºC for 40 min). Particles produced with MTGase were spherical and had a smooth, dent-free surface while heat-gelled particles were roughly spherical in shape and had a porous, wrinkled surface [244]. Oxidative stability was estimated by measuring the p-anisidine value (PAV) for samples stored at 50ºC over 14 days. Both MTGase-treated and heat-gelled particles provided better oxidative stability than free fish oil and there was no significant difference in PAV values between the heat-gelled and MTGase-gelled particles. The MTGase-gelled particles were less water soluble than the heat-treated particles by almost a factor of ten. Upon determining the release of fish oil in an aqueous pepsin solution MTGase-gelled particles exhibited a sustained release of fish oil, whereas the heat-gelled particles showed a “burst-effect” and first order release kinetics for fish oil probably due to the fast release of oil from the surface pores [244]. The sustained release of fish oil might be advantageous for food product applications. However, during formation of the double emulsion and the long incubation required for cross-linking with MTGase, as well as during the

washing steps afterwards, fish oil was lost because it might have been flushed away during this long process.

Hogan *et al.* [245] encapsulated fish oil by means of spray drying using water-soluble and lipid-soluble antioxidants as well as different shell material formulations, such as sodium caseinate incorporating carbohydrates with dextrose equivalents ranging from 5.5 to 38. The authors [245] failed to clearly specify the carbohydrates used, but from their discussion it might be concluded that they used maltodextrins. Nevertheless, they found that sodium caseinate and 'carbohydrates' with a DE of 38 resulted in the best oxidative stability as determined by peroxide value (PV) and anisidine value (AV). However, as the authors clearly realized, the determination of PV and AV might be insufficient in properly evaluating the oxidative stability of microencapsulated fish oils, because strong fishy off-flavors at very low concentrations can develop long before the AV and PV reach alarming levels. The fishy odors of the fish oil powders were considered to be too strong by the authors [245], so that they decided not to present the powders to a sensory panel. Obviously, the human nose is much more sensitive to off-flavors than crude wet-chemical analysis such as AV or PV. Improvements in the analysis of encapsulated fish oil therefore calls for the use of more sophisticated analytical methods or sensory analysis.

Baik *et al.* [246] used corn syrup, sodium caseinate and lecithin to encapsulate fish oil by means of spray drying. The objective of their study was to investigate the influence of lipophilic and amphipilic antioxidants (α-tocopherol and ascorbyl palmitate, respectively) and relative humidity (RH) ranging from 0% to 43% on the oxidative stability of spray-dried microencapsulated fish oil during storage at 30ºC. The authors [246] evaluated the oxidative stability by means of PV, thiobarbituric acid reactive substances (TBARS) and sensory evaluation performed by ten trained judges rating the fish oil powders on a 9-point hedonic scale (from 1= no rancid or fishy odor to 9= extremely rancid or fishy odor). Interestingly, the PV of the fish oil bulk gradually increased from 9.5 mmol/kg oil in fresh fish oil to about 17 mmol/kg oil in the spray-dried powder. This clearly indicates that lipid oxidation takes place during processing due to exposure to air,

heat, high pressure and moisture. Consequently, the sensory evaluation of all the fish oil powders right after spray drying resulted in an odor intensity in the range of 3.8-5.5, with no significant difference between the antioxidants used. All powder samples ranked higher than 5 after 14 days of storage (11% RH, 30ºC) [245]. However, determination of the PV of surface oil and encapsulated oil separately showed that α-tocopherol significantly improved the oxidative stability of both surface and encapsulated oil during storage, whereas ascorbyl palmitate had only a limited effect. Furthermore, the effect of RH on oxidative stability during storage, which was monitored by measuring the trend for TBARS was quite significant. The best oxidative stability was achieved at 11% RH for encapsulated fish oil containing α-tocopherol. Unfortunately, the authors [246] did not study the influence of RH on the trend for TBARS over storage for the encapsulated fish oil containing ascorbyl palmitate. Humidity could play a significant role in 'activating' the amphipilic antioxidant at the surface of the capsules. Nevertheless, Baik *et al.* [246] illustrated again that processing of fish oil is challenging and sensory evaluation is very important to evaluate the organoleptic quality of the fish oil powder.

Jónsdóttir *et al.* [247] evaluated the oxidative stability of fish oil encapsulated by spray drying using a variety of coating materials. First, they used mixtures of caseinate with different carbohydrates, such as lactose, sucrose and maltodextrin. Then, they improved their best mixture by using lecithin as emulsifier and adding α-tocopherol to the fish oil. A combination of high-molecular-weight fish skin gelatin with gum acacia and maltodextrin (DE =20) and using Span 80 (Sorbitan monooleate) as emulsifier were tested [246]. The stability of the fish oil powders was assessed by several methods, including measuring the resistance of the particles to pressurized oxygen (Oxypress), which provided valuable information about induction periods of lipid oxidation, TBARS and sensory analysis with a trained experienced panel to assess odor intensity. The sensory panel found the intensity for rancid off-flavors to be the best (i.e. at threshold detectable levels) for the coating mixture of caseinate and lactose using lecithin as emulsifier for fish oil containing α-tocopherol [247]. Key odor

compounds were identified by headspace solid phase microextraction (HS-SPME) followed by gas chromatography-olfactometry (GC-O) in combination with flame ionization detector (GC-FID) and mass spectrometry (GC-MS). Oxidatively derived compounds such as hexanal, 2-nonenal, and 2,4-decadienal were identified, which can be used as quality markers to test the oxidative stability of microencapsulated fish oil, according to the authors [247]. A major improvement for analyzing the development of oxidatively derived volatile substances causing off-flavors and to determine key odor compounds was the use of gas chromatography (GC) of headspace samples combined with olfactometric measurements (GC-O). However, it seems that the best evaluation tool for the oxidative stability of fish oil powders is still the human nose, which can detect volatile off-flavor compounds such as cis-4-heptenal at sub-ppb levels (0.04 ppb), a lower detection limit than some FID or MS can achieve [248].

Drusch and Schwarz [249] reported on fish oil encapsulation without adding antioxidants by means of a spray dryer equipped with a rotating disc for atomization and using two types of n-octenylsuccinate-derivatised starch (n-OSA starch) and glucose syrup as coating material. Furthermore, two different spray drying conditions in terms of inlet and outlet temperatures were examined. The two types of n-OSA had an equal degree of substitution but differed in viscosity (132 mPa.s and 340 mPa.s at 25ºC and a solid concentration of 30% in water). The influence of viscosity was important for the stability of the emulsion prior to spray drying since there was a significant interaction effect between the type of starch used and the oil content of the emulsion on oil droplet size after homogenization [249]. At high oil contents (50%) smaller droplets were obtained in the emulsion with medium-viscosity starch than in the emulsion with low-viscosity starch [249]. The authors [249] contributed the improved emulsion stability to increased starch viscosity due to hydrodynamic stabilization. However, stabilization of the emulsion could also be accomplished by adjusting the pH. Lowering the pH to 4.5 has an impact on electrophoretic mobility of the starch molecules due to the presence of carboxyl groups, which get protonated leading to a surface charge close to zero. According to scanning electron

microscopy images spray drying conditions had a dramatic influence on particle size and morphology. At high temperature conditions, with the air temperature being 210ºC and 90ºC at inlet and outlet, respectively, they found that particles were larger, and exhibited a large central void and lower powder density [249].

This change in particle properties was caused by a "ballooning" effect as described by Walton and Mumford [250]. "Ballooning" can lead to inflated hollow particles by spray drying skin forming solutions. Obviously, inclusion of air into the particles is highly detrimental to oxidative stability of encapsulated fish oil and thus should be avoided. Consequently, the oxidative status of the particles produced at high temperature conditions as determined by PV, conjugated dienes and headspace propanal contents was worse than that for the particles produced at low temperature conditions [249]. Again, Drusch and Schwarz [249] found that spray drying can lead to increased lipid oxidation during processing, which can be deleterious to the sensory quality of the product; however, sensory evaluation of their spray-dried powder was not performed.

Augustin *et al.* [251] reported on the feasibility of using Maillard reaction products as encapsulants for fish oil powders. A spray-drying technique was applied to encapsulate fish oil using pre-heated protein-carbohydrate mixtures as coating material [251]. The Maillard reaction products formed by pre-heating of the protein-carbohydrate mixtures up to 100ºC for up to 90 min are supposed to have antioxidant activity, which was confirmed by their findings for the oxidative stability of fish oil powder stored at 35°C for 4 weeks, as quantified by measuring headspace propanal concentrations [251]. The higher the temperature for the heat treatment, the more Maillard reaction products were formed and the lower was the headspace propanal, which indicated antioxidative activity and improvement of oxidative stability of the fish oil powders [251]. However, sensory analysis was not included in this study, which could be important to determine the impact of Maillard browning on the flavor of the fish oil powders and possible unwanted effects on foods enriched with those powders.

Tan *et al.* [252] report the encapsulation of fish oil using alginate/starch blends as wall material in a spray drying process. They demonstrated that the

addition of alginate resulted in rounder microspheres with higher oil encapsulation efficiencies. The effect of surface oil and extractable oil close to the surface of microspheres containing fish oil prepared by spray drying on shelf life and oxidative stability was studied by Drusch and Berg [253]. The authors [253] found that surface oil may protect some of the extractable oil and suggested that determination of extractable oil alone cannot be used to predict shelf life of microencapsulated fish oil.

Based on the above summary, it can be concluded that encapsulation of fish oil is very challenging, because PUFA present in fish oil are highly unstable in the presence of oxygen and can undergo autooxidation easily, which leads to the development of volatile off-flavors, such as fishy or rancid odors with extremely low detection limits for the human nose. Furthermore, the incorporation of fish oil powders into food products deserves careful consideration and research, because fish oil could be set free due to various release mechanisms taking place in the food matrix during storage.

### 2.3.3 Particle formation using supercritical fluid technology

Particle formation using SCF technology has been observed by some early pioneering researchers of supercritical fluids, namely Hannay and Hogarth [254], who observed in 1879 the precipitation of solid solutes as ‘snow’ when pressure in supercritical solutions was lowered. Since then several processes have been developed for particle formation using SCF technology, which allow production of micron and submicron sized particles with a great variety of morphologies and applications. Today, particle formation using SCF has reached commercial scale and is used for production of powderous lecithin, drug delivery systems, or concentrated powder forms of essential oils [255]. Numerous variations of the basic particle formation processes have been patented and published. Excellent reviews describing the numerous options for particle formation using SCF were presented previously [255-263]. Additionally, the design and processing aspects of lab scale SCF particle formation systems have been discussed [264]. The basic concepts of particle formation and encapsulation processes using SCF technology

are outlined in this section. However, up to date there has been no publication reporting encapsulation of fish oil using SCF technology [32].

#### 2.3.3.1 Rapid expansion of supercritical solutions (RESS)

The RESS process was developed by Matson *et al.* [265] to produce particles of inorganic (silica) and organic (polymers) materials where precipitation of particles can be achieved by rapidly lowering the pressure of a supercritical solution. The principal mechanism for the "rapid expansion of supercritical solutions" or RESS process is based on the fact that solubility in SCF is closely related to the density and thus pressure of the SCF. A schematic diagram for RESS is presented in Fig. 2-12. A solution under supercritical conditions is rapidly expanded through a nozzle to a lower pressure, thus causing the solute to precipitate. The main parameters influencing the performance of the RESS process are the solute solubility in the SCF, dimensions of the orifice, pressure and temperature in the collection chamber and agglomeration phenomena during expansion of the supercritical solution [256].

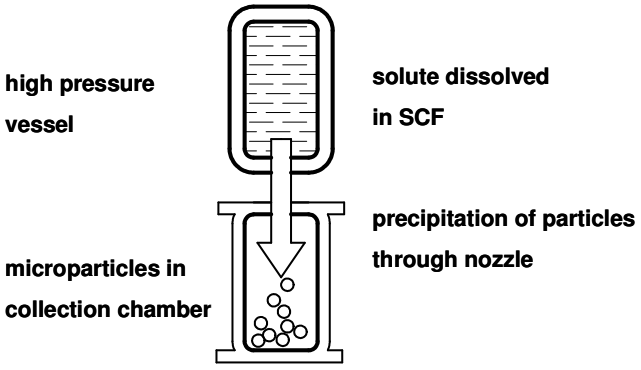


**Figure 2-12.** Rapid expansion of supercritical solutions (RESS).

Over 100 different substances have been micronized using RESS with the majority being pharmaceutical drugs or other high-value substances [255], such as ibuprofen, caffeine, aspirin, polylactic acid (PLA) + lovastatin, and PLA + naproxen [266]. In the case of ibuprofen, the micronization using the RESS

process is very efficient, so that the original particle size of the drug of about 250 μm could be reduced to about 3 μm [266]. The main limitation of the RESS process is that the solute must be soluble in the SCF at appreciable levels, otherwise large quantities of SCF are required to precipitate a certain amount of solute. For example, it has been estimated that depending on solute solubility about 10 to 100 kg of $CO_2$ would be required to precipitate about 1 kg of solute [255].

A variation of the RESS process is to expand the supercritical solution into a chamber filled with a liquid solvent, hence the process is called "rapid expansion of a supercritical solution into a liquid solvent" or RESOLV [267]. In the RESOLV process the growth of particles could be quenched and by adding reactants into the receiving solvent, it is possible to combine particle formation with a chemical reaction step. One example where the RESOLV process was successfully employed was to encapsulate vitamin A in the form of retinyl palmitate in a matrix of poly(l-lactide) (PLLA), generating nanocapsules with diameters ranging from 40–110 nm [268].

#### 2.3.3.2 Particles from gas-saturated solutions (PGSS)

In the PGSS process, the particles are formed by spraying a solution or a melt containing a SCF into a chamber at lower pressure. The process is based on the ability of SCF to dissolve into organic compounds up to relatively high levels, thereby reducing the melting point, viscosity and interfacial tension of the material. Thus, gas-saturated solutions formed at elevated pressures with reduced viscosity and interfacial tension can be sprayed through a nozzle into a chamber at lower pressure to achieve atomization, rapid depressurization and release of the gas from the condensed phase. A schematic of the PGSS process is presented in Fig. 2-13. Due to the rapid expansion a substantial decrease in temperature due to the Joule-Thomson effect can be achieved, which can lead to solidification of the molten solute and formation of fine particles. The solidification takes place in a very short time ranging from 10 to 100 ms [255]. Materials processed into micronized powders using PGSS with applications in the food industry include

chocolate, lecithin, citric acid, butter, cocoa butter, hardened cheese and menthol [255].

A variation of the PGSS process is the "depressurization of an expanded liquid organic solution" (DELOS) process. In the DELOS process, a compressed gas is dissolved into a solution consisting of the solute and an organic solvent, which causes the solvent to expand. However, in this case the SCF acts as a co-solvent and precipitation does not occur. Then, the pressure is rapidly reduced to atmospheric pressure so that SCF is removed instantaneously and a sharp decrease in temperature occurs, which leads to supersaturation and precipitation of particles [260].

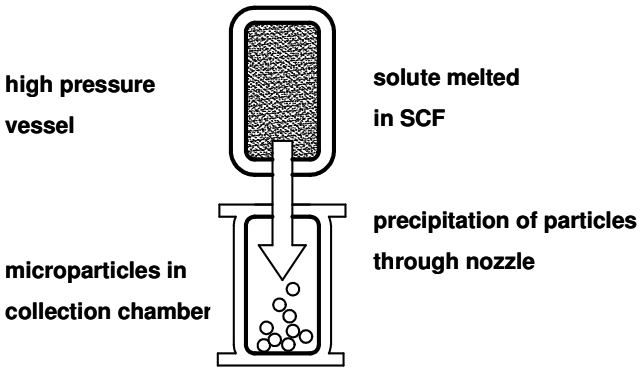


**Figure 2-13.** Particles from gas-saturated solutions (PGSS).

#### 2.3.3.3 Gas antisolvent process (GAS)

In the GAS process, also referred to as 'supercritical fluid antisolvent' (SAS) process, the solute is first dissolved in an organic solvent and filled into an autoclave. Particles are then produced by introducing a SCF into the solution, which causes expansion of the organic solvent [181, 269] and change in solvent properties [180], leading to precipitation of the solute. Additionally, depending on the pressure, temperature and mass transfer the organic solvent can be removed by the SCF, which leads to saturation and supersaturation causing nucleation and precipitation of the solute. The basic flow chart for a GAS process is illustrated in Fig. 2-14.

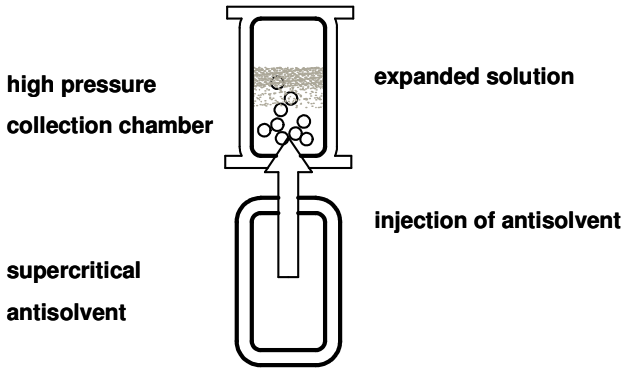


**Figure 2-14.** Gas antisolvent process (GAS).

Variations of the GAS process are the 'aerosol solvent extraction system' (ASES), the 'precipitation with a compressed antisolvent' (PCA) process and the 'solution-enhanced dispersion by supercritical fluids' (SEDS) process, which differ in the way the contact between the solution and the SCF is achieved [258]. In the PCA and ASES processes, the solution is sprayed into a chamber filled with pressurized bulk SCF [257] as illustrated in Fig. 2-15. Additionally, instead of a batch-wise operation the process can be carried out semi-continuously by feeding the pressurized SCF continuously through a separate inlet into the chamber and removing SCF+solvent through a filter plate to collect the particles until the chamber is full. Spraying the solvent into the SCF leads to the formation of fine droplets, which facilitates faster mass transfer and rapid supersaturation due to the increased surface area so that formation of small particles is improved. The GAS and PCA processes have been successfully scaled-up for industrial production of particles, mostly pharmaceutical drugs with high value but also for food applications, such as for precipitation of lecithin. In the industrial PCA process about 200 kg lecithin powder per h can be produced by injecting raw lecithin containing 60% phospholipids and 40% oil into a chamber with SC-$CO_2$, where the oil is dissolved and lecithin precipitates [255].

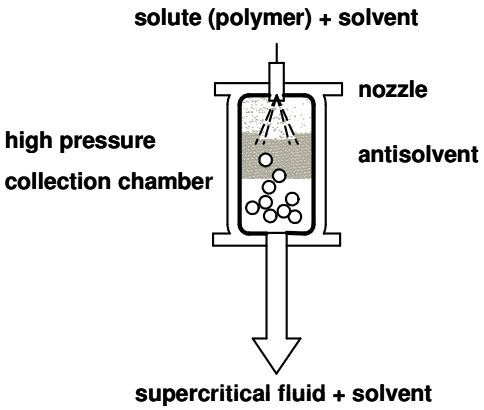


**Figure 2-15.** Precipitation with a compressed antisolvent (PCA).

Another improvement was implemented in the SEDS process, where the SCF and the solution containing the solute are mixed in a coaxial nozzle and sprayed together into the precipitation chamber so that the SCF is used as an antisolvent and due to a high flow rate can generate a much higher velocity at the nozzle outlet acting as a "spray enhancer" improving the atomization [257].

#### 2.3.3.4 Concentrated powder form (CPF)

Particles produced with the RESS, GAS or PGSS processes are usually dry powders. The CPF process presented by Weidner in 1997 [255] allows production of free-flowing powders with a very high liquid content of up to 90% by weight. In the CPF process, the liquid is mixed with the compressed gas and injected into a chamber forming very fine drops, while a solid carrier material is blown into the spray by means of an inert gas, leading to intensive mixing and formation of agglomerates. This process is particularly interesting for the food industry because the particles are formed in an oxygen-free environment at mild temperatures, which is beneficial to convert sensitive materials such as flavor components or essential oils into easy-to-handle powder with extended shelf life [255].

## 2.4 References


1. J.B. Rossell, Fish Oils. 2009, Leatherhead, Surrey; Chichester, West Sussex, U.K.: Leatherhead Food International; Wiley-Blackwell.

2. Fisheries and Oceans Canada, Domestic exports of selected commodities by species group and species quantity, http://www.dfo-mpo.gc.ca/stats/trade-commerce/can/export/xsps09-eng.htm. (accessed on: March 5, 2010).

3. FAO Fisheries and Aquaculture Department, The state of world fisheries and aquaculture 2008. 2009, Rome, Italy: Food and Agriculture Organization of the United Nations.

4. A.P. Bimbo, Raw material sources for the long-chain omega-3 market: Trends and sustainability. Part 1. INFORM 20 (2009) 178-181.

5. A.P. Bimbo, Guidelines for characterizing food-grade fish oil. INFORM 9 (1998) 473-483.

6. R.G. Ackman, Oils and fats group international lecture - the year of the fish oils. Chem. Ind. (1988) 139-145.

7. F. Shahidi, U.N. Wanasundara, Omega-3 fatty acid concentrates: Nutritional aspects and production technologies. Trends Food Sci. Technol. 9 (1998) 230-240.

8. O.S. Privett, Nadenice.Jd, F.J. Pusch, E.C. Nickell, Application of high vacuum fractional distillation to complex mixtures of methyl esters of polyunsaturated fatty acids. J. Am. Oil Chem. Soc. 46 (1969) 13-17.

9. F.A. Norris, I.I. Rusoff, E.S. Miller, G.O. Burr, Fractional distillation of unsaturated fatty acids. I. The effect of vacuum distillation on the absorption spectra of polyethenoid esters from cod liver oil. J. Biol. Chem. 139 (1941) 199-206.

10. F.A. Norris, Rusoff, II, E.S. Miller, G.O. Burr, Fractional distillation of unsaturated fatty acids II. The effect of heat on the rearrangements produced in unsaturated fatty acid esters. J. Biol. Chem. 147 (1943) 273-280.

11. R.G. Ackman, P.J. Ke, P.M. Jangaard, Fractional vacuum distillation of Herring oil methyl esters. J. Am. Oil Chem. Soc. 50 (1973) 1-8.

12. H. Breivik, G.G. Haraldsson, B. Kristinsson, Preparation of highly purified concentrates of eicosapentaenoic acid and docosahexaenoic acid. J. Am. Oil Chem. Soc. 74 (1997) 1425-1429.

13. J.B. Brown, D.K. Kolb, Applications of low temperature crystallization in the separation of the fatty acids and their compounds. Prog. Chem. Fats Other Lipids 3 (1955) 73-94.

14. K.T. Lee, T.A. Foglia, Fractionation of menhaden oil and partially hydrogenated menhaden oil: Characterization of triacylglycerol fractions. J. Am. Oil Chem. Soc. 78 (2001) 297-303.

15. S.K. Lee, Method for isolating high-purified unsaturated fatty acids using crystallization Patent #: US6664405, 2003.

16. W.M.N. Ratnayake, B. Olsson, D. Matthews, R.G. Ackman, Preparation of omega-3 PUFA concentrates from fish oils via urea complexation. Fett Wiss. Technol. 90 (1988) 381-386.

17. M.A. Grompone, Enrichment of omega-3 PUFAs from fur-seal oil. Fett Wiss. Technol. 94 (1992) 388-394.

18. U.N. Wanasundara, F. Shahidi, Concentration of omega 3-polyunsaturated fatty acids of seal blubber oil by urea complexation: optimization of reaction conditions. Food Chem. 65 (1999) 41-49.

19. S. Senanayake, F. Shahidi, Concentration of docosahexaenoic acid (DHA) from algal oil via urea complexation. J. Food Lipids 7 (2000) 51-61.

20. N. Gámez-Meza, J.A. Noriega-Rodríguez, L.A. Medina-Juárez, J. Ortega-García, J. Monroy-Rivera, F.J. Toro-Vázquez, H.S. García, O. Angulo-Guerrero, Concentration of eicosapentaenoic acid and docosahexaenoic acid from fish oil by hydrolysis and urea complexation. Food Res. Int. 36 (2003) 721-727.

21. C.P. Zuta, B.K. Simpson, H.M. Chan, L. Phillips, Concentrating PUFA from mackerel processing waste. J. Am. Oil Chem. Soc. 80 (2003) 933-936.

22. A. Staby, J. Mollerup, Separation of constituents of fish oil using supercritical fluids: a review of experimental solubility, extraction, and chromatographic data. Fluid Phase Equilib. 91 (1993) 349-386.

23. N.R. Bottino, G.A. Vandenburg, R. Reiser, Resistance of certain long-chain polyunsaturated fatty acids of marine oils to pancreatic lipase hydrolysis. Lipids 2 (1967) 489-493.

24. T. Hoshino, T. Yamane, S. Shimizu, Bioreactor for enzymatic reaction of fat and fatty acid derivatives. 12. Selective hydrolysis of fish oil by lipase to concentrate n-3 polyunsaturated fatty acids. Agric. Biol. Chem. 54 (1990) 1459-1467.

25. Y. Tanaka, J. Hirano, T. Funada, Concentration of docosahexaenoic acid in glyceride by hydrolysis of fish oil with *Candida cylindracea* lipase. J. Am. Oil Chem. Soc. 69 (1992) 1210-1214.

26. Y. Shimada, K. Maruyama, S. Okazaki, M. Nakamura, A. Sugihara, Y. Tominaga, Enrichment of polyunsaturated fatty-acids with *Geotrichum candidum* lipase. J. Am. Oil Chem. Soc. 71 (1994) 951-954.

27. M. Linder, E. Matouba, J. Fanni, M. Parmentier, Enrichment of salmon oil with n-3 PUFA by lipolysis, filtration and enzymatic re-esterification. Eur. J. Lipid Sci. Technol. 104 (2002) 455-462.

28. A. Ramírez Fajardo, L. Esteban Cerdán, A. Robles Medina, M.M. Muñío Martínez, E. Hita Peña, E. Molina Grima, Concentration of eicosapentaenoic acid by selective esterification using lipases. J. Am. Oil Chem. Soc. 83 (2006) 215-221.

29. G.P. McNeill, R.G. Ackman, S.R. Moore, Lipase-catalyzed enrichment of long-chain polyunsaturated fatty acids. J. Am. Oil Chem. Soc. 73 (1996) 1403-1407.

30. U.N. Wanasundara, F. Shahidi, Lipase-assisted concentration of n-3 polyunsaturated fatty acids in acylglycerols from marine oils. J. Am. Oil Chem. Soc. 75 (1998) 945-951.

31. W. Eltringham, O.J. Catchpole, Processing of fish oils by supercritical fluids, in Supercritical Fluid Extraction of Nutraceuticals and Bioactive Compounds, J.L. Martinez, Editor. 2008, CRC Press, Taylor and Francis Group: Boca Raton, FL.

32. N. Rubio-Rodríguez, S. Beltrán, I. Jaime, S.M. de Diego, M.T. Sanz, J.R. Carballido, Production of omega-3 polyunsaturated fatty acid concentrates: A review. Innov. Food Sci. Emerg. Technol. 11 (2010) 1-12.

33. A.P. Bimbo, Raw material sources for the long-chain omega-3 market: Trends and sustainability. Part 2. INFORM 20 (2009) 264-266.

34. FAO, Food outlook - June 2008. 2008, Food and Agriculture Organization of the United Nations: Rome, Italy.

35. FAO, Food outlook - December 2009. 2009, Food and Agriculture Organization of the United Nations: Rome, Italy.

36. W. Kolanowski, G. Laufenberg, Enrichment of food products with polyunsaturated fatty acids by fish oil addition. Eur. Food Res. Technol. 222 (2006) 472-477.

37. FAO, International commodity prices - http://www.fao.org/es/esc/prices. 2010, Food and Agriculture Organization of the United Nations (accessed on: Feb 28, 2010).

38. F. Sahena, I.S.M. Zaidul, S. Jinap, N. Saari, H.A. Jahurul, K.A. Abbas, N.A. Norulaini, PUFAs in fish: Extraction, fractionation, importance in health. Compr. Rev. Food Sci. Food Safety 8 (2009) 59-74.

39. J.V. Visentainer, M. D'Addio Noffs, P. De Oliveira Carvalho, V.V. De Almeida, C.C. De Oliveira, N.E. De Souza, Lipid content and fatty acid composition of 15 marine fish species from the southeast coast of Brazil. J. Am. Oil Chem. Soc. 84 (2007) 543-547.

40. E.H. Gruger, R.W. Nelson, M.E. Stansby, Fatty acid composition of oils from 21 species of marine fish, freshwater fish and shellfish. J. Am. Oil Chem. Soc. 41 (1964) 662-667.

41. Y. Özogul, F. Özogul, Fatty acid profiles of commercially important fish species from the Mediterranean, Aegean and Black Seas. Food Chem. 100 (2007) 1634-1638.

42. A.S. McGill, C.F. Moffat, A study of the composition of fish liver and body oil triglycerides. Lipids 27 (1992) 360-370.

43. F.D. Gunstone, J.L. Harwood, A.J. Dijkstra, The Lipid Handbook. 2007, Boca Raton, FL: CRC Press.

44. O.P. Ward, A. Singh, Omega-3/6 fatty acids: Alternative sources of production. Process Biochem. 40 (2005) 3627-3652.

45. C. Ratledge, Fatty acid biosynthesis in microorganisms being used for Single Cell Oil production. Biochimie 86 (2004) 807-815.

46. A. Robles Medina, E. Molina Grima, A. Gimenez Gimenez, M.J. Ibanez Gonzalez, Downstream processing of algal polyunsaturated fatty acids. Biotechnol. Adv. 16 (1998) 517-580.

47. A. Mendes, A. Reis, R. Vasconcelos, P. Guerra, T. Lopes Da Silva, Crypthecodinium cohnii with emphasis on DHA production: A review. J. Appl. Phycol. 21 (2009) 199-214.

48. L.H. Reddy, P. Couvreur, Squalene: A natural triterpene for use in disease management and therapy. Adv. Drug Delivery Rev. 61 (2009) 1412-1426.

49. P.K. Skiadas, J.G. Lascaratos, Dietetics in ancient Greek philosophy: Plato's concepts of healthy diet. Eur. J. Clin. Nutr. 55 (2001) 532-537.

50. T. Percival, Observations on the medicinal uses of the Oleum Jecoris Aselli, or cod liver oil in the chronic rheumatism, and other painful disorders. London Med. J. 3 (1783) 393-401.

51. A. Strøm, R.A. Jensen, Mortality from circulatory diseases in Norway 1940-1945. Lancet 1 (1951) 126-129.

52. J. Dyerberg, H.O. Bang, N. Hjorne, Fatty acid composition of the plasma lipids in Greenland Eskimos. Am. J. Clin. Nutr. 28 (1975) 958-966.

53. H.O. Bang, J. Dyerberg, N. Hjorne, The composition of food consumed by Greenland Eskimos. Acta Med. Scand. 200 (1976) 69-73.

54. J. Dyerberg, H.O. Bang, E. Stoffersen, Eicosapentaenoic acid and prevention of thrombosis and atherosclerosis?. Lancet 2 (1978) 117-119.

55. A.P. Simopoulos, Omega-3 fatty acids in health and disease and in growth and development. Am. J. Clin. Nutr. 54 (1991) 438-463.

56. L.A. Horrocks, Y.K. Yeo, Health benefits of docosahexaenoic acid (DHA). Pharmacol. Res. 40 (1999) 211-225.

57. E.B. Schmidt, J. Dyerberg, Omega-3 fatty acids. Current status in cardiovascular medicine. Drugs 47 (1994) 405-424.

58. D.J. Holub, B.J. Holub, Omega-3 fatty acids from fish oils and cardiovascular disease. Mol. Cell. Biochem. 263 (2004) 217-225.

59. P. Sanderson, Y.E. Finnegan, C.M. Williams, P.C. Calder, G.C. Burdge, S.A. Wootton, B.A. Griffin, D.J. Millward, N.C. Pegge, W.J.E. Bemelmans, UK Food Standards Agency α-linolenic acid workshop report. Br. J. Nutr. 88 (2002) 573-579.

60. C. Wang, W.S. Harris, M. Chung, A.H. Lichtenstein, E.M. Balk, B. Kupelnick, H.S. Jordan, J. Lau, n-3 Fatty acids from fish or fish-oil supplements, but not α-linolenic acid, benefit cardiovascular disease outcomes in primary- and secondary-prevention studies: A systematic review. Am. J. Clin. Nutr. 84 (2006) 5-17.

61. C.E. Friedberg, M.J.F.M. Janssen, R.J. Heine, D.E. Grobbee, Fish oil and glycemic control in diabetes: a meta-analysis. Diabetes Care 21 (1998) 494-500.

62. V.M. Montori, A. Farmer, P.C. Wollan, S.F. Dinneen, Fish oil supplementation in type 2 diabetes: A quantitative systematic review. Diabetes Care 23 (2000) 1407-1415.

63. J.A. Nettleton, R. Katz, n-3 long-chain polyunsaturated fatty acids in type 2 diabetes: A review. J. Am. Diet. Assoc. 105 (2005) 428-440.

64. A.P. Simopoulos, Omega-3 fatty acids in inflammation and autoimmune diseases. J. Am. Coll. Nutr. 21 (2002) 495-505.

65. M. Martinez, Tissue levels of polyunsaturated fatty acids during early human development. J. Pediatr. 120 (1992) 129-138.

66. M.A. Crawford, F. Muskiet, J.E. Blundell, K.S. Bjerve, The role of essential fatty acids in neural development: Implications for perinatal nutrition. Am. J. Clin. Nutr. 57 (1993) 703-710.

67. M. Makrides, M.A. Neumann, R.W. Byard, K. Simmer, R.A. Gibson, Fatty acid composition of brain, retina, and erythrocytes in breast- and formula-fed infants. Am. J. Clin. Nutr. 60 (1994) 189-194.

68. J.A. Conquer, M.C. Tierney, J. Zecevic, W.J. Bettger, R.H. Fisher, Fatty acid analysis of blood plasma of patients with Alzheimer's disease, other types of dementia, and cognitive impairment. Lipids 35 (2000) 1305-1312.

69. R. Uauy, D.R. Hoffman, P. Peirano, D.G. Birch, E.E. Birch, Essential fatty acids in visual and brain development. Lipids 36 (2001) 885-895.

70. I.B. Helland, L. Smith, K. Saarem, O.D. Saugstad, C.A. Drevon, Maternal supplementation with very-long-chain n-3 fatty acids during pregnancy and lactation augments children's IQ at 4 years of age. Pediatrics 111 (2003) 39-44.

71. J.C. McCann, B.N. Ames, Is docosahexaenoic acid, an n-3 long-chain polyunsaturated fatty acid, required for development of normal brain function? An overview of evidence from cognitive and behavioral tests in humans and animals. Am. J. Clin. Nutr. 82 (2005) 281-295.

72. L.D. Lawson, B.G. Hughes, Human absorption of fish oil fatty acids as triacylglycerols, free acids, or ethyl esters. Biochem. Biophys. Res. Commun. 152 (1988) 328-335.

73. S. El Boustani, C. Colette, L. Monnier, B. Descomps, A. Crastes De Paulet, F. Mendy, Enteral absorption in man of eicosapentaenoic acid in different chemical forms. Lipids 22 (1987) 711-714.

74. H.E. Krokan, K.S. Bjerve, E. Mørk, The enteral bioavailability of eicosapentaenoic acid and docosahexaenoic acid is as good from ethyl esters as from glyceryl esters in spite of lower hydrolytic rates by pancreatic lipase in vitro. Biochim. Biophys. Acta, Lipids Lipid Metab. 1168 (1993) 59-67.

75. A. Nordoy, L. Barstad, W.E. Connor, L. Hatcher, Absorption of the n - 3 eicosapentaenoic and docosahexaenoic acids as ethyl esters and triglycerides by humans. Am. J. Clin. Nutr. 53 (1991) 1185-1190.

76. M.S. Christensen, C.E. Hoy, C.C. Becker, T.G. Redgrave, Intestinal absorption and lymphatic transport of eicosapentaenoic (EPA), docosahexaenoic (DHA), and decanoic acids: Dependence on intramolecular triacylglycerol structure. Am. J. Clin. Nutr. 61 (1995) 56-61.

77. A.H. Lichtenstein, L.J. Appel, M. Brands, M. Carnethon, S. Daniels, H.A. Franch, B. Franklin, P. Kris-Etherton, W.S. Harris, B. Howard, N. Karanja, M. Lefevre, L. Rudel, F. Sacks, L. Van Horn, M. Winston, J. Wylie-Rosett, Diet and lifestyle recommendations revision 2006: A scientific statement from the American heart association nutrition committee. Circulation 114 (2006) 82-96.

78. P.M. Kris-Etherton, W.S. Harris, L.J. Appel, Fish consumption, fish oil, omega-3 fatty acids, and cardiovascular disease. Circulation 106 (2002) 2747-2757.

79. A. Kamal-Eldin, N.V. Yanishlieva, N-3 fatty acids for human nutrition: Stability considerations. Eur. J. Lipid Sci. Technol. 104 (2002) 825-836.

80. G. Brunner, Gas Extraction: An Introduction to Fundamentals of Supercritical Fluids and the Application to Separation Processes. Topics in Physical Chemistry, vol. 4. 1994, Darmstadt; New York: Steinkopff; Springer.

81. M.A. McHugh, V.J. Krukonis, Supercritical Fluid Extraction: Principles and Practice. 1986, Boston: Butterworths.

82. NIST, Isothermal properties for carbon dioxide. http://webbook.nist.gov. (accessed on: June 10, 2009).

83. A. Fenghour, W.A. Wakeham, V. Vesovic, The viscosity of carbon dioxide. J. Phys. Chem. Ref. Data 27 (1998) 31-39.

84. A. Michels, A. Botzen, W. Schuurman, The viscosity of carbon dioxide between 0°C and 75°C and at pressures up to 2000 atmospheres. Physica 23 (1957) 95-102.

85. J. Kestin, T.F. Zien, J.H. Whitelaw, The viscosity of carbon dioxide in the neighbourhood of the critical point. Physica 30 (1964) 161-181.

86. D.Q. Tuan, J.A. Zollweg, P. Harriott, S.S.H. Rizvi, Measurement and modeling of viscosity of supercritical carbon dioxide/biomaterial(s) mixtures. Ind. Eng. Chem. Res. 38 (1999) 2129-2136.

87. M.E. Yener, P. Kashulines, S.S.H. Rizvi, P. Harriott, Viscosity measurement and modeling of lipid supercritical carbon dioxide mixtures. J. Supercrit. Fluids 11 (1998) 151-162.

88. K.D. Tilly, N.R. Foster, S.J. Macnaughton, D.L. Tomasko, Viscosity correlations for binary supercritical fluids. Ind. Eng. Chem. Res. 33 (1994) 681-688.

89. K.K. Liong, P.A. Wells, N.R. Foster, Diffusion in supercritical fluids. J. Supercrit. Fluids 4 (1991) 91-108.

90. J.J. Suárez, I. Medina, J.L. Bueno, Diffusion coefficients in supercritical fluids: available data and graphical correlations. Fluid Phase Equilib. 153 (1998) 167-212.

91. I. Raspo, C. Nicolas, E. Neau, S. Meradji, Diffusion coefficients of solids in supercritical carbon dioxide: Modelling of near critical behaviour. Fluid Phase Equilib. 263 (2008) 214-222.

92. L.S. Darken, Diffusion, mobility and their interrelation through free energy in binary metallic systems. Trans. Am. Inst. Min. Metall. Eng. 175 (1948) 184-201.

93. H. Higashi, Y. Iwai, Y. Nakamura, S. Yamamoto, Y. Arai, Correlation of diffusion coefficients for naphthalene and dimethylnaphthalene isomers in supercritical carbon dioxide. Fluid Phase Equilib. 166 (1999) 101-110.

94. T. Funazukuri, S. Hachisu, N. Wakao, Measurements of binary diffusion coefficients of $C_{16}$-$C_{24}$ unsaturated fatty acid methyl esters in supercritical carbon dioxide. Ind. Eng. Chem. Res. 30 (1991) 1323-1329.

95. K.A. Rezaei, F. Temelli, Using supercritical fluid chromatography to determine diffusion coefficients of lipids in supercritical $CO_2$. J. Supercrit. Fluids 17 (2000) 35-44.

96. T. Funazukuri, C.Y. Kong, S. Kagei, Effects of molecular weight and degree of unsaturation on binary diffusion coefficients for lipids in supercritical carbon dioxide. Fluid Phase Equilib. 219 (2004) 67-73.

97. T. Funazukuri, C.Y. Kong, S. Kagei, Impulse response techniques to measure binary diffusion coefficients under supercritical conditions. J. Chromatogr. A 1037 (2004) 411-429.

98. O.J. Catchpole, M.B. King, Measurement and correlation of binary diffusion coefficients in near critical fluids. Ind. Eng. Chem. Res. 33 (1994) 1828-1837.

99. V. Vesovic, W.A. Wakeham, G.A. Olchowy, J.V. Sengers, J.T.R. Watson, J. Millat, The transport properties of carbon dioxide. J. Phys. Chem. Ref. Data 19 (1990) 763-808.

100. G. Wiegand, E.U. Franck, Interfacial tension between water and non-polar fluids up to 473 K and 2800 bar. Ber. Bunsen Ges. - Phys. Chem. Chem. Phys. 98 (1994) 809-817.

101. N. Hiller, H. Schiemann, E. Weidner, S. Peter, Interfacial tension in systems with a supercritical component at high pressures. Chem. Eng. Technol. 16 (1993) 206-212.

102. C.A. Lockemann, Interfacial tensions of the binary systems carbon dioxide oleic acid, carbon dioxide methyl myristate, and carbon dioxide methyl palmitate and of the ternary system carbon dioxide methyl myristate methyl palmitate at high pressures. Chem. Eng. Process. 33 (1994) 193-198.

103. N. Czerwonatis, R. Eggers, Disintegration of liquid jets and drop drag coefficients in pressurized nitrogen and carbon dioxide. Chem. Eng. Technol. 24 (2001) 619-624.

104. A.W. Kerst, B. Judat, E.U. Schlünder, Flow regimes of free jets and falling films at high ambient pressure. Chem. Eng. Sci. 55 (2000) 4189-4208.

105. S. Li, G.S. Varadarajan, S. Hartland, Solubilities of theobromine and caffeine in supercritical carbon dioxide: correlation with density-based models. Fluid Phase Equilib. 68 (1991) 263-280.

106. E.H. Chimowitz, K.J. Pennisi, Process synthesis concepts for supercritical gas extraction in the crossover region. AIChE J. 32 (1986) 1665-1676.

107. H.C.E. Stahl, W. Schilz, Extraktion mit überkritischen Gasen in direkter Kopplung mit der Dünnschicht Chromatographie. Anwendungsmöglichkeiten auf dem Naturstoffgebiet. Chem. Ing. Tech. 48 (1976) 773-778.

108. E. Stahl, K.W. Quirin, Dense gas extraction on a laboratory scale: A survey of some recent results. Fluid Phase Equilib. 10 (1983) 269-278.

109. M.P. Ekart, K.L. Bennett, S.M. Ekart, G.S. Gurdial, C.L. Liotta, C.A. Eckert, Cosolvent interactions in supercritical fluid solutions. AIChE J. 39 (1993) 235-248.

110. J.M. Walsh, G.D. Ikonomou, M.D. Donohue, Supercritical phase behavior - the entrainer effect. Fluid Phase Equilib. 33 (1987) 295-314.

111. J.G. Van Alsten, C.A. Eckert, Effect of entrainers and of solute size and polarity in supercritical fluid solutions. J. Chem. Eng. Data 38 (1993) 605-610.

112. E. Ruckenstein, I. Shulgin, Entrainer effect in supercritical mixtures. Fluid Phase Equilib. 180 (2001) 345-359.

113. G. Brunner, S. Peter, On the solubility of glycerides and fatty acids in compressed gases in the presence of an entrainer. Sep. Sci. Technol. 17 (1982) 199-214.

114. G. Brunner, Selectivity of supercritical compounds and entrainers with respect to model substances. Fluid Phase Equilib. 10 (1983) 289-298.

115. E. Ruckenstein, I. Shulgin, The solubility of solids in mixtures composed of a supercritical fluid and an entrainer. Fluid Phase Equilib. 200 (2002) 53-67.

116. W.J. Schmitt, R.C. Reid, The use of entrainers in modifying the solubility of phenanthrene and benzoic acid in supercritical carbon dioxide and ethane. Fluid Phase Equilib. 32 (1986) 77-99.

117. J.M. Dobbs, J.M. Wong, K.P. Johnston, Nonpolar cosolvents for solubility enhancement in supercritical fluid carbon-dioxide. J. Chem. Eng. Data 31 (1986) 303-308.

118. M. Skerget, Z. Knez, Solubility of binary solid mixture β-carotene-capsaicin in dense $CO_2$. J. Agric. Food. Chem. 45 (1997) 2066-2069.

119. B.P. Nobre, R.L. Mendes, E.M. Queiroz, F.P. Pessoa, J.P. Coelho, A.F. Palavra, Calculation of solubilities for systems containing multiple non-volatile solutes and supercritical carbon dioxide. Ind. Eng. Chem. Res. 48 (2009) 1551-1555.

120. F.P. Lucien, N.R. Foster, Solubilities of solid mixtures in supercritical carbon dioxide: A review. J. Supercrit. Fluids 17 (2000) 111-134.

121. R. Murga, R. Ruiz, S. Beltran, J.L. Cabezas, Extraction of natural complex phenols and tannins from grape seeds by using supercritical mixtures of carbon dioxide and alcohol. J. Agric. Food. Chem. 48 (2000) 3408-3412.

122. Ö. Güçlü-Üstündag, F. Temelli, Solubility behavior of ternary systems of lipids, cosolvents and supercritical carbon dioxide and processing aspects. J. Supercrit. Fluids 36 (2005) 1-15.

123. Ö. Güçlü-Üstündag, F. Temelli, Solubility behavior of ternary systems of lipids in supercritical carbon dioxide. J. Supercrit. Fluids 38 (2006) 275-288.

124. C.K. Ooi, A. Bhaskar, M.S. Yener, D.Q. Tuan, J. Hsu, S.S.H. Rizvi, Continuous supercritical carbon dioxide processing of palm oil. J. Am. Oil Chem. Soc. 73 (1996) 233-237.

125. O.J. Catchpole, J.B. Grey, K.A. Noermark, Fractionation of fish oils using supercritical $CO_2$ and $CO_2$ plus ethanol mixtures. J. Supercrit. Fluids 19 (2000) 25-37.

126. R. Dohrn, G. Brunner, High-pressure fluid-phase equilibria: Experimental methods and systems investigated (1988-1993). Fluid Phase Equilib. 106 (1995) 213-282.

127. K. Nagahama, VLE measurements at elevated pressures for process development. Fluid Phase Equilib. 116 (1996) 361-372.

128. U.K. Deiters, G.M. Schneider, High pressure phase equilibria: experimental methods. Fluid Phase Equilib. 29 (1986) 145-160.

129. J.C. de la Fuente, B. Oyarzún, N. Quezada, J.M. del Valle, Solubility of carotenoid pigments (lycopene and astaxanthin) in supercritical carbon dioxide. Fluid Phase Equilib. 247 (2006) 90-95.

130. Ö. Güçlü-Üstündag, F. Temelli, Correlating the solubility behavior of minor lipid components in supercritical carbon dioxide. J. Supercrit. Fluids 31 (2004) 235-253.

131. Ö. Güçlü-Üstündag, F. Temelli, Correlating the solubility behavior of fatty acids, mono-, di-, and triglycerides, and fatty acid esters in supercritical carbon dioxide. Ind. Eng. Chem. Res. 39 (2000) 4756-4766.

132. M.J. Cocero, S. González, S. Pérez, E. Alonso, Supercritical extraction of unsaturated products. Degradation of β-carotene in supercritical extraction processes. J. Supercrit. Fluids 19 (2000) 39-44.

133. K. Sakaki, Solubility of β-carotene in dense carbon-dioxide and nitrous-oxide from 308 to 323 K and from 9.6 to 30 MPa. J. Chem. Eng. Data 37 (1992) 249-251.

134. R.L. Mendes, B.P. Nobre, J.P. Coelho, A.F. Palavra, Solubility of β-carotene in supercritical carbon dioxide and ethane. J. Supercrit. Fluids 16 (1999) 99-106.

135. M.D.A. Saldaña, L. Sun, S.E. Guigard, F. Temelli, Comparison of the solubility of β-carotene in supercritical $CO_2$ based on a binary and a multicomponent complex system. J. Supercrit. Fluids 37 (2006) 342-349.

136. C.P. Hicks, A bibliography of thermodynamic quantities for binary fluid mixtures, in Chemical Thermodynamics, M.L. McGlashan, Editor. 1978, Chemical Society: London.

137. H. Knapp, R. Döring, L. Oellrich, U. Plöcker, J.M. Prausnitz, Vapor-liquid equilibria for mixtures of low-boiling substances, in DECHEMA Chem. Data Series VI. 1981.

138. M. Christov, R. Dohrn, High-pressure fluid phase equilibria: Experimental methods and systems investigated (1994-1999). Fluid Phase Equilib. 202 (2002) 153-218.

139. R.E. Fornari, P. Alessi, I. Kikic, High pressure fluid phase equilibria: experimental methods and systems investigated (1978-1987). Fluid Phase Equilib. 57 (1990) 1-33.

140. R. Dohrn, S. Peper, J.M.S. Fonseca, High-pressure fluid-phase equilibria: Experimental methods and systems investigated (2000-2004). Fluid Phase Equilib. 288 (2010) 1-54.

141. K.D. Bartle, A.A. Clifford, S.A. Jafar, G.F. Shilstone, Solubilities of solids and liquids of low volatility in supercritical carbon-dioxide. J. Phys. Chem. Ref. Data. 20 (1991) 713-756.

142. H. Higashi, Y. Iwai, Y. Arai, Solubilities and diffusion coefficients of high boiling compounds in supercritical carbon dioxide. Chem. Eng. Sci. 56 (2001) 3027-3044.

143. R.B. Gupta, J.J. Shim, Solubility in Supercritical Carbon Dioxide. 2007, Boca Raton: CRC Press.

144. B. Diaz-Reinoso, A. Moure, H. Dominguez, J.C. Parajo, Supercritical $CO_2$ extraction and purification of compounds with antioxidant activity. J. Agric. Food. Chem. 54 (2006) 2441-2469.

145. R. Hartono, G.A. Mansoori, A. Suwono, Prediction of solubility of biomolecules in supercritical solvents. Chem. Eng. Sci. 56 (2001) 6949-6958.

146. G.R. Somayajulu, Estimation procedures for critical constants. J. Chem. Eng. Data 34 (1989) 106-120.

147. J. Chrastil, Solubility of solids and liquids in supercritical gases. J. Phys. Chem. 86 (1982) 3016-3021.

148. D.H. Ziger, C.A. Eckert, Correlation and prediction of solid-supercritical fluid phase equilibria. Ind. Eng. Chem. Process Des. Dev. 22 (1983) 582-588.

149. W.J. Schmitt, R.C. Reid, The influence of the solvent gas on solubility and selectivity in supercritical extraction, in Supercritical Fluid Technology, J.M.L. Penninger, M. Radosz, M.A. McHugh, and V.J. Krukonis, Editors. 1985, Elsevier: New York. p. 123-147.

150. G.S. Gurdial, P.A. Wells, N.R. Foster, R.P. Chaplin, The role of polarity in correlations of solid-supercritical fluid phase systems. J. Supercrit. Fluids 2 (1989) 85-96.

151. M. Skerget, A. Knez, M. Habulin, Solubility of β-carotene and oleic acid in dense $CO_2$ and data correlation by a density based model. Fluid Phase Equilib. 109 (1995) 131-138.

152. C. Borch-Jensen, A. Staby, J.M. Mollerup, Phase equilibria of urea-fractionated fish oil fatty acid ethyl esters and supercritical carbon dioxide. Ind. Eng. Chem. Res. 33 (1994) 1574-1579.

153. C. Borch-Jensen, J. Mollerup, Phase equilibria of fish oil in sub- and supercritical carbon dioxide. Fluid Phase Equilib. 138 (1997) 179-211.

154. C. Borch-Jensen, J. Mollerup, Phase equilibria of long-chain polyunsaturated fish oil fatty acid ethyl esters and carbon dioxide, ethane, or ethylene at reduced gas temperatures of 1.03 and 1.13. Fluid Phase Equilib. 161 (1999) 169-189.

155. A. Staby, T. Forskov, J. Mollerup, Phase equilibria of fish oil fatty acid ethyl esters and sub- and supercritical $CO_2$. Fluid Phase Equilib. 87 (1993) 309-340.

156. A. Staby, J. Mollerup, Solubility of fish oil fatty acid ethyl esters in sub and supercritical carbon dioxide. J. Am. Oil Chem. Soc. 70 (1993) 583-588.

157. V. Riha, G. Brunner, Phase equilibrium of fish oil ethyl esters with supercritical carbon dioxide. J. Supercrit. Fluids 15 (1999) 33-50.

158. J.N. Jaubert, L. Coniglio, F. Denet, From the correlation of binary systems involving supercritical $CO_2$ and fatty acid esters to the prediction of ($CO_2$-fish oils) phase behavior. Ind. Eng. Chem. Res. 38 (1999) 3162-3171.

159. L. Coniglio, K. Knudsen, R. Gani, Prediction of supercritical fluid-liquid equilibria for carbon dioxide and fish oil related compounds through the equation of state - Excess function (EOS-$g^E$) approach. Fluid Phase Equilib. 116 (1996) 510-517.

160. L. Coniglio, K. Knudsen, R. Gani, Model prediction of supercritical fluid-liquid equilibria for carbon dioxide and fish oil related compounds. Ind. Eng. Chem. Res. 34 (1995) 2473-2484.

161. V.K. Mishra, F. Temelli, B. Ooraikul, Extraction and purification of omega-3 fatty acids with an emphasis on supercritical fluid extraction - a review. Food Res. Int. 26 (1993) 217-226.

162. W. Eisenbach, Supercritical fluid extraction: a film demonstration. Phys. Chem. Chem. Phys. 88 (1984) 882-887.

163. W.B. Nilsson, Gauglitz E.J, Jr., J.K. Hudson, V.F. Stout, J. Spinelli, Fractionation of menhaden oil ethyl esters using supercritical fluid $CO_2$. J. Am. Oil Chem. Soc. 65 (1988) 109-117.

164. W.B. Nilsson, E.J. Gauglitz, J.K. Hudson, Supercritical fluid fractionation of fish oil esters using incremental pressure programming and a temperature gradient. J. Am. Oil Chem. Soc. 66 (1989) 1596-1600.

165. U. Fleck, C. Tiegs, G. Brunner, Fractionation of fatty acid ethyl esters by supercritical $CO_2$: high separation efficiency using an automated countercurrent column. J. Supercrit. Fluids 14 (1998) 67-74.

166. V. Riha, G. Brunner, Separation of fish oil ethyl esters with supercritical carbon dioxide. J. Supercrit. Fluids 17 (2000) 55-64.

167. O.J. Catchpole, J.C. Von Kamp, J.B. Grey, Extraction of squalene from shark liver oil in a packed column using supercritical carbon dioxide. Ind. Eng. Chem. Res. 36 (1997) 4318-4324.

168. G. Perretti, A. Motori, E. Bravi, F. Favati, L. Montanari, P. Fantozzi, Supercritical carbon dioxide fractionation of fish oil fatty acid ethyl esters. J. Supercrit. Fluids 40 (2007) 349-353.

169. F. Gironi, M. Maschietti, Separation of fish oils ethyl esters by means of supercritical carbon dioxide: Thermodynamic analysis and process modelling. Chem. Eng. Sci. 61 (2006) 5114-5126.

170. A. Blaha-Schnabel, A. Beyer, B. Czech, H. Jakob, H. Schiemann, E. Weidner, S. Peter, Influence of interfacial tension and viscosity on the behavior of a packed column in near-critical fluid extraction. Chem. Eng. Commun. 146 (1996) 13-31.

171. R. Stockfleth, G. Brunner, Holdup, pressure drop, and flooding in packed countercurrent columns for the gas extraction. Ind. Eng. Chem. Res. 40 (2001) 347-356.

172. R. Ruivo, M.J. Cebola, P.C. Simoes, M. Nunes da Ponte, Fractionation of edible oil model mixtures by supercritical carbon dioxide in a packed column. 2. A mass-transfer study. Ind. Eng. Chem. Res. 41 (2002) 2305-2315.

173. A. Martín, M.J. Cocero, Mathematical modeling of the fractionation of liquids with supercritical $CO_2$ in a countercurrent packed column. J. Supercrit. Fluids 39 (2007) 304-314.

174. G. Brunner, Counter-current separations. J. Supercrit. Fluids 47 (2009) 574-582.

175. O.J. Catchpole, S.J. Tallon, W.E. Eltringham, J.B. Grey, K.A. Fenton, E.M. Vagi, M.V. Vyssotski, A.N. MacKenzie, J. Ryan, Y. Zhu, The extraction and fractionation of specialty lipids using near critical fluids. J. Supercrit. Fluids 47 (2009) 591-597.

176. O.J. Catchpole, A.N. MacKenzie, J.B. Grey, Improvements in or relating to separation technology Patent #: NZ518504, WO03089399, 2002.

177. M. Jakobsson, B. Sivik, P.A. Bergqvist, B. Strandberg, C. Rappe, Counter-current extraction of dioxins from cod liver oil by supercritical carbon dioxide. J. Supercrit. Fluids 7 (1994) 197-200.

178. M. Jakobsson, B. Sivik, P.A. Bergqvist, B. Strandberg, M. Hjelt, C. Rappe, Extraction of dioxins from cod liver oil by supercritical carbon dioxide. J. Supercrit. Fluids 4 (1991) 118-123.

179. A.P. Antunes-Corrêa, C. Arantes-Peixoto, L.A. Guaraldo-Gonçalves, F.A. Cabral, Fractionation of fish oil with supercritical carbon dioxide. J. Food Eng. 88 (2008) 381-387.

180. P.G. Jessop, B. Subramaniam, Gas-expanded liquids. Chem. Rev. 107 (2007) 2666-2694.

181. A. Kordikowski, A.P. Schenk, R.M. Van Nielen, C.J. Peters, Volume expansions and vapor-liquid equilibria of binary mixtures of a variety of polar solvents and certain near-critical solvents. J. Supercrit. Fluids 8 (1995) 205-216.

182. R. Sih, M. Armenti, R. Mammucari, F. Dehghani, N.R. Foster, Viscosity measurements on saturated gas-expanded liquid systems-Ethanol and carbon dioxide. J. Supercrit. Fluids 43 (2008) 460-468.

183. R. Sih, F. Dehghani, N.R. Foster, Viscosity measurements on gas expanded liquid systems-Methanol and carbon dioxide. J. Supercrit. Fluids 41 (2007) 148-157.

184. R. Sih, N.R. Foster, Viscosity measurements on saturated gas expanded liquid systems-Acetone and carbon dioxide. J. Supercrit. Fluids 47 (2008) 233-239.

185. S. Peter, E. Weidner, H. Jakob, Die Viskosität koexistierender Phasen bei der überkritischen Fluidextraktion. Chem. Ing. Tech. 59 (1987) 59-62.

186. C.A. Lockemann, E.U. Schlünder, Liquid-phase viscosities of the binary systems carbon dioxide-oleic acid, carbon dioxide-methyl myristate, and carbon dioxide-methyl palmitate at high pressures. Chem. Eng. Process. 34 (1995) 487-493.

187. A. Wesch, N. Dahmen, K.H. Ebert, Measuring the static dielectric constants of pure carbon dioxide and carbon dioxide mixed with ethanol and toluene at elevated pressures. Ber. Bunsen Ges. - Phys. Chem. Chem. Phys. 100 (1996) 1368-1371.

188. F.M. Orr Jr, J.P. Heller, J.J. Taber, Carbon dioxide flooding for enhanced oil recovery - promise and problems. J. Am. Oil Chem. Soc. 59 (1982) 810-817.

189. M. Nobakht, S. Moghadam, Y. Gu, Effects of viscous and capillary forces on $CO_2$ enhanced oil recovery under reservior conditions. Energy Fuels 21 (2007) 3469-3476.

190. S. Voges, R. Eggers, A. Pietsch, Gas assisted oilseed pressing. Sep. Purif. Technol. 63 (2008) 1-14.

191. P. Willems, N.J.M. Kuipers, A.B. de Haan, Gas assisted mechanical expression of oilseeds: Influence of process parameters on oil yield. J. Supercrit. Fluids 45 (2008) 298-305.

192. O.J. Catchpole, J.B. Grey, K.A. Mitchell, J.S. Lan, Supercritical antisolvent fractionation of propolis tincture. J. Supercrit. Fluids 29 (2004) 97-106.

193. F. Shahidi, X.Q. Han, Encapsulation of food ingredients. Crit. Rev. Food Sci. Nutr. 33 (1993) 501-547.

194. B.K. Green, L. Schleicher, Oil-containing microscopic capsules and method of making them. Patent #: US2800457, 1957.

195. M.E. Malone, I.A.M. Appelqvist, T.C. Goff, J.E. Homan, J.P.G. Wilkins, A novel approach to the selective control of lipophilic flavor release, in Low Fat Foods, ACS Sym. Ser. 763. 2000. p. 212-227.

196. S. Gouin, Microencapsulation: industrial appraisal of existing technologies and trends. Trends Food Sci. Technol. 15 (2004) 330-347.

197. K.S. Miller, J.M. Krochta, Oxygen and aroma barrier properties of edible films: A review. Trends Food Sci. Technol. 8 (1997) 228-237.

198. I. Goubet, J.L. Le Quere, A.J. Voilley, Retention of aroma compounds by carbohydrates: Influence of their physicochemical characteristics and of their physical state. A review. J. Agric. Food. Chem. 46 (1998) 1981-1990.

199. Y. Roos, M. Karel, Applying state diagrams to food processing and development. Food Technol. 45 (1991) 66, 68-71, 107.

200. Y. Roos, M. Karel, Phase transitions of mixtures of amorphous polysaccharides and sugars. Biotechnol. Progr. 7 (1991) 49-53.

201. Y.H. Roos, M. Karel, Plasticizing effect of water on thermal-behavior and crystallization of amorphous food models. J. Food Sci. 56 (1991) 38-43.

202. J.D. Dziezak, Microencapsulation and encapsulated ingredients. Food Technol. 42 (1988) 136-151.

203. K. Dewettinck, A. Huyghebaert, Fluidized bed coating in food technology. Trends Food Sci. Technol. 10 (1999) 163-168.

204. C.I. Beristain, A. Vazquez, H.S. Garcia, E.J. Vernon-Carter, Encapsulation of orange peel oil by co-crystallization. Food Sci. Technol. 29 (1996) 645-647.

205. A.C. Chen, M.F. Veiga, A.B. Rizzuto, Cocrystallization: An encapsulation process. Food Technol. 42 (1988) 87-90.

206. J. Szejtli, Cyclodextrins: a new group of industrial basic materials. Nahrung 29 (1985) 911-24.

207. T.A. Reineccius, G.A. Reineccius, T.L. Peppard, Flavor release from cyclodextrin complexes: Comparison of alpha, beta, and gamma types. J. Food Sci. 68 (2003) 1234-1239.

208. L. Szente, J. Szejtli, Cyclodextrins as food ingredients. Trends Food Sci. Technol. 15 (2004) 137-142.

209. A. Hedges, C. McBride, Utilization of beta-cyclodextrin in food. Cereal Foods World 44 (1999) 700-704.

210. M.M. Meier, D.A. Drunkler, M.T. Bordignon Luiz, R. Fett, B. Szpoganicz, The influence of beta-cyclodextrin on goaty flavour: characterization of synthetic inclusion complexes with capric acid and caprylic acid. Brit. Food J. 103 (2001) 281-290.

211. T.A. Reineccius, G.A. Reineccius, T.L. Peppard, Utilization of beta-cyclodextrin for improved flavor retention in thermally processed foods. J. Food Sci. 69 (2004) FCT58-FCT62.

212. Y. Yeo, E. Bellas, W. Firestone, R. Langer, D.S. Kohane, Complex coacervates for thermally sensitive controlled release of flavor compounds. J. Agric. Food. Chem. 53 (2005) 7518-7525.

213. J.C. Soper, Utilization of coacervated flavors. Encapsulation and Controlled Release of Food Ingredients - ACS Symp. Series no. 590, ed. S.J. Risch and G.A. Reineccius. 1995, Washington: American Chemical Society. 104-112.

214. R.J. Versic, Coacervation for Flavor Encapsulation. ACS Symp. Series 370 (1988) 126-131.

215. A. Lamprecht, U. Schaefer, C.M. Lehr, Influences of process parameters on preparation of microparticle used as a carrier system for n - 3 unsaturated fatty acid ethyl esters used in supplementary nutrition. J. Microencapsulation 18 (2001) 347-357.

216. S. Keipert, P. Melegari, Oil containing microparticles prepared by simple coacervation [Oelhaltige, mittels einfachkoazervation hergestellte Mikropartikeln.]. PZ Wissenschaft 137 (1992) 84-89.

217. K.G. Wu, X.H. Chai, Y. Chen, Microencapsulation of fish oil by simple coacervation of hydroxypropyl methylcellulose. Chin. J. Chem. 23 (2005) 1569-1572.

218. V.B. Junyaprasert, A. Mitrevej, N. Sinchaipanid, P. Boonme, D.E. Wurster, Effect of process variables on the microencapsulation of vitamin A palmitate by gelatin-acacia coacervation. Drug Dev. Ind. Pharm. 27 (2001) 561-566.

219. M. Van De Weert, M.B. Andersen, S. Frokjaer, Complex coacervation of lysozyme and heparin: Complex characterization and protein stability. Pharm. Res. 21 (2004) 2354-2359.

220. H.L. Jiang, K.J. Zhu, Polyanion/gelatin complexes as pH-sensitive gels for controlled protein release. J. Appl. Polym. Sci. 80 (2001) 1416-1425.

221. D.J. Burgess, S. Ponsart, Beta-glucuronidase activity following complex coacervation and spray drying microencapsulation. J. Microencapsulation 15 (1998) 569-579.

222. G.R. Chilvers, V.J. Morris, Coacervation of gelatin-gellan gum mixtures and their use in microencapsulation., Carbohydr. Polym. 7 (1987) 111-120.

223. R. Arshady, Microspheres and microcapsules, a survey of manufacturing techniques. Part II. Coacervation. Polym. Eng. Sci. 30 (1990) 905-914.

224. D.J. Burgess, Practical analysis of complex coacervate systems. J. Colloid Interface Sci. 140 (1990) 227-238.

225. F. Weinbreck, R. de Vries, P. Schrooyen, C.G. de Kruif, Complex coacervation of whey proteins and gum arabic. Biomacromolecules 4 (2003) 293-303.

226. E. Mathiowitz, Encyclopedia of Controlled Drug Delivery. 1999, New York: Wiley.

227. D.D. Lasic, Novel applications of liposomes. Trends Biotechnol. 16 (1998) 307-321.

228. T.M. Taylor, P.M. Davidson, B.D. Bruce, J. Weiss, Liposomal nanocapsules in food science and agriculture. Crit. Rev. Food Sci. Nutr. 45 (2005) 587-605.

229. A. Picon, P. Gaya, M. Medina, M. Nunez, Proteinases encapsulated in stimulated release liposomes for cheese ripening. Biotechnol. Lett. 19 (1997) 345-348.

230. R.O. Benech, E.E. Kheadr, C. Lacroix, I. Fliss, Impact of nisin producing culture and liposome-encapsulated nisin on ripening of *Lactobacillus* added-Cheddar cheese. J. Dairy Sci. 86 (2003) 1895-909.

231. E.E. Kheadr, J.C. Vuillemard, S.A. El-Deeb, Impact of liposome-encapsulated enzyme cocktails on cheddar cheese ripening. Food Res. Int. 36 (2003) 241-252.

232. S. Xia, S. Xu, Ferrous sulfate liposomes: Preparation, stability and application in fluid milk. Food Res. Int. 38 (2005) 289-296.

233. R. Sharma, D. Lal, Fortification of milk with microencapsulated vitamin C and its thermal stability. J. Food Sci. Technol. 42 (2005) 191-194.

234. C.J. Kirby, C.J. Whittle, N. Rigby, D.T. Coxon, B.A. Law, Stabilization of ascorbic acid by microencapsulation in liposomes. Int. J. Food Sci. Technol. 26 (1991) 437-449.

235. S. Higgins, Y.L. Carroll, N.M. O'Brien, P.A. Morrissey, Use of microencapsulated fish oil as a means of increasing n-3 polyunsaturated fatty acid intake. J. Hum. Nutr. Diet. 12 (1999) 265-271.

236. J.M.W. Wallace, A.J. McCabe, P.J. Robson, M.K. Keogh, C.A. Murray, P.M. Kelly, G. Marquez-Ruiz, H. McGlynn, W.S. Gilmore, J.J. Strain, Bioavailability of n-3 polyunsaturated fatty acids (PUFA) in foods enriched with microencapsulated fish oil. Ann. Nutr. Metab. 44 (2000) 157-162.

237. C.J. Barrow, C. Nolan, B.J. Holub, Bioequivalence of encapsulated and microencapsulated fish-oil supplementation. J. Function. Foods 1 (2009) 38-43.

238. M. Cansell, F. Nacka, N. Combe, Marine lipid-based liposomes increase in vivo FA bioavailability. Lipids 38 (2003) 551-559.

239. Y.F. Hsieh, T.L. Chen, Y.T. Wang, J.H. Chang, H.M. Chang, Properties of liposomes prepared with various lipids. J. Food Sci. 67 (2002) 2808-2813.

240. K. Heinzelmann, K. Franke, B. Jensen, A.M. Haahr, Protection of fish oil from oxidation by microencapsulation using freeze-drying techniques. Eur. J. Lipid Sci. Technol. 102 (2000) 114-121.

241. K. Heinzelmann, K. Franke, J. Velasco, G. Marquez-Ruiz, Microencapsulation of fish oil by freeze-drying techniques and influence of process parameters on oxidative stability during storage. Eur. Food Res. Technol. 211 (2000) 234-239.

242. G. Marquez-Ruiz, J. Velasco, C. Dobarganes, Evaluation of oxidation in dried microencapsulated fish oils by a combination of adsorption and size exclusion chromatography. Eur. Food Res. Technol. 211 (2000) 13-18.

243. M.K. Keogh, B.T. O'Kennedy, J. Kelly, M.A. Auty, P.M. Kelly, A. Fureby, A.M. Haahr, Stability to oxidation of spray-dried fish oil powder microencapsulated using milk ingredients. J. Food Sci. 66 (2001) 217-224.

244. Y.H. Cho, H.K. Shim, J. Park, Encapsulation of fish oil by an enzymatic gelation process using transglutaminase cross-linked proteins. J. Food Sci. 68 (2003) 2717-2723.

245. S.A. Hogan, E.D. O'Riordan, M. O'Sullivan, Microencapsulation and oxidative stability of spray-dried fish oil emulsions. J. Microencapsulation 20 (2003) 675-688.

246. M.Y. Baik, E.L. Suhendro, W.W. Nawar, D.J. McClements, E.A. Decker, P. Chinachoti, Effects of antioxidants and humidity on the oxidative stability of microencapsulated fish oil. J. Am. Oil Chem. Soc. 81 (2004) 355-360.

247. R. Jónsdóttir, M. Bragadóttir, G.O. Arnarson, Oxidatively derived volatile compounds in microencapsulated fish oil monitored by solid-phase microextraction (SPME). J. Food Sci. 70 (2005) C433-C440.

248. A.S. McGill, R. Hardy, J.R. Burt, Hept-cis-4-enal and its contribution to the off-flavour in cold stored cod. J. Sci. Food Agric. 25 (1974) 1477-1489.

249. S. Drusch, K. Schwarz, Microencapsulation properties of two different types of n-octenylsuccinate-derivatised starch. Eur. Food Res. Technol. 222 (2006) 155-164.

250. D.E. Walton, C.J. Mumford, The morphology of spray-dried particles. The effect of process variables upon the morphology of spray-dried particles. Chem. Eng. Res. Des. 77 (1999) 442-460.

251. M.A. Augustin, L. Sanguansri, O. Bode, Maillard reaction products as encapsulants for fish oil powders. J. Food Sci. 71 (2006).

252. L.H. Tan, L.W. Chan, P.W.S. Heng, Alginate/starch composites as wall material to achieve microencapsulation with high oil loading. J. Microencapsulation 26 (2009) 263-271.

253. S. Drusch, S. Berg, Extractable oil in microcapsules prepared by spray-drying: Localisation, determination and impact on oxidative stability. Food Chem. 109 (2008) 17-24.

254. J.B. Hannay, J. Hogarth, On the solubility of solids in gases. Proc. R. Soc. London 29 (1879) 324-326.

255. E. Weidner, High pressure micronization for food applications. J. Supercrit. Fluids 47 (2009) 556-565.

256. P. York, Strategies for particle design using supercritical fluid technologies. Pharm. Sci. Technol. Today 2 (1999) 430-440.

257. J. Jung, M. Perrut, Particle design using supercritical fluids: Literature and patent survey. J. Supercrit. Fluids 20 (2001) 179-219.

258. Z. Knez, E. Weidner, Particles formation and particle design using supercritical fluids. Curr. Opin. Solid State Mater. Sci. 7 (2003) 353-361.

259. E. Reverchon, G. Della Porta, Particle design using supercritical fluids. Chem. Eng. Technol. 26 (2003) 840-845.

260. A. Shariati, C.J. Peters, Recent developments in particle design using supercritical fluids. Curr. Opin. Solid State Mater. Sci. 7 (2003) 371-383.

261. E.M. Martin Del Valle, M.A. Galan, Supercritical fluid technique for particle engineering: Drug delivery applications. Rev. Chem. Eng. 21 (2005) 33-69.

262. M.J. Cocero, A. Martín, F. Mattea, S. Varona, Encapsulation and co-precipitation processes with supercritical fluids: Fundamentals and applications. J. Supercrit. Fluids 47 (2009) 546-555.

263. A. Martín, M.J. Cocero, Micronization processes with supercritical fluids: Fundamentals and mechanisms. Adv. Drug Delivery Rev. 60 (2008) 339-350.

264. C. Vemavarapu, M.J. Mollan, M. Lodaya, T.E. Needham, Design and process aspects of laboratory scale SCF particle formation systems. Int. J. Pharm. 292 (2005) 1-16.

265. D.W. Matson, J.L. Fulton, R.C. Petersen, R.D. Smith, Rapid expansion of supercritical fluid solutions: solute formation of powders, thin films, and fibers. Ind. Eng. Chem. Res. 26 (1987) 2298-2306.

266. N. Foster, R. Mammucari, F. Dehghani, A. Barrett, K. Bezanehtak, E. Coen, G. Combes, L. Meure, A. Ng, H.L. Regtop, A. Tandya, Processing pharmaceutical compounds using dense gas technology. Ind. Eng. Chem. Res. 42 (2003) 6476-6493.

267. E. Reverchon, R. Adami, Nanomaterials and supercritical fluids. J. Supercrit. Fluids 37 (2006) 1-22.

268. A. Sane, J. Limtrakul, Formation of retinyl palmitate-loaded poly(l-lactide) nanoparticles using rapid expansion of supercritical solutions into liquid solvents (RESOLV). J. Supercrit. Fluids 51 (2009) 230-237.

269. J.C. De La Fuente Badilla, C.J. Peters, J. De Swaan Arons, Volume expansion in relation to the gas-antisolvent process. J. Supercrit. Fluids 17 (2000) 13-23.

# 3 Density of Marine Lipids in Equilibrium with Carbon Dioxide[1]

## 3.1 Introduction

Modelling and design of fractionation processes using supercritical fluids (SCF), in terms of mass transfer and understanding flooding behaviour of countercurrent packed columns, falling film extraction or spray processes, require physical properties such as density and viscosity of both the liquid and gaseous phases as well as interfacial tension [1-5]. However, experimental data for the density of fish oil triglycerides (TG) and fatty acid ethyl esters (FAEE) are limited in the literature.

Chang *et al.* [6] determined the density of highly concentrated fish oil ethyl esters containing high amounts of docosahexaenoic acid (DHA) and eicosapentaenoic acid (EPA) (90% and 96%, respectively) in equilibrium with $CO_2$ at 40 and 60°C and pressures of up to about 23 MPa using a U-tube densitometer. Smith *et al.* [7] assessed the density and volumetric swelling factors of mixtures of $CO_2$ with fish oil and fish oil ethyl esters at various compositions using a vibrating tube densitometer at 40°C and pressures ranging from 0.1 to about 20 MPa. A high-pressure pycnometer was used by Staby and Mollerup [8] to determine the density of a fish oil ethyl ester mixture at 10, 40 and 70°C and pressures up to 5.9, 15.64 and 22 MPa, respectively; however, they reported large uncertainty in their density data, presumably caused by flashing of the gas saturated esters into the evacuated pycnometer during the sampling procedure. Tegetmeier *et al.* [9] determined the density of corn oil in equilibrium with $CO_2$ using a magnetically coupled balance and sinker based on Archimedes' principle similar to the device used in this study.

Due to the lack of experimental density data for marine lipids in the literature, the objective of this study was to measure the density of fish oil TG and FAEE in equilibrium with $CO_2$ at 40, 55 and 70°C and pressures ranging from 0.1

[1] A version of this chapter has been published in J. Supercrit. Fluids 50 (2009) 97-104.

to 25 MPa. For this purpose, a view cell together with a novel device consisting of a spring balance equipped with a sinker was designed and built. The second objective was to determine the volumetric expansion of fish oil TG and FAEE in equilibrium with $CO_2$ at 40°C and pressures ranging from 0.1 to about 22 MPa. Furthermore, the results of density and volumetric expansion for both TG and FAEE were analysed in relation to the solubility data of $CO_2$ in the liquid phase taken from literature.

## 3.2 Experimental

### 3.2.1 Materials

Corn oil (Mazola®) was purchased at a local store and used without further treatment for density measurements. Refined fish oil extracted from anchovy and sardine was kindly provided by Ocean Nutrition Canada (Halifax, NS, Canada) in the form of TG and FAEE for the density measurements. The fatty acid profiles as provided by the manufacturer for the fish oil in the form of TG (Ocean Nutrition product code: XOTDHA-NG) stated a level of 8% and 25%, whereas that for the FAEE (Ocean Nutrition product code: XO4020EE) was 42% and 21% for EPA and DHA, respectively. Further specifications for both the fish oil TG and FAEE are listed in Table 3-1. Both TG and FAEE were used without further treatment and stored at 4ºC in aluminum bottles with nitrogen filled headspace to minimize any degradation. Food grade anhydrous ethanol (Commercial Alcohol, Winnipeg, MB, Canada) was used for cleaning and density measurements. Bone dry carbon dioxide with a purity of 99.9% (Praxair, Edmonton, AB, Canada) was used for the density measurements. Nitrogen with a purity of 99.998% (Praxair, Edmonton, AB, Canada) was used to fill the headspace of the aluminum bottles containing the fish oil after each opening and to flush the syringe used to inject fish oil into the apparatus.

**Table 3-1.** Fatty acid profile and specifications for FAEE and TG as provided by the manufacturer.

| | **FAEE** | **TG** |
|---|---|---|
| **Fatty acid profile** | expressed as EE | expressed as TG |
| EPA, mg/g | 390 (42%) | 70 (8%) |
| DHA, mg/g | 200 (21%) | 230 (25%) |
| Total ω-3 PUFA, mg/g | 670 (72%) | 330 (36%) |
| **Specifications** | | |
| Free fatty acids, % oleic acid | 0.5 | 0.2 |
| Acid value, mg KOH/g | 1.0 | 0.4 |
| p-Anisidine value | 8 | 12 |
| Peroxide value, meq/kg | 3 | 0 |
| Moisture level, % | 0 | 0 |

### 3.2.2 Volumetric expansion measurements

#### 3.2.2.1 Apparatus to determine volumetric expansion

The apparatus (Phase Monitor II, Supercritical Fluid Technologies, Inc., Newark, DE, USA) to measure the volumetric expansion of fish oil TG and FAEE is shown in Fig. 3-1. It consists of a variable volume high pressure view cell (3 to 30 mL) equipped with a CCD camera and temperature controlled electric heaters. The view cell was pressurized with $CO_2$ by means of a syringe pump (ISCO Model 250D, Isco Inc., Lincoln, NE, USA) instead of the original hand-operated pump of the system. The internal volume of the view cell was adjusted to about 5 mL by movement of the piston. The apparatus equipped with a thermocouple and pressure transducer was connected to a computer, which allowed continuous recording of temperature and pressure along with the images from the CCD camera. Thus, images were recorded continuously facilitating the observation of the volumetric expansion.

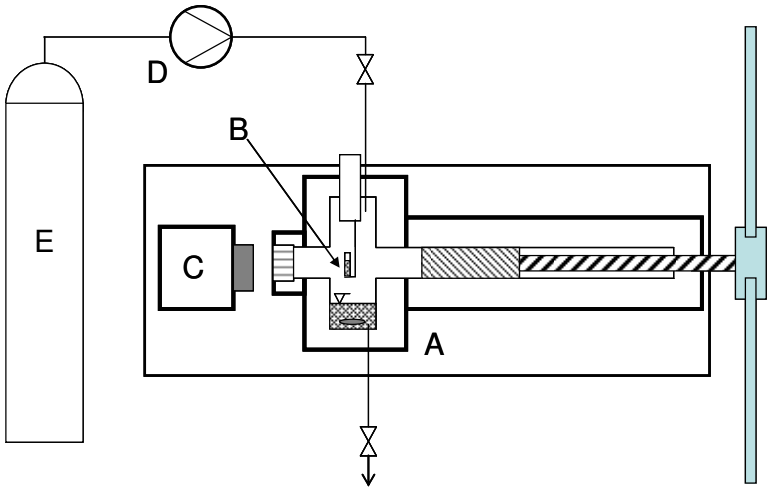


**Figure 3-1.** Apparatus to study volumetric expansion: A) thermostated view cell with magnetic stir bar, B) holder with glass capillary, C) CCD camera D) syringe pump, E) $CO_2$ tank.

#### 3.2.2.2 Determination of volumetric expansion

The volumetric expansion of fish oil in the form of TG and FAEE in equilibrium with $CO_2$ was determined in triplicate at 40°C and pressures ranging from 0.1 to about 22 MPa. Prior to experiments, fish oil (3 mL) was placed at the bottom of the view cell and continuously stirred during experiments. Furthermore, a bottom capped capillary with an inner diameter of 1.5 mm and height of 15 mm was filled with fish oil up to a height of approximately 3 mm under nitrogen using a syringe with a fine needle tip to avoid inclusion of gas bubbles. The filled capillary was then placed in the capillary holder and inserted into the preheated view cell. Fish oil was placed at the bottom of the view cell to minimize the amount of FAEE or TG extracted by SC-$CO_2$ from within the capillary during expansion studies. Most of the lipids dissolving into the $CO_2$ to reach phase equilibrium are estimated to come from the oil placed at the bottom part of the view cell, since mass transfer is proportional to the mass transfer area. The mass transfer area between the oil at the bottom of the view cell and the $CO_2$ phase was about 200 times larger than that inside the capillary. Furthermore, the oil at the bottom of the view cell was vigorously stirred to further enhance mass transfer as opposed to the capillary where there was no mixing and mainly diffusion-controlled transfer would take

place. Therefore, the effect of lipids extracted out of the capillary on the measured height of the expanded oil was considered to be negligible.

Once the oil and capillary were in place, the system was carefully flushed with $CO_2$ and equilibrated at 40°C and atmospheric pressure until the oil level in the capillary reached a constant level. At this point, the initial oil level was recorded and used as the reference height ($h_0$) as illustrated in Fig. 3-2.

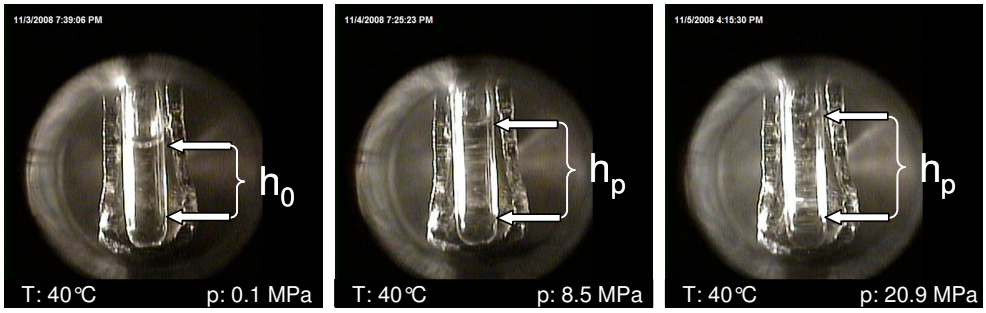


**Figure 3-2.** Images of fish oil TG in equilibrium with $CO_2$ at various pressures showing the initial height ($h_0$) and the height for expanded oil ($h_p$).

The oil level was determined by measuring the distance between the flat inside bottom of the capillary and the lowest point of the oil meniscus. The height of the liquid inside the capillary is directly proportional to the oil volume, since the diameter of the capillary is constant over its entire length. After measuring the initial height, the system was pressurized with $CO_2$ using the syringe pump. The oil was equilibrated at elevated pressure until a constant oil level inside the capillary was observed ($h_p$). At each pressure level, the volumetric expansion was followed until no change in height over 3 consecutive measurements, 30-60 min apart, indicated that the oil inside the capillary was equilibrated. The relative volume change ($\Delta V_{rel}$) was calculated according to the following equation:

$$\Delta V_{rel} = \frac{(V_p - V_0)}{V_0} = \frac{(h_p - h_0)}{h_0} \qquad (3\text{-}1)$$

where $V_p$ and $V_0$ are the volume, and $h_p$ and $h_0$ are the height of the oil at elevated and atmospheric $CO_2$ pressure, respectively.

### 3.2.3 Density measurements

#### 3.2.3.1 Apparatus to determine density

The apparatus to determine the density of liquids under high pressure conditions consisted of a 200 mL high-pressure view cell with an internal diameter of 40 mm (Nova-Swiss, Effretikon, Switzerland) equipped with electric heaters and placed in a temperature controlled insulated air bath (Fig. 3-3). The temperatures of both the air bath and electric heaters were individually controlled by means of J-type thermocouples connected to controllers (Chromalox 1601, Pittsburgh, PA, USA). The temperatures of both the liquid inside the view cell and the circulating air bath were continuously recorded to a computer by means of thermistors connected to a custom made data acquisition (DAQ) system. The DAQ system consisted of a signal amplifier and conditioner designed to linearize and transform the nonlinear response of the thermistors into voltage, which was measured by a 10 bit DAQ card (DI-194RS, DATAQ Instruments, Inc., Akron, OH, USA) and visualized by means of a chart recorder software (WinDaq/Lite, DATAQ Instruments, Inc., Akron, OH, USA). The thermistor DAQ system was calibrated against a precision digital thermometer (Model 4000, Control Company, Friendswood, TX, USA) with a resolution of 0.001ºC using an insulated heating water bath (Haake H3, Karlsruhe, Germany). With a sampling rate of 50 Hz the DAQ system allowed continuous monitoring and recording of the air bath temperature as well as liquid temperature inside the view cell with a resolution of 0.01ºC. The air bath and the electric heaters were usually capable of maintaining the liquid circulated inside the view cell at a constant temperature to within ±0.1ºC. However, in case of fish oil TG and FAEE following a stepwise increase in $CO_2$ pressure the oil temperature fluctuated by about ±0.5ºC due to exothermic and endothermic mixing effects caused by dissolution of $CO_2$ into the lipids. The view cell was pressurized with $CO_2$ by means of a piston pump (ISCO Model 250D, Isco Inc., Lincoln, NE, USA). The pressure was monitored using a digital pressure indicator with 0.05% full scale accuracy (Druck Model DPI 104, General Electrics Sensing, Billerica, MA, USA).

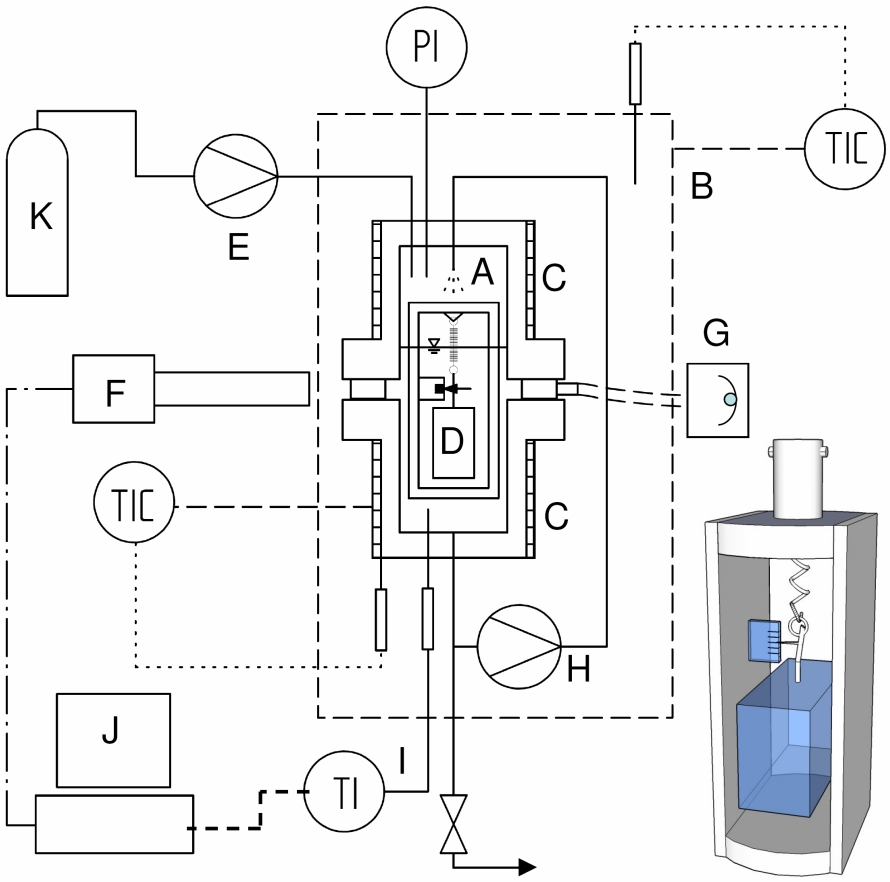


**Figure 3-3.** Apparatus for measuring density of liquids in equilibrium with $CO_2$. A) view cell, B) temperature controlled air bath, C) electric heaters, D) glass sinker, E) syringe pump, F) CMOS camera with microscope lens, G) light source, H) circulation pump, I) thermistor, J) computer, K) $CO_2$ tank.

Insert: 3D model of spring balance with sinker and microscopic scale to measure density.

The equilibration process was accelerated by circulating the liquid from the bottom of the view cell by means of a custom made magnetically-driven piston pump and spraying it into the upper $CO_2$-rich phase. The pump was designed and built in our lab, the details of which are described in the Appendix of this thesis [10]. The pump was placed inside the air bath ensuring constant temperature of the circulated oil. The flow rate of the pump was set to

approximately 25 mL/min, which allowed circulation of the entire oil content inside the view cell in about 5 min.

In order to determine the density of the liquid phase a novel device based on Archimedes' law was designed and constructed. According to Archimedes' law, the upward buoyancy force is equal to the weight of fluid displaced by the submersed body, which is related to the volume of the body and the density of the displaced fluid. The spring balance used in this work to measure density, consisted of a stainless steel frame with an adjustable tube at the top to hold the extension spring attached to the glass sinker, as illustrated in Fig. 3-3. The movable tube holding the spring allowed adjustment of the initial position of the sinker, so that a wide range of densities could be measured. The sinker was connected to the spring by means of a hook equipped with a fine needle, pointing at a microscopic glass scale. The extension spring used in this device had a constant of about 5.5 N/m. The volume of the glass sinker was approximately 16 $cm^3$. The microscopic scale used to determine the position of the sinker had 100 lines incised in glass equally spaced over a range of 5 mm. During density measurements, the sinker, needle and spring were entirely submersed in the liquid oil sample. Thus, the force on the extension spring resulting from the weight of the sinker minus the net upward buoyant force was linearly correlated to the density of the liquid. Furthermore, by calibrating the system with a fluid of known density such as $CO_2$ over a range of pressure levels, it was possible to determine the density easily by reading the position of the needle on the microscopic scale.

The position of the sinker was determined precisely by means of a CMOS camera (A602f, Basler Vision Technologies, Ahrensburg, Germany) equipped with a telecentric microscope lens having a zoom factor of up to 4.5 (VZM 450, Edmund Optics, Barrington, NJ, USA). The camera was hooked up to a personal computer to store and analyze the images. Thereby, it was possible to detect movement of the sinker as low as 2 μm, which translated to detectable density changes of about 0.1 $kg/m^3$ with the set of spring and sinker used.

### 3.2.3.2 Calibration and performance

The density device was calibrated before each density measurement using SC-$CO_2$. For a given pressure and temperature the density of pure $CO_2$ can be calculated according to the equation of state by Span and Wagner [11]. For the calibration procedure, the apparatus was heated up to the calibration temperature and pressurized with $CO_2$. The calibration was carried out at the same temperature as the subsequent density measurements for fish oil TG or FAEE. Thus, variations in the spring constant or volume of the sinker due to temperature were taken into account. For a typical calibration curve, the position of the sinker versus density of $CO_2$ was determined in triplicate at a constant temperature and at a minimum of four different pressure levels. Thereby, a linear regression line ($r^2$=0.9997) was obtained as the calibration curve for the spring balance level versus density, which allowed straightforward determination of the density in subsequent measurements.

The performance of the system was first tested at atmospheric pressure by measuring the density of anhydrous ethanol at 40, 55, and 70°C and compared to literature data. The average density of ethanol determined after triplicate measurements with the spring balance after calibration with $CO_2$ was 0.7677, 0.7527 and 0.7324 g/mL at 40, 55, and 70°C, respectively. The literature data for the density of ethanol were 0.7680, 0.7505 and 0.7323 g/mL at 40, 55, and 70°C, respectively [30]. Thus, the deviation between the density of ethanol determined with the spring balance and the literature data was less than 0.3%.

The performance of the system at elevated pressures was tested by measuring the density of an ethanol-water mixture up to a hydrostatic pressure of 30 MPa and comparing to literature data. For this purpose, a mixture of anhydrous ethanol and distilled water with a mole fraction of ethanol, $x_{EtOH}$=0.4968 was prepared. The view cell was completely filled with this mixture, thereby removing all gas from the cell. The cell was then pressurized by means of an HPLC pump (Beckman Model 110A, Fullerton, CA, USA) using the same ethanol-water mixture. The measured density of the ethanol-water mixture compared favorably to literature data [12], as illustrated in Fig. 3-4. Considering the slight

concentration difference ($x_{EtOH}$=0.4968 in this study vs 0.498 in Ref. [12]), the maximum deviation in density of the ethanol-water mixture compared to literature data of less than 0.1% over the entire pressure range was considered acceptable.

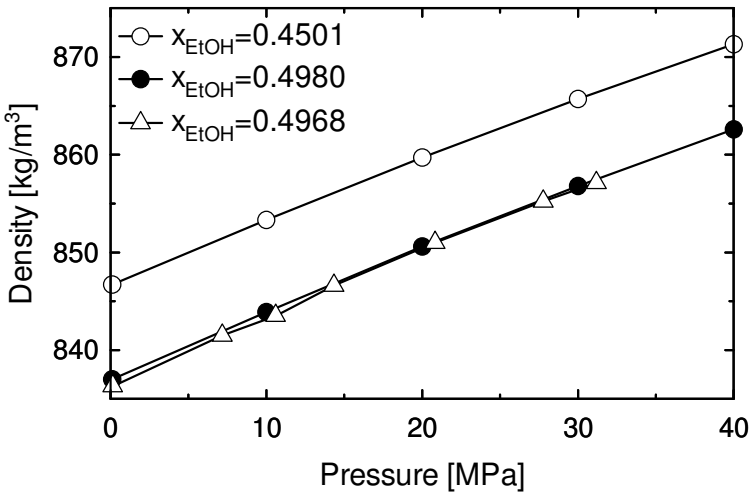


**Figure 3-4.** Density of EtOH+water mixtures at various ethanol mole fractions ($x_{EtOH}$) measured at 50°C and pressures of up to 40 MPa using the spring balance (triangles) in this study compared to literature data (circles) from Ref. [12].

To test the performance with gas-expanded liquids, the density of corn oil in contact with $CO_2$ was determined at 40ºC at pressures ranging from 0.1 to about 25 MPa and compared to literature data [9]. Considering the fact that corn oil is a natural product, for which properties can vary between batches, the measurements performed with the spring balance were in good agreement with the literature data, as shown in Fig. 3-5. The maximum deviation between the measured density of corn oil and literature values over the entire pressure range studied was less than 0.35%.

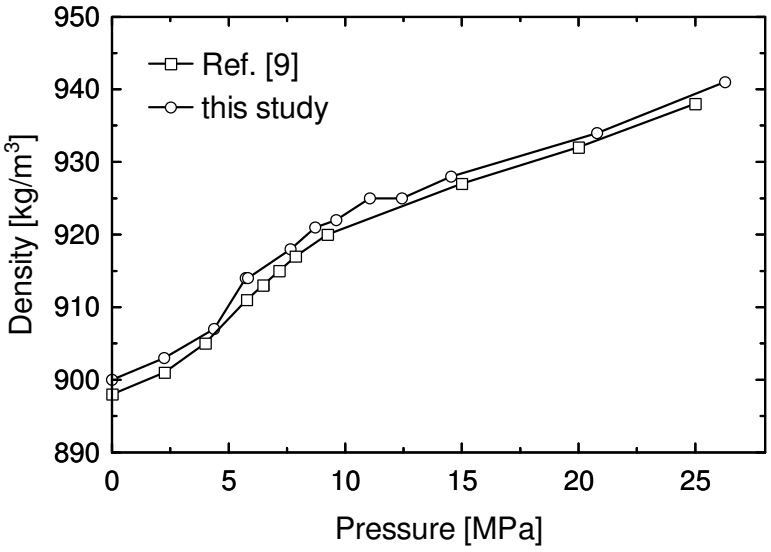


**Figure 3-5.** Density of corn oil in equilibrium with $CO_2$ at 40°C determined with the spring balance in this study (circles) compared to literature data (squares). Literature data obtained by digitizing chart in Ref. [9].

#### 3.2.3.3 Determination of density

The densities of fish oil TG and FAEE were determined at temperatures of 40, 55 and 70ºC and pressures ranging from 0.1 to about 25 MPa. Triplicate measurements were carried out for all isotherms. Prior to each density measurement, the apparatus was thoroughly flushed with $CO_2$ removing any residual air in the cell. The apparatus was then filled with 120 mL of fish oil up to a level just above the window of the view cell, thereby ensuring complete submersion of the sinker. A disposable plastic syringe was used to fill the fish oil into the cell to minimize air contact. For this purpose, a new syringe was flushed with nitrogen prior to usage and then filled with the fish oil under nitrogen atmosphere. The filled syringe was then connected to a fitting at the outlet of the view cell facilitating injection of the oil and minimizing contact with air. The headspace of the storage bottles for fish oil was filled with nitrogen after each opening. Fish oil TG and FAEE were stored at 4ºC in aluminum bottles and warmed up slowly to room temperature before filling the view cell to avoid crystallization and precipitation of fish oil components.

After filling the view cell with oil, the system was kept at atmospheric pressure and the fish oil was circulated using the magnetic piston pump so that the temperature of the oil stabilized and the oil became saturated with $CO_2$. During density measurements images of the microscopic scale with the needle showing the position of the sinker were taken about every 15 min. The images were analyzed on the computer to determine the exact position of the sinker, which was related to the density of the liquid using the calibration curve. The change in density could be followed *in situ* by observing the sinker position until a constant level was reached, which indicated equilibration. While taking an image for density readings the circulation pump was stopped for a few seconds to avoid vibration of the sinker caused by the moving fluid. Once equilibrium was reached and constant density observed, the pressure of the system was increased to the next desired level and the liquid was circulated again to facilitate equilibration. The pressure was increased stepwise starting from atmospheric pressure up to about 25 MPa. Throughout the entire measurement the temperature of the liquid phase was continuously monitored. Thereby, changes in temperature upon each increase in $CO_2$ pressure could be observed, which were caused by exothermic or endothermic mixing effects as discussed below.

## 3.3 Results and discussion

### 3.3.1 Volumetric expansion of fish oil TG and FAEE

With an increase in pressure a pronounced increase in volume was observed for both FAEE and TG up to about 10 MPa (Fig. 3-6). Increasing the pressure further from 10 to 15 MPa resulted in a less pronounced increase in oil volume and at pressures ranging from 15 to 22 MPa a nearly constant oil level inside the capillary was observed for both TG and FAEE. These results for volumetric expansion of oil saturated with $CO_2$ are in good agreement with observations reported for gas-assisted mechanical extrusion (GAME) of oilseeds, where a significant increase in oil yield was observed with an increase in $CO_2$ pressure from 8 to 10 MPa, but only little improvement was achieved with a further increase to 15 MPa [13]. The maximum relative volumetric expansion calculated

using Eq. (3-1) for fish oil FAEE and TG in equilibrium with $CO_2$ was about 67% and 38%, respectively. Such a difference in volumetric expansion between FAEE and TG can be attributed to the difference in the solubility of $CO_2$ in the liquid phase.

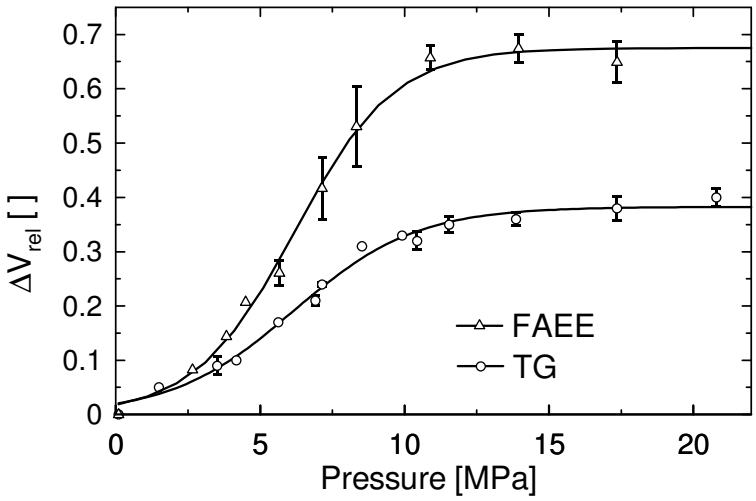


**Figure 3-6.** Volumetric expansion of fish oil TG and FAEE in equilibrium with $CO_2$ at 40°C and pressures of up to about 22 MPa. Error bars represent standard deviation for triplicate measurements.

In order to analyse the volumetric expansion in relation to $CO_2$ loading of the liquid phase for both fish oil TG and FAEE literature data were used [14, 15]. The mass fraction of $CO_2$ in the liquid phase for both TG and FAEE at 40°C as a function of pressure is illustrated in Fig. 3-7. At 40°C, the solubility of $CO_2$ in FAEE (42 and 55 wt.% at 10 and 15 MPa, respectively) is significantly higher than that in TG (25 and 29 wt.% at 10 and 15 MPa, respectively) at any given pressure level [14, 15]. The higher solubility of $CO_2$ in FAEE leads to the observed larger volume expansion compared to TG. According to the classification of gas-expanded liquids suggested by Jessop and Subramaniam [16], both TG and FAEE when expanded with $CO_2$ can be considered as Class 3 liquids, which expand less than Class 2 liquids, such as most organic solvents that can dissolve large amounts of $CO_2$. Class 3 liquids, such as high molecular weight

liquids or ionic liquids expand only moderately when saturated with $CO_2$ due to their moderate gas solubility, which is usually around 15 to 20 wt% at pressures of 6 to 8 MPa and 40°C [16]. The relatively large experimental error in the volumetric expansion data of FAEE observed at pressure levels close to the critical pressure of $CO_2$ and at high pressure levels (Fig. 3-6) were caused by slightly blurred images, which made it difficult to determine the exact position of the oil meniscus.

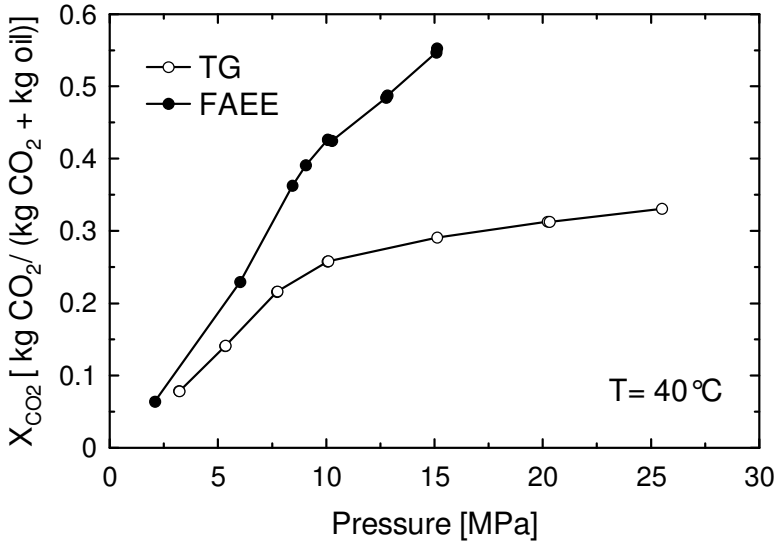


**Figure 3-7.** Mass fraction of $CO_2$ ($X_{CO2}$) in the saturated liquid phase for fish oil FAEE and TG versus $CO_2$ pressure at 40°C based on data from Ref. [14, 15].

In the case of fish oil TG, the solubility in $CO_2$ at the studied conditions is relatively low, supporting the assumption that the amount of oil extracted into the $CO_2$ phase out of the capillary compared to that from the oil phase at the bottom of the view cell is negligible. However, solubility of fish oil FAEE in $CO_2$ is higher, leading to a larger driving force for the diffusion of FAEE out of the capillary, which may be responsible for the blurry images and explain the slight downward trend noticed for the height of the expanded FAEE at high pressure conditions. However, the slight decrease in FAEE level may also be attributed to the compression of the liquid phase at elevated pressure levels.

When relative volume change is plotted against $CO_2$ loading in the liquid phase ($L_{CO2}$) defined as (kg $CO_2$/ kg oil) (Fig. 3-8), a linear trend was observed up to relatively high $CO_2$ loadings for both TG and FAEE with an almost identical slope of about 0.9. A similar trend in terms of volumetric expansion versus $CO_2$ loading was also found by Tegetmeier *et al.* [9] for corn oil with a slope of 0.87, as illustrated in Fig. 3-8. However, in this work it was observed that the

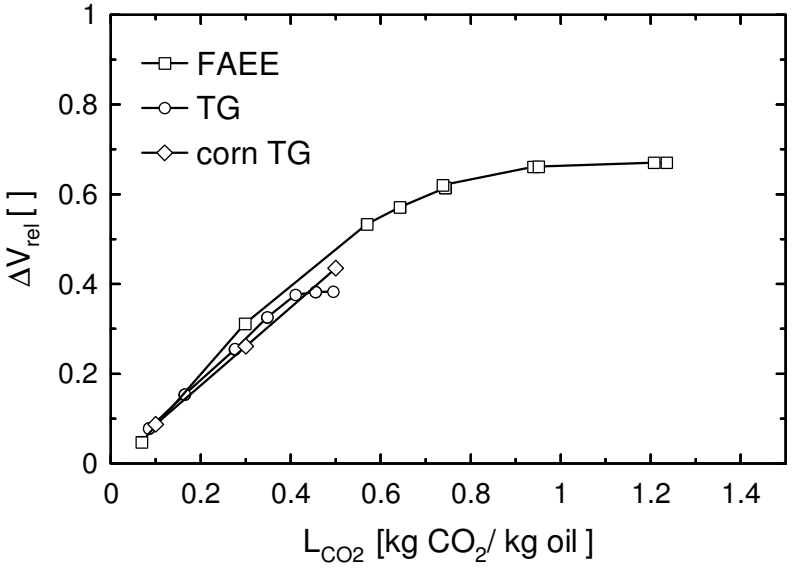


**Figure 3-8.** Relative volumetric expansion ($\Delta V_{rel}$) versus $CO_2$ loading ($L_{CO2}$) of the saturated liquid phase for fish oil FAEE and TG at 40°C. Data for $CO_2$ loading in the liquid phase for fish oil FAEE and TG were calculated using mass fraction data from Refs. [14, 15]. Data for corn oil adapted from Ref. [9].

relationship between the oil expansion and $CO_2$ loading was linear only up to about 0.4 and 0.6 for fish oil TG and FAEE, respectively. At higher $CO_2$ loadings the volumetric expansion levelled off and reached a nearly constant level, which may be caused by the compression of liquid molecules due to the high pressures required to reach such high $CO_2$ loadings. Tegetmeier *et al.* [9] studied the volumetric expansion of corn oil between 22.5 and 76.8°C and found that the slope of this linear correlation between $CO_2$ loading and relative volume change was independent of temperature.

### 3.3.2 Density of fish oil TG and FAEE

The densities of fish oil TG and FAEE saturated with $CO_2$ at 40, 55 and 70°C and pressures of up to 25 MPa are presented in Figs. 3-9 and 3-10, respectively. The density increased with pressure and decreased with temperature for both TG and FAEE.

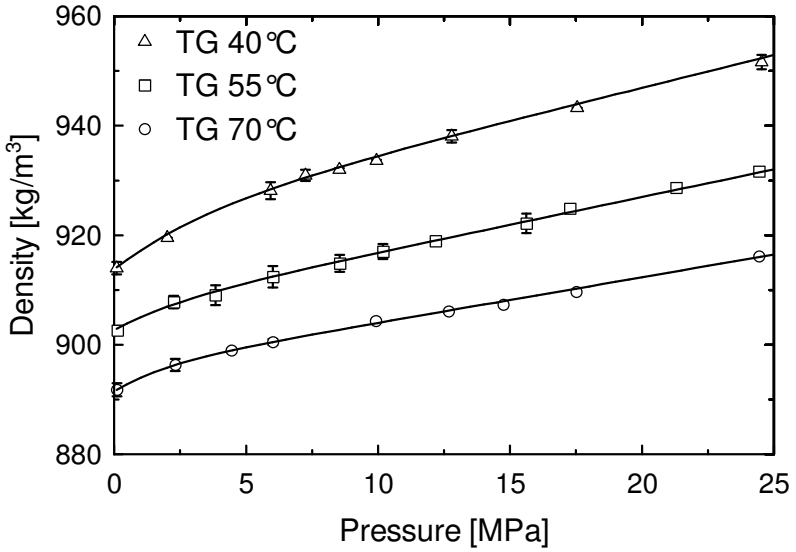


**Figure 3-9.** Density of fish oil triglycerides (TG) at 40, 55 and 70°C in equilibrium with $CO_2$ at various pressures. Curves represent the correlation given in Eq. (3-2). Error bars represent standard deviation for triplicate measurements.

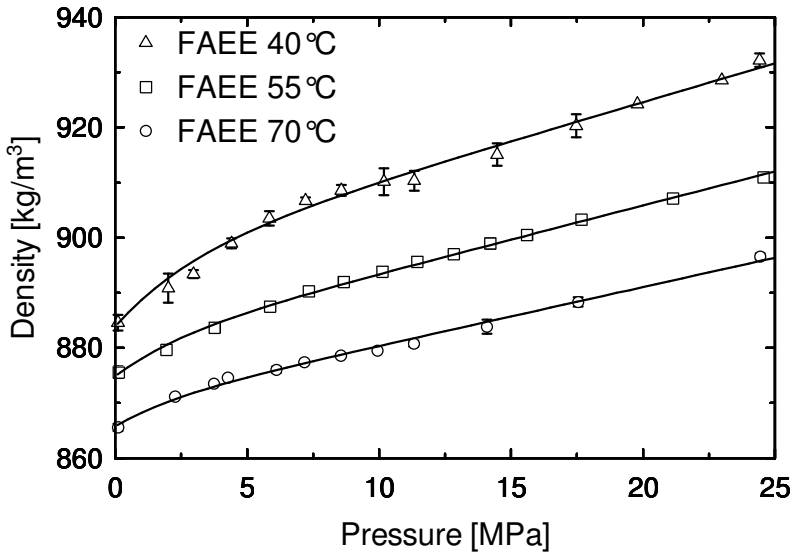


**Figure 3-10.** Density of fish oil fatty acid ethyl esters (FAEE) at 40, 55 and 70°C in equilibrium with $CO_2$ at various pressures. Curves represent the correlation given in Eq. (3-2). Error bars represent standard deviation for triplicate measurements.

In the pressure and temperature ranges studied, the densities of $CO_2$-expanded fish oil TG and FAEE [kg/m$^3$] were correlated to pressure [MPa] and temperature [°C] using the following equation:

$$\rho(P,T) = \rho_0(T) + k_1(T) * (P - 0.1) + k_2(T) * \left(1 - e^{-k_3(T)*(P-0.1)}\right) \quad (3\text{-}2)$$

where the first term describes the temperature dependence of density at atmospheric pressure, the second term corresponds to the linear increase of density with pressure at high pressure levels and the exponential third term describes the nonlinear increase in density with pressure at low pressures with temperature dependent fitting parameters, $k_1(T)$, $k_2(T)$ and $k_3(T)$. The density of fish oil TG and FAEE at atmospheric pressure is a linear function of temperature and can be calculated using Eq. (3-3):

$$\rho_0(T) = A_1 + A_2 * T \quad (3\text{-}3)$$

The temperature dependant slope for the density with increasing pressure at high pressure levels can be evaluated with Eq. (3-4):

$$k_1(T) = A_3 + A_4 * T \quad (3\text{-}4)$$

The nonlinear increase in density with pressure at low pressure levels could be described by the exponential term in Eq. (3-2), with

$$k_2(T) = A_5 + A_6 * T + A_7 * T^2 \quad (3\text{-}5)$$

and

$$k_3(T) = A_8 + A_9 * T \quad (3\text{-}6)$$

The exponential term in Eq. (3-2) approaches zero with increasing pressure so that at pressures above about 5 to 7 MPa the increase in density with pressure follows a linear trend. The slope of this linear trend was found to be slightly temperature dependent, which decreased with temperature. The fitting parameters $A_1$ to $A_9$ listed in Table 3-2 were obtained by performing a least square fit of Eqs. (3-2) to (3-6) to experimental data using a Quasi-Newton algorithm. This correlation (Eq. 3-2) describes the experimental data well in the pressure and temperature ranges studied.

**Table 3-2.** Parameters for Eq. (3-2) for FAEE and TG.

| | **FAEE** | **TG** |
|---|---|---|
| $A_1$ | 908.9 | 943.9 |
| $A_2$ | -0.6129 | -0.7442 |
| $A_3$ | 1.871 | 1.670 |
| $A_4$ | -0.01151 | -0.01198 |
| $A_5$ | 47.73 | 49.05 |
| $A_6$ | -1.240 | -1.471 |
| $A_7$ | 0.008752 | 0.01182 |
| $A_8$ | 0.1525 | -0.01972 |
| $A_9$ | 0.004186 | 0.007462 |

The uptake of $CO_2$ into the liquid phase caused a pronounced increase in density for both TG and FAEE below pressures of about 5 MPa. As reported by Tegetmeier *et al.* [9] for corn oil, the increase in density for the saturated oil + $CO_2$ mixture with increasing $CO_2$ pressure is astonishing since the density of $CO_2$ is lower than that of the oil at all temperatures and pressures investigated. The increase in density observed for TG and FAEE saturated with pressurized $CO_2$

may be attributed to a combination of compression effects due to both the hydrostatic pressure and $CO_2$ dissolution as demonstrated for the system $CO_2$+corn oil by Tegetmeier *et al.* [9]. Dittmar *et al.* [17] hypothesized that $CO_2$ molecules placed between the large lipid molecules act like a lubricant, thus facilitating a more tightly packed fluid and enhanced compressibility. Therefore, the slope of the density isotherm depends both on the solubility of $CO_2$ in the liquid phase and on the compressibility of the liquid under high pressure. Up to about 5 to 7 MPa, which is close to the critical pressure of $CO_2$, the density increase with pressure is more pronounced than that above the critical region, where the change in density with pressure follows a linear trend. At high pressure levels above the critical region, the density increase with increasing $CO_2$ pressure is less pronounced for fish oil TG than that for FAEE. The slopes for the linear part of the isotherms, $k_1(T)$ can be evaluated using Eq. (3-4). The slope, $k_1(T)$ for FAEE is steeper than that for TG, which could be caused by both the higher solubility of $CO_2$ in FAEE and the higher compressibility of $CO_2$ saturated FAEE compared to that of TG. The difference in compressibility between TG and FAEE under high pressure could be related to the size of the molecules and their bulkiness. Triglycerides being large and bulky do not pack as tightly compared to the smaller FAEE molecules. For both TG and FAEE, $k_1(T)$ decreased with increasing temperature. This trend could be caused by a decreased solubility of $CO_2$ in the liquid phase with temperature as well as by a higher kinetic energy of the molecules inhibiting compression. Examining the solubility of $CO_2$ in the liquid phase, which was reported for fish oil FAEE and TG by Borch-Jensen and Mollerup [14, 15], reveals that the increase in $CO_2$ solubility with pressure follows a similar trend like the density as illustrated in Fig. 3-7. For both fish oil TG and FAEE at 40°C, the increase in $CO_2$ mass fraction in the liquid phase is more pronounced up to pressures of about 7-10 MPa. In the case of TG, an increase of the $CO_2$ mass fraction in the liquid phase from about 25 to 30% requires an increase in $CO_2$ pressure from about 10 to 20 MPa, whereas for FAEE the mass fraction of $CO_2$ in the liquid phase increases from about 40 to over 70% by increasing the pressure from 10 to 17 MPa [14, 15].

The density of the $CO_2$-saturated liquid phase for fish oil TG and FAEE versus mass fraction of $CO_2$ is shown in Fig. 3-11.

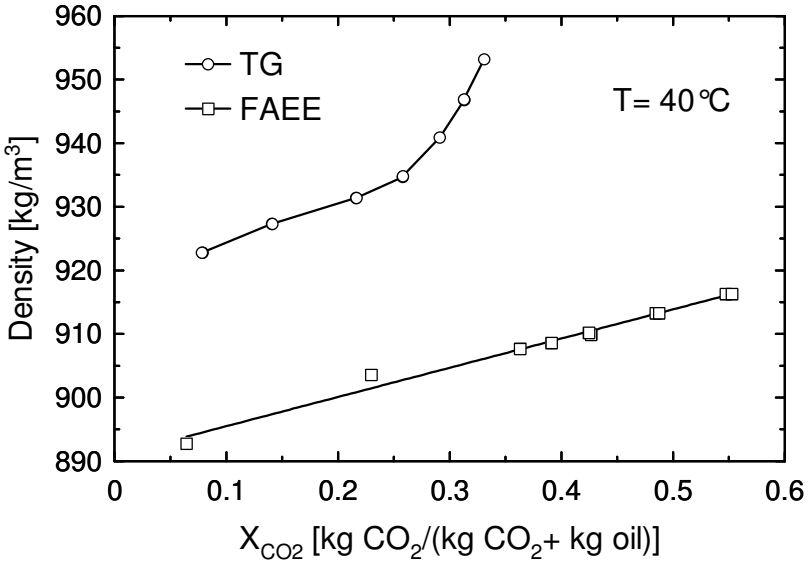


**Figure 3-11.** Density as a function of mass fraction of $CO_2$ in the liquid phase ($X_{CO2}$) for fish oil TG and FAEE at 40°C. Mass fraction data taken from Refs. [14, 15].

The increase in density with increasing mass fraction follows a linear trend for both TG and FAEE at low mass fractions of $CO_2$. However, in the case of TG there is a sudden sharp increase in density once a $CO_2$ mass fraction level of about 0.25 is reached, which corresponds to a $CO_2$ pressure of about 10 MPa, where the increase in density for TG is no longer mainly caused by the uptake of $CO_2$ in the liquid phase but by compression of the liquid phase. However, in the case of FAEE the increase in density follows a linear trend up to mass fractions of $CO_2$ as high as 0.55, corresponding to a $CO_2$ pressure of about 15 MPa. Noteworthy, the increase in density with increasing mass fraction of $CO_2$ follows nearly the same linear slope for both TG and FAEE at pressures below 10 MPa and $CO_2$ mass fractions of up to 0.25. This indicates, that the density increase for each kg of $CO_2$ added per kg of lipid is little influenced by compression up to pressures of about 10 MPa. The FAEE do not exhibit this sharp increase in density with an increase in $CO_2$ concentration. This leads to the conclusion that in the case of FAEE where

the $CO_2$ solubility is higher, the density change is mainly caused by the uptake of $CO_2$ into the liquid phase.

### 3.3.3 Temperature

During the density measurements, the temperature was constantly monitored by means of a thermistor immersed in the liquid phase at the bottom of the view cell, which allowed detecting temperature changes in the order of about 0.01ºC, as illustrated in Fig. 3-12.

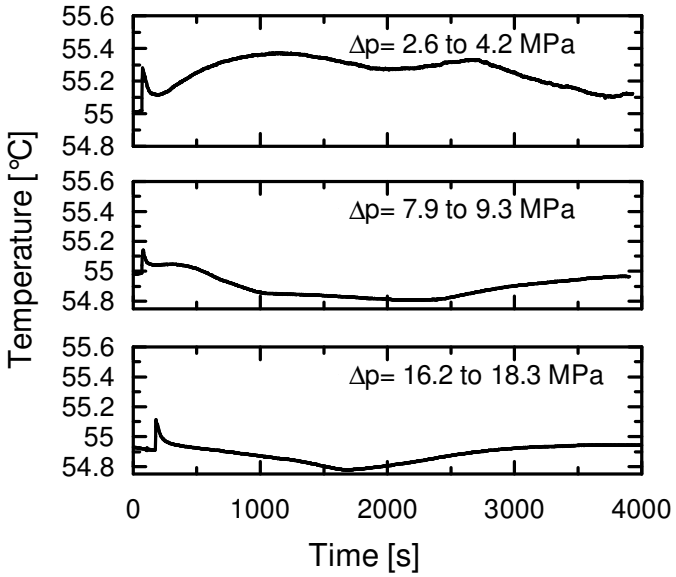


**Figure 3-12.** Change of liquid phase temperature over time during density measurements of fish oil TG at 55°C upon stepwise increase in $CO_2$ pressure.

There was an initial spike in temperature, which was probably caused by charging the vessel with $CO_2$. However, this initial spike quickly decreased in all cases likely due to the circulation of the liquid phase and dissipation of heat into the temperature controlled vessel and air bath. For fish oil TG at 55ºC and pressures of up to about 7.9 MPa, an increase in pressure caused an increase in oil temperature, whereas at higher pressures a decrease in temperature was observed, as depicted in Fig. 3-12. This thermal effect continued for up to 4000 s (up to

more than 1 h), which was about the same time frame it took for the oil to equilibrate with $CO_2$.

This observation is in agreement with the findings of Mock *et al.* [18], who investigated the excess enthalpies for mixtures of $CO_2$ and olive oil. Using an isothermal flow calorimeter at 35°C, the excess enthalpy was found to be considerably exothermic at 9 MPa, moderately endothermic in the oil-rich region and exothermic in the $CO_2$-rich region at 15 MPa, and moderately endothermic at 17 MPa [18]. In a similar manner, the temperature changes observed in this study for fish oil TG may therefore be due to the exothermic or endothermic dissolution of $CO_2$ into the liquid oil phase. Furthermore, the observed temperature effect may be a result of the combined effects of the heat of compression, which is exothermic, and the heat of mixing for $CO_2$ dissolving into the liquid phase, which could be either endo- or exothermic. Thus, it seems that at low pressures the heat of compression dominates the mixing effect leading to an overall exothermic effect, while at high pressures an endothermic effect due to dissolution prevails.

## 3.4 Conclusions

The volumetric expansion of fish oil TG and FAEE was assessed using a view cell at 40°C and pressures of up to 22 MPa. Both TG and FAEE expand significantly up to pressures of about 10 MPa and to a lesser extent above that pressure. The relative volumetric expansion reached a maximum level at about 15 MPa with 38 and 67% for TG and FAEE, respectively.

A spring balance based on Archimedes' principle was built to determine the density of liquids under high pressure conditions. The performance of this novel device was validated using anhydrous ethanol, ethanol+water mixture and corn oil in comparison to literature density values. The density of fish oil in the form of TG and FAEE in equilibrium with $CO_2$ was measured at temperatures of 40, 55 and 70°C and pressures ranging from 0.1 to 25 MPa. During density measurements slight changes in temperature of the oil were recorded likely due to exothermic and endothermic dissolution of $CO_2$ into the lipid phase at low and

high pressure conditions, respectively. The density of fish oil TG and FAEE increased with increasing pressure and decreased with temperature. The increase in density of TG and FAEE with pressure was more pronounced at lower pressures of up to about 5-10 MPa. At higher pressures above 10 MPa the increase in density followed a linear trend with pressure up to about 25 MPa for both fish oil TG and FAEE. However, an examination of the liquid phase density versus mass fraction of $CO_2$ in the liquid phase revealed a linear relationship with similar slopes for both TG and FAEE up to $CO_2$ mass fractions of 0.25. In the case of FAEE, the linear trend of density versus $CO_2$ mass fraction continued up to a mass fraction of about 0.55 corresponding to a $CO_2$ pressure of 17 MPa due to a much higher $CO_2$ solubility in FAEE. However, in the case of TG the linear trend between density and $CO_2$ mass fraction could only be observed up to pressures of about 10 MPa, corresponding to a mass fraction of 0.25. Thus, above 10 MPa the increase in TG density is mainly caused by compression of the liquid phase. Within the experimental envelope a correlation for the density of fish oil TG and FAEE in equilibrium with $CO_2$ was developed. The volumetric expansion data along with the density correlation for fish oil TG and FAEE can help to better model and understand the performance of mass transfer equipment for processes involving marine lipids in equilibrium with high pressure $CO_2$, such as spray towers or countercurrent packed columns.

## 3.5 References


1. A. Blaha-Schnabel, A. Beyer, B. Czech, H. Jakob, H. Schiemann, E. Weidner, S. Peter, Influence of interfacial tension and viscosity on the behavior of a packed column in near-critical fluid extraction. Chemical Engineering Communications 146 (1996) 13-31.

2. R. Ruivo, M.J. Cebola, P.C. Simoes, M. Nunes da Ponte, Fractionation of edible oil model mixtures by supercritical carbon dioxide in a packed column. 2. A mass-transfer study. Industrial and Engineering Chemistry Research 41 (2002) 2305-2315.

3. R. Stockfleth, G. Brunner, Hydrodynamics of a packed countercurrent column for the gas extraction. Industrial and Engineering Chemistry Research 38 (1999) 4000-4006.

4. R. Stockfleth, G. Brunner, Holdup, pressure drop, and flooding in packed countercurrent columns for the gas extraction. Industrial and Engineering Chemistry Research 40 (2001) 347-356.

5. A. Martín, M.J. Cocero, Mathematical modeling of the fractionation of liquids with supercritical $CO_2$ in a countercurrent packed column. Journal of Supercritical Fluids 39 (2007) 304-314.

6. C.M.J. Chang, M.S. Lee, B.C. Li, P.Y. Chen, Vapor-liquid equilibria and densities of $CO_2$ with four unsaturated fatty acid esters at elevated pressures. Fluid Phase Equilibria 233 (2005) 56-65.

7. R.L. Smith, T. Yamaguchi, T. Sato, H. Suzuki, K. Arai, Volumetric behavior of ethyl acetate, ethyl octanoate, ethyl laurate, ethyl linoleate, and fish oil ethyl esters in the presence of supercritical $CO_2$. Journal of Supercritical Fluids 13 (1998) 29-36.

8. A. Staby, J. Mollerup, Solubility of fish oil fatty acid ethyl esters in sub and supercritical carbon dioxide. Journal of the American Oil Chemists Society 70 (1993) 583-588.

9. A. Tegetmeier, D. Dittmar, A. Fredenhagen, R. Eggers, Density and volume of water and triglyceride mixtures in contact with carbon dioxide. Chemical Engineering and Processing 39 (2000) 399-405.

10. B. Seifried, F. Temelli, Design of a high-pressure circulating pump for viscous liquids. submitted to Rev. of Sci. Instr. (2009).

11. R. Span, W. Wagner, A new equation of state for carbon dioxide covering the fluid region from the triple-point temperature to 1100 K at pressures up to 800 MPa. Journal of Physical and Chemical Reference Data 25 (1996) 1509-1596.

12. D. Pecar, V. Dolecek, Volumetric properties of ethanol-water mixtures under high temperatures and pressures. Fluid Phase Equilibria 230 (2005) 36-44.

13. P. Willems, N.J.M. Kuipers, A.B. de Haan, Gas assisted mechanical expression of oilseeds: Influence of process parameters on oil yield. Journal of Supercritical Fluids 45 (2008) 298-305.

14. C. Borch-Jensen, J. Mollerup, Phase equilibria of long-chain polyunsaturated fish oil fatty acid ethyl esters and carbon dioxide, ethane,

or ethylene at reduced gas temperatures of 1.03 and 1.13. Fluid Phase Equilibria 161 (1999) 169-189.

15. C. Borch-Jensen, J. Mollerup, Phase equilibria of fish oil in sub- and supercritical carbon dioxide. Fluid Phase Equilibria 138 (1997) 179-211.

16. P.G. Jessop, B. Subramaniam, Gas-expanded liquids. Chem. Rev. 107 (2007) 2666-2694.

17. D. Dittmar, A.M. De Arevalo, C. Beckmann, R. Eggers, Interfacial tension and density measurement of the system corn germ oil - Carbon dioxide at low temperatures. European Journal of Lipid Science and Technology 107 (2005) 20-29.

18. D. Mock, A. Cabanas, J.A.R. Renuncio, C. Pando, Excess enthalpies of mixtures of olive oil and supercritical carbon dioxide. Journal of Supercritical Fluids 14 (1999) 173-180.

# 4 Interfacial Tension of Marine Lipids in Contact with High Pressure Carbon Dioxide[1]

## 4.1 Introduction

Interfacial phenomena play an important role in high pressure processes involving liquid/liquid or gas/liquid systems, where the interface between immiscible phases influences mass transfer, heat transfer and hydrodynamic flow regimes. Interfacial tension (IFT) is an important parameter to characterize the interface. IFT is correlated to the amount of energy required to increase interfacial area, which is a key parameter for drop formation, spray jet break-up as well as falling film stability, important in many unit operations. The IFT is largely affected by pressure in high pressure systems with a considerable solubility of the dense gas in the liquid. Therefore, IFT has major implications for the design of processes involving lipids and supercritical $CO_2$ (SC-$CO_2$). It has been observed that a falling film of fatty acids in contact with SC-$CO_2$ disintegrates into a swarm of fine droplets once a certain pressure is exceeded, even under flow regimes with very little mechanical energy input [1]. IFT in those systems was identified to be one of the reasons for that film disintegration [2]. However, it was shown later that a combination of fluid dynamic (liquid velocity) and physicochemical (property) effects is the cause of film disintegration [3]. Nevertheless, IFT is a key parameter to characterize the boundaries for different flow regimes of a falling film as well as jet break-up.

Moser and Trepp [3] studied falling films of squalene and α-tocopherol in high pressure $CO_2$ at various liquid flow rates. They found that the transition from a stable film to disintegration into droplets can be characterized by the dimensionless Weber number (*We*), Reynolds number (*Re*) and film number ($K_F$) [3]. IFT is required for the calculation of *We* and $K_F$. Besides IFT, viscosity is an important factor in the film disintegration as well, which is also influenced by the increasing solubility of $CO_2$ in lipids with pressure [4]. Flow regimes of falling

[1] A version of this chapter has been published in J. Supercrit. Fluids 52 (2010) 203-214.

films and break-up of free jets in the binary system methyl myristate and $CO_2$ were studied by Kerst *et al.* [5] using a high pressure view cell and photo imaging. They developed correlations based on dimensionless numbers such as *Re*, $K_F$ and Ohnesorge number (*Oh*), to characterize the flow regime of falling films and the jet disintegration length [5], where IFT is again required for calculating *Oh.* Stockfleth and Brunner [6] investigated film thickness, flow regimes, and flooding points for the countercurrent annular flow of corn oil and $CO_2$ at 65°C and pressures of up to 20.6 MPa using an experimental setup, which allowed varying both the liquid and gas flow rates. The breakup of the falling film was influenced by the countercurrent gas flow rate leading to increased shear forces, thereby shifting the transition between the flow regimes (crest and drop formation) to lower *Re* for the liquid film. A newly introduced gas resistance factor was used to calculate a modified *Re*, which was then plotted versus $K_F$, thereby facilitating the prediction of the transition zones between flow regimes in situations with a countercurrent gas flow. Jet break-up in a high pressure environment was studied by Czerwonatis [7], who developed a correlation based on a new dimensionless number, which requires IFT, to characterize the transition between regimes of jet disintegration, such as Rayleigh break-up, sinuous wave break-up and atomization. Furthermore, Badens *et al.* [8] studied the jet formation and break-up of water, methylene chloride and ethyl alcohol into pressurized $CO_2$, and developed a new correlation between *Oh* and the jet *Re* to determine the transition to the atomization regime, which required the knowledge of IFT. Sutjiadi-Sia and Eggers [9] studied the lateral wetting angle of falling films consisting of water in dense $CO_2$, and found that the wettability on a horizontal glass or stainless steel surface decreased with increasing pressure. The IFT between each of the three adjacent phases (solid, liquid, vapor) influences the wettability and thus the contact angle between the solid surface and the liquid falling film [10].

IFT of lipids in contact with $CO_2$ has been investigated in numerous studies. Schiemann [11, 12] determined the IFT of several lipids (pelargonic acid, stearic acid, oleic acid, monoglycerides, and vegetable oils) in contact with

various gases, including $CO_2$, ethane, nitrogen, argon, helium, and hydrogen applying the pendant drop method, the capillary rise method and the du Noüy ring method using a high pressure view cell. In most systems investigated, the gas was soluble in the non-volatile liquid phase, which caused a decrease in IFT with increasing pressure. However, for the binary system pelargonic acid+helium the IFT increased with pressure [11, 12]. Such pressure induced increase of IFT in systems where the gas exhibits a very low solubility in the non-volatile phase had been suggested by Rice [13]. However, in most systems the gases exhibit an appreciable solubility in the liquid phase and therefore this pressure effect has been overcome and not observed. The pendant drop method to determine IFT has been employed for other binary $CO_2$+lipid systems, which include olive oil [14], corn germ oil [15], wheat germ oil and palm oil [16]. Furthermore, Lockemann [17] determined the IFT of binary $CO_2$+lipid systems including oleic acid, methyl myristate, methyl palmitate as well as the ternary system $CO_2$+methyl myristate+methyl palmitate using the capillary rise method.

Literature is lacking IFT data for marine lipids in contact with high pressure $CO_2$. Therefore, the objective of this study was to determine the interfacial tension of marine lipids in the form of TG and FAEE in contact with high pressure $CO_2$ and to develop a correlation to describe the data. An apparatus for measuring interfacial tension of liquids under high pressure based on the pendant drop method was designed and built for this purpose. Using the correlation for IFT, the ideal pendant drop volume was calculated according to Tate's law by balancing interfacial, buoyant and gravitational forces. Furthermore, this study aimed to elucidate the change in IFT of TG over time in high pressure $CO_2$. Additionally, the surface excess of $CO_2$ was assessed by using the correlation derived for the data in this study.

## 4.2 Experimental

### 4.2.1 Theory of pendant drop method and prerequisites

To determine the IFT for high pressure systems the pendant drop method introduced in 1938 by Andreas *et al.* [18] seems to be the most reliable method to

date. The contour of a pendant drop suspended from a capillary needle depends on the capillary diameter, IFT and density difference between the drop and surrounding fluid. A balance between gravitational, buoyant and interfacial forces acting on the interface of a drop of liquid suspended in another immiscible fluid leads to the Young-Laplace equation [19, 20]:

$$\gamma\left(\frac{1}{R_1}+\frac{1}{R_2}\right)=\frac{2\gamma}{R}-\Delta\rho g z \tag{4-1}$$

where $\gamma$ is the interfacial tension, $R$ the radius of curvature in the apex, $\Delta\rho$ the density difference between drop forming liquid and the surrounding fluid, $g$ the acceleration due to gravity and $z$ the distance from the apex. As illustrated in Fig. 4-1, $R_1$ and $R_2$ are the principal radii of the drop interface at distance $z$ from the apex, with $R_1$ being the radius of curvature in the plane of Fig. 4-1 and $R_2$ the radius of curvature in a plane perpendicular to Fig. 4-1.

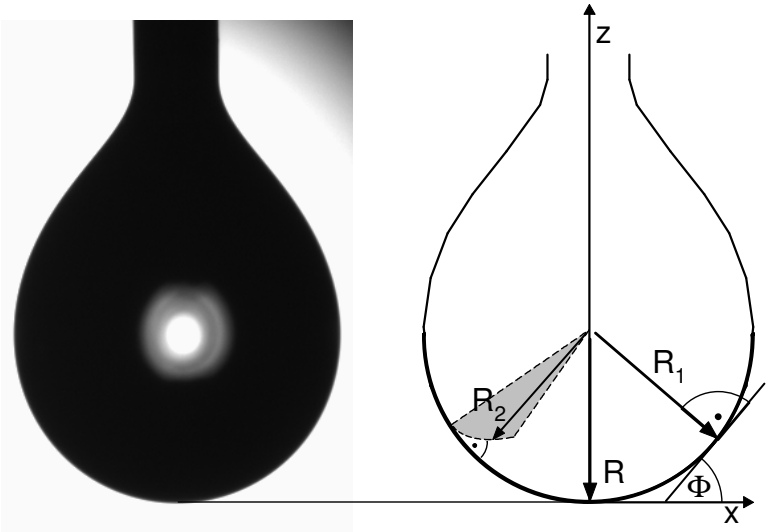


**Figure 4-1**. Image and geometry of an axisymmetric pendant drop.

In case of an axisymmetric system, which is the case for a pendant drop, the following geometrical relationships are used to substitute $R_1$ and $R_2$ in Eq. (4-1):

$$R_1=\frac{\left[1+(dz/dx)^2\right]^{3/2}}{d^2z/dx^2} \tag{4-2}$$

$$R_2 = \frac{x}{\sin(\Phi)} \tag{4-3}$$

with

$$\sin(\Phi) = \frac{dz/dx}{\left[(1 + dz/dx)^2\right]^{1/2}}. \tag{4-4}$$

Hence, a non-linear differential equation of second order is derived, which was solved numerically by Bashford and Adams in 1883 for sessile drops [21]. Since then numerical algorithms have been implemented in software capable of performing axisymmetrical drop shape analysis (ADSA) by numerically integrating the differential equation describing the drop profile of the pendant drop [22].

In order to evaluate the IFT based on the image of a pendant drop the densities of both the liquid forming the drop as well as the surrounding fluid are required. In high pressure systems, especially those where the surrounding fluid is highly soluble in the liquid phase the liquid density may increase (lipid+$CO_2$) (see Chapter 3, [23]) or decrease (lipid+propane or ethane) [11] with pressure and needs to be known prior to IFT measurements.

### 4.2.2 Materials

Refined fish oil extracted from anchovy and sardine was obtained from Ocean Nutrition Canada (ONC, Halifax, NS, Canada) in the form of triglycerides (TG) and fatty acid ethyl esters (FAEE), as described in Section 3.2.1. As stated by the manufacturer, the oils contain about 8 mg/g of antioxidants, including a mix of natural tocopherols and citric acid. All other material specifications and handling protocols were similar to those described in Section 3.2.1.

### 4.2.3 IFT measurements

#### 4.2.3.1 Apparatus to determine IFT

The apparatus to determine the IFT under high pressure conditions according to the pendant drop method consisted of a 200 mL high-pressure view cell with an internal diameter of 40 mm (Nova-Swiss, Effretikon, Switzerland) equipped with

electric heaters and placed in a temperature controlled insulated air bath (Fig. 4-2). The temperatures of both the air bath and electric heaters were individually controlled by means of J-type thermocouples connected to controllers (Chromalox 1601, Pittsburgh, PA, USA).

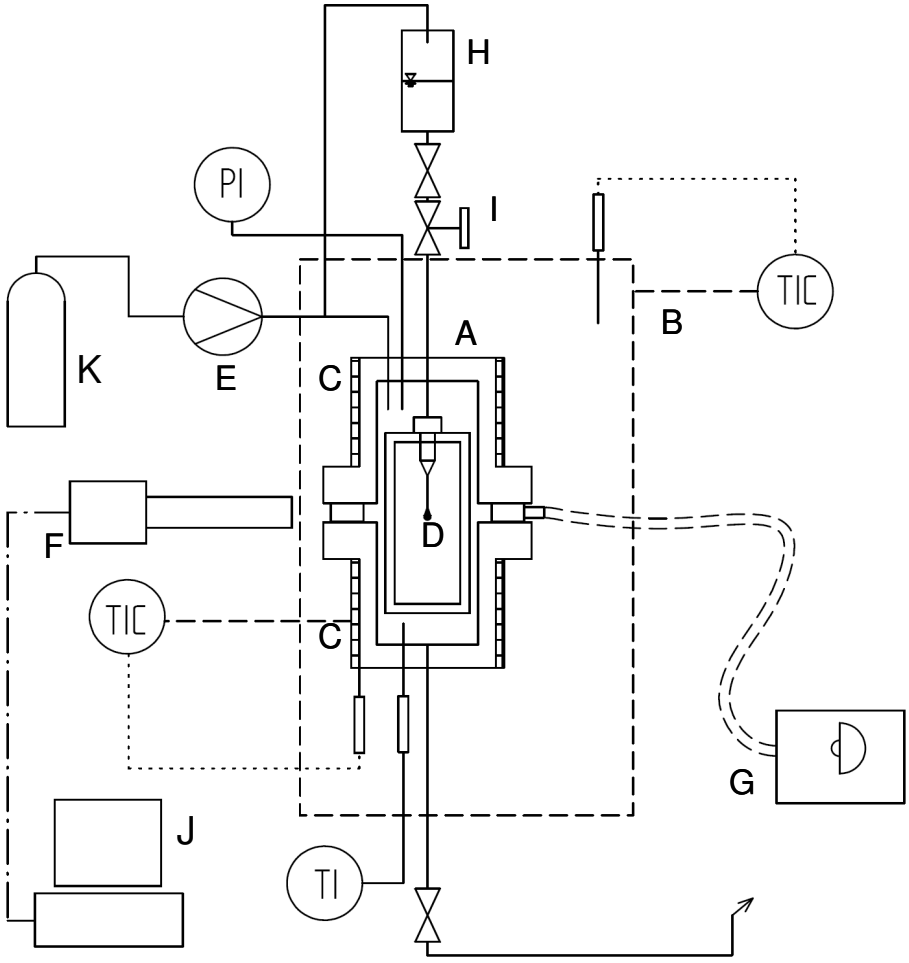


**Figure 4-2.** Apparatus used for measuring interfacial tension: A) view cell, B) temperature controlled air bath, C) electric heaters, D) needle, E) syringe pump, F) CMOS camera, G) light source, H) top reservoir, I) micrometering valve, J) computer, K) $CO_2$ cylinder.

The temperatures of both the continuous fluid phase inside the view cell and the circulating air bath were continuously recorded to a computer by means of thermistors connected to a custom made data acquisition (DAQ) system. The DAQ system consisted of a signal amplifier and conditioner designed to linearize and transform the nonlinear response of the thermistors into voltage, which was

measured by a 10-bit DAQ card (DI-194RS, DATAQ Instruments, Inc., Akron, OH, USA) and visualized by means of a chart recorder software (WinDaq/Lite, DATAQ Instruments, Inc., Akron, OH, USA). With a sampling rate of 50 Hz the DAQ system allowed continuous monitoring and recording of the temperatures with a resolution of 0.01ºC. The thermistor DAQ system was calibrated against a precision digital thermometer (Model 4000, Control Company, Friendswood, TX, USA) with a resolution of 0.001ºC using an insulated heating water bath (Haake H3, Karlsruhe, Germany). The supercritical fluid inside the view cell was usually maintained at a constant temperature to within ±0.1ºC. The view cell was pressurized with $CO_2$ by means of a syringe pump (ISCO Model 250D, Isco Inc., Lincoln, NE, USA). The pressure was monitored using a digital pressure indicator with 0.05% full scale accuracy (Druck Model DPI 104, General Electrics Sensing, Billerica, MA, USA).

The thin walled stainless steel capillary holding the pendant drop had an outer diameter (OD) of 0.9020 mm and 0.4572 mm in the case of TG and FAEE, respectively, with a wall thickness of about 0.1 mm (Type 304 SS dispensing needle 20 and 26 Gauge, McMaster-Carr, Atlanta, GA, USA). The stainless steel capillary was connected to a fitting by means of a luer lok connector, which facilitated changing of the capillary between experiments. By means of a packing-type seal, the fitting holding the capillary was connected to the stainless steel inlet tubing coming from the top reservoir (H, 60 mL high pressure stainless steel cell), in such a way that the vertical position of it could be adjusted freely (Fig. 4-2). Furthermore, the fitting was mounted into a stainless steel frame located inside the view cell. The vertical position of the frame holding the capillary was adjusted precisely by means of a set screw at the bottom of the frame, so that a pendant drop could be fully visible at the center of the view cell's window. The diameter of the sapphire windows of the view cell was about 5 mm. The two valves installed on the tubing between the top reservoir and the capillary were used to generate pendant drops, as described in Section 4.2.3.3.

The view cell was equipped with a fiberoptic light source (intralux4000, Volpi, Schlieren, Switzerland) and an opal diffuser (NT46-165, Edmund Optics,

Barrington, NJ, USA) to illuminate the drop resulting in a sharp image of the contour of the drop and capillary as shown in Fig. 4-1. The images of the pendant drops were recorded by means of a CMOS camera (A602f, Basler Vision Technologies, Ahrensburg, Germany) equipped with a telecentric microscope lens having a zoom factor of up to 4.5 (VZM 450, Edmund Optics, Barrington, NJ, USA). The images were recorded on a personal computer and analyzed by means of a commercial software (FTA32 Version 2.0, First Ten Angstroems Inc., Portsmouth, VA, USA) to perform ADSA, which was used to ascertain IFT and volume of the pendant drops.

#### 4.2.3.2 Calibration and performance

The software to perform ADSA requires calibration of the optical system to factor in the magnification of the images in order to ascertain the IFT. Thus, the OD of the capillary tip was used as a reference to detect the magnification using the software. The tip diameters indicated above were confirmed using the camera and microscopic lens at maximum magnification after calibrating the camera and lens against a microscopic glass scale (NT54-421, Edmund Optics, Barrington, NJ, USA), which had 100 lines incised in glass equally spaced over a range of 5 mm to an overall accuracy stated by the supplier of ±3 μm. The OD determined using the camera deviated from the OD stated by the manufacturer by less than 0.009 mm. Thus, the OD of the capillary tip as stated by the supplier was used as reference.

The performance of the system was verified by measuring the IFT of EtOH in contact with $CO_2$ at atmospheric as well as elevated pressures up to 2.6 MPa, which compared favorably to literature data [24]. Furthermore, IFT of corn oil in contact with $CO_2$ was measured at 40°C and pressures ranging from 0.1 to 25 MPa and compared to literature data [16]. Considering the fact that corn oil is a natural product, for which properties can vary between batches, the results for IFT were in good agreement with literature data, as shown in Fig. 4-3. In order to evaluate the IFT of EtOH and corn oil in contact with $CO_2$, the density for the $CO_2$-saturated liquid phase forming the drops was obtained from Ref. [25, 26].

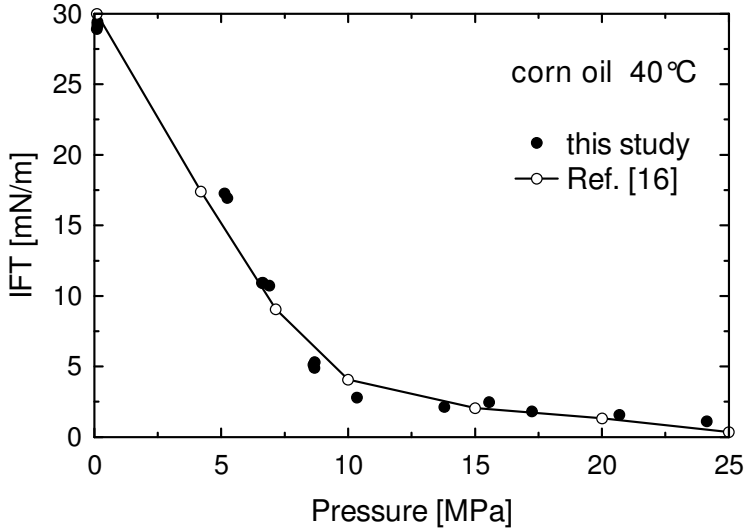


**Figure 4-3.** IFT for corn oil in contact with $CO_2$ at 40°C and pressures up to 25 MPa compared to literature. IFT data for corn oil adapted from Ref. [16].

#### 4.2.3.3 Determination of IFT

The IFT of fish oil TG and FAEE were determined at temperatures of 40, 55 and 70ºC and pressures ranging from 0.1 to about 25 MPa. Triplicate measurements were carried out for all isotherms. IFT measurements are very sensitive to contamination, therefore the capillary and all wetted parts needed to be cleaned properly. Thus, prior to each IFT measurement the apparatus was thoroughly cleaned and flushed with anhydrous EtOH+SC-$CO_2$ at 25 MPa and experimental temperature for several hours. Then, the apparatus was flushed with pure SC-$CO_2$ at 25 MPa and experimental temperature to remove any contaminants as well as any residual EtOH and air in the cell. The top reservoir was then filled with approximately 15 mL of fish oil, using a disposable plastic syringe to minimize air contact. For this purpose, a new syringe was flushed with nitrogen prior to usage and then filled with the fish oil under nitrogen atmosphere. The fish oil was then injected into the top reservoir, which had been flushed with $CO_2$ previously. The top inlet of the reservoir was then connected to the $CO_2$ inlet line. Fish oil TG and FAEE were stored at 4ºC in aluminum bottles and warmed up slowly to room

temperature before taking a sample and filling the top reservoir to avoid crystallization and precipitation of fish oil components.

After filling the top reservoir with fish oil, the system was kept at atmospheric pressure while warming up to the desired temperature. Then, the capillary tip was flushed with fish oil by fully opening both valves installed below the reservoir for a few seconds. Thereby, the tubing connecting the reservoir to the capillary tip as well as both valves were rinsed and filled completely with fish oil. After several drops fell from the capillary tip, the needle valve above the micrometering valve (I) was closed but the micrometering valve was left fully open. Then, the fish oil was equilibrated for at least 1 h prior to measurements at each experimental condition.

To generate drops, the knob of the micrometering valve was turned clockwise. Thus, the needle of the valve displaced a small amount of liquid inside the valve body, which then formed a drop at the capillary tip. In this manner, it was possible to generate very small pendant drops, especially in the case of FAEE having a volume of less than 0.5 μL. Before each IFT measurement, several drops were generated and allowed to drip from the capillary.

The IFT isotherms of fish oil FAEE and TG reported in this study were determined using the image of a freshly formed pendant drop taken about 5 s after formation. However, determination of the time dependance of IFT required keeping the same pendant drop suspended at the capillary tip and taking several images of that same drop for IFT analysis over a period of up to about 1000 s. Shortly before and during the formation of a pendant drop and while taking images for IFT measurements, the fan of the circulating air bath mounted on the same steel frame as the view cell was switched off for a few seconds to avoid any vibration in the system, which could cause the drop to oscillate or fall leading to erroneous results. For each replication and at each temperature and pressure setting, about 5 individual pendant drops were photographed, analyzed and the mean IFT values are reported. Then, the pressure of the system was increased to the next desired level and the liquid inside the capillary tubing was allowed to equilibrate again for approximately 1 h. The pressure was increased stepwise

starting from atmospheric pressure up to about 25 MPa at constant temperature to obtain IFT data along isotherms. In the case of FAEE, the pressure was increased until the IFT reached ultra low levels and eventually vanished. Throughout the entire measurement, the temperature and pressure of the $CO_2$ phase inside the view cell was continuously monitored.

The images of the pendant drops were analysed using the ADSA software to obtain the IFT and volume of the pendant drops as described above. The density of pure $CO_2$ was used for the surrounding fluid phase in all measurements, which was calculated according to the equation of state by Span and Wagner [27]. This approach seems acceptable considering that the view cell was filled and pressurized with pure $CO_2$ at the beginning of each experiment. Additionally, the solubility of TG in SC-$CO_2$ under the conditions studied is relatively low. Furthermore, for the liquids studied only a very small amount accumulated during an experiment inside the view cell due to falling pendant drops. With the volume of a pendant drop generally being <10 μL in this study and taking into account that at most about 250 drops per experiment were formed throughout one run the accumulation of test liquid inside the view cell was less than 1-2% of the total volume of the view cell (200 mL). Therefore, the effect of the accumulated liquid potentially dissolved in the $CO_2$ phase on the $CO_2$ density was considered negligible. On the other hand, given the relatively high solubility of $CO_2$ in all the liquids investigated, the liquid phase forming the drops was considered to be saturated with $CO_2$. In an earlier study (Chapter 3, [23]), the density of fish oil TG and FAEE in equilibrium with $CO_2$ was measured and was found to increase with an increase of pressure from 0.1 to 25 MPa by about 4.1% and 5.3% at 40°C for TG and FAEE, respectively. Prior to drop formation and after each pressure increase the test liquid was in contact with $CO_2$ for about an hour being located in the tube and capillary situated inside the view cell. Therefore, in order to evaluate IFT at each pressure and temperature condition, the density of the drop phase consisting of FAEE or TG saturated with $CO_2$ was calculated using previously developed correlations based on actual density values measured for the same lipid-$CO_2$ systems (Chapter 3, [23]).

## 4.3 Results and discussion

### 4.3.1 Interfacial tension versus $CO_2$ pressure

The isotherms showing IFT of fish oil TG and FAEE versus pressure of $CO_2$ at 40, 55, and 70°C are presented in Figs. 4-4 and 4-5, respectively. The IFT decreased with pressure for both TG and FAEE. In the case of TG, the IFT ranging initially between 25 to 30 mN/m at atmospheric pressure decreased sharply with a pressure increase up to 10 MPa to values of 3.6, 6.7 and 9.8 mN/m at 40, 55, and 70°C, respectively. Likewise, the IFT of FAEE decreased in the same pressure range, from initially about 25 to 30 mN/m to values of 1.2, 4.6 and 7.7 mN/m at 40, 55, and 70°C, respectively. For both TG and FAEE, at pressures below about 2.5 MPa the IFT decreased with temperature, whereas at higher pressures an increase in temperature caused an increase in IFT resulting in a cross-over of the isotherms. For the system olive oil and $CO_2$, a comparable crossover pressure was reported previously at about 2.8 MPa [11].

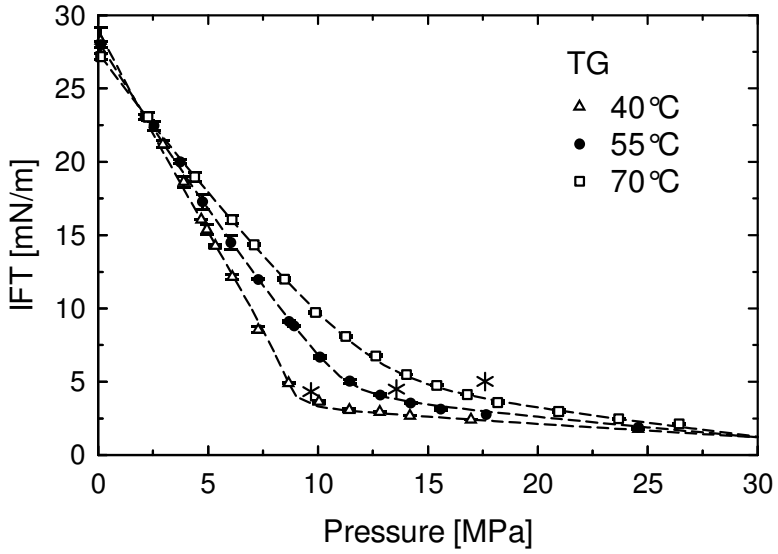


**Figure 4-4**. IFT of fish oil TG in contact with $CO_2$ as a function of temperature and pressure. Error bars represent standard deviation for triplicate measurements (5 freshly formed drops per replication). Dashed lines were calculated using the model given in Eq. (4-5). The star (*) indicates the pressure where $CO_2$ density is 0.6 g/mL.

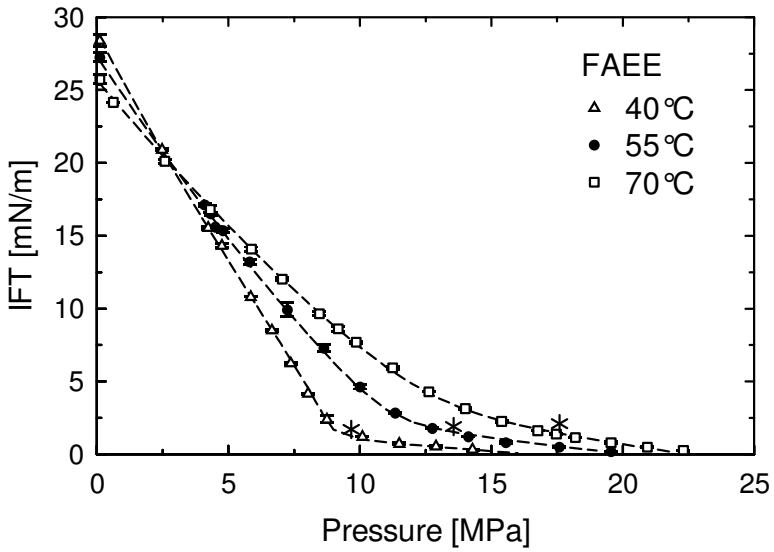


**Figure 4-5.** IFT of fish oil FAEE in contact with $CO_2$ as a function of temperature and pressure. Error bars represent standard deviation for triplicate measurements (5 freshly formed drops per replication). Dashed lines were calculated using the model given in Eq. (4-5). The star (*) indicates the pressure where $CO_2$ density is 0.6 g/mL.

At elevated pressures, the IFT of TG approached a value of approximately 2 mN/m at all temperatures investigated (Fig. 4-4), whereas the IFT of FAEE decreased to ultra-low levels and then vanished at different pressures depending on the temperature (Fig. 4-5). The pressure, at which the IFT of FAEE decreased to zero, is hereinafter referred to as pressure of vanishing interfacial tension ($P_{VIT}$). With increasing pressure below the $P_{VIT}$, the mutual solubility of both phases increased considerably affecting the interface, as illustrated for FAEE at 70°C in Fig. 4-6.

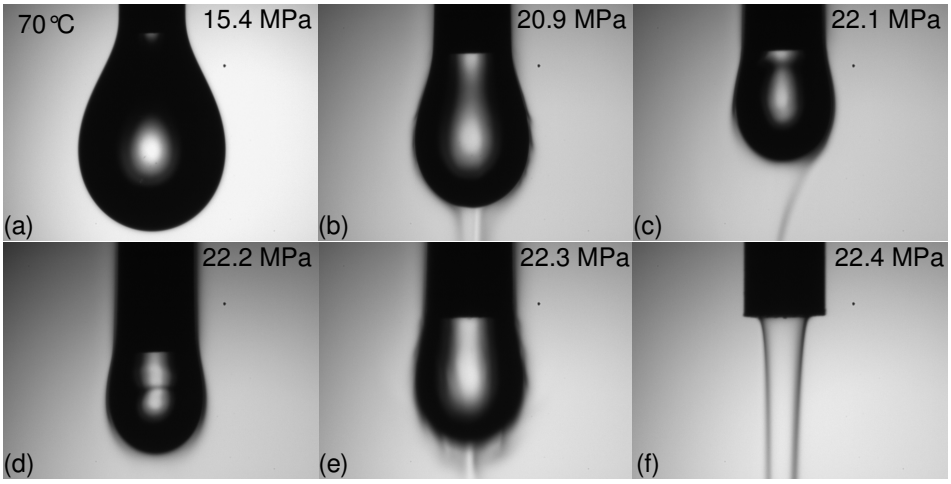


**Figure 4-6.** Images of pendant drops for FAEE in contact with $CO_2$ at 70°C approaching the pressure of vanishing IFT ($P_{VIT}$), illustrating the formation of 'schlieren'. In all images the OD of the capillary is 0.4572 mm.

At pressures far below the $P_{VIT}$ (Fig. 4-6a), the interface was clearly defined and the drop size was relatively large compared to the OD (0.4572 mm) of the capillary. However, as pressure was increased to the vicinity of $P_{VIT}$ the interface became broader and slightly blurry, caused by increased solubility of FAEE into the surrounding fluid (Figs. 4-6b, 4-6c). The dissolution of FAEE into $CO_2$ led to an increased fluid density around the drop, thereby causing a downward convective flow of $CO_2$ enriched with FAEE, which resulted in the formation of so-called 'schlieren', which are fluid regions characterized by refractive index inhomogeneities causing the light to be deflected differently. The 'schlieren technique' has been applied for mass and heat transfer studies as described elsewhere [28, 29]. Schlieren formation close to the mixture critical pressure (MCP) was also described for the system styrene and $CO_2$ by Jaeger [30]. In Figs. 4-6b to 4-6e, schlieren are visible underneath the apex of the drops at pressures above 20.9 MPa. As pressure increased, the droplet size decreased and the interface became increasingly blurry, which rendered edge detection and locating the apex of the drop progressively difficult for the software. This can lead to inaccuracies, because the exact position of the apex is essential for the evaluation of IFT [22]. Additionally, with increasing pressure it became

increasingly difficult to form stable drops and keep them suspended due to the ultra-low IFT. In that case, the capillary OD was too large to permit drop formation. Hence, at 22.4 MPa the formation of a pendant drop was impossible and FAEE pushed out of the capillary formed a stream dissolving rapidly into $CO_2$ as shown in Fig. 4-6f. Besides, the very small size of the pendant drops observed, at high pressures, especially in the case of FAEE, could also lead to errors in the numerical analysis of the spherical drop profile leading to incorrect IFT values [22]. Spherical drops are observed, when the effect of interfacial tension prevails over gravitational forces. It is best to avoid completely spherical drops for the pendant drop method to deliver accurate results. To estimate the minimum diameter of the pendant drop required to allow sufficient deformation due to gravitational forces one can calculate capillary length defined as the square root of the ratio between IFT and the product of gravity times the density difference ($\Delta\rho$) between the drop forming fluid and the surrounding fluid [10]. In this study, both IFT and ($\Delta\rho$) decrease with pressure so that their ratio would have a finite value and therefore, the actual diameters of the pendant drops generated were sufficiently large to apply the pendant drop method. Thus, the proper selection of OD for the capillary depends on the range of IFT to be measured in order to generate a well-deformed (i.e. non-spherical) pendant drop. In the case of FAEE, the smallest pendant drop evaluated in this study was generated at 55°C and 19.6 MPa and had a volume of about 0.2 μL with the corresponding IFT value of 0.22 mN/m. To generate even smaller drops, would require a capillary OD smaller than 0.4572 mm.

It has been suggested previously [31] that the minimum miscibility pressure (MMP) [31] or apparent MCP [32] can be predicted by extrapolating the isotherms on the IFT versus pressure diagram to zero IFT. According to Rao [31], reaching an IFT of zero may arguably be considered necessary and sufficient to attain miscibility between two fluids. Thus, $P_{VIT}$ is practically equivalent to MMP and MCP referring to the pressure, where no stable interface can be formed due to zero IFT, suggesting that both phases become miscible. The extrapolation to zero IFT has been used for various liquids with high pressure $CO_2$ to predict the MCP,

such as MCP for ethanol+$CO_2$ [32] or the MMP for crude oil+$CO_2$ [31], where IFT was investigated for applications of enhanced oil recovery. The IFT of FAEE in this study vanished at approximately 16.5, 20.4 and 22.4 MPa at 40, 55, and 70°C, respectively. Previous phase equilibrium data [33] for a comparable binary system of fish oil FAEE+$CO_2$ suggested the MCP at 40 and 70°C to be located at pressures of about 17 MPa and 25 MPa, respectively, which agrees reasonably well with the values found in this study.

### 4.3.2 Interfacial tension versus $CO_2$ density

The IFT isotherms showing IFT of fish oil TG and FAEE as a function of $CO_2$ density are presented in Figs. 4-7 and 4-8, respectively.

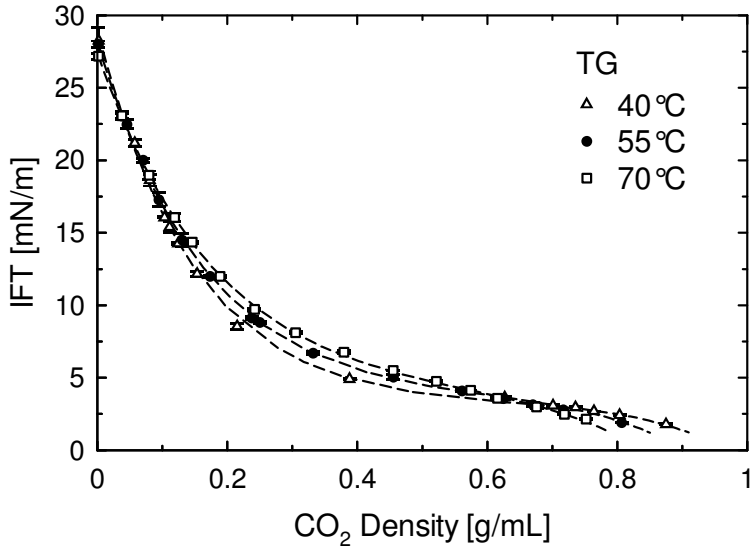


**Figure 4-7.** IFT of fish oil TG in contact with $CO_2$ at various temperatures versus $CO_2$ density. Error bars represent standard deviation for triplicate measurements (5 drops each). Dashed lines were calculated using the model given in Eq. (4-5).

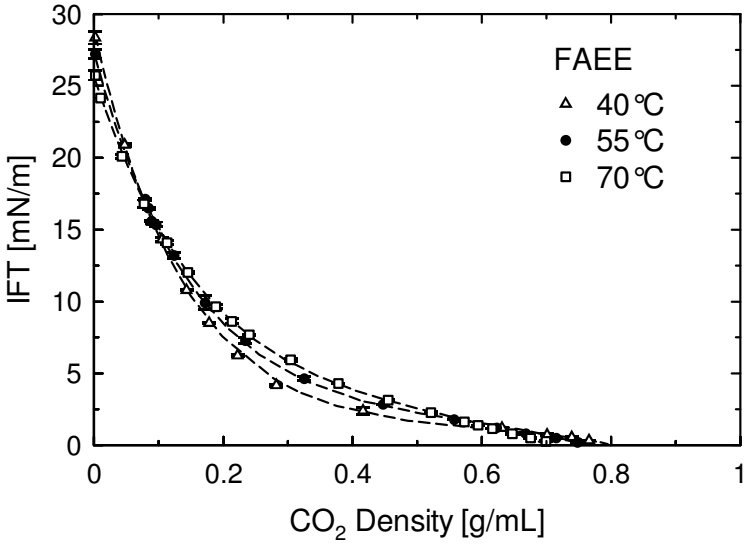


**Figure 4-8.** IFT of fish oil FAEE in contact with $CO_2$ at various temperatures versus $CO_2$ density. Error bars represent standard deviation for triplicate measurements (5 drops each). Dashed lines were calculated using the model given in Eq. (4-5).

In Figs. 4-4 and 4-5, in the low-pressure region ($P < P^*$ and $\rho_{CO2} < 0.6$ g/mL) a pronounced decrease of IFT with pressure is observed, whereas in the high-pressure region ($P > P^*$ and $\rho_{CO2} > 0.6$ g/mL) the slope of the isotherms is noticeably smaller approaching a linear trend with pressure. In the low-pressure region, the $CO_2$ density increases substantially with pressure until a density of about 0.6 g/mL is reached, above which the change in $CO_2$ density is much smaller. The pressure dependence of $CO_2$ density and IFT is linked, which results in a much smaller reduction in IFT as soon as $P^*$ is exceeded. However, above the crossover density of 0.6 g/mL, the lipid solubility in $CO_2$ increases substantially, which leads to an increased interaction of the lipids with the surrounding $CO_2$-rich phase, thereby decreasing IFT. Therefore, on the IFT versus density diagrams (Figs. 4-7 and 4-8), the IFT decreases exponentially with density until the $CO_2$ density approaches 0.6 g/mL, where an inflection point can be observed on the isotherms. At this point, the decrease of IFT with density is gaining momentum again, potentially due to the marked increase in lipid solubility with density (and thus pressure) causing a deviation from the purely exponential decrease initially observed.

### 4.3.3 Interfacial tension correlated to $CO_2$ density and pressure

In the pressure and temperature range studied, the IFT of TG and FAEE, $\gamma$ (mN/m), was correlated to pressure, $P$ (MPa), temperature, $T$ (°C) and $CO_2$ density, $\rho_{CO2}$ (g/mL). A model was developed for this purpose, which takes into account the exponential decrease of IFT with $CO_2$ density as well as the linear decrease of IFT with pressure observed at elevated pressures and thus higher $CO_2$ densities. The model including an exponential term for the density dependence and a linear term for the pressure dependence of IFT reads as follows:

$$\gamma(P,T,\rho_{CO2}) = \gamma_0(T) - k_1(T)*(P-0.1) - k_2(T)*\left(1-e^{k_3(T)*(\rho_{CO2}-\rho^0_{CO2})}\right) \qquad (4\text{-}5)$$

where $\gamma_0(T)$ is the IFT at 0.1 MPa as a function of temperature $T$, the second term includes $k_1(T)$ as the temperature dependent linear slope of IFT with pressure $P$ and the last term describes the exponential decrease of IFT with increasing $CO_2$ density, with $\rho_{CO2}$ as the corresponding $CO_2$ density at pressure $P$ and temperature $T$, and $\rho^0_{CO2}$ as the $CO_2$ density at 0.1 MPa and temperature $T$. The term $\gamma_0(T)$ as well as the parameters $k_1(T)$ to $k_3(T)$ are defined as follows:

$$\gamma_0(T) = A_1 + A_2 * T \qquad (4\text{-}6)$$

$$k_1(T) = A_3 + A_4 * T \qquad (4\text{-}7)$$

$$k_2(T) = A_5 + A_6 * T \qquad (4\text{-}8)$$

$$k_3(T) = A_7 + A_8 * T \qquad (4\text{-}9)$$

The fitting parameters $A_1$ to $A_8$ listed in Table 4-1 were obtained by performing a least square fit of Eqs. (4-5) to (4-9) to experimental data using a Quasi-Newton algorithm. This correlation (Eq. (4-5)) describes the experimental data very well in the pressure and temperature ranges studied, as illustrated by the dashed lines in Figs. 4-4, 4-5, 4-7 and 4-8.

**Table 4-1.** Parameters for Eq. (4-5) for FAEE and TG.

| | FAEE | TG |
|---|---|---|
| $A_1$ | 32.73 | 30.66 |
| $A_2$ | -0.1039 | -0.04884 |
| $A_3$ | -0.02586 | -0.02322 |
| $A_4$ | 0.003849 | 0.002796 |
| $A_5$ | 34.85 | 30.01 |
| $A_6$ | -0.2077 | -0.1277 |
| $A_7$ | -8.848 | -8.043 |
| $A_8$ | 0.04053 | 0.03431 |

### 4.3.4 Interfacial tension versus time

The IFT isotherms presented in Figs. 4-4, 4-5, 4-7 and 4-8 were obtained by analyzing images of freshly formed drops, which were taken about 5 s after drop formation. It was necessary to wait about 5 s in order to avoid errors due to small oscillations in the drop caused by the drop generation. This approach was chosen to detect the IFT as close as possible to the moment when the fresh interface was formed. The IFT obtained in that manner appears to be more relevant to processes, where the interface is formed and renewed in a short time interval, such as spraying and may allow one to estimate effects on IFT, which are mainly caused by the immediate mutual interactions of the lipid components with $CO_2$ at the interface. However, in other processes the interface remains stable over a longer period of time so that slower diffusion processes inside the drop affect the IFT. Therefore, an experiment was conducted with TG to assess the change of IFT over time.

The change of IFT over time for TG at 55°C in contact with $CO_2$ at various pressures is illustrated in Fig. 4-9. At low pressures, the IFT decreased substantially over time, whereas at elevated pressures the IFT remained nearly constant over time. At low pressures, the equilibration and arrangement of molecules at the interface linked to the adsorption of $CO_2$ may take longer due to

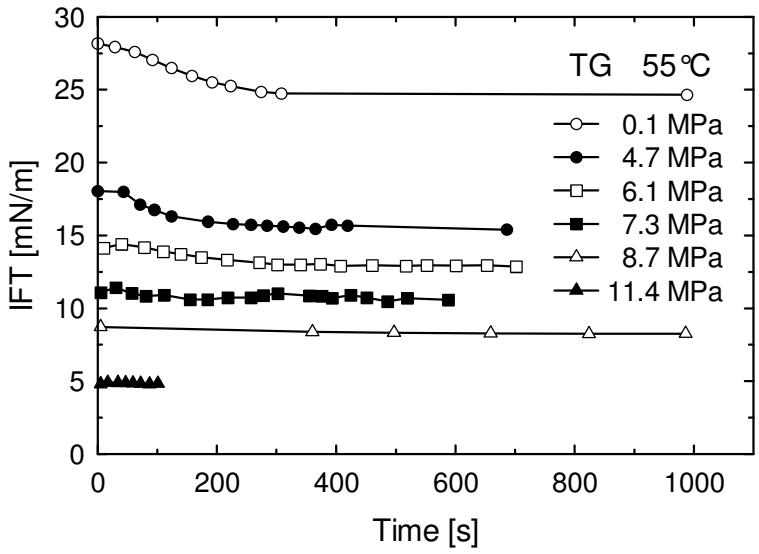


**Figure 4-9.** IFT of fish oil TG in contact with $CO_2$ at 55°C and various pressures versus time.

the lower $CO_2$ density, which is the driving force for adsorption. Furthermore, accumulation of potentially surface active substances which were present in the fish oil samples used, such as free fatty acids (FFA), citric acid and tocopherols, may have an effect on the IFT even though it is less likely due to the non-polar nature of the coexisting phases, as discussed in more detail below. At high pressures, the mutual interaction of $CO_2$ with the lipids at the interface may be stronger than the effect of other potentially surface active substances contained in the liquid drop. Furthermore, the viscosity of lipids in equilibrium with $CO_2$ at elevated pressures is reduced [4], thereby accelerating diffusion processes in the liquid phase, which may be another reason for the faster attainment of a stable IFT at high pressures, besides the smaller drop size and thus shorter diffusion path. Adsorption of $CO_2$ at the interface and diffusion of $CO_2$ into the drop, as well as diffusion of components from inside the drop to the interface and into the surrounding $CO_2$ phase are the main factors determining the time scale required for reaching a constant IFT. The results shown in Fig. 4-9 indicate that with increasing pressure the decrease of IFT over time occurs faster and to a lesser extent in the TG+$CO_2$ system investigated in this study.

The tocopherols and citric acid contained in the fish oil TG and FAEE (8 mg/g) may accumulate at the interface by diffusing from the bulk liquid inside the drop to the interface thereby impacting the IFT over a longer time period. However, the tendency for antioxidants to accumulate at the interface depends on the polarity of the antioxidant as well as the nature of the surrounding media [35, 36]. The dielectric constant ε is one measure to quantify the polarity of a compound. For example, at 40°C and atmospheric pressure the value of ε is about 3 and 1 for triolein and $CO_2$, respectively [37, 38]. Furthermore, the dielectric constant of $CO_2$ increases with pressure up to a value of 1.56 at 30 MPa and 40°C [38]. Thus, there is a difference in dielectric constant at low pressures between the lipid and $CO_2$ phase, which may be sufficient to cause some of the compounds present in the fish oil to be surface active. However, it can be anticipated that the dielectric constant ε of the drop phase decreases with increasing pressure as $CO_2$ dissolves into the drop phase, similar to the change in ε measured for the systems methanol-$CO_2$ [39] and dimethylether-$CO_2$ [40], thereby reducing the difference in dielectric constants between the continuous and drop phases.

Furthermore, especially in case of $CO_2$ the dielectric constant alone may not be sufficient to describe the solvent behavior of the non-dipolar $CO_2$, which can indeed dissolve and interact with relatively polar materials such as sugar acetates [41, 42]. Thus, specific solute-solvent interactions such as in the case of surfactants with fluorocarbon tails can greatly enhance their solubility and interaction with $CO_2$ [43]. It has been suggested that the hydrogen atoms of partially fluorinated hydrocarbons can form hydrogen bonds with the oxygen from the $CO_2$ molecule [42], where it has been shown that more polar fluoromethanes interact stronger with $CO_2$ than the less polar ones [43]. A study by Harrison *et al.* [44] investigating the effect of surfactants in the system SC-$CO_2$ with polyethylene glycol (PEG) on the IFT revealed that a surfactant consisting of perfluoropolyether ammonium carboxylate (PFPE) was most active, due to the carboxylate head group strongly interacting with the more polar PEG (ε=10) and the $CO_2$-philic nature of the amorphous fluoroalkane tail [44]. Thus, a

compound with interactions on each side of the interphase and appreciable solubility in both phases may substantially affect IFT.

Another example for the impact of polarity of both the adjacent phases and the surfactant is δ-tocopherol, which decreased the IFT of a water-hexadecane bilayer more effectively than the less polar α-tocopherol [35]. However, in the case of lipid+$CO_2$ systems at elevated pressures both coexisting phases can be considered fairly non-polar suggesting that the effect of surface active substances may be less pronounced, which is supported by previous observations [15] regarding the instability of foams of unrefined vegetable oils rich in surface active substances (FFA, etc.) in a high pressure $CO_2$ environment. Besides tocopherols, the fish oil used in this study also contained citric acid, a metal chelator, to improve its storage stability. In terms of the surface activity of citric acid in lipid systems, there is little information available in the literature. However, it can be anticipated that in the lipid+$CO_2$ system due to the compact polar nature of the citric acid molecule and lack of a non-polar tail, citric acid is less likely to be surface active. The non-polarity of the surrounding $CO_2$-phase may further reduce the potential of citric acid to accumulate at the interface.

The FFA present in the fish oil TG (0.2%, expressed as oleic acid) appear as likely candidates for surface activity. According to Simoes *et al.* [14], the difference between the IFT of refined corn oil and crude corn oil was very small, where the FFA content of the crude and refined corn oils was 1.6 wt% and <0.16 wt%, respectively [14]. Slight differences in their IFT results could also be attributed to the presence of phospholipids in the crude corn oil [14].

Thus, it can be concluded that due to the non-polar nature of $CO_2$ the surface activity of tocopherols, citric acid and FFA seems likely to be reduced. Nevertheless, the molecules may still tend to diffuse to the interface, especially if traces of water are present in the system as shown for milkfat [15], thereby affecting the IFT. However, the results (Fig. 4-9) demonstrate that the change in IFT depended on $CO_2$ pressure. Due to the pronounced effect of $CO_2$ pressure on the density, viscosity and diffusion coefficient in both coexisting phases, the dominating effects dictating the time dependent decrease of IFT observed for the

TG+$CO_2$ system can be attributed to adsorption of $CO_2$ at the interface, and the mass transfer of $CO_2$ into the drop as well as mutual solubility of the coexisting phases.

### 4.3.5 Pendant drop volume versus $CO_2$ pressure

The experimentally observed volume ($V^{exp}$) of pendant drops formed at the tip of the capillary for TG and FAEE versus $CO_2$ pressure is illustrated in Figs. 4-10 and 4-11, respectively. The drop volume of TG decreased with pressure until a minimum volume was observed and then increased again with pressure. With increasing temperature the location of the minimum drop volume shifted to higher pressures together with an increase in the minimum drop volume. The ideal pendant drop volume ($V^{id}$) was calculated according to Tate's law by using the model for IFT ($\gamma$) given by Eq. (4-5) and by calculating the balance between interfacial, gravitational and buoyant forces acting upon the drop as follows:

$$\left(\rho_{drop} - \rho_{CO2}\right) * g * V^{id} = d_{cap} * \pi * \gamma \qquad (4\text{-}10)$$

where $\rho_{drop}$ and $\rho_{CO2}$ are the density of the drop forming liquid and the surrounding $CO_2$, respectively, $g$ is the acceleration due to gravity and $\gamma$ the IFT. The diameter of the capillary tip, $d_{cap}$ was 0.9020 and 0.4572 mm for TG and FAEE, respectively. In the case of TG, the $V^{exp}$ was about 80% of the $V^{id}$.

The pressures where the minima of $V^{exp}$ and $V^{id}$ are located are practically identical. The size of a pendant drop and potentially the size of a resulting falling drop depend on the pressure and temperature, which influence both the IFT and buoyant force by affecting the density of $CO_2$. For TG, the model calculations predict a maximum ideal drop size at elevated pressures above 20 MPa, and a moderate decrease thereafter at higher temperatures.

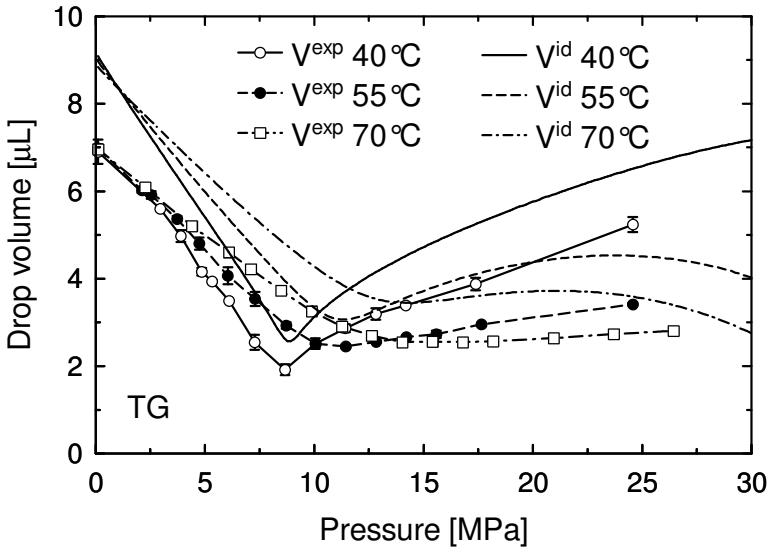


**Figure 4-10.** Volume of pendant drops of TG in contact with $CO_2$ at various temperatures versus $CO_2$ pressure. $V^{exp}$ is the experimentally observed drop volume. $V^{id}$ was calculated according to Tate's law. Error bars represent standard deviation for triplicate measurements.

In the case of FAEE, the drop volume decreased over the entire pressure range studied for both $V^{exp}$ and $V^{id}$. For the system FAEE+$CO_2$, the effect of decreasing IFT outweighs the effect of increasing $CO_2$ density; therefore, the drop volume decreases with pressure. However, at 40°C $V^{exp}$ of FAEE was nearly constant at pressures above 9 MPa, where the effects of decreased IFT and increased $CO_2$ density cancel each other. It can be observed for FAEE that $V^{exp}$ was about 95% of $V^{id}$, except at high pressures, where $V^{exp}$ approaches the maximum volume possible, namely $V^{id}$. In those cases, due to the ultra low IFT, the drops were very small, difficult to generate and to suspend at the capillary tip. A smaller diameter for the capillary tip may alleviate that difficulty.

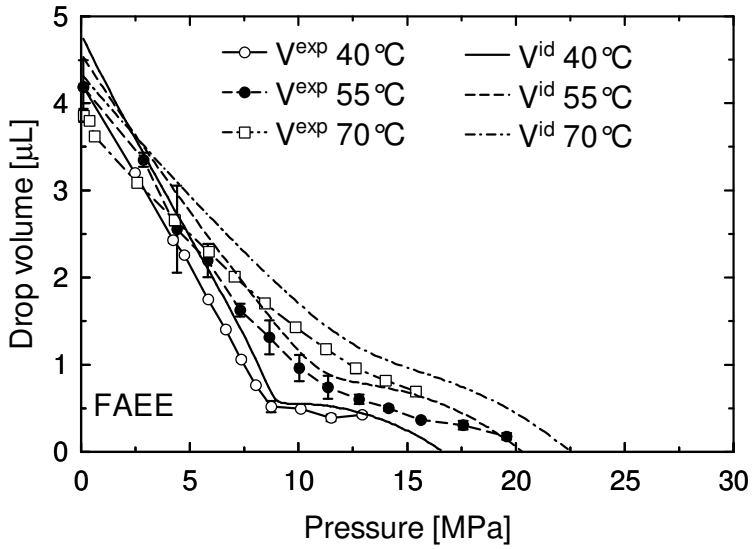


**Figure 4-11.** Volume of pendant drops of FAEE in contact with $CO_2$ at various temperatures versus $CO_2$ pressure. $V^{exp}$ is the experimentally observed drop volume. $V^{id}$ was calculated according to Tate's law. Error bars represent standard deviation for triplicate measurements.

The size of the ideal pendant drop as illustrated in Figs. 4-10 and 4-11 can give a clue about how the size of a falling drop may change with pressure. However, the size of a falling drop under situations of static drop formation is generally smaller than that of the ideal pendant drop, which was investigated for systems under atmospheric pressure by Harkins and Brown [45]. The volume of the falling drop ($V$) is related to the volume of the ideal pendant drop ($V^{id}$) by the Harkins and Brown factor, $\Psi$, which is defined as the ratio $V/V^{id}$ [45]. The factor $\Psi$ depends on the shape of the pendant drop and is a function of the ratio $r_k/V^{1/3}$, with the capillary radius $r_k$. Harkins and Brown [45] studied the density range of 0.87 to 2.18 g/mL, surface tension range of 26.6 to 71.96 mN/m, and viscosities less than 1.5 mPa.s. Further investigations by numerous researchers led to the development of correlations for $\Psi$ expanding those ranges to higher densities and viscosities, as compiled in a recent review [46]. The correlations were mostly developed for static drop volumes at atmospheric pressure, where only limited solubility of the gas in the liquid occurs. However, Hobbie [47] found that for values of $r_k/V^{1/3}$ between 0.4 and 1.6 the data of Harkins and Brown [45] agreed well with experimental data obtained for the water+$CO_2$ system at pressures of 10

- 31 MPa and temperatures of 40 - 70°C. However, in order to prove the validity of such correlations for other systems with higher mutual solubility more research is required. Furthermore, the situation in high pressure processes is often far from static drop formation. In cases of dynamic drop formation where a constant flow rate through the capillary leads to continuous drop formation, or in situations where the liquid flow rate is much higher, leading to jet formation or even atomization, kinetic forces caused by the velocity of the liquid as well as friction forces caused by the dense gas need to be considered. Drop formation under high pressure conditions was studied for a wide range of *Re* and *Oh* [7, 8, 47, 48] using high speed cameras. Czerwonatis [7] characterized liquid jets in pressurized gases by introducing a new dimensionless number, which besides IFT takes into account the ratios of the gas to liquid densities and viscosities.

### 4.3.6 Surface excess

The surface excess amount of $CO_2$ ($n_{CO2}$), is defined as the excess of the amount of $CO_2$ present in the actual system over that present in an ideal reference system, for which the bulk concentrations of both phases remain uniform up to the so-called Gibbs dividing surface [49]. The surface excess concentration ($\Gamma_{CO2}$) is then calculated by dividing the surface excess amount $n_{CO2}$ by the interfacial area ($A_s$). In other words, $\Gamma_{CO2}$ may loosely be described as the excess of $CO_2$ adsorbed at the interface compared to the surrounding bulk phases, which can take positive or negative values and is defined as the number of moles per unit area. A detailed explanation of surface excess can be found in Ref. [10]. Based on the Gibbs adsorption equation [49], for an isothermal case the surface excess concentration $\Gamma_{CO2}$ can be expressed as:

$$\Gamma_{CO_2} = -\frac{d\gamma}{d\mu_{CO_2}} \tag{4-11}$$

where the chemical potential $\mu_{CO2}$ of a dense gas at a given pressure $P$ can be calculated by Eq. (4-12):

$$\mu_{CO_2} = \mu^0_{CO_2} + \int_{P^0}^{P} v_{CO_2} * dP \tag{4-12}$$

if accurate volumetric data for the gas are available, which further leads to

$$d\mu_{CO_2} = v_{CO_2} * dP \tag{4-13}$$

where $v_{CO2}$ is the molar volume of $CO_2$. Hence, $\Gamma_{CO2}$ can be calculated using the following equation:

$$\Gamma_{CO_2} = -\frac{1}{v_{CO_2}} * \left(\frac{d\gamma}{dP}\right) \tag{4-14}$$

In Eq. (4-14), it is assumed that the solubility of the liquid components in $CO_2$ is negligible, so that the density or molar volume of $CO_2$ is not affected. Thus, molar volume of pure $CO_2$ was used in the calculations, which was obtained using an equation of state [27]. In order to calculate the surface excess shown in Fig. 4-12 the interfacial tension $\gamma$ was modeled for each temperature over the entire pressure range using Eq. (4-5), which was then numerically differentiated.

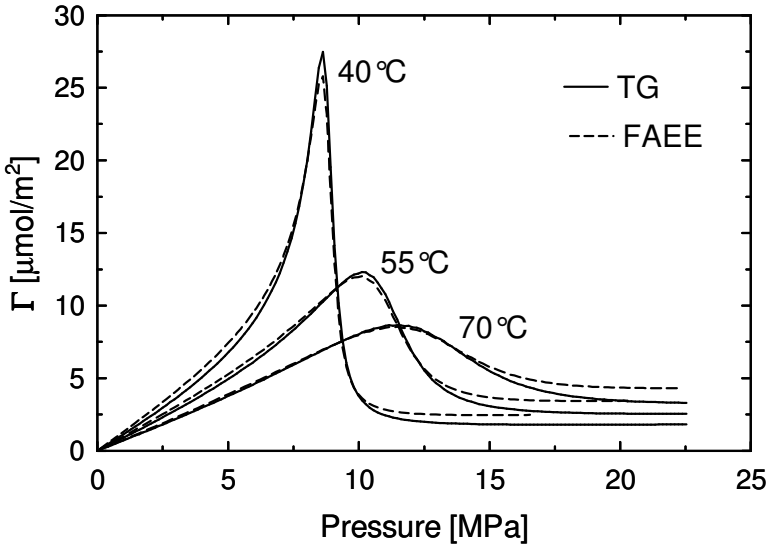


**Figure 4-12.** Calculated surface excess of $CO_2$ ($\Gamma_{CO2}$) at the interface for TG and FAEE at various temperatures versus pressure.

The isotherms shown in Fig. 4-12 for $\Gamma_{CO2}$ were almost identical for both TG and FAEE. They increased from initially around zero up to the maximum value and then decreased markedly with pressure. The location of the maximum for $\Gamma_{CO2}$ was found to be temperature dependent. Furthermore, the value of the maximum decreased with increasing temperature. It is noted that the decrease of

$\Gamma_{CO2}$ was more pronounced after the maximum at lower temperatures, where a small change in pressure led to a large decrease in $\Gamma_{CO2}$. Using the model for IFT given in Eq. (4-5), the value of ($d\gamma/dP$) in Eq. (4-14) approaches the value of the slope $-k_1(T)$ at elevated pressure plus a small contribution caused by the density contained in the exponential term, which is a function of pressure. Therefore, the term ($d\gamma/dP$) in these calculations, although falling to a nearly constant low value, did not approach zero. For FAEE, the values of $\Gamma_{CO2}$ calculated close to the MCP were 2.47, 3.44, 4.32 μmol/m$^2$ at 40, 55, and 70°C and pressures of 16.5, 20.4, and 22.4 MPa, respectively. The values close to the MCP reported for $\Gamma_{CO2}$ in the literature for the system pelargonic acid+$CO_2$, for which IFT approaches zero as well, were 4.8, 5.2 and 6.4 μmol/m$^2$ at 40, 60 and 80°C, respectively [11]. However, it appears reasonable that at elevated pressures, where IFT vanishes and the two phases become miscible, $\Gamma_{CO2}$ should approach zero. Thus, it can be concluded that the underlying assumptions, namely that of limited solubility of the lipids in $CO_2$ are not valid anymore close to the MCP, and thus the density of the gas phase in the vicinity of the interface differs from that of pure $CO_2$. Hence, the chemical potential at the interface is affected by the enhanced mutual solubility of the coexisting phases when approaching the MCP. Therefore, the values of $\Gamma_{CO2}$ reported at elevated pressures approaching the MCP of FAEE+$CO_2$ may not be in accordance with the actual concentration occurring at the drop interface and thus require further research. With these limitations in mind, the surface excess was calculated only up to a pressure where an interface exists and the interfacial tension has a positive value, as illustrated in Fig. 4-12.

Nevertheless, the obtained maximum values for $\Gamma_{CO2}$ are comparable to literature values and provide some insight into the mechanism affecting IFT, despite the aforementioned limitations and simplifying assumptions. At 40, 55, and 70°C, the maximum values of $\Gamma_{CO2}$ for TG were 27.5, 12.3 and 8.6 μmol/m$^2$ at pressures of 8.6, 10.1 and 11.5 MPa, respectively. According to Hiller *et al.* [2], the gas surface excess for the system linoleic acid+$CO_2$ reached a maximum of about 17.5 μmol/m$^2$ at 40°C and a pressure of about 8 MPa. They also observed that falling films of fatty acids in contact with high pressure $CO_2$ disintegrated

into tiny droplets close to pressures corresponding to the maximum of the surface excess [2]. Schiemann [11] determined the surface excess and IFT for lipid+$CO_2$ systems, including olive oil+$CO_2$ and found that the maxima for $\Gamma_{CO2}$ were 13.9, 10.0 and 6.7 μmol/$m^2$ at pressures of 7.9, 10.2 and 12.1 MPa at temperatures of 40, 60, and 80°C, respectively. While the maximum values of $\Gamma_{CO2}$ for fish oil TG at 55 and 70°C are close to the values of olive oil at 60 and 80°C, those at 40°C are different (27.5 vs 13.9 μmol/$m^2$). Calculation of $\Gamma_{CO2}$ is very sensitive to the inverse of molar volume ($1/v_{CO2}$) and the slope of the isotherms ($d\gamma/dP$), both changing considerably with pressure especially around the location of the maximum for $\Gamma_{CO2}$, which is in the vicinity of the critical pressure for $CO_2$. It seems that the difference between the results of Schiemann [11] and this study stems mainly from the factor $1/v_{CO2}$, which takes a value of about 6000 and 10500 mol/$m^3$ at 7.9 and 8.6 MPa, respectively. Thus, the discrepancy between the results may be attributed to the factor $1/v_{CO2}$, which is nearly doubled by increasing the pressure from 7.9 to 8.6 MPa, thereby greatly affecting the value of $\Gamma_{CO2}$ even if the slopes of the isotherms ($d\gamma/dP$) were the same in both studies. Thus, the precise position of the maximum, which is dictated by the maximum for the slope ($d\gamma/dP$) becomes important and affects the calculations of $\Gamma_{CO2}$ to a great extent. The calculations of Schiemann [11] are based on a piecewise approximation of the IFT isotherms using a 3$^{rd}$ degree polynomial to interpolate the data, while the calculations in this study are based on a model (Eq. (4-5)) that correlates well over the entire pressure range.

The approach taken in this study, using $CO_2$ density (or molar volume) to calculate $\Gamma_{CO2}$ was also used by Sutjiadi-Sia *et al.* [50], who reported the maximum $\Gamma_{CO2}$ as 17 μmol/$m^2$ for the system corn oil+$CO_2$ at 40°C and a $CO_2$ density and pressure of about 0.63 g/mL and 10 MPa, respectively. Discrepancies between the reported literature values can most likely be attributed to the different approaches used for the interpolation or correlation of the actual IFT isotherms. However, the pressure range of the surface excess maximum is in most cases comparable. At the pressure where the maximum surface excess is found, the maximum amount of $CO_2$ is adsorbed at the interface because mass transfer

resistance into the liquid phase is considerable. However, as soon as the pressure reaches higher values, where $CO_2$ density reaches about 0.6 g/mL, the mutual solubility is greatly enhanced and mass transfer from the interface into the bulk phase takes place, thereby greatly reducing the surface excess concentration.

As demonstrated above, accurate IFT data over the entire pressure range is paramount for the calculation of the surface excess concentration, especially around the pressure where the surface excess maximum is expected, which is in the vicinity of the critical point of $CO_2$. It is further beneficial to use a correlation capable of describing the experimental data over the range of conditions studied to calculate the slope of the IFT isotherms ($d\gamma/dP$).

### 4.3.7 Potential mechanisms affecting IFT

The isotherms depicted in Figs. 4-4 and 4-5 can be divided into three pressure regions according to the observed behavior of IFT. The first region spans from atmospheric pressure up to the crossover pressure at about 2.5 MPa. The second region ranges from 2.5 MPa to the pressure $P^*$, which corresponds to the crossover density of 0.6 g/mL (Figs. 4-7, 4-8). The third region relates to the high pressure region at pressures above $P^*$. The following is a discussion about potential driving mechanisms affecting the IFT in each of these regions for the lipid+$CO_2$ systems investigated in this study.

At atmospheric pressure, the IFT is decreased with increasing temperature due to the increased mobility of molecules at the interface, which keeps them at a distance and thus reduces cohesive forces. This temperature effect seems to play a role up to pressures of about 2.5 MPa. However, as pressure increases the density of $CO_2$ increases and thus more and more $CO_2$ is adsorbed onto the interface leading to a decrease in IFT besides the temperature effect mentioned above. Furthermore, the density of $CO_2$ is pressure and temperature dependent, where at isobaric conditions an increase in temperature brings about a decrease in density. Therefore, the effect of temperature on IFT at pressures above 2.5 MPa is reversed.

Above the crossover pressure of 2.5 MPa the effect of temperature on the surrounding fluid density and hence on adsorption prevails over the pure temperature effect. With increasing pressure the dominating factor affecting IFT is $CO_2$ density as influenced by temperature. However, with increasing pressure other effects begin to play a role besides $CO_2$ adsorption and the pure temperature effect on molecule mobility. With increasing pressure, both the solubility of $CO_2$ in the liquid phase as well as the solubility of the lipids in the surrounding $CO_2$ phase increase as well. For example, the solubility of $CO_2$ in the liquid phase in the case of fish oil TG and FAEE increases with pressure and decreases with temperature for $CO_2$ pressures below about 28 MPa [33, 51]. Thus, with increasing pressure more $CO_2$ is present in the vicinity of the interface, thereby affecting cohesive forces at the interface, leading to a further decrease in IFT. The findings for the surface excess (Fig. 4-12) suggest that with increasing temperature the amount of adsorbed $CO_2$ at the interface is reduced. The surface excess maxima for $CO_2$ are located at pressures ranging from 7.9 to 12.1 MPa corresponding to a $CO_2$ density of 0.3 to 0.4 g/mL, respectively. At the surface excess maximum, the adsorption of $CO_2$ onto the interface reaches a maximum. Further increase in pressure and thus $CO_2$ density to about 0.6 g/mL leads to a substantial decrease in $CO_2$ adsorbed at the interface. It is noted that the surface excess concentration of $CO_2$ at the interface decreased to levels below 5 $\mu mol/m^2$ at 0.6 g/mL for all temperatures investigated. These findings suggest that the influence of adsorption becomes less dominant as soon as $CO_2$ density exceeds 0.6 g/mL.

Following the isotherms in Figs. 4-4 and 4-5 to pressures close to $P^*$ leads to a sudden change in the slopes of the isotherms. This pressure $P^*$ delineates the transition of the isotherms to the next region on the IFT versus pressure diagram, which is most apparent for the isotherms at 40°C. The location of this sudden change in slope coincides with the pressures at which the $CO_2$ density reaches a value of about 0.6 g/mL, which relates to the crossover points in the IFT versus $CO_2$ density diagrams, as illustrated in Figs. 4-7 and 4-8. Above $P^*$ a further increase in pressure does not increase $CO_2$ density as much, and the surface

excess maximum has been passed already, so that adsorption at the interface has a less prominent effect on IFT. However, the solubility behavior of both $CO_2$ in the liquid phase as well as the solubility of lipids in the $CO_2$ phase change substantially at pressures above *P**. For example, the concentration of $CO_2$ ($X_{CO2}$) in vegetable oils, such as olive oil, at temperatures ranging from 40 to 80°C increases practically linearly with pressure up to about 6 MPa to a level of about 65 to 70 mol%, and then to a lesser extent from 5-10 MPa where $X_{CO2}$ reaches a plateau of approximately 85-90 mol%, depending on temperature [11]. Further increase in pressure from 10 MPa to 25 MPa causes a much lower increase to a level for $X_{CO2}$ around 90 mol% (see Ref. [11] page 62). Furthermore, the solvent power of $CO_2$ is enhanced at pressures above *P**, where the solubility of the lipids in the $CO_2$ phase increases. For example, at 40°C the solubility of fish oil FAEE in $CO_2$ increases five-fold from about 0.04 $kg/kg_{CO2}$ at a $CO_2$ density of 0.6 g/mL to about 0.2 $kg/kg_{CO2}$ at 0.8 g/mL [52]. This sudden increase in solubility is shifted to lower $CO_2$ densities with an increase in temperature, which correlates well to the observed onset of IFT decrease at elevated temperatures in the vicinity of the crossover point at 0.6 g/mL. At pressures above *P** the compressibility of the $CO_2$ molecules is approaching its maximum, as evidenced by the decreasing slope of $CO_2$ density versus pressure. The increase in solubility leads to more mass transfer at the interface, which then becomes broader and increasingly similar in composition to both of the surrounding phases. Moser *et al.* [53] considered the mutual solubility of tocopherol and $CO_2$ being one of the main factors determining IFT. The authors [53] also concluded that both the mutual solubility of the coexisting liquid and supercritical phases and the $CO_2$ density are the most important parameters influencing IFT. It was further suggested, that the high solubility of $CO_2$ in the liquid phase weakens the interactive forces thus reducing the energy required to bring molecules from the bulk phase to the interface to form new interfacial area, therefore reducing IFT. In a study by Harrison *et al.* [44] the interfacial tension between SC-$CO_2$ and polyethylene glycol (PEG) was measured and correlated to a theoretical model based on a gradient model in combination with a lattice fluid equation of state, in which the

free energy density in the interfacial region was calculated. The authors [44] found that as the density of $CO_2$ increases with increasing pressure, the free energy densities of both the $CO_2$ and PEG phases become closer, thereby reducing IFT. They further concluded that the decrease in IFT was primarily due to the increase in free energy density of $CO_2$ (and thus $CO_2$ density) and to a lesser extent due to the increased solubility of $CO_2$ in PEG.

## 4.4 Conclusions

The IFT of marine lipids in the form of TG and FAEE was determined at pressures ranging from 0.1 to about 25 MPa at 40, 55, and 70°C, where IFT decreased substantially with $CO_2$ pressure. IFT was correlated using a model consisting of three terms accounting for the influence of pressure, temperature and density of $CO_2$ on IFT, which described the experimental data well. Furthermore, in the case of TG it was shown that at constant temperature the volume of the generated pendant drops decreased up to about 8-15 MPa exhibiting a minimum and then increased in volume with further increase in $CO_2$ pressure. The change in pendant drop volume is due to the dominating effect of decreasing IFT at low pressures, while at higher pressures the dominating buoyant effect caused by increasing $CO_2$ density prevails. Surface excess of $CO_2$ exhibited a maximum at about 8.5, 10 and 11.5 MPa for both TG and FAEE at 40, 55, and 70°C. The IFT depends on interactive forces between the molecules in the vicinity of the interface, which are influenced by the composition of the interface and both coexisting phases close to the interface. The mechanisms affecting the interactions between molecules at the interface depend on the $CO_2$ pressure and temperature, and thus $CO_2$ density. At atmospheric pressure, where adsorption at the interface is low the intermolecular forces are mainly affected by temperature. With increasing pressure more $CO_2$ is adsorbed at the interface, thus lowering IFT. Furthermore, at intermediate pressures ($\rho_{CO2}$ < 0.6 g/mL), temperature strongly influences $CO_2$ density and thereby the adsorption of $CO_2$ at the interface, which influences interactive forces at the interface. At elevated pressures ($\rho_{CO2}$ > 0.6 g/mL), the mutual solubility of lipids and $CO_2$ leads to a

broadening of the interface and eventually a similar composition for both coexisting phases, thereby strongly affecting IFT.

For lipid processing using SC-$CO_2$ these findings should help to better design contacting equipment or to adjust processing parameters, such as pressure, temperature or flow rates of gas and liquid feeds using correlations developed for characterization of flow regimes, which require the knowledge of IFT.

## 4.5 References


1. A. Beyer, M. Seekamp, S. Peter, Mass-transfer of low-volatility substances with anisometric molecular-structure. Chem. Ing. Tech. 61 (1989) 405-407.

2. N. Hiller, H. Schiemann, E. Weidner, S. Peter, Interfacial tension in systems with a supercritical component at high pressures. Chem. Eng. Technol. 16 (1993) 206-212.

3. M. Moser, C. Trepp, Investigating the stability of falling films at round vertical film carriers under high pressure. Chem. Eng. Technol. 20 (1997) 612-616.

4. C.A. Lockemann, E.U. Schlunder, Liquid-phase viscosities of the binary systems carbon dioxide oleic acid, carbon dioxide methyl myristate, and carbon dioxide methyl palmitate at high pressures. Chem. Eng. Process. 34 (1995) 487-493.

5. A.W. Kerst, B. Judat, E.U. Schlunder, Flow regimes of free jets and falling films at high ambient pressure. Chem. Eng. Sci. 55 (2000) 4189-4208.

6. R. Stockfleth, G. Brunner, Film thickness, flow regimes, and flooding in countercurrent annular flow of a falling film at high pressures. Ind. Eng. Chem. Res. 40 (2001) 6014-6020.

7. N. Czerwonatis, R. Eggers, Disintegration of liquid jets and drop drag coefficients in pressurized nitrogen and carbon dioxide. Chem. Eng. Technol. 24 (2001) 619-624.

8. E. Badens, O. Boutin, G. Charbit, Laminar jet dispersion and jet atomization in pressurized carbon dioxide. J. Supercrit. Fluids 36 (2005) 81-90.

9. Y. Sutjiadi-Sia, R. Eggers, Lateral wetting angle of falling film in dense fluid. Int. J. Heat Mass Transfer 51 (2008) 3608-3614.

10. A.W. Adamson, A.P. Gast, Physical Chemistry of Surfaces. 1997, New York: J. Wiley.

11. H. Schiemann, PhD Thesis: Die Grenzflächenspannung von Lipiden in Gegenwart dichter Gase. 1993, TU Erlangen-Nuremberg: Erlangen, Germany.

12. H. Schiemann, E. Weidner, S. Peter, Interfacial tension in binary systems containing a dense gas. J. Supercrit. Fluids 6 (1993) 181-189.

13. O.K. Rice, The effect of pressure on surface tension. J. Chem. Phys. 15 (1947) 333-335.

14. P.C. Simoes, R. Eggers, P.T. Jaeger, Interfacial tension of edible oils in supercritical carbon dioxide. Eur. J. Lipid Sci. Technol. 102 (2000) 263-265.

15. P.T. Jaeger, J. von Schnitzler, R. Eggers, Interfacial tension of fluid systems considering the nonstationary case with respect to mass transfer. Chem. Eng. Technol. 19 (1996) 197-202.

16. D. Dittmar, R. Eggers, H. Kahl, S. Enders, Measurement and modelling of the interfacial tension of triglyceride mixtures in contact with dense gases. Chem. Eng. Sci. 57 (2002) 355-363.

17. C.A. Lockemann, Interfacial tensions of the binary systems carbon dioxide-oleic acid, carbon dioxide-methyl myristate, and carbon dioxide-methyl palmitate and of the ternary system carbon dioxide-methyl myristate-methyl palmitate at high pressures. Chem. Eng. Process. 33 (1994) 193-198.

18. J.M. Andreas, E.A. Hauser, W.B. Tucker, Boundary tension by pendant drops. J. Phys. Chem. 42 (1938) 1001-1019.

19. T. Young, An essay on the cohesion of fluids. Philos. Trans. R. Soc. London 95 (1805) 65-87.

20. P.S. Laplace, Traité de Mécanique Céleste. Supplement to Book 10. 1806, Paris: Gauthier–Villars.

21. F. Bashford, J.C. Adams, An attempt to test the theory of capillary action. 1883, Cambridge: The University Press.

22. M. Hoorfar, A.W. Neumann, Recent progress in Axisymmetric Drop Shape Analysis (ADSA). Adv. Colloid Interface Sci. 121 (2006) 25-49.

23. B. Seifried, F. Temelli, Density of marine lipids in equilibrium with carbon dioxide. J. Supercrit. Fluids 50 (2009) 97-104.

24. D. Dittmar, S.B. Oei, R. Eggers, Interfacial tension and density of ethanol in contact with carbon dioxide. Chem. Eng. Technol. 25 (2002) 23-27.

25. C.M.J. Chang, K.L. Chiu, C.Y. Day, A new apparatus for the determination of P-x-y diagrams and Henry's constants in high pressure alcohols with critical carbon dioxide. J. Supercrit. Fluids 12 (1998) 223-237.

26. A. Tegetmeier, D. Dittmar, A. Fredenhagen, R. Eggers, Density and volume of water and triglyceride mixtures in contact with carbon dioxide. Chem. Eng. Process. 39 (2000) 399-405.

27. R. Span, W. Wagner, A new equation of state for carbon dioxide covering the fluid region from the triple-point temperature to 1100 K at pressures up to 800 MPa. J. Phys. Chem. Ref. Data 25 (1996) 1509-1596.

28. A. Okhotsimskii, M. Hozawa, Schlieren visualization of natural convection in binary gas-liquid systems. Chem. Eng. Sci. 53 (1998) 2547-2573.

29. G. Tanda, F. Devia, Application of a schlieren technique to heat transfer measurements in free-convection. Exp. Fluids 24 (1998) 285-290.

30. P.T. Jaeger, R. Eggers, H. Baumgartl, Interfacial properties of high viscous liquids in a supercritical carbon dioxide atmosphere. J. Supercrit. Fluids 24 (2002) 203-217.

31. D.N. Rao, A new technique of vanishing interfacial tension for miscibility determination. Fluid Phase Equilib. 139 (1997) 311-324.

32. Y.D. Sun, B.Y. Shekunov, Surface tension of ethanol in supercritical $CO_2$. J. Supercrit. Fluids 27 (2003) 73-83.

33. C. Borch-Jensen, J. Mollerup, Phase equilibria of long-chain polyunsaturated fish oil fatty acid ethyl esters and carbon dioxide, ethane, or ethylene at reduced gas temperatures of 1.03 and 1.13. Fluid Phase Equilib. 161 (1999) 169-189.

34. D. Dittmar, A. Fredenhagen, S.B. Oei, R. Eggers, Interfacial tensions of ethanol-carbon dioxide and ethanol-nitrogen. Dependence of the interfacial tension on the fluid density - prerequisites and physical reasoning. Chem. Eng. Sci. 58 (2003) 1223-1233.

35. W. Chaiyasit, D.J. McClements, E.A. Decker, The relationship between the physicochemical properties of antioxidants and their ability to inhibit lipid oxidation in bulk oil and oil-in-water emulsions. J. Agric. Food. Chem. 53 (2005) 4982-4988.

36. M. Iwatsuki, J. Tsuchiya, E. Komuro, Y. Yamamoto, E. Niki, Effects of solvents and media on the antioxidant activity of alpha-tocopherol. BBA-Gen. Subj. 1200 (1994) 19-26.

37. T.H. Gouw, J.C. Vlugter, Physical properties of triglycerides IV. Dielectric constant. Fette Seifen Anstr. 69 (1967) 223-226.

38. A. Wesch, N. Dahmen, K.H. Ebert, Measuring the static dielectric constants of pure carbon dioxide and carbon dioxide mixed with ethanol and toluene at elevated pressures. Ber. Bunsen Ges. - Phys. Chem. Chem. Phys. 100 (1996) 1368-1371.

39. D.L. Goldfarb, D.P. Fernandez, H.R. Corti, Dielectric and volumetric properties of supercritical carbon dioxide(1) plus methanol(2) mixtures at 323.15 K. Fluid Phase Equilib. 158 (1999) 1011-1019.

40. W. Eltringham, S.J. Tallon, O.J. Catchpole, K. Fenton, Relative permittivity measurements of dimethyl ether plus carbon dioxide mixtures. J. Chem. Eng. Data 53 (2008) 826-829.

41. P. Raveendran, S.L. Wallen, Sugar acetates as novel, renewable $CO_2$-philes. J. Am. Chem. Soc. 124 (2002) 7274-7275.

42. P. Raveendran, Y. Ikushima, S.L. Wallen, Polar attributes of supercritical carbon dioxide. Acc. Chem. Res. 38 (2005) 478-485.

43. P. Raveendran, S.L. Wallen, Exploring $CO_2$-philicity: Effects of stepwise fluorination. J. Phys. Chem. B 107 (2003) 1473-1477.

44. K.L. Harrison, K.P. Johnston, I.C. Sanchez, Effect of surfactants on the interfacial tension between supercritical carbon dioxide and polyethylene glycol. Langmuir 12 (1996) 2637-2644.

45. W.D. Harkins, F.E. Brown, The determination of surface tension (free surface energy), and the weight of falling drops - The surface tension of water and benzene by the capillary height method. J. Am. Chem. Soc. 41 (1919) 499-524.

46. B.B. Lee, P. Ravindra, E.S. Chan, A critical review: Surface and interfacial tension measurement by the drop weight method. Chem. Eng. Commun. 195 (2008) 889-924.

47. M. Hobbie, PhD Thesis: Bildung von Tropfen in verdichteten Gasen und stationäre Umströmung fluider Partikel bei Drücken bis zu 50 MPa. 2006, TU Hamburg-Harburg: Hamburg, Germany.

48. H.C. Hahm, B. Veriansyah, J. Kim, W.J. Kim, J.D. Kim, S.G. Oh, Y.W. Lee, A new correlation to predict the stability of liquid jet in dense carbon dioxide. J. Ind. Eng. Chem. 14 (2008) 824-829.

49. J.W. Gibbs, The collected works of J. Willard Gibbs. 1948, New Haven: Yale Univ. Press.

50. Y. Sutjiadi-Sia, H. Marckmann, R. Eggers, C. Holzknecht, S. Kabelac, The effect of in liquids dissolved dense gases on interfacial and wetting characteristics. Forsch. Ingenieurwes. – Eng. Res. 71 (2007) 29-45.

51. C. Borch-Jensen, J. Mollerup, Phase equilibria of fish oil in sub- and supercritical carbon dioxide. Fluid Phase Equilib. 138 (1997) 179-211.

52. C. Borch-Jensen, A. Staby, J.M. Mollerup, Phase equilibria of urea-fractionated fish oil fatty acid ethyl esters and supercritical carbon dioxide. Ind. Eng. Chem. Res. 33 (1994) 1574-1579.

53. M. Moser, W. Pietzonka, C. Trepp, Interfacial tension measurements between alpha-tocopherol and carbon dioxide at high pressures. Chem. Eng. Technol. 19 (1996) 462-466.

# 5 Density of Carbon Dioxide-Expanded Ethanol[1]

## 5.1 Introduction

Gas-expanded liquids have gained great attention in recent years due to their tunable solvent properties [1]. A gas-expanded liquid consists of an organic solvent equilibrated and expanded by dissolving a compressible gas such as $CO_2$ or ethane as described in Section 2.2.5. In this manner, a fairly polar solvent such as ethanol can be tuned by expanding it with pressurized $CO_2$. Thereby, its polarity can be altered and the solvent properties adjusted to solubilize or precipitate a specific compound.

The density of $CO_2$-expanded ethanol is required for optimum process design. Density data of saturated $CO_2$-expanded ethanol are available in the literature [2-8]. However, there are discrepancies between and within some of the available density data. Besides being scattered, most of the published data fail to describe the maximum value of $CO_2$-expanded ethanol density and the pronounced decrease in the vicinity of the mixture critical point. Furthermore, even though correlations exist for specific temperatures [9], based on pressure, temperature and compositional vapor-liquid equilibrium data using empirical equations or an equation of state approach [7, 10], it seems that a simple correlation based on pressure and temperature alone for the density of saturated $CO_2$-expanded ethanol covering the temperature range from 40 to 70°C has not been reported. Therefore, the objective of this study was to determine the density of saturated $CO_2$-expanded ethanol at 40, 55 and 70°C and pressures ranging from atmospheric pressure up to about 8 to 12 MPa, which is close to the mixture critical point. Another objective was to develop a correlation for saturated $CO_2$-expanded ethanol density covering the temperature range from 40 to 70°C and pressures up to the mixture critical point.

---

[1] A version of this chapter has been published online on March 29, 2010 in the J. Chem. Eng. Data.

## 5.2 Experimental

### 5.2.1 Materials

For the density measurements, food grade anhydrous ethanol (Commercial Alcohols - GreenField Ethanol Inc., Winnipeg, MB, Canada) was used with a stated purity and water content of 99.99% and 0.008% by volume, respectively. Bone dry carbon dioxide with a purity of 99.9% (Praxair, Edmonton, AB, Canada) was used for the density measurements. Both ethanol and carbon dioxide were used without further purification.

### 5.2.2 Apparatus

The experimental apparatus consisted of a high pressure view cell equipped with a spring balance and has been described in detail in Section 3.2.3 [11]. The main feature of the apparatus is a spring balance consisting of a glass sinker attached to an extension spring with a needle pointing at a microscopic glass scale. By means of a camera equipped with a microscopic lens the position of the sinker submersed in the liquid can be determined precisely by locating the position of the needle pointing at the microscopic glass scale. Due to the magnification and high resolution of the images, the position of the sinker could be determined precisely by analyzing the images on the computer, so that density changes of about 0.1 $kg/m^3$ could be detected with this device. The view cell equipped with electric heaters was placed inside a temperature-controlled circulating air bath, which allowed maintaining the liquid circulated inside the view cell at a constant temperature to within ±0.1°C. However, due to exothermic mixing effects following a stepwise increase in $CO_2$ pressure caused by dissolution of $CO_2$ into ethanol the liquid temperature fluctuated by about ±0.5°C. Furthermore, a stepwise increase in $CO_2$ pressure of about 1 to 2 MPa also caused a spike in temperature due to compression of $CO_2$, which along with the exothermic effects decayed over the time required for equilibration. Equilibration was achieved usually within 2 h by continuously pumping the liquid from the bottom of the view cell and spraying it into the pressurized $CO_2$ headspace at the top. The temperatures of the liquid inside the view cell and that of the air bath were

measured by means of a custom made data acquisition (DAQ) system calibrated against a precision digital thermometer (Model 4000, Control Company, Friendswood, TX, USA) with a resolution of 0.001°C using an insulated heating water bath (Haake H3, Karlsruhe, Germany). The DAQ system was connected to a computer and allowed continuous monitoring and recording of the temperatures with a resolution of 0.01°C. The overall estimated uncertainty in the reported temperature was about ±0.15°C. The system was pressurized with $CO_2$ by means of a piston pump (ISCO Model 250D, Isco Inc., Lincoln, NE, USA). The pressure was monitored using a calibrated digital pressure indicator (Druck Model DPI 104, General Electrics Sensing, Billerica, MA, USA) with 0.05% full scale accuracy and a maximum operating pressure of 35 MPa. The uncertainty in the pressure readings was ±0.02 MPa.

### 5.2.3 Determination of density

The apparatus was calibrated prior to each measurement by using pure $CO_2$ at various pressure levels ranging from about 20 to 30 MPa at the same temperature as the subsequent measurements. The density of $CO_2$ at each calibration point was calculated using the equation of state (EoS) of Span and Wagner [12]. According to the authors [12], the estimated uncertainty in density is 0.03% at pressures up to 30 MPa and temperatures of up to about 80°C translating into uncertainty in the calculated density of ±0.25 kg/m$^3$. With the uncertainty in the measured pressure and temperature in this study, the overall uncertainty of the calculated density used for calibration is about ±0.75 kg/m$^3$ or ±0.1%. The performance of the spring balance at elevated pressures was tested by measuring the density of a water+ethanol mixture under hydrostatic pressures of up to 30 MPa, which compared favorably to literature data with less than 0.1% deviation, as described previously in Chapter 3 [11]. After calibration with $CO_2$ the apparatus was filled by injecting ethanol through the bottom port of the view cell using a syringe until the liquid level of ethanol was just above the window ensuring that the sinker was completely submersed in liquid. Ethanol was warmed up to the desired temperature inside the view cell while being circulated using the circulation pump

described in the Appendix. Once the experimental temperature was reached the circulation pump was switched off for a few seconds to avoid a downward flow of ethanol, which could cause vibrations and errors while measuring the position of the sinker. Then, as soon as the fluid inside the view cell came to a rest the position of the sinker was determined by taking an image of the needle attached to the hook holding the sinker pointing at the microscopic scale. After recording an image the circulation pump was switched on again. During density measurements images of the microscopic scale with the needle showing the position of the sinker were taken about every 15 to 30 min. The images were analyzed on the computer to determine the exact position of the sinker, which was translated into density of the liquid using the calibration curve. The change in density could be followed *in situ* by observing the sinker position until a constant level was reached, which indicated equilibration. Usually, at least three images were taken and analysed after equilibrium was reached at a given pressure setting for each replication. Three replications were performed for each density isotherm. Statistical analysis of the data was carried out using statistical software (SPSS version 17, SPSS Inc., Chicago, IL, USA). Once equilibrium was reached and constant density observed, the pressure of the system was increased to the next desired level and the liquid was circulated again to facilitate equilibration. The pressure was increased stepwise starting from atmospheric pressure up to about 12 MPa, until the density dropped and the mixture critical point was reached. Throughout the entire measurement cycle the temperature of the liquid phase was continuously monitored ensuring that enough time was allowed for thermal equilibration after temperature fluctuations caused by the pressure increase. The increase in $CO_2$ pressure caused the liquid phase consisting of ethanol saturated with $CO_2$ to expand substantially, which can be more than 300% in volume at elevated $CO_2$ pressures, as reported by Kordikowski *et al.* [2]. Therefore, the liquid level was adjusted and kept constant just above the window of the view cell during experiments by carefully bleeding ethanol out of the bottom of the view cell after every stepwise pressure increase. Thereby, enough headspace inside the view cell was maintained for the ethanol to expand while reaching equilibrium.

## 5.3 Results and discussion

### 5.3.1 Density of $CO_2$-expanded ethanol

The accuracy of the system was first tested at atmospheric pressure by measuring the density of anhydrous ethanol at 40, 55 and 70°C. The average densities of ethanol determined after triplicate measurements with the spring balance after calibration with $CO_2$ were compared to literature data, as shown in Table 5-1.

**Table 5-1.** Comparison between experimental (Exp.) and literature data (Lit.) for the density of anhydrous ethanol ( $\rho^0_{EtOH}$ ) at atmospheric pressure and 40, 55 and 70°C.

| | $\rho^0_{EtOH}$ [kg/m$^3$] | | | |
|---|---|---|---|---|
| **T [°C]** | **Exp.** | **Lit.** | **Ref.** | **100 Δρ/ρ[a]** |
| 40 | 768.9±1.73 | 768.0 | [13] | 0.12 |
| | | 772.3 | [14] | -0.43 |
| | | 771.7 | [15] | -0.36 |
| | | 772.1 | [16] | -0.41 |
| 55 | 752.7±0.60 | 750.5 | [13] | 0.30 |
| | | 758.1 | [14] | -0.71 |
| | | 758.4 | [15] | -0.75 |
| | | 758.5 | [16] | -0.77 |
| 70 | 740.2±0.12 | 732.3 | [13] | 1.08 |
| | | 743.3 | [14] | -0.41 |
| | | 744.9 | [15] | -0.63 |
| | | 744.5 | [16] | -0.57 |

[a] $100\ \Delta\rho/\rho = 100 \cdot \frac{\rho^{exp}_{EtOH} - \rho^{lit}_{EtOH}}{\rho^{lit}_{EtOH}}$

The density of anhydrous ethanol at atmospheric pressure agreed reasonably well with literature data [13, 14] even though there were some inconsistencies in the literature data. However, the data obtained by using the following so-called Rackett equation for the density of pure ethanol at atmospheric pressure (Eq. 5-1) from Ref. [14] agrees well with other literature data [15-19]:

$$\rho^0_{EtOH} = \frac{M_{EtOH} \cdot C_1}{C_2^{\,1+\left(1-\frac{T}{C_3}\right)^{C_4}}} \qquad (5\text{-}1)$$

where $T$ is the temperature in K, $M$ is the molecular weight of ethanol (46.069 kg/kmol) and the model parameters are $C_1$ = 1.648, $C_2$ = 0.27627, $C_3$ = 513.92 and $C_4$ = 0.2331. The deviations between the literature values reported for pure ethanol density and those found in this study could be attributed to the purity of the ethanol used. Ethanol of purity 99.99% and water content of 0.008% by volume as stated by the manufacturer was used in this study without any further treatment, whereas the reported purities of ethanol used in the literature were as follows: 99 mol % in Ref. [2], 99.8% in Ref. [5], ≥ 99.8% with water < 0.2% by mass in Ref. [17], 99.5% by volume in Ref. [18], > 99.8% in Ref. [3] and Ref. [4], 99.7% with 0.3 mass% water in Ref. [19]. In some reports the purity of ethanol was not specified [7]. Furthermore, for the ethanol used in this study the manufacturer stated a density of 788.4 kg/m$^3$ at 20°C, which is slightly lower than the value obtained by using Eq. (5-1) (790.4 kg/m$^3$), indicating that, as expected, the density of ethanol was affected by its purity. In addition, using pressurized $CO_2$ for the calibration of the spring balance added uncertainty to the measured density data as described above. Nevertheless, the agreement with literature data seemed acceptable considering the differences in ethanol purities between different studies.

The isotherms for the density of $CO_2$-expanded ethanol were measured in triplicate at 40, 55 and 70°C up to about 12 MPa. The results for density of $CO_2$-expanded ethanol are illustrated in Fig. 5-1 and listed in Table 5-2, with the corresponding confidence intervals of 95% based on the standard deviation of the mean of N observations at each pressure level. The precision of the apparatus at elevated pressures was acceptable considering that the variability in the measured data was less than 0.25% for pressures up to a level where the maximum density was reached (Table 5-2). The pressure where the maximum density was reached was temperature dependent. At pressures above the maximum density in the vicinity of the mixture critical point the variability in the measured density data increased.

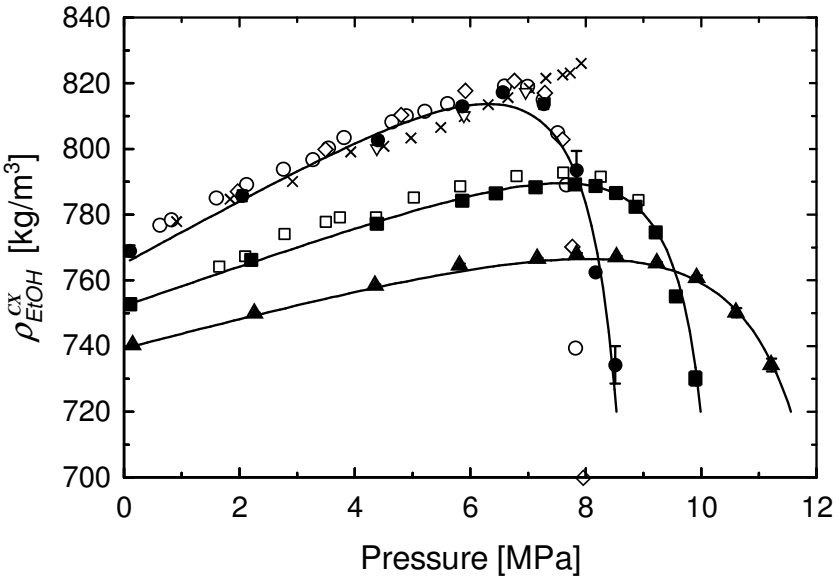


**Figure 5-1.** Measured density of saturated $CO_2$-expanded ethanol ( $\rho_{EtOH}^{CX}$ ) versus pressure of $CO_2$ at various temperatures from this study: ●, 40°C; ■, 55°C; ▲, 70°C. Error bars represent confidence interval of 95% for N observations (see Table 5-2). Lines were calculated using Eq. (5-2).

Literature data at T = 40°C: ○, Ref. [6]; ×, Ref. [4]; ▽, Ref. [8]; ◇, Ref. [9]; T = 55°C: □, Ref. [6].

**Table 5-2.** Experimental results[a] for density of $CO_2$-expanded ethanol ( $\rho_{EtOH}^{CX}$ ) at 40, 55 and 70°C and up to pressures near the mixture critical point.

| 40°C | | | | 55°C | | | | 70°C | | | |
|---|---|---|---|---|---|---|---|---|---|---|---|
| ***P*** **[MPa]** | **N** | $\rho_{EtOH}^{CX}$ **[kg/m$^3$]** | **Δ%[b]** | ***P*** **[MPa]** | **N** | $\rho_{EtOH}^{CX}$ **[kg/m$^3$]** | **Δ%[b]** | ***P*** **[MPa]** | **N** | $\rho_{EtOH}^{CX}$ **[kg/m$^3$]** | **Δ%[b]** |
| 0.10 | 9 | 768.9±1.73 | 0.23 | 0.11 | 9 | 752.7±0.60 | 0.08 | 0.16 | 9 | 740.2±0.12 | 0.02 |
| 2.05 | 9 | 785.8±1.65 | 0.21 | 2.20 | 9 | 766.2±0.81 | 0.11 | 2.27 | 9 | 749.8±0.33 | 0.04 |
| 4.40 | 9 | 802.6±1.17 | 0.15 | 4.38 | 9 | 777.2±0.21 | 0.03 | 4.36 | 9 | 758.3±0.40 | 0.05 |
| 5.86 | 9 | 813.0±1.04 | 0.13 | 5.86 | 9 | 784.2±0.53 | 0.07 | 5.82 | 12 | 764.5±0.64 | 0.08 |
| 6.56 | 9 | 817.2±1.18 | 0.14 | 6.44 | 3 | 786.5±0.13 | 0.02 | 7.17 | 9 | 766.5±0.29 | 0.04 |
| 7.27 | 15 | 813.7±1.59 | 0.20 | 7.13 | 9 | 788.3±0.30 | 0.04 | 7.85 | 9 | 767.8±0.45 | 0.06 |
| 7.84 | 8 | 793.5±5.87 | 0.74 | 7.81 | 6 | 789.2±0.19 | 0.02 | 8.54 | 9 | 767.0±0.49 | 0.06 |
| 8.17 | 3 | 762.5±0.10 | 0.01 | 8.17 | 9 | 788.7±0.12 | 0.01 | 9.24 | 9 | 765.2±0.46 | 0.06 |
| 8.51 | 11 | 734.3±5.69 | 0.77 | 8.52 | 9 | 786.6±0.35 | 0.04 | 9.93 | 9 | 760.7±0.85 | 0.11 |
| | | | | 8.86 | 6 | 782.4±0.16 | 0.02 | 10.61 | 9 | 750.1±1.42 | 0.19 |
| | | | | 9.21 | 9 | 774.6±0.17 | 0.02 | 11.22 | 11 | 734.2±1.97 | 0.27 |
| | | | | 9.56 | 6 | 755.2±0.74 | 0.10 | | | | |
| | | | | 9.90 | 6 | 730.1±2.12 | 0.29 | | | | |

[a] The uncertainties were determined from the standard deviation of the mean of N observations at a confidence interval of 95%.
[b] Δ% denotes the variability determined from the standard deviation as a percentage of the mean of N observations at a confidence interval of 95%.

### 5.3.2 Correlation of density to temperature and pressure

The measured density of saturated $CO_2$-expanded ethanol ( $\rho_{EtOH}^{CX}$ in kg/m$^3$) was correlated to $CO_2$ pressure ($P$ in MPa) and temperature ($T$ in K) by using the following empirical equation:

$$\rho_{EtOH}^{CX} = \frac{k_1(T) + k_2(T) \cdot P}{1 + k_3(T) \cdot P + k_4(T) \cdot P^2} \tag{5-2}$$

with the temperature dependent coefficients $k_1$ to $k_4$ defined as follows:

$$k_1(T) = A_1 \cdot T + A_2 \tag{5-3}$$

$$k_2(T) = A_3 \cdot T^2 + A_4 \cdot T + A_5 \tag{5-4}$$

$$k_3(T) = \left(A_6 \cdot T^2 + A_7 \cdot T + A_8\right) \cdot 10^{-4} \tag{5-5}$$

$$k_4(T) = \left(A_9 \cdot T^2 + A_{10} \cdot T + A_{11}\right) \cdot 10^{-4} \tag{5-6}$$

The parameters $A_1$ to $A_{11}$ for Eqs. 5-3 to 5-6 are listed in Table 5-3. The correlation is valid within the temperature range of 40 to 70°C. The deviations between the experimental density values and the correlated density using Eq. (5-2) are illustrated in Fig. 5-2. The deviation between calculated and experimental values is less than about 0.5% for pressures up to the maximum density. Above the maximum density, the deviation is slightly more pronounced (< 1.5%) due to the much greater sensitivity of the measured density to small pressure variations in the vicinity of the mixture critical point, which causes greater uncertainty.

**Table 5-3.** Parameters for the correlation given in Eq. (5-2).

| $i$ | $A_i$ |
|---|---|
| 1 | $-8.6337 \times 10^{-1}$ |
| 2 | $1.0355 \times 10^{3}$ |
| 3 | $3.6834 \times 10^{-3}$ |
| 4 | -1.5085 |
| 5 | $2.7000 \times 10^{1}$ |
| 6 | $5.1143 \times 10^{-3}$ |
| 7 | 9.7372 |
| 8 | $-4.7748 \times 10^{3}$ |
| 9 | $9.1586 \times 10^{-3}$ |
| 10 | -6.3279 |
| 11 | $1.0985 \times 10^{3}$ |

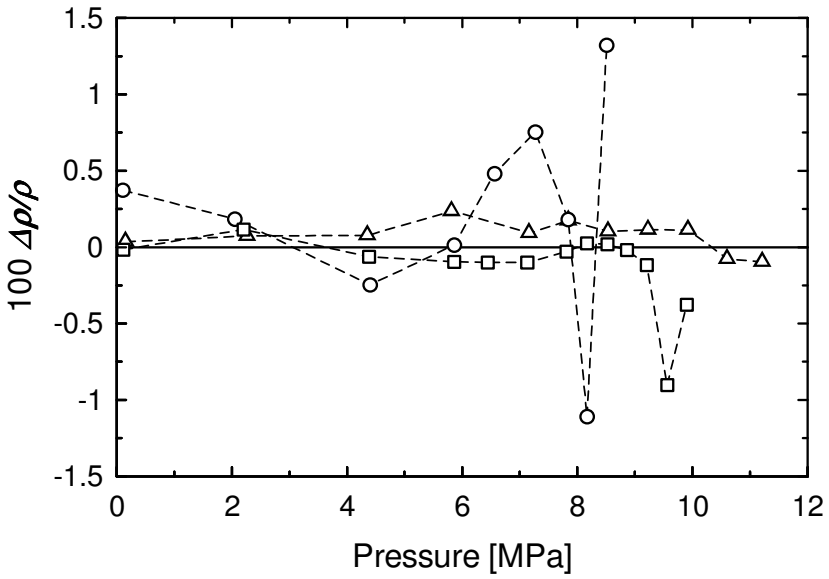


**Figure 5-2.** Deviation $\Delta\rho/\rho = (\rho_{exp} - \rho_{calc}) / \rho_{calc}$ between the experimental density values found in this study and calculated density values obtained by using Eq. (5-2) for $CO_2$-expanded ethanol at various temperatures: ○, 40°C; □, 55°C; △, 70°C.

The deviations between correlated density values of $CO_2$-expanded ethanol using Eq. (5-2) and values found in the literature [2, 3, 5-7] in the range of 25 to 82°C are illustrated in Fig. 5-3. In order to test the performance of the correlation outside of the temperature range of 40 to 70°C of this study, the density of $CO_2$-expanded ethanol was also correlated at 25, 35 and 82°C using Eq. (5-2). The deviations were less than 5% at pressures up to about 7.5 MPa for all temperatures. However, the literature data to compare with are quite scattered. As well, because not all literature data exhibit the sharp decrease in density at elevated pressure some of the data may not be reliable in the vicinity of the mixture critical point, such as those reported in Refs. [3-5]. Furthermore, the data of Ref. [3] have been omitted in the comparison because the reported values are about 18% below comparable literature data.

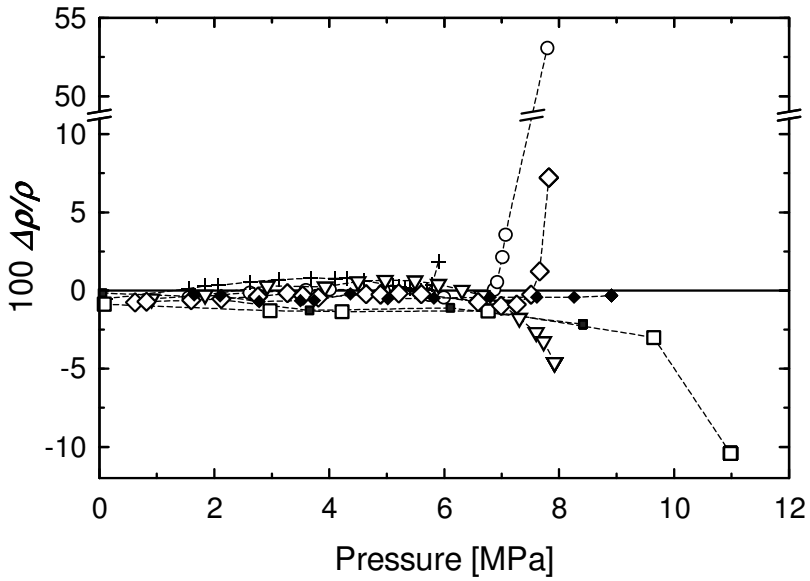


**Figure 5-3.** Deviation $\Delta\rho/\rho = (\rho_{calc} - \rho_{lit}) / \rho_{lit}$ between the density values calculated using Eq. (5-2) and available literature data at various temperatures: +, 25°C Ref. [2]; ○, 35°C Ref. [7]; ▽, 40°C Ref. [4]; ◇, 40°C Ref. [6]; □, 62.8°C Ref. [5]; ◆ , 65°C Ref. [6]; ■, 81.8°C Ref. [5].

The data for $CO_2$-expanded ethanol density reported in Refs. [2, 6, 7] seem to be more accurate at pressures above the maximum density, since they follow a pronounced decrease close to the mixture critical point. As anticipated, the deviation between the correlation (Eq. 5-2) and literature values outside of the recommended temperature range can be rather large especially at elevated pressures. Therefore, the correlation (Eq. 5-2) should preferably be used within the temperature limit of 40 to 70°C from atmospheric pressure up to pressure levels close the mixture critical point. The pressures required to reach the mixture critical point of the system $CO_2$-ethanol were reported by Joung *et al.* [20] for the temperature range from 40 to 72°C. The reported pressures [20] for the mixture critical point compare fairly well with the pressures obtained in this study where the isotherms exhibit a sudden decrease. Within the pressure region between that corresponding to the density maximum and the mixture critical point the uncertainty in the measured data and therefore in the correlation is larger. Therefore, the suggested upper pressure limit ($P_{limit}$ in MPa), which is temperature

dependent, for the correlation (Eq. 5-2) can be evaluated using the following empirical equation (Eq. 5-7), which was derived by correlating the pressures for the mixture critical point from Ref. [20] to temperature ($T$ in K):

$$P_{limit} = 0.1233 \cdot T - 30.5 \tag{5-7}$$

### 5.3.3 Correlation of density to reduced $CO_2$ density

The density of $CO_2$-expanded ethanol ($\rho_{EtOH}^{CX}$) was further analyzed by plotting the relative density of ethanol ($\rho_{EtOH}^{R}$) against the reduced density of $CO_2$ ($\rho_{CO2}^{R}$), which were calculated as follows:

$$\rho_{EtOH}^{R} = \frac{\rho_{EtOH}^{CX}(P,T)}{\rho_{EtOH}^{0}(P_0,T)} \tag{5-8}$$

where $\rho_{EtOH}^{0}$ is the density of ethanol at atmospheric pressure $P_0$ and temperature $T$, and $\rho_{EtOH}^{CX}$ is the density of $CO_2$-expanded ethanol at elevated pressure $P$ and temperature $T$. The reduced density of $CO_2$ was calculated using the density of $CO_2$ at the critical point ($\rho_{CO2}^{C}$ = 467.6 kg/m$^3$) from literature [21] and calculating the density of $CO_2$ ($\rho_{CO2}$) at pressure $P$ and temperature $T$ using the EoS from Span and Wagner [12] according to:

$$\rho_{CO2}^{R} = \frac{\rho_{CO2}(P,T)}{\rho_{CO2}^{C}} \tag{5-9}$$

The results are presented in Fig. 5-4, which shows a distinct trend for the density of $CO_2$-expanded ethanol with the reduced density of $CO_2$. The maximum density of $CO_2$-expanded ethanol was observed at a reduced $CO_2$ density of about 0.4 at all temperatures investigated. Furthermore, the curves intersected at $\rho_{CO2}^{R}$ = 0.6, where the density of the $CO_2$-expanded ethanol reached a value close to $\rho_{EtOH}^{0}$.

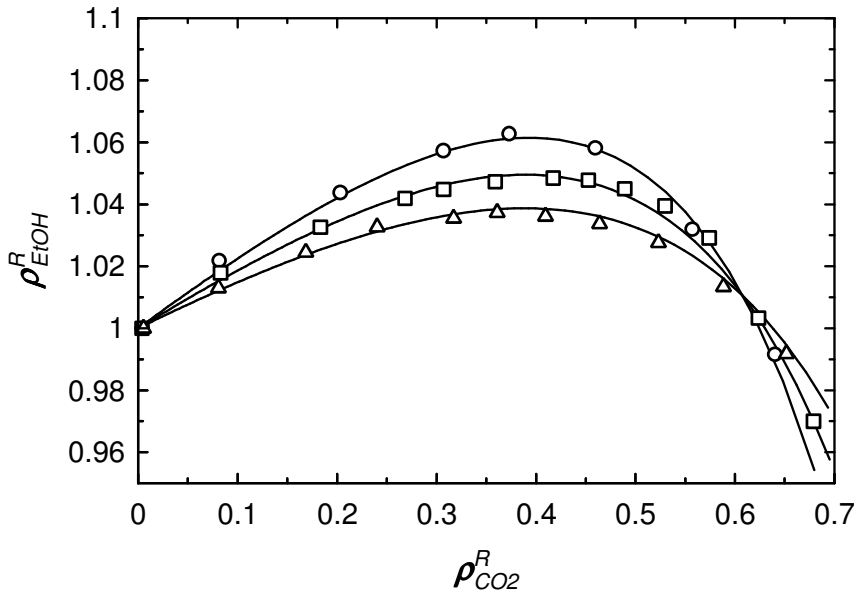


**Figure 5-4.** Relative density of saturated $CO_2$-expanded ethanol ( $\rho^R_{EtOH}$ ) versus reduced density of $CO_2$ ( $\rho^R_{CO2}$ ) from this study at various temperatures: ○, 40°C; □, 55°C; △, 70°C. Lines were calculated using (Eq. 5-10).

Due to the striking relationship between the reduced density of $CO_2$ ( $\rho^R_{CO2}$ ) and the reduced density of $CO_2$-expanded ethanol ( $\rho^R_{EtOH}$ ) the following correlation was developed:

$$\rho^R_{EtOH} = \frac{1 + h_1(T) \cdot \rho^R_{CO2}}{1 + h_2(T) \cdot \rho^R_{CO2} + h_3(T) \cdot \left(\rho^R_{CO2}\right)^2} \tag{5-10}$$

with the temperature dependent parameters $h_i(T)$, with $i$ = 1 to 3 being defined as:

$$h_i(T) = B_i + C_i \cdot T \tag{5-11}$$

using the temperature $T$ in K and the parameters $B_i$ and $C_i$ listed in Table 5-4.

**Table 5-4.** Parameters for the correlation given in Eq. (5-10).

| $i$ | $B_i$ | $C_i$ |
|---|---|---|
| 1 | -2.2890 | $3.9840 \times 10^{-3}$ |
| 2 | -3.3291 | $6.5564 \times 10^{-3}$ |
| 3 | 1.7185 | $-4.2896 \times 10^{-3}$ |

With this correlation (Eq. 5-10) the density of $CO_2$-expanded ethanol ( $\rho_{EtOH}^{CX}$ ) can be calculated up to pressures corresponding to a reduced $CO_2$ density of $\rho_{CO2}^{R}$ = 0.7. The deviations between the calculated values for density of $CO_2$-expanded ethanol obtained by using Eq. (5-10) together with experimental values for ( $\rho_{EtOH}^{0}$ ) listed in Table 5-1 and the experimental values listed in Table 5-2 are illustrated in Fig. 5-5. The deviations are less than about 0.5% over the entire pressure range for which $\rho_{CO2}^{R}$ < 0.7. The performance of this correlation is superior to that given in Eq. (5-2). However, it requires the calculation of $\rho_{CO2}^{R}$ using the Span and Wagner EoS [12].

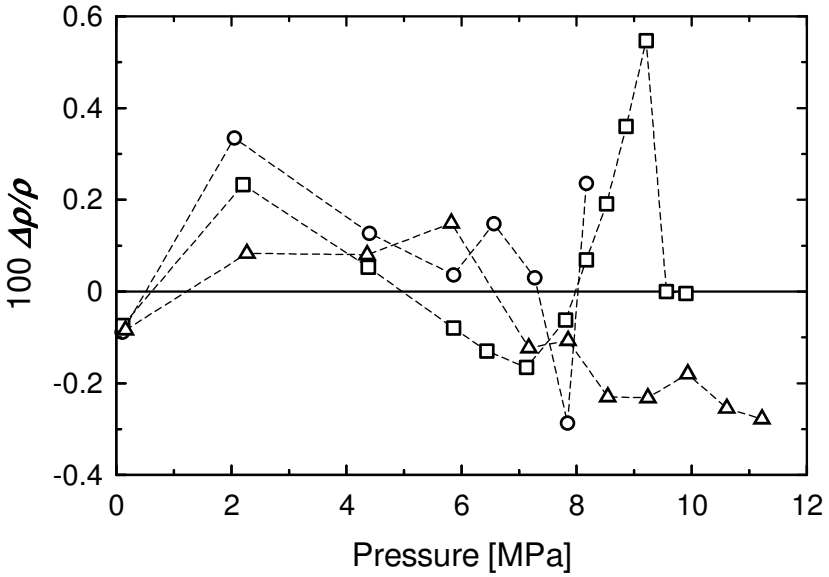


**Figure 5-5.** Deviation $\Delta\rho/\rho = (\rho_{exp} - \rho_{calc}) / \rho_{calc}$ between the experimental density values found in this study and calculated density values obtained by using Eq. (5-10) for $CO_2$-expanded ethanol at various temperatures: ○, 40°C; □, 55°C; △, 70°C.

The correlation (Eq. 5-10) was also tested against literature data [2, 6, 7] at temperatures of 20, 35, 40 and 55°C. For this purpose, the density of ethanol at atmospheric pressure $\rho_{EtOH}^{0}$ was first calculated using Eq. (5-1) at 20, 35, 40 and 55°C. Then, the reduced density of $CO_2$ ( $\rho_{CO2}^{R}$ ) was computed at those pressure

and temperature conditions of 20, 35, 40 and 55°C for which densities of $CO_2$-expanded ethanol were reported in Refs. [2, 6, 7] using the Span and Wagner EoS [12]. Finally, the density of $CO_2$-expanded ethanol was calculated using Eq. (5-10) with values of $\rho_{EtOH}^{0}$ obtained from Eq. (5-1) and compared to the density values reported in Refs. [2, 6, 7]. The results are plotted in Fig. 5-6, which shows that the correlation (Eq. 5-10 with Eq. 5-1) was able to predict the density of $CO_2$-expanded ethanol both inside and outside of the temperature range of this study quite well, with deviations of less than 1% up to the maximum density.

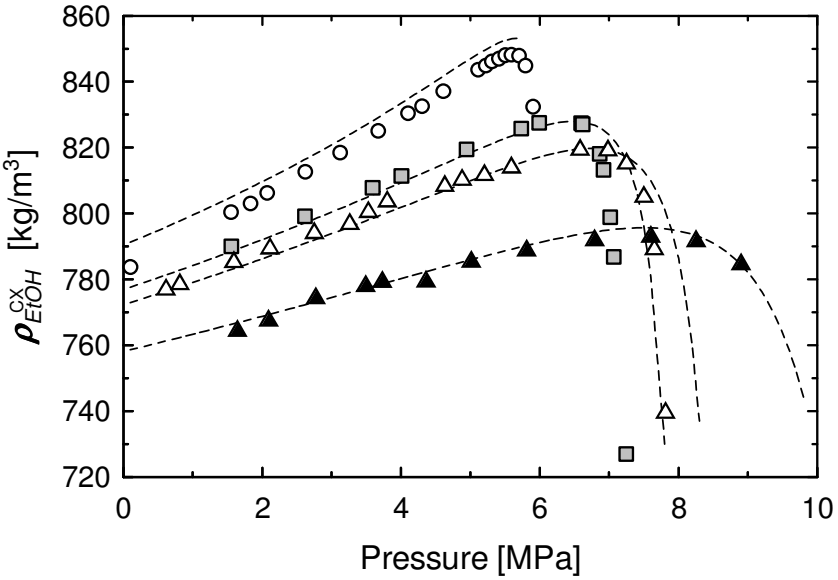


**Figure 5-6.** Comparison between the density values of $CO_2$-expanded ethanol ($\rho_{EtOH}^{CX}$) calculated using the correlation based on the reduced density of $CO_2$ (Eq. 5-10) and values available in the literature at various pressures and temperatures: ○, 20°C Ref. [2]; □, 35°C Ref. [7]; △, 40°C Ref. [6]; ▲, 55°C Ref. [6]. The dashed lines were calculated using Eqs. (5-1) and (5-10) to obtain $\rho_{EtOH}^{0}$ and $\rho_{EtOH}^{CX}$, respectively.

Furthermore, it is remarkable that the correlation based on the reduced density of $CO_2$ also predicted reasonably well the density of $CO_2$-expanded ethanol at temperatures below the critical temperature of $CO_2$ ($T_c$ = 31.1°C). However, as mentioned above the correlation (Eq. 5-10) should only be used up to a reduced $CO_2$ density of 0.7 ($\rho_{CO2}^{R}$ < 0.7), if the temperature is above the

critical temperature of $CO_2$ ($T > T_c$). However, if the temperature is below the critical temperature ($T < T_c$), the correlation works well only up to pressures where $CO_2$ is still in the form of vapor and not liquefied. For example, at 20°C the maximum density of $CO_2$-expanded ethanol could be calculated at a pressure of 5.7 MPa coinciding with the transition from vapor to liquid. At that point (20°C and 5.7 MPa ), the reduced density of $CO_2$ is close to 0.4, the same value as that found for temperatures above the critical temperature of $CO_2$. A further increase in pressure leads to the decrease in $CO_2$-expanded ethanol density as reported in Ref. [2]. At 20°C and 5.73 MPa, the vapor to liquid phase transition of $CO_2$ has occurred, leading to a liquid $CO_2$ density of 773.4 kg/m$^3$, which translates into a reduced density of $\rho_{CO2}^R = 1.6$. Therefore, the upper limit for the correlation (Eq. 5-10) was exceeded ( $\rho_{CO2}^R > 0.7$) and $CO_2$-expanded ethanol density could not be calculated beyond that pressure using Eq. (5-10). Nevertheless, as evidenced in Fig. 5-6, the correlation performed well up to the maximum density of $CO_2$-expanded ethanol at all temperatures. The deviations between the density values reported in Refs. [2, 6, 7] and the correlated values for $CO_2$-expanded ethanol using Eq. (5-10) and Eq. (5-1) to compute $\rho_{EtOH}^{CX}$ and $\rho_{EtOH}^{0}$, respectively, were generally less than 1% up to pressures corresponding to the maximum density. However, at pressures above the maximum density closer to the mixture critical point the deviations between the correlation (Eq. 5-10 with Eq. 5-1) and literature data were larger, which in the case of data from Ref. [7] at a temperature of 35°C reached up to 37% for pressures above 7 MPa. Moreover, the deviations may be attributed to the larger variability in the available experimental values in the pressure region close to the mixture critical point potentially due to the increased pressure sensitivity for the density of $CO_2$-expanded ethanol.

## 5.4 Conclusions

The density of saturated $CO_2$-expanded ethanol ( $\rho_{EtOH}^{CX}$ ) was measured in triplicate along isotherms at 40, 55 and 70°C and pressures up to the mixture critical point using a spring balance equipped with a glass sinker. The density was first

correlated to pressure and temperature using an empirical equation, which described $\rho_{EtOH}^{CX}$ well within the temperature limits of this study and up to pressures in the vicinity of the mixture critical point. Furthermore, a novel correlation was presented based on the reduced density of $CO_2$ ($\rho_{CO2}^{R}$) and temperature. The correlation based on reduced $CO_2$ density, along with correlations from literature for the density of ethanol at atmospheric conditions, can be used to calculate the density of saturated $CO_2$-expanded ethanol satisfactorily up to a reduced $CO_2$ density of about 0.7 ($\rho_{CO2}^{R} < 0.7$). Furthermore, it was shown that the correlation based on $\rho_{CO2}^{R}$ was able to predict the density of $CO_2$-expanded ethanol outside of the temperature range of this study as well. Even at temperatures below the critical temperature of $CO_2$ ($T < T_c$= 31.1°C) the correlation performed reasonably well up to the maximum density of $CO_2$-expanded ethanol with deviations of less than 1%. At all temperatures investigated and at those evaluated outside of the temperature range of this study, the maximum density of $CO_2$-expanded ethanol was observed at a pressure corresponding to a reduced $CO_2$ density of about 0.4 ($\rho_{CO2}^{R}$ =0.4).

## 5.5 References


1. P.G. Jessop, B. Subramaniam, Gas-expanded liquids. Chem. Rev. 107 (2007) 2666-2694.

2. A. Kordikowski, A.P. Schenk, R.M. Van Nielen, C.J. Peters, Volume expansions and vapor-liquid equilibria of binary mixtures of a variety of polar solvents and certain near-critical solvents. J. Supercrit. Fluids 8 (1995) 205-216.

3. C.Y. Day, C.J. Chang, C.Y. Chen, Phase equilibrium of ethanol plus $CO_2$ and acetone plus $CO_2$ at elevated pressures. J. Chem. Eng. Data 41 (1996) 839-843.

4. C.M.J. Chang, K.L. Chiu, C.Y. Day, A new apparatus for the determination of P-x-y diagrams and Henry's constants in high pressure alcohols with critical carbon dioxide. J. Supercrit. Fluids 12 (1998) 223-237.

5. D. Dittmar, S.B. Oei, R. Eggers, Interfacial tension and density of ethanol in contact with carbon dioxide. Chem. Eng. Technol. 25 (2002) 23-27.

6. I. Tsivintzelis, D. Missopolinou, K. Kalogiannis, C. Panayiotou, Phase compositions and saturated densities for the binary systems of carbon dioxide with ethanol and dichloromethane. Fluid Phase Equil. 224 (2004) 89-96.

7. H. Tanaka, M. Kato, Vapor-liquid-equilibrium properties of carbon-dioxide plus ethanol mixture at high-pressures. J. Chem. Eng. Japan 28 (1995) 263-266.

8. M. Stievano, N. Elvassore, High-pressure density and vapor-liquid equilibrium for the binary systems carbon dioxide-ethanol, carbon dioxide-acetone and carbon dioxide-dichloromethane. J. Supercrit. Fluids 33 (2005) 7-14.

9. M. Kato, D. Kodama, T. Ono, M. Kokubo, Volumetric properties of carbon dioxide + ethanol at 313.15 K. J Chem. Eng. Data 54 (2009) 2953-2956.

10. C. Secuianu, V. Feroiu, D. Geana, Phase behavior for carbon dioxide plus ethanol system: Experimental measurements and modeling with a cubic equation of state. J. Supercrit. Fluids 47 (2008) 109-116.

11. B. Seifried, F. Temelli, Density of marine lipids in equilibrium with carbon dioxide. J. Supercrit. Fluids 50 (2009) 97-104.

12. R. Span, W. Wagner, A new equation of state for carbon dioxide covering the fluid region from the triple-point temperature to 1100 K at pressures up to 800 MPa. J. Phys. Chem. Ref. Data 25 (1996) 1509-1596.

13. D.R. Lide, CRC Handbook of Chemistry and Physics. 89$^{th}$ ed. 2008, Boca Raton, FL; London: CRC Press.

14. R.H. Perry, D.W. Green, J.O. Maloney, Perry's Chemical Engineers' Handbook. 7$^{th}$ ed. McGraw-Hill chemical engineering series. 1997, New York: McGraw-Hill.

15. P. Sauermann, K. Holzapfel, J. Oprzynski, F. Kohler, W. Poot, T.W. de Loos, The pρT properties of ethanol + hexane. Fluid Phase Equil. 112 (1995) 249-272.

16. C.K. Zeberg-Mikkelsen, L. Lugo, J. Garcia, J. Fernandez, Volumetric properties under pressure for the binary system ethanol + toluene. Fluid Phase Equil. 235 (2005) 139-151.

17. D. Pecar, V. Dolecek, Volumetric properties of ethanol-water mixtures under high temperatures and pressures. Fluid Phase Equil. 230 (2005) 36-44.

18. Y. Takiguchi, M. Uematsu, Densities for liquid ethanol in the temperature range from 310 K to 480 K at pressures up to 200 MPa. J. Chem. Thermodyn. 28 (1996) 7-16.

19. T.F. Sun, J.A. Schouten, N.J. Trappeniers, S.N. Biswas, Measurements of the densities of liquid benzene, cyclohexane, methanol, and ethanol as functions of temperature at 0.1 MPa. J. Chem. Thermodyn. 20 (1988) 1089-1096.

20. S.N. Joung, C.W. Yoo, H.Y. Shin, S.Y. Kim, K.-P. Yoo, C.S. Lee, W.S. Huh, Measurements and correlation of high-pressure VLE of binary $CO_2$-alcohol systems (methanol, ethanol, 2-methoxyethanol and 2-ethoxyethanol). Fluid Phase Equil. 185 (2001) 219-230.

21. W. Duschek, R. Kleinrahm, W. Wagner, Measurement and correlation of the (pressure, density, temperature) relation of carbon dioxide. II. Saturated-liquid and saturated-vapour densities and the vapour pressure along the entire coexistence curve. J. Chem. Thermodyn. 22 (1990) 841-864.

# 6 Interfacial Tension of Fish Oil Triglycerides in Contact with Gas-Expanded Ethanol Part 1: Measurement and Correlation[1]

## 6.1 Introduction

The use of organic solvents has been restricted in many areas of the food industry due to the associated environmental and health concerns. The total emissions of non-methane volatile organic compounds (VOC) from anthropogenic sources in the European Community, the United States and the world are estimated at about 9, 15 and 60-140 million metric tons per year, respectively [1-3]. Approximately 40% of the VOC emissions has been attributed to solvent usage and industrial processes [2]. Many organic solvents are carcinogenic [4, 5] and when released into the atmosphere can additionally lead to the formation of organic peroxy radicals and ozone [3], thereby contributing to adverse health effects, such as increased cancer and asthma rates [6]. Thus, there is a need to reduce and minimize the usage of solvents and their release into the environment.

Gas-expanded liquids (GXL) have attracted considerable attention in recent years due to their potential as 'green solvents' and unique properties, which have been discussed in Section 2.2.5 [7]. Due to the safety and environmental advantages of $CO_2$ the most common GXL are the so-called $CO_2$-expanded liquids (CXL), which combine the beneficial properties of compressed $CO_2$ and conventional solvents. Lipids such as vegetable and marine oils can also be expanded with $CO_2$, which affects their properties [8]. It has been shown that the viscosity of acetone, methanol, ethanol and lipids can be substantially reduced by dissolution of pressurized $CO_2$ [9-12]. Furthermore, even though the liquid phase is expanded by dissolution of $CO_2$, the density of CXL increases with increasing $CO_2$ content, as demonstrated for CX lipids [8, 13, 14]. In the case of ethanol, the density increases to a maximum at moderate pressure levels in the range between 6 to 10 MPa [15-17] and then decreases substantially just before the mixture

[1] A version of this chapter has been submitted to J. Supercrit. Fluids (2010) for consideration for publication.

critical point is reached.

The interfacial properties such as interfacial tension (IFT) of liquids in contact with pressurized $CO_2$ have been investigated as well. For example, triglycerides, ethanol and water exhibit a substantial decrease of IFT with pressure [18-25]. Due to its importance for enhanced oil recovery IFT has been studied extensively for systems containing hydrocarbons+$CO_2$ [26-30] as well as for $CO_2$ injected crude oil+reservoir water [31], showing a decrease in IFT with increasing $CO_2$ pressure. As well, the wetting characteristics and contact angle for liquids equilibrated with $CO_2$ in contact with a packing material such as steel, glass and teflon® have been investigated for several systems, including water, lipids and ethanol [32-34]. In aqueous systems, the contact angle increased with $CO_2$ pressure, thereby reducing wettability and thus affecting mass transfer area and efficiency of packing material in separation processes [35-37]. Dickson *et al.* [34] measured the wetting angle of water on two glass substrates with different hydrophilicities in a high pressure $CO_2$ atmosphere at 23°C, showing that the wetting angle increased substantially as the pressure was increased to the vapor pressure of $CO_2$ (6.1 MPa). However, in the case of triglycerides and steel, the contact angle decreased leading to improved wettability at elevated pressures [38]. Jaeger and Eggers [39] studied IFT of corn oil in contact with water using the pendant drop method up to very high pressures of 250 MPa finding that IFT of the corn oil+water system increased slightly with pressure. However, when $CO_2$ was introduced into the corn oil prior to drop formation the IFT was reduced to about 20% of that observed for the pure system [39]. The authors [39] also found that at such high pressures the density of corn oil presaturated with $CO_2$ was higher than that of water. As well, the onset of pressure-induced crystallization of corn oil was observed at lower pressures in the presence of $CO_2$ [39]. Wiegand and Franck [40] determined IFT between water and non-polar fluids such as helium, neon, argon, nitrogen, methane, propane, n-hexane, n-decane, and toluene up to high temperatures and pressures of 280 MPa. IFT was found to increase with pressure for the water+hydrocarbon systems, whereas it decreased with pressure and passed through a flat minimum around 100 MPa for water+gas

systems except for the system water+helium for which IFT increased continuously with pressure [40].

The IFT and interfacial phenomena for lipids in contact with CXL have not been reported. Therefore, the objective of this study was to measure the IFT of fish oil TG in contact with CX EtOH at 40, 55, and 70°C using the pendant drop method at pressures of up to about 6 MPa and to correlate the data to pressure and temperature. Additionally, the influence of the molar fraction of $CO_2$ ($x_{CO2}$) in CX EtOH on IFT of fish oil TG was assessed by using the literature data for $x_{CO2}$. As well, the impact of interfacial turbulence and diffusion of EtOH into the drop upon change of IFT over time during drop formation and aging of a drop of fish oil TG in contact with CX EtOH are discussed.

## 6.2 Experimental

### 6.2.1 Materials

Refined fish oil extracted from anchovy and sardine was obtained from Ocean Nutrition Canada (ONC, Halifax, NS, Canada) in the form of triglycerides (TG) and fatty acid ethyl esters (FAEE), as described in Section 3.2.1. As stated by the manufacturer, the oils contain about 8 mg/g of antioxidants, including a mix of natural tocopherols and citric acid. All other material specifications and handling protocols were similar to those described in Section 3.2.1. Food grade anhydrous ethanol (Commercial Alcohol, Winnipeg, MB, Canada) with a stated purity and water content of 99.99% and 0.008% by volume, respectively, was used without further purification for IFT measurements.

### 6.2.2 Interfacial tension measurements

#### 6.2.2.1 Apparatus to determine interfacial tension

The apparatus used to determine the IFT of fish oil in contact with CX EtOH under high pressure conditions according to the pendant drop method consisted of a 200 mL high-pressure view cell with an internal diameter of 40 mm (Nova-Swiss, Effretikon, Switzerland) equipped with electric heaters and placed in a

temperature controlled insulated air bath (Fig. 6-1). The apparatus has been described in more detail in Section 4.2.3.1 [18]. However, the apparatus was modified as follows to allow determination of ultra low interfacial tension of TG in contact with CX EtOH. A custom made circulation pump (D) described in the Appendix was added to the setup to accelerate saturation and equilibration of EtOH with $CO_2$ [41]. Furthermore, the custom made capillary (K) to generate and hold the pendant drops consisted of a deactivated fused silica tubing (Dionex Inc., Sunnyvale, CA, USA) with an ID of 100 µm.

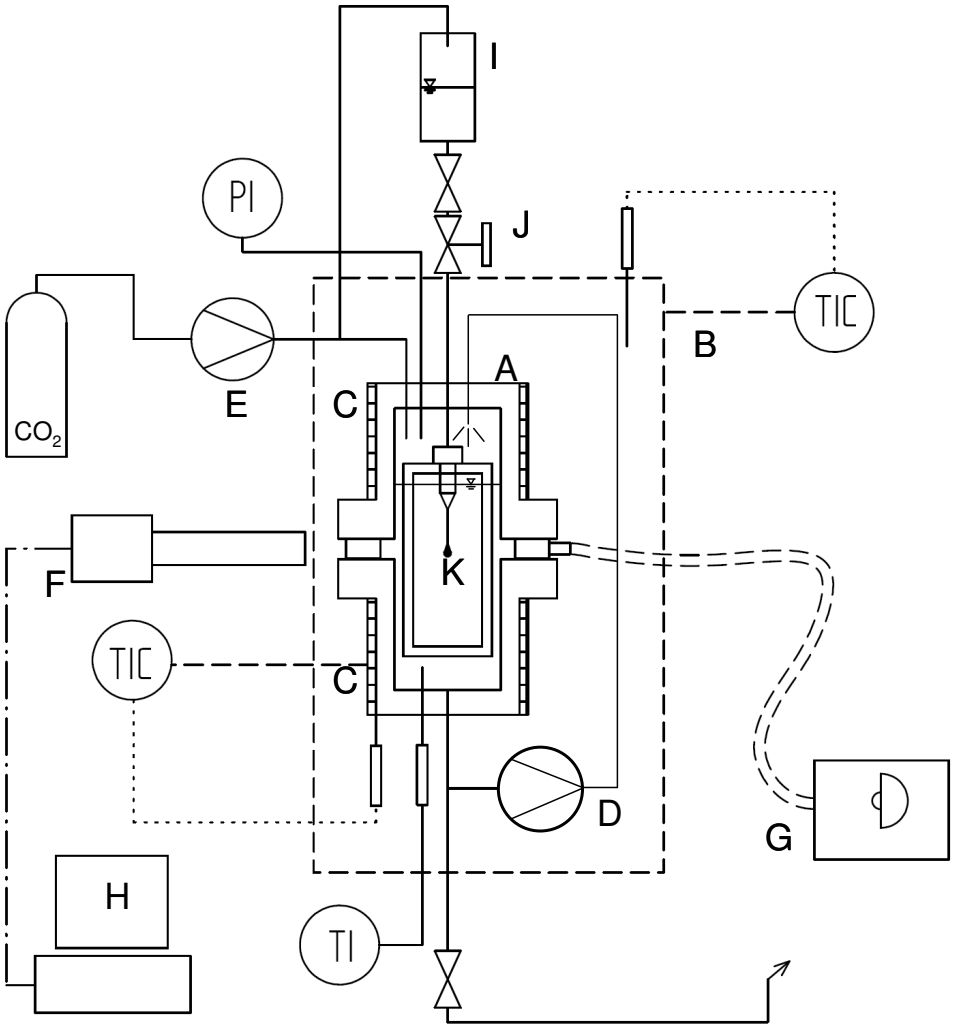


**Figure 6-1.** Apparatus used for measuring interfacial tension: A) view cell, B) temperature controlled air bath, C) electric heaters, D) circulating pump, E) syringe pump, F) CMOS camera, G) light source, H) personal computer, I) oil reservoir, J) micrometering valve, K) capillary.

The silica tubing was originally coated on the outside with a thin polymer layer (polyimide), which was removed by scorching the capillary for a few seconds in the flame of a bunsen burner. Thus, the polymer layer was removed rendering the capillary with an OD of 175 μm. The silica capillary was inserted into a thin walled stainless steel dispensing needle having a luer lock connector (Type 304 SS dispensing needle 26 Gauge, McMaster-Carr, Atlanta, GA, USA). The capillary extending out of the dispensing needle was sealed and held in place using a teflon® tape as compression packing against a luer lock fitting. The luer lock fitting with the silica capillary was held in place by means of a stainless steel frame located inside the view cell. The capillary was connected to the top reservoir (I) (60 mL) by means of a tubing equipped with a needle valve and a micrometering valve (J), which were used to generate drops. The temperature control, syringe pump and optical measurement system were described in detail previously (Section 4.2.3.1).

#### 6.2.2.2 Calibration and performance

In order to calibrate the software to quantify the IFT the magnification of the images is required. Thus, to assess the magnification of the optical system and to calibrate the software the ID of the silica capillary was used as a reference, which was 100 μm as stated by the manufacturer (Dionex Inc., Sunnyvale, CA, USA). Once the optical system was calibrated the OD of the capillary (polyimide coating removed) was ascertained to be 175 μm using the microscopic lens. The performance of the system using the silica capillary was verified by measuring the IFT of anhydrous EtOH in contact with air at atmospheric pressure and 25°C. The IFT of EtOH deviated by 1.5% from literature data [42], which is considered acceptable taking into account the differences in EtOH purity. Furthermore, IFT of fish oil in contact with $CO_2$ was measured at 40°C and atmospheric pressure using the silica capillary and compared to that found in the previous study reported in Chapter 4 [18] obtained by using a stainless steel capillary with an OD of 0.902 mm. The values of IFT for fish oil TG using the steel capillary and the silica capillary differed by less than 0.25%. For the subsequent measurements at

elevated $CO_2$ pressures the densities for both CX EtOH and the fish oil in equilibrium with $CO_2$ (CX TG) are required in order to evaluate the IFT, which were determined in previous studies reported in Chapters 5 and 3, respectively [8, 15].

#### 6.2.2.3 Determination of IFT

The IFT of fish oil TG in contact with CX EtOH was determined at temperatures of 40, 55 and 70ºC and pressures ranging from 0.1 to about 6 MPa. Triplicate measurements were carried out for all isotherms. Since IFT measurements are very sensitive to contamination, the capillary and all wetted parts were cleaned prior to each experiment. Thus, the apparatus was thoroughly cleaned by circulating anhydrous EtOH+SC-$CO_2$ at 25 MPa and experimental temperature inside the view cell for several hours. Then, the apparatus was flushed with pure SC-$CO_2$ at 25 MPa and experimental temperature to remove any residual fish oil, EtOH and air from inside the apparatus. The top reservoir, which had been flushed and dried with $CO_2$ as well to remove EtOH, was then filled with approximately 10 mL of fish oil and then connected to the $CO_2$ inlet line. In order to avoid deterioration of fish oil TG, they were stored at 4ºC in aluminum bottles with nitrogen-filled headspace. The bottles were warmed up slowly to room temperature before taking a sample to avoid crystallization and precipitation of fish oil components. After filling the top reservoir (I) with fish oil, the tubing connecting to the capillary tip was flushed with fish oil by fully opening both valves installed below the reservoir for a few seconds releasing several drops. Thereby, the tubing connecting the reservoir to the capillary tip as well as both valves were rinsed and filled completely with fish oil. After that, the needle valve above the micrometering valve (J) was closed, while keeping the micrometering valve fully open to be used later for generating drops. The view cell was then filled with EtOH up to a level just above the window ensuring that the capillary tip was well submersed in liquid and that there was enough headspace for EtOH to expand. Then, the system was kept at atmospheric pressure and EtOH was

circulated from the bottom to the top of the view cell using the circulation pump while equilibrating and warming the system up to the desired temperature.

The system was equilibrated for at least 1 h at each experimental condition before the IFT was measured, by generating pendant drops at the tip of the capillary using the micrometering valve. The knob of the micrometering valve was turned clockwise in small steps. Thus, the needle of the micrometering valve displaced a small amount of liquid inside the valve body, thereby pressing liquid out of the capillary forming a pendant drop at the capillary tip. Before each IFT measurement, several drops were generated and allowed to drip from the capillary, so that fresh TG was exposed to CX EtOH. Since EtOH expands substantially when equilibrated with pressurized $CO_2$ [16], excess EtOH was removed from the bottom of the view cell after each pressure increase to maintain the liquid level just above the window and to ensure that the EtOH could expand unrestricted during equilibration in the view cell.

The IFT isotherms of fish oil TG in contact with CX EtOH reported in this study were determined by analyzing the images of freshly formed pendant drops taken about 5 s after formation as soon as the drop was stable and turbulence at the interface had vanished. While taking images for IFT measurements, both the fan of the circulating air bath as well as the circulation pump were switched off shortly before and during the formation of a pendant drop to avoid any vibration in the system, which could cause the drop to oscillate or fall leading to incorrect results. For each replication and at each temperature and pressure setting, the images of at least 3 freshly formed pendant drops were analyzed and the mean IFT values calculated. After recording the images, the pressure of the system was increased to the next desired level by injecting $CO_2$ using the syringe pump. CX EtOH was circulated and allowed to equilibrate with $CO_2$ for at least 1 h at each pressure setting. During equilibration, small amounts of EtOH were removed from the bottom of the view cell to keep the level of EtOH at a fairly constant level just above the window until equilibrium was reached. Once equilibrium was reached, the expansion of EtOH came to a halt and the liquid level did not change further. Then, drops were generated again and analyzed as described above. For

all isotherms, the pressure was increased stepwise starting from atmospheric pressure up to about 6 MPa until the IFT reached ultra low levels and eventually vanished. Throughout the entire measurement period the temperature and pressure of the CX EtOH phase inside the view cell was monitored continuously.

The images of the pendant drops were analyzed using the ADSA software to obtain the IFT. The density of CX EtOH determined previously in Chapter 5 [15] was used for the surrounding continuous fluid phase in all measurements. The influence of dissolved oil on the density of the CX EtOH phase was considered negligible since only a very small amount was released from the capillary during an experiment. With the volume of a pendant drop generally being <0.25 μL in this study and taking into account that at most about 200 drops were formed throughout one experimental run the accumulation of fish oil inside the view cell was less than 0.05% of the total volume of CX EtOH (about 100 mL). In order to evaluate the IFT, the density of the fish oil forming the drops is required as well. As discussed in more detail below, the density of the drop was assumed to be that of fish oil saturated with $CO_2$, which has been determined previously [8].

## 6.3 Results and discussion

### 6.3.1 IFT versus pressure and $x_{CO2}$

The isotherms showing IFT of fish oil TG in contact with CX EtOH versus pressure at 40, 55, and 70°C are presented in Table 6-1 and illustrated in Fig. 6-2. The IFT decreased fairly linearly with pressure at 40 and 55°C, with a steeper slope at 40°C. At 40°C, the IFT decreased from about 0.68 mN/m at atmospheric pressure to ultra low levels of <0.005 mN/m with an increase in $CO_2$ pressure from 0.1 to 6.0 MPa. At 55°C, the IFT decreased from an initial value of about 0.26 mN/m to ultra low levels upon increasing the $CO_2$ pressure from atmospheric pressure to about 4.3 MPa, respectively. At 70°C, ultra low levels of IFT were observed at atmospheric pressure conditions, which can be attributed to the greatly enhanced mutual solubility between anhydrous EtOH and triglycerides at

that temperature [43]. Therefore, at 70°C, applying higher $CO_2$ pressure rendered generation and holding of pendant drops impossible due to the vanishing IFT.

**Table 6-1.** IFT of fish oil in contact with CX EtOH at 40, 55, and 70°C.

| T [°C] | $P_{CO2}$ [MPa] | IFT[a] [mN/m] |
|---|---|---|
| 40 | 0.12 | 0.677±0.081 |
| | 1.54 | 0.526±0.057 |
| | 2.92 | 0.359±0.033 |
| | 3.63 | 0.246±0.004 |
| | 4.31 | 0.186±0.032 |
| | 5.03 | 0.109±0.017 |
| | 5.69 | 0.047±0.016 |
| | 5.98 | 0.018±0.007 |
| 55 | 0.14 | 0.259±0.020 |
| | 1.51 | 0.154±0.049 |
| | 2.88 | 0.076±0.051 |
| | 4.27 | 0.008±0.001 |
| 70 | 0.19 | 0.005±0.002 |

[a] Mean±standard deviation based on triplicate determinations with (at least 3 freshly formed drops per replication).

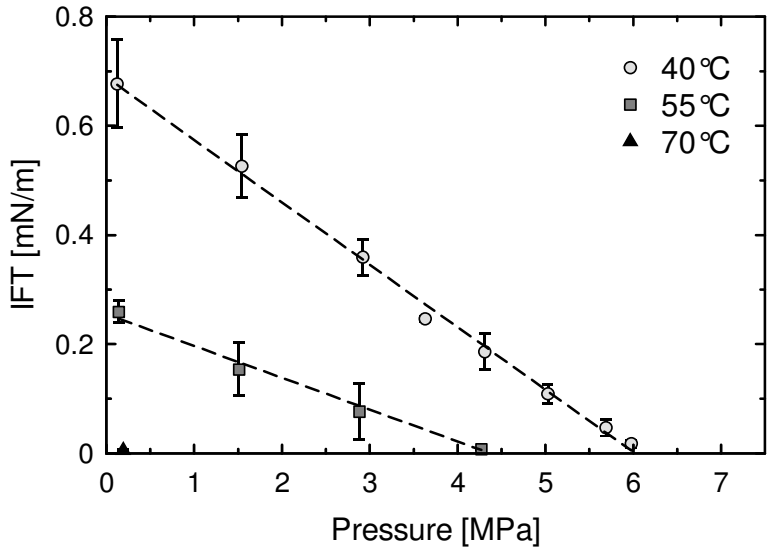


**Figure 6-2.** IFT of fish oil TG in contact with CX EtOH at 40, 55, and 70°C versus $CO_2$ saturation pressure. The lines were calculated using Eq (1). Error bars represent standard deviation for triplicate measurements (at least 3 drops per replication).

The isotherms of IFT versus $CO_2$ mole fraction ($x_{CO2}$) in CX EtOH at 40 and 55°C are illustrated in Fig. 6-3, which was generated by adopting literature data for $x_{CO2}$ reported by Tsivintzelis *et al.* [17], who studied the phase equilibrium of the system $CO_2$+EtOH at pressures ranging from 1.6 to 9.4 MPa. Analyzing their composition data [17] revealed a fairly linear relationship between pressure and $x_{CO2}$ in the liquid EtOH phase up to about 4.5 MPa at 40 and 55°C. Therefore, in order to estimate the concentration of $CO_2$ in CX EtOH ($x_{CO2}$) for pressures between 0.1 and 1.6 MPa, $x_{CO2}$ was obtained by linear extrapolation using the available data up to 4.5 MPa [17]. It should be noted however, that at 40°C and pressures above 5 MPa a marked increase in $CO_2$ concentration with pressure was observed [17].

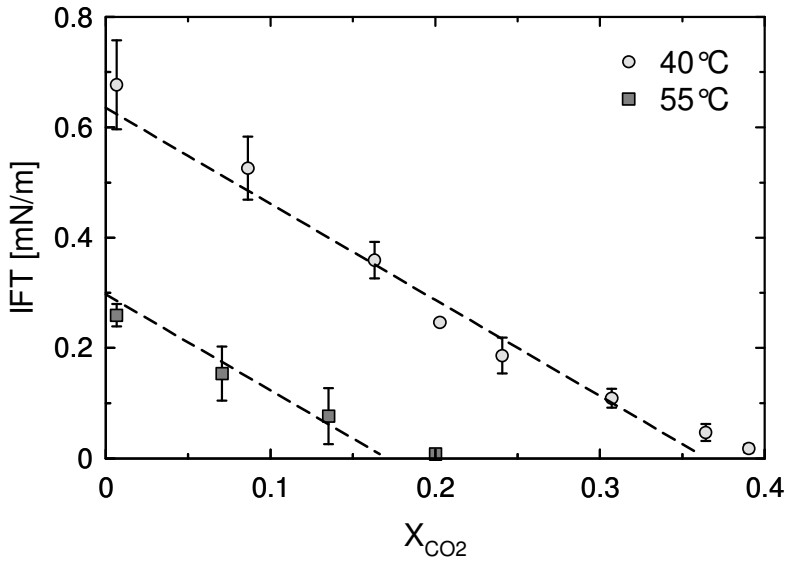


**Figure 6-3.** IFT of fish oil TG in contact with CX EtOH at 40 and 55°C versus molar fraction of $CO_2$ in EtOH ($x_{CO2}$). Mol fraction data adapted from [17]. The lines were calculated using Eq (4) using the slope K'= 1.75 mN/m/$x_{CO2}$. Error bars represent standard deviation for triplicate measurements (at least 3 freshly formed drops per replication).

It is noteworthy that a further increase in pressure causes a very pronounced increase in $x_{CO2}$ ultimately leading to a very large volumetric expansion of CX EtOH [16] upon approaching the mixture critical point (MCP) [44]. However, the IFT of fish oil TG in contact with CX EtOH reached ultra low levels at about 6 and 4.3 MPa at 40 and 55°C, respectively, which is far below the reported MCP of the system $CO_2$+EtOH [44] especially at the higher temperatures. Thus, reaching the MCP of $CO_2$+EtOH appears not to be a requirement to obtain ultra low or vanishing IFT for TG in contact with CX EtOH.

Mutual solubility between TG and CX EtOH as affected by temperature and $x_{CO2}$ seems to contribute to ultra low IFT. The temperature dependent linear trend for IFT versus pressure observed in Fig. 6-2, where at 40°C the IFT decreased at a more pronounced rate with pressure than at 55°C, is in agreement with the trends of $x_{CO2}$ versus pressure observed for the phase equilibrium data reported by Tsivintzelis *et al.* [17]. Furthermore, at both temperatures the IFT

decreased with $x_{CO2}$ in a fairly linear manner until ultra low levels of IFT were reached at $x_{CO2}$ of about 0.4 and 0.2 at 40 and 55°C, respectively. For both isotherms, the rate of IFT decrease with $x_{CO2}$ was practically the same, as indicated by the dashed lines in Fig. 6-3. Thus, the temperature mainly affected the initial IFT of TG in contact with CX EtOH at atmospheric pressure, whereas the slope of IFT versus $x_{CO2}$ plot appeared to be rather independent of temperature. To summarize, the decrease of IFT with pressure appears to be mainly caused by the increase in $x_{CO2}$ in CX EtOH, which is also linked to substantial volumetric expansion of CX EtOH [16], enhanced mutual solubility of triglycerides and CX EtOH [45] and change in solvent polarity [46], thereby affecting the intermolecular forces at the interface causing a decrease in IFT.

### 6.3.2 Correlation of IFT to pressure, temperature and $x_{CO2}$

The IFT ($\gamma_{TG}$, mN/m) of fish oil TG in contact with CX EtOH was correlated to pressure ($P$, MPa) and temperature ($T$, °C) by using the following empirical correlation:

$$\gamma_{TG}(P,T) = \gamma_0(T) - K(T) \cdot (P - 0.1) \quad (6\text{-}1)$$

with the first term $\gamma_0(T)$ corresponding to the IFT of fish oil in contact with CX EtOH at atmospheric pressure (0.1 MPa) as a function of temperature. The second term accounts for the linear temperature-dependent decrease of IFT with pressure ($P$). $\gamma_0(T)$ is correlated to temperature using the following quadratic equation:

$$\gamma_0(T) = A_1 \cdot T^2 + A_2 \cdot T + A_3 \quad (6\text{-}2)$$

with the fitting parameters $A_1$, $A_2$, and $A_3$ being $4.0977 \times 10^{-4}$, $-6.7482 \times 10^{-2}$, 2.7211, respectively. The decrease of IFT with pressure is approximated by the linear term $K(T) \cdot (P-0.1)$ with the temperature dependent slope $K(T)$ calculated according to:

$$K(T) = \frac{A_4}{(T + 273.15)} + A_5 \quad (6\text{-}3)$$

with the fitting parameters $A_4$ and $A_5$ being $3.7029 \times 10^2$ and -1.0680, respectively. Since IFT was found to be closely related to $x_{CO2}$, Eq. (6-3) corresponds to the temperature dependence for the slope of $x_{CO2}$ versus pressure up to about 4.5

MPa. As well, Eq. (6-3) reflects the linear temperature dependence of the Henry's law constant for $CO_2$ in EtOH [47, 48].

As illustrated in Fig. 6-3, the isotherms for IFT of fish oil TG in contact with CX EtOH may also be readily correlated to $x_{CO2}$ in CX EtOH. Since, the IFT decreased with $x_{CO2}$ practically with the same slope at both 40 and 55°C, it may be approximated using a relationship in the form of:

$$\gamma_{TG}(T, x_{CO2}) = \gamma_0(T) - K' \cdot x_{CO2} \qquad (6\text{-}4)$$

where the slope *K'* was found to be 1.75 mN/m/$x_{CO2}$. Thus, since *K'* seems to be practically independent of temperature it may be sufficient for a given lipid+CX EtOH system to determine $\gamma_0(T)$ at atmospheric conditions over the temperature range of interest and the slope *K'* for just one isotherm by measuring IFT up to elevated pressures at a temperature for which $x_{CO2}$ data are available. Once *K'* is known at one temperature the isotherms for IFT versus $x_{CO2}$ at other temperatures could be readily predicted using Eq. (6-4). Furthermore, the isotherms obtained for IFT versus $x_{CO2}$ could be related to pressure using experimental $x_{CO2}$ data or an equation of state model [17, 47]. However, further research is required to substantiate this straightforward approach and to assess its applicability for TG in other CX solvent systems. In this context, Jaeger and Eggers [39] reported that the IFT of water in contact with corn oil containing $CO_2$ decreased with increasing $CO_2$ mass fraction in the oil. IFT was found to depend mainly on $CO_2$ concentration rather than pressure [39].

### 6.3.3 Change of IFT over time

During drop formation of fish oil TG in CX EtOH at all conditions studied strong interfacial turbulence was observed for up to a few seconds. During this time the interface appeared rough and very turbulent, as is shown for the drops at 0.1 MPa and 40°C (Fig. 6-4a) and 55°C (Fig. 6-4g). Then after a few seconds, the interfacial turbulence ceased and the drop interface became smooth and clear (Fig. 6-4b). Interfacial turbulence can be linked to mass transfer [49], which can be anticipated in both directions from the continuous CX EtOH phase into the TG drop phase and *vice versa* particularly at elevated pressures and temperatures.

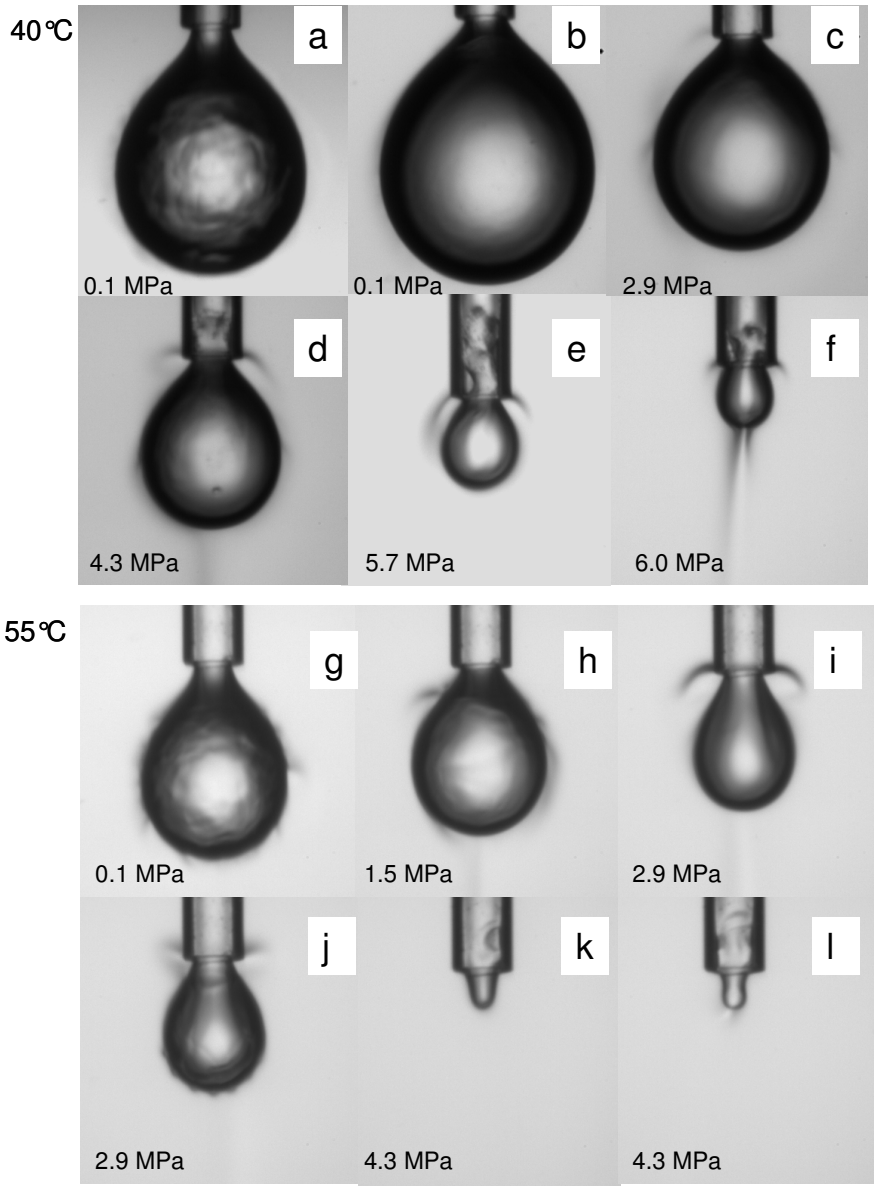


**Figure 6-4.** Images of pendant drops of fish oil TG in contact with CX EtOH at 40 and 55°C at various pressures.

Mass transfer can cause interfacial turbulence and Marangoni convection. Marangoni convection can be induced by solutal or thermal effects due to mass transfer at the interface that generate local gradients in IFT resulting in spontaneous convective motion [50]. It has been reported that mass transfer of acetone during formation of a drop of toluene in water in the system toluene+acetone+water [51] was greatly enhanced due to Marangoni effects,

which were stronger for the mass transfer from the continuous phase to drop phase during drop formation. In the case of fish oil TG exposed to CX EtOH, mass transfer from the drop to the continuous phase was evidenced by the schlieren visible around and under the drops (Fig. 6-4). Furthermore, at elevated pressure the shape of a pendant drop approached that of a sphere upon aging indicating a change in drop density caused by dissolution of EtOH into the drop, as shown in Fig. 6-5 for a drop aged up to 140 s at 40°C and 1.54 MPa. Mass transfer between CX EtOH and TG into or out of the drop could potentially lead to thermal effects as well because the dissolution of $CO_2$ into both TG and EtOH is exothermic under the conditions of this study [52-54]. Thermal effects in the system fish oil TG+CX EtOH could also contribute to local variations in IFT causing oscillations and turbulence; however, further research is required to prove that assumption.

In the system TG+CX EtOH, the value of IFT obtained by the ADSA software decreased to a minimum during drop formation until a smooth interface was visible, which took about 6 s for the drop shown in Fig. 6-5. The IFT of that drop in Fig. 6-5 was obtained by analyzing images of the pendant drop taken at 25 frames per second (fps) using the ADSA software. The IFT values reported in Table 6-1 were determined for freshly formed drops immediately after the surface seemed to become smooth, indicating equilibration of the interface. Up to equilibration of the interface, the impact of dissolved EtOH on the bulk density of the drop and thus IFT was considered negligible. However, further dissolution of EtOH into the drop caused the density of the drop to approach that of the surrounding continuous phase as evidenced by the spherical drop shape (Fig. 6-5) after a longer time. Concomitantly, as the real density of the drop decreased the values for IFT calculated by the software seemed to increase. However, this apparent increase in IFT is due to the fact that at each pressure and temperature condition, constant densities for both the continuous EtOH phase and fish oil TG drop phase were used in the ADSA software to calculate IFT. However, it can be assumed that over time the drop density was lowered by EtOH diffusion into the drop.

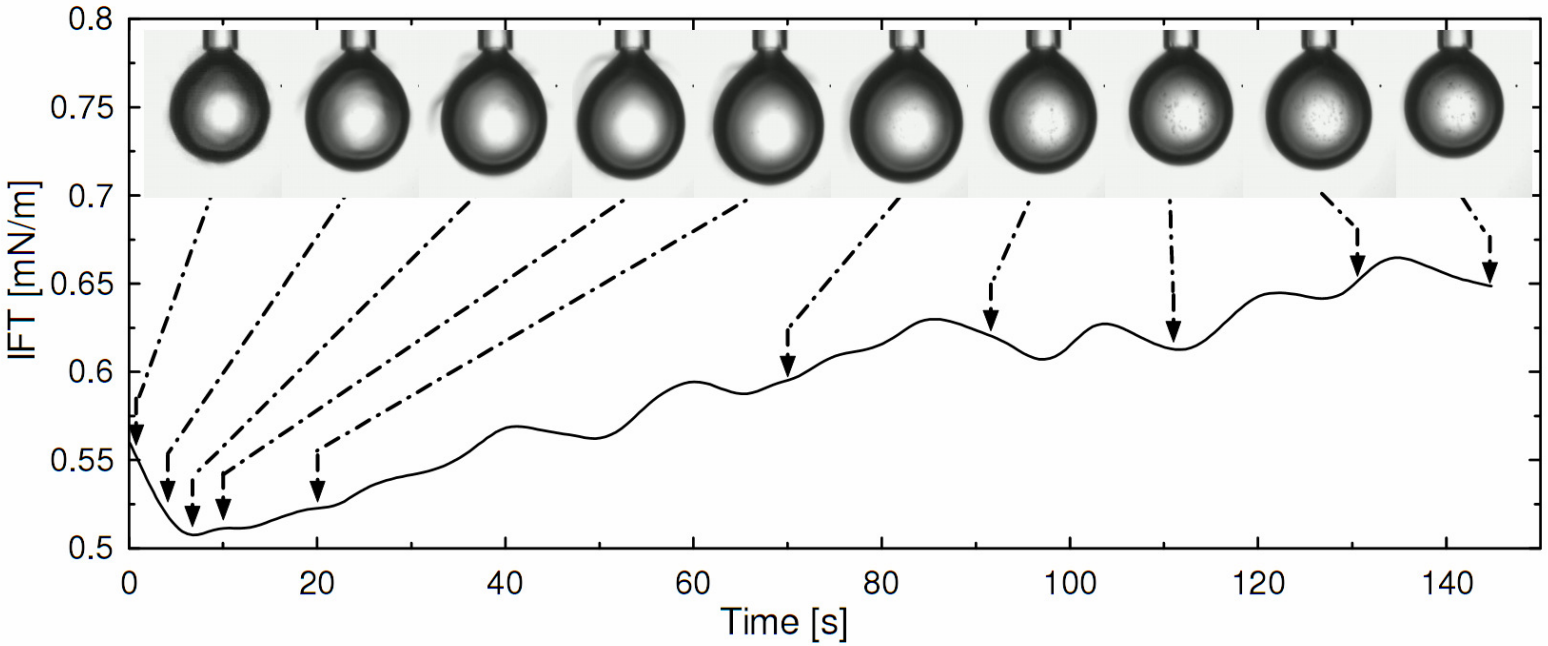


**Figure 6-5.** Values of IFT and images for a pendant drop of fish oil TG in contact with CX EtOH at 40°C and 1.54 MPa versus time showing an apparent increase in IFT caused by the change in drop density due to dissolution of EtOH into the drop. Fine gas bubbles are visible in the aged drop after 60 s.

As illustrated in Fig. 6-5, the drop equilibrated for up to about 140 s gradually assumed a spherical shape indicating that the density of the drop approached that of the surrounding CX EtOH phase, leading to nearly isopycnic conditions. At elevated pressures, this change in drop shape appeared to happen more rapidly due to faster mass transfer and the smaller droplet sizes under those conditions (Fig. 6-4). From the discussion above, it seems obvious that this increase in IFT is an artifact caused by the software using a constant density and does not reflect the IFT actually exerted at the interface. Nevertheless, Fig. 6-5 provides an estimate for the time scale required for EtOH to fully penetrate and equilibrate in the drop interface. Furthermore, after the interface appeared smooth and IFT reached an apparent minimum (at about 7 s) the effect of EtOH dissolving into the drop thereby lowering drop density became stronger as evidenced by the increasing trend for IFT (Fig. 6-5), which is caused by the change in drop density that is not being accounted for in the software calculations rather than by an actual increase in the IFT. Therefore, because IFT values reported in this study were evaluated as soon as interfacial turbulence ceased, the bulk density for the drop phase was assumed to be practically unaffected by EtOH dissolution up to that point. Thus, density of fish oil TG saturated with $CO_2$ was used in the calculations, which had been determined previously in Chapter 3 [8]. Furthermore, as EtOH dissolves into the oil drop, the solubility of $CO_2$ seems to be affected as evidenced by the formation of fine $CO_2$ bubbles inside the drop after about 60 s (Fig. 6-5). EtOH dissolves relatively large amounts of $CO_2$ at 40°C for pressures up to about 5 MPa reaching $CO_2$ mole fractions of $x_{CO2} > 0.25$ [17, 55]. However, under the same conditions the mole fraction of $CO_2$ in fish oil TG can reach much higher values of up to about $x_{CO2} > 0.75$ [56]. Therefore, when CX EtOH enters the TG drop, the solubility of $CO_2$ inside the drop may be substantially reduced leading to the formation of bubbles of $CO_2$.

As described above, the images for IFT measurements were taken as soon as the interfacial turbulence disappeared thus capturing the minimum IFT corresponding to the equilibrated interface. It seems reasonable to assume that up to that point, the bulk density of the drop was not substantially altered by the

EtOH diffusing into the drop, thereby justifying the assumption to use the density of CX EtOH and CX fish oil TG for IFT calculations. Preferably however, the density of the pendant drop should be determined *in situ* taking into account the mass transfer from the drop to the continuous phase and *vice versa* to accurately determine the IFT over time. Such an approach was presented by Arendt *et al.* [57] using a capillary connected to a magnetically coupled balance, which allowed determination of the mass and volume of the drop to assess density and mass transfer *in situ*. However, due to the very low IFT for the drops generated in this study, the drop diameters ranged from about 0.1 to 0.7 mm, which were much smaller than those studied by Arendt *et al.* (2.5 mm) [57]. Thus, it can be anticipated that it would be challenging to use a similar approach as described by Arendt *et al.* [57] for systems with extremely small drops due to very low IFT.

## 6.4 Conclusions

The IFT of fish oil in contact with CX EtOH was determined at pressures ranging from 0.1 to about 6 MPa at 40, 55, and 70°C. IFT decreased substantially with $CO_2$ pressure to ultra low levels. IFT was correlated to pressure and temperature using an empirical model describing the linear decrease with pressure depending on temperature, which agreed well with the experimental data. Furthermore, it was shown that IFT decreased linearly with increasing molar fraction of $CO_2$ in EtOH ($x_{CO2}$) having a slope practically independent of temperature. Interfacial turbulence was observed for up to several seconds for freshly formed drops in CX EtOH, which could be attributed to mass transfer between the drop and continuous phase. Intermolecular forces at the interface and therefore IFT are affected by pressure and temperature, while both influence the interfacial composition, mutual solubility and molar fraction of $CO_2$ in the drop and continuous phases. For lipid processing using gas-expanded liquids these findings could be beneficial for novel process development and in determination of optimum processing parameters, such as pressure and temperature.

## 6.5 References


1. K. Marečková, NEC Directive status report 2008; EEA Technical report No 11/2009. 2009, European Environment Agency (EEA): Copenhagen, Denmark.

2. US Environmental Protection Agency, National Emissions Inventory (NEI) Air Pollutant Emissions Trends Data: 1970 - 2008 Average annual emissions, all criteria pollutants in MS Excel. 2009, US EPA, http://www.epa.gov/ttn/chief/eiinformation.html (accessed on November 10th, 2009).

3. R. Atkinson, Atmospheric chemistry of VOCs and NO(x). Atmos. Environ. 34 (2000) 2063-2101.

4. P. Boffetta, N. Jourenkova, P. Gustavsson, Cancer risk from occupational and environmental exposure to polycyclic aromatic hydrocarbons. Cancer Causes and Control 8 (1997) 444-472.

5. E. Lynge, A. Anttila, K. Hemminki, Organic solvents and cancer. Cancer Causes and Control 8 (1997) 406-419.

6. L. Curtis, W. Rea, P. Smith-Willis, E. Fenyves, Y. Pan, Adverse health effects of outdoor air pollutants. Environ. Int. 32 (2006) 815-830.

7. P.G. Jessop, B. Subramaniam, Gas-expanded liquids. Chem. Rev. 107 (2007) 2666-2694.

8. B. Seifried, F. Temelli, Density of marine lipids in equilibrium with carbon dioxide. J. Supercrit. Fluids 50 (2009) 97-104.

9. B. Seifried, F. Temelli. Viscosity of marine lipids in equilibrium with high pressure carbon dioxide. in Proceedings: 9th International Symposium on Supercritical Fluids (ISSF). 2009. Arcachon, France.

10. R. Sih, M. Armenti, R. Mammucari, F. Dehghani, N.R. Foster, Viscosity measurements on saturated gas-expanded liquid systems - Ethanol and carbon dioxide. J. Supercrit. Fluids 43 (2008) 460-468.

11. R. Sih, N.R. Foster, Viscosity measurements on saturated gas expanded liquid systems - Acetone and carbon dioxide. J. Supercrit. Fluids 47 (2008) 233-239.

12. R. Sih, F. Dehghani, N.R. Foster, Viscosity measurements on gas expanded liquid systems - Methanol and carbon dioxide. J. Supercrit. Fluids 41 (2007) 148-157.

13. A. Tegetmeier, D. Dittmar, A. Fredenhagen, R. Eggers, Density and volume of water and triglyceride mixtures in contact with carbon dioxide. Chem. Eng. Process. 39 (2000) 399-405.

14. D. Dittmar, A.M. De Arevalo, C. Beckmann, R. Eggers, Interfacial tension and density measurement of the system corn germ oil - carbon dioxide at low temperatures. Eur. J. Lipid Sci. Technol. 107 (2005) 20-29.

15. B. Seifried, F. Temelli, Density of carbon dioxide-expanded ethanol at (313.2, 328.2 and 343.2) K. J. Chem. Eng. Data (2010) (published online March 29, 2010; DOI: 10.1021/je900830s).

16. A. Kordikowski, A.P. Schenk, R.M. VanNielen, C.J. Peters, Volume expansions and vapor-liquid equilibria of binary mixtures of a variety of polar solvents and certain near-critical solvents. J. Supercrit. Fluids 8 (1995) 205-216.

17. I. Tsivintzelis, D. Missopolinou, K. Kalogiannis, C. Panayiotou, Phase compositions and saturated densities for the binary systems of carbon dioxide with ethanol and dichloromethane. Fluid Phase Equilib. 224 (2004) 89-96.

18. B. Seifried, F. Temelli, Interfacial tension of marine lipids in contact with high pressure carbon dioxide. J. Supercrit. Fluids 52 (2010) 203-214.

19. Y.D. Sun, B.Y. Shekunov, Surface tension of ethanol in supercritical $CO_2$. J. Supercrit. Fluids 27 (2003) 73-83.

20. D. Dittmar, A. Fredenhagen, S.B. Oei, R. Eggers, Interfacial tensions of ethanol-carbon dioxide and ethanol-nitrogen. Dependence of the interfacial tension on the fluid density - prerequisites and physical reasoning. Chem. Eng. Sci. 58 (2003) 1223-1233.

21. P.C. Simoes, R. Eggers, P.T. Jaeger, Interfacial tension of edible oils in supercritical carbon dioxide. Eur. J. Lipid Sci. Technol. 102 (2000) 263-265.

22. M. Moser, W. Pietzonka, C. Trepp, Interfacial tension measurements between alpha-tocopherol and carbon dioxide at high pressures. Chem. Eng. Technol. 19 (1996) 462-466.

23. P.T. Jaeger, J. von Schnitzler, R. Eggers, Interfacial tension of fluid systems considering the nonstationary case with respect to mass transfer. Chem. Eng. Technol. 19 (1996) 197-202.

24. C.A. Lockemann, Interfacial tensions of the binary systems carbon dioxide oleic acid, carbon dioxide methyl myristate, and carbon dioxide methyl palmitate and of the ternary system carbon dioxide methyl myristate

methyl palmitate at high pressures. Chem. Eng. Process. 33 (1994) 193-198.

25. H. Schiemann, E. Weidner, S. Peter, Interfacial tension in binary systems containing a dense gas. J. Supercrit. Fluids 6 (1993) 181-189.

26. J.J.C. Hsu, N. Nagarajan, R.L. Robinson, Equilibrium phase compositions, phase densities, and interfacial tensions for $CO_2$ + hydrocarbon systems. 1. $CO_2$ + n-butane. J. Chem. Eng. Data 30 (1985) 485-491.

27. N. Nagarajan, R.L. Robinson, Equilibrium phase compositions, phase densities, and interfacial tensions for $CO_2$ + hydrocarbon systems. 2. $CO_2$ + n-decane. J. Chem. Eng. Data 31 (1986) 168-171.

28. N. Nagarajan, R.L. Robinson, Equilibrium phase compositions, phase densities, and interfacial tensions for $CO_2$ + hydrocarbon systems. 3. $CO_2$ + cyclohexane. 4. $CO_2$ + benzene. J. Chem. Eng. Data 32 (1987) 369-371.

29. K.A.M. Gasem, K.B. Dickson, P.B. Dulcamara, N. Nagarajan, R.L. Robinson, Equilibrium phase compositions, phase densities, and interfacial tensions for $CO_2$ + hydrocarbon systems. 5. $CO_2$ + n-tetradecane. J. Chem. Eng. Data 34 (1989) 191-195.

30. N. Nagarajan, K.A.M. Gasem, R.L. Robinson, Equilibrium phase compositions, phase densities, and interfacial tensions for $CO_2$ + hydrocarbon systems. 6. $CO_2$ + n-butane + n-decane. J. Chem. Eng. Data 35 (1990) 228-231.

31. C.Y. Sun, G.J. Chen, Measurement of interfacial tension for the $CO_2$ injected crude oil plus reservoir water system. J. Chem. Eng. Data 50 (2005) 936-938.

32. Y. Sutjiadi-Sia, H. Marckmann, R. Eggers, C. Holzknecht, S. Kabelac, The effect of in liquids dissolved dense gases on interfacial and wetting characteristics. Forsch. Ingenieurwes. - Eng. Res. 71 (2007) 29-45.

33. Y. Sutjiadi-Sia, R. Eggers, Lateral wetting angle of falling film in dense fluid. Int. J. Heat Mass Transf. 51 (2008) 3608-3614.

34. J.L. Dickson, G. Gupta, T.S. Horozov, B.P. Binks, K.P. Johnston, Wetting phenomena at the $CO_2$/water/glass interface. Langmuir 22 (2006) 2161-2170.

35. A. Wesch, N. Dahmen, K. Ebert, J. Schon, Interfacial tension, drop size, and angle of contact in the $H_2O/CO_2$ binary system at temperatures of 298-333 K and pressures up to 30 MPa. Chem. Ing. Tech. 69 (1997) 942-946.

36. Y. Sutjiadi-Sia, P. Jaeger, R. Eggers, Interfacial phenomena of aqueous systems in dense carbon dioxide. J. Supercrit. Fluids 46 (2008) 272-279.

37. R. Eggers, P.T. Jaeger, Der Einfluß von Grenzflächenerscheinungen auf den Stoffübergang und die Prozeßführung in Gegenstromkolonnen mit überkritischem $CO_2$. Wärme- und Stoffübertragung - Heat and Mass Transf. 29 (1994) 373-377.

38. P.T. Jaeger, Grenzflächen und Stofftransport in verfahrenstechnischen Prozessen am Beispiel der Hochdruck-Gegenstromfraktionierung mit überkritischem Kohlendioxid. 1998, Aachen: Shaker.

39. P. Jaeger, R. Eggers, Liquid-liquid interphases at high pressures in presence of compressible fluids. Thermochim. Acta 438 (2005) 16-21.

40. G. Wiegand, E.U. Franck, Interfacial tension between water and non-polar fluids up to 473 K and 2800 bar. Ber. Bunsen Ges. - Phys. Chem. Chem. Phys. 98 (1994) 809-817.

41. B. Seifried, F. Temelli, Design of a high-pressure circulating pump for viscous liquids. Rev. Sci. Instr. 80 (2009) art. no. 075104.

42. G. Vazquez, E. Alvarez, J.M. Navaza, Surface tension of alcohol + water from 20 to 50°C. J. Chem. Eng. Data 40 (1995) 611-614.

43. R.K. Rao, M.G. Krishna, S.H. Zaheer, L.K. Arnold, Alcoholic extraction of vegetable oils.1. Solubilities of cottonseed, peanut, sesame, and soybean oils in aqueous ethanol. J. Am. Oil Chem. Soc. 32 (1955) 420-423.

44. S.N. Joung, C.W. Yoo, H.Y. Shin, S.Y. Kim, K.-P. Yoo, C.S. Lee, W.S. Huh, Measurements and correlation of high-pressure VLE of binary $CO_2$-alcohol systems (methanol, ethanol, 2-methoxyethanol and 2-ethoxyethanol). Fluid Phase Equilib. 185 (2001) 219-230.

45. E.J. Hernandez, G.D. Mabe, F.J. Senorans, G. Reglero, T. Fornari, High-pressure phase equilibria of the pseudoternary mixture sunflower oil plus ethanol plus carbon dioxide. J. Chem. Eng. Data 53 (2008) 2632-2636.

46. A. Wesch, N. Dahmen, K.H. Ebert, Measuring the static dielectric constants of pure carbon dioxide and carbon dioxide mixed with ethanol and toluene at elevated pressures. Ber. Bunsen Ges. - Phys. Chem. Chem. Phys. 100 (1996) 1368-1371.

47. C.J. Chang, K.-L. Chiu, C.-Y. Day, A new apparatus for the determination of P-x-y diagrams and Henry's constants in high pressure alcohols with critical carbon dioxide. J. Supercrit. Fluids 12 (1998) 223-237.

48. I. Dalmolin, E. Skovroinski, A. Biasi, M.L. Corazza, C. Dariva, J.V. Oliveira, Solubility of carbon dioxide in binary and ternary mixtures with ethanol and water. Fluid Phase Equilib. 245 (2006) 193-200.

49. C.V. Sternling, L.E. Scriven, Interfacial turbulence - Hydrodynamic instability and the Marangoni effect. AIChE J 5 (1959) 514-523.

50. N.M. Kovalchuk, D. Vollhardt, Marangoni instability and spontaneous non-linear oscillations produced at liquid interfaces by surfactant transfer. Adv. Colloid Interface Sci. 120 (2006) 1-31.

51. M. Wegener, A.R. Paschedag, M. Kraume, Mass transfer enhancement through Marangoni instabilities during single drop formation. Int. J. Heat Mass Transfer 52 (2009) 2673-2677.

52. D. Mock, A. Cabanas, J.A.R. Renuncio, C. Pando, Excess enthalpies of mixtures of olive oil and supercritical carbon dioxide. J. Supercrit. Fluids 14 (1999) 173-180.

53. R.A. Hauser, J.P. Zhao, P.R. Tremaine, A.E. Mather, Excess molar enthalpies of six (carbon dioxide + a polar solvent) mixtures at the temperatures 298.15 K and 308.15 K and pressures from 7.5 MPa to 12.6 MPa. J. Chem. Thermodyn. 28 (1996) 1303-1317.

54. D.R. Cordray, R.M. Izatt, J.J. Christensen, J.L. Oscarson, The excess enthalpies of (carbon dioxide + ethanol) at 308.15, 325.15, 373.15, 413.15, and 473.15 K from 5.00 to 14.91 MPa. J. Chem. Thermodyn. 20 (1988) 655-663.

55. Z. Knez, M. Skerget, L. Ilic, C. Lutge, Vapor-liquid equilibrium of binary $CO_2$-organic solvent systems (ethanol, tetrahydrofuran, ortho-xylene, meta-xylene, para-xylene). J. Supercrit. Fluids 43 (2008) 383-389.

56. C. Borch-Jensen, J. Mollerup, Phase equilibria of fish oil in sub- and supercritical carbon dioxide. Fluid Phase Equilib. 138 (1997) 179-211.

57. B. Arendt, R. Eggers, Interaction of Marangoni convection with mass transfer effects at droplets. Int. J. Heat Mass Transfer 50 (2007) 2805-2815.

# 7 Interfacial Tension of Fish Oil Triglycerides in Contact with Gas-Expanded Ethanol Part 2: Drop Phenomena and Jet Formation[1]

## 7.1 Introduction

Even though interfacial phenomena such as Marangoni effects have been the subject of interest for many decades, most of the studies have been performed for systems under atmospheric conditions. Interfacial and drop phenomena as well as enhanced mass transfer have been studied for liquid-liquid and gas-liquid systems at atmospheric and elevated pressures [1-5]. Interfacial turbulence was observed during absorption of $CO_2$ into methanol and toluene reporting that the onset of interfacial turbulence started about 0.1 s after absorption started and was then superimposed by a density driven convection pattern after 5-50 s [1]. Furthermore, Hozawa *et al.* [1] found that the liquid phase mass transfer coefficient was inversely proportional to interfacial tension (IFT). Mass transfer enhancement during drop formation was reported for the ternary system toluene+acetone+water [3] with Marangoni effects being stronger for the mass transfer from the continuous to drop phase. The mass transfer from continuous to drop phase also inhibited coalescence of the drops and intensity of lateral drop movements was found to depend on initial solute concentration [3].

IFT and Marangoni effects have received considerable attention especially in relation to enhanced oil recovery technologies [6-9] due to increasing oil demands and depleting global oil reserves. Besides studies related to enhanced oil recovery only few investigations have been carried out to study Marangoni effects in high pressure systems with and without a compressible gas such as $CO_2$ [2, 4, 5, 10]. Arendt *et al.* [4] studied the mass transfer through a plane interface for the system $CO_2$+water at pressures up to 36 MPa with and without added surfactant, showing that the surfactant enforced the Marangoni convection. The authors [4] simulated the mass transfer through a plane interface by linear superposition of free convection and Marangoni convection. The mass transfer for the system

[1] A version of this chapter has been submitted to J. Supercrit. Fluids (2010) for consideration for publication.

water+acetone+toluene was measured up to a pressure of 20 MPa [2] with water forming the drop and toluene the continuous phase. Marangoni convection occurred in the case of solute (acetone) transfer from the drop to the continuous phase, which was dampened by the addition of a surfactant [2]. However, according to Arendt and Eggers [2] the criteria to predict the impact of the direction of mass transfer on the development of spontaneous interfacial convection still require more research since controversial observations even for the same component systems exist, suggesting that the shape of the interface (flat, spherical) and the relative movement of the phases have to be considered as well [2]. In fact, as discussed below, the criteria valid for a plane interface developed by Sternling and Scriven [11] cannot always be applied for spherical interfaces for which stability criteria were developed by Sørensen [12]. However, it was found that the criteria developed by Sørensen [12] for spherical interfaces could not predict instabilities in systems containing water, higher alcohols and a petroleum-based mixture of paraffins, naphthenes and aromatics [7] indicating that some of the assumptions underlying these criteria may not be valid for real systems.

Interfacial phenomena leading to kicking drops, schlieren formation around the drop as well as bubble formation and intense mixing inside the drop in the system water+$CO_2$ at elevated pressures with added EtOH in the continuous $CO_2$ phase were reported [5]. Sutjiadi-Sia *et al.* [5] suggested that mass transfer of EtOH carrying $CO_2$ across the interface into the water drop led to the formation of tiny gas bubbles due to stranding of $CO_2$, which coagulated to form larger bubbles in the vicinity of the interface inside the drop and by rising towards the top induced a convective flow inside the drop. The effect of a compressible gas ($CO_2$) on liquid-liquid interfaces was studied by Jaeger *et al.* [10] for the system water+refined corn oil. Although Jaeger *et al.* [10] did not observe the occurrence of Marangoni effects, they found that IFT in the system water+corn oil slightly increased with pressure in the absence of $CO_2$. However, when a mixture of corn oil+$CO_2$ with fairly high $CO_2$ levels but below saturation was in contact with water, the IFT values decreased to about 20% of that for the pure water+corn oil

system. Furthermore, they found that for a given $CO_2$ concentration in oil the IFT values were rather independent of pressure [10].

Drop phenomena in systems consisting of triglycerides such as fish oil as drop phase in contact with a gas-expanded liquid such as $CO_2$-expanded ethanol (CX EtOH) could not be found in literature. In addition, there is a need for an assessment of the theoretical background for the mechanisms involved in drop phenomena. Therefore, the objectives of this study were to review the mechanisms involved and to investigate interfacial phenomena, including interfacial turbulence, occurrence of an oscillating drop with convective patterns inside and outside of the drop, gas bubble formation inside a drop, jet formation at atmospheric and elevated pressures including a whipping jet at pressures up to 10.3 MPa at 40°C.

## 7.2 Mechanisms and key factors

Heat and mass transfer through an interface is often accompanied by interfacial phenomena, which have been studied intensively for many decades due to their relevance for liquid-liquid extraction and gas-liquid absorption processes [2, 3, 11]. Spontaneously auto-oscillating drops due to Marangoni effects have attracted considerable attention for more than 50 years [13]. Marangoni effects have been shown to lead to several-fold enhancement of mass transfer in liquid-liquid extraction, especially with solute transfer from the drop to the continuous phase [2, 3, 14]. The criteria for the development of spontaneous convective motion due to solute transfer have been recently reviewed by Kovalchuk and Vollhardt [15]. The basic mechanisms [11, 15] involved in the development of spontaneous convective motion are related to: i) gravitational effects due to changes in density and thus buoyancy caused by thermal effects (heat of solution) or by solute transfer from one phase to another leading to free convection; ii) so-called Marangoni instability caused by thermal effects and dependence of the interfacial tension on temperature; iii) solutal Marangoni instability due to dependence of the interfacial tension on the solute concentration. Thus, solutal Marangoni

instabilities occur if the local solute concentration varies along the interface, leading to gradients in IFT thus causing interfacial convection.

Gravitational effects due to density changes caused by a thermal gradient were first studied theoretically by Rayleigh [16], which led to the development of the critical Rayleigh number, describing the instability onset for thermal and solutal gravity effects. In the case of a thermally induced density gradient ($d\rho/dz$), thermal conductivity ($\alpha$), the influence of the temperature gradient ($dT/dz$) and temperature-dependence of density ($d\rho/dT$) are key factors. On the other hand, in case of systems involving mass transfer the solute diffusion coefficient ($D$), the concentration gradient ($dc/dz$) and concentration-dependence of density ($d\rho/dc$) are relevant for development of gravitational effects. Furthermore, the value of the critical Rayleigh number depends on the system geometry and boundary conditions. It was found that in systems with two superimposed liquid layers buoyancy forces stemming from a density gradient can lead only to steady cellular convection but they cannot produce oscillatory instability neither by heat nor mass transfer through the interface due to dampening [15].

Thermal effects due to dissolution at the interface in binary systems consisting of two partially miscible components where IFT decreases with temperature ($d\gamma/dT < 0$) can lead to Marangoni instabilities if the interface acts like a heat source (heat of solution) causing IFT gradients at the interface independent of mass transfer direction [17-19]. However, it has been suggested [17] that in those systems oscillatory instability can only occur if the direction of mass transfer is out of the phase of higher viscosity. It should be highlighted that Marangoni effects due to thermal effects caused by dissolution are quite different from those occurring in systems with an externally imposed thermal gradient [20], which is not relevant for the system of this study under thermal equilibrium.

Solutal Marangoni effects are the cause for convective instability in systems with mass transfer of a solute between two immiscible fluids (ternary system) or by dissolution of one fluid into the other in cases where IFT is affected by mutual saturation (binary system) [15]. For a normal surfactant, IFT decreases with increasing concentration at the interface ($d\gamma/dc < 0$), but when this coincides

with surfactant mass transfer out of the phase with the lower diffusion coefficient it always leads to an unstable system with respect to interfacial perturbation [11, 15]. Such unstable ternary systems can lead to oscillatory regimes or stationary convective cells depending on the ratio of the kinematic viscosities $(\nu_1/\nu_2)$ between the two phases [11]. Furthermore, in ternary systems with solute mass transfer, the thermal effects accompanying mass transfer causing local fluctuations in temperature were in general found to be negligible compared to solutal effects with respect to Marangoni instability [21]. However, thermal effects can lead to Marangoni instability in systems that are stable in the absence of thermal effects if the solute diffusion coefficients are equal in both phases ($D_1=D_2$) [21]. Thus, in such systems, Marangoni instability can occur if $d\gamma/dc<0$ and $d\gamma/dT<0$ when the interface acts as a heat source, or if $d\gamma/dc>0$ and $d\gamma/dT<0$ when the interface acts as a heat sink [15]. Since normal surfactants cause a decrease in IFT with increasing concentration ($d\gamma/dc<0$), mass transfer causing exothermic effects at the interface (heat source) leads to Marangoni instability.

Most of the earlier studies and stability criteria mentioned above were developed for plane surfaces [11], with numerous assumptions to simplify the matter, such as non-deformable interface, semi-infinite liquid layers, linear concentration profiles in both liquid phases, no accumulation of surfactant at the interface, and neglecting interfacial diffusion and convection. However, several researchers [12, 22-24] investigated solute transfer directed normal to the interface in three dimensional systems, leading to very complex equations, which did not result in simple stability criteria. However, it has been suggested by Sørensen [12] that for a spherical interface instability caused by mass transfer out of a drop can only be possible for systems with high IFT, whereas instability is possible for any IFT for the opposite direction of mass transfer [15]. In other words, systems with low IFT and mass transfer from the drop to continuous phase are always stable [12]. Other factors such as surface elasticity and the effect of adsorption/desorption kinetics on instabilities were also investigated, establishing that for systems with solute transfer out of the phase with the lower diffusion coefficient, a system is unstable independent of adsorption/desorption rates [25,

26]. Further discussion of mechanisms and influencing factors on interfacial convection, including interfacial chemical reactions [27] and others is beyond the scope of this study, and the reader is referred to an excellent review of stability criteria by Kovalchuk and Vollhardt [15]. It must be stressed that most criteria developed are valid for systems with only diffusional mass transfer in the reference state. However, in real systems convection may be initially present, thereby affecting the development of subsequent interfacial turbulence. Furthermore, one has to keep in mind that the stability criteria for plane and spherical interfaces are different [15]. Additionally, it was reported that the onset of surface instabilities in growing drops depends on the flow rate of the drop forming liquid, capillary diameter and drop lifetime [28].

From the above summary of mechanisms and key factors, it becomes clear that more research is required to better understand interfacial convection and oscillatory regimes due to Marangoni effects in real systems. Nevertheless, the key factors impacting the mechanisms most relevant for this study, leading to the occurrence of interfacial turbulence and potentially oscillations in IFT are [11, 15, 21]: a) the dependence of interfacial tension on temperature ($d\gamma/dT$); b) dependence of interfacial tension on solute concentration ($d\gamma/dc$); c) the ratio of the solute diffusion coefficients ($D_1/D_2$) in both phases; d) the ratio of kinematic viscosities ($\nu_1/\nu_2$) in both phases; and e) the direction of solute transfer. Furthermore, according to stability criteria developed for plane interfaces by Sternling and Scriven [11] it can be stated that most systems are unstable to perturbations at the interface if mass transfer takes place from the phase of lower diffusivity into a phase with higher diffusivity causing either convective cells or an oscillatory regime [15]. Furthermore, according to the same criteria [11] oscillatory instabilities can be observed only in systems where the mass transfer occurs out of the phase with higher viscosity [15, 18].

## 7.3 Experimental

### 7.3.1 Materials

All materials used in this study, such as refined fish oil, anhydrous ethanol, bone dry $CO_2$ and nitrogen were similar to those described in Section 6.2.1.

### 7.3.2 Measurements and observations

#### 7.3.2.1 Apparatus

The apparatus used to observe interfacial phenomena of pendant drops and jet formation for the system of fish oil in contact with CX EtOH under high pressure conditions has been described in Section 6.2.2.1. However, some details of the optical system are highlighted here. A fiber-optic light source (intralux4000, Volpi, Schlieren, Switzerland) and an opal diffuser (NT46-165, Edmund Optics, Barrington, NJ, USA) were used to illuminate the pendant drops and jets, which were recorded at up to 40 frames per second (fps) using a CMOS camera (A602f, Basler Vision Technologies, Ahrensburg, Germany) equipped with a telecentric microscope lens having a zoom factor of up to 4.5 (VZM 450, Edmund Optics, Barrington, NJ, USA). The images were recorded on a personal computer and analyzed by means of commercial software (FTA32 Version 2.0, First Ten Angstroems Inc., Portsmouth, VA, USA) to perform axisymmetric drop shape analysis (ADSA) to ascertain volume, apex position and interfacial tension (IFT). The optical system required calibration in order to use the software for measurements. The magnification of the camera and lens was calibrated against the inner diameter of the silica capillary, which was 100 μm as stated by the manufacturer (Dionex Inc., Sunnyvale, CA, USA). The magnification for the software was also calibrated against a microscopic glass scale having incised 100 lines equally spaced over 5 mm (NT54-246, Edmund Optics, Barrington, NJ, USA) with an overall stated accuracy of ±2 μm.

#### 7.3.2.2 Pendant drop and jet formation

The pendant drops and jets were generated as described previously in Chapter 6 [29] by using a needle valve and a micrometering valve installed between the top

liquid reservoir and the capillary. Prior to drop and jet formation, the tubing between the top reservoir and capillary was filled and flushed with several drops of fish oil TG by fully opening both valves. The fish oil TG was saturated with $CO_2$ in the top reservoir at the same pressure as the bottom view cell. Then after several drops of fish oil TG were released from the capillary, the needle valve was closed to stop the flushing. The micrometering valve located between the capillary and the needle valve was then used to press drops or jets into the view cell by turning the knob clockwise. In order to evaluate the volumetric flow rate for a jet, the change of drop volume versus time was calculated using the ADSA software by analyzing drop images taken during formation at a rate of 40 frames per second (fps).

## 7.4 Results and discussion

The freshly formed pendant drops of fish oil TG in contact with CX EtOH at elevated pressures exhibited pronounced interfacial activity giving rise to several phenomena, including interfacial turbulence, internal mixing of the drop, gas bubble formation at the interface inside the drop, and oscillation of a pendant drop. The potential mechanisms and key factors most relevant for the development of interfacial phenomena in binary and ternary systems were briefly outlined above to set the stage for interpreting the observed drop phenomena in the complex system of fish oil TG in contact with CX EtOH. In this section, some additional factors specific to the fish oil TG+CX EtOH system, which could affect mechanisms of interfacial turbulence and drop phenomena by affecting relevant properties, such as density, IFT and viscosity are outlined.

### 7.4.1 Mechanisms and factors affecting drop phenomena in the system fish oil TG+CX EtOH

Several known effects can be anticipated to impact interfacial activity in the case of a fish oil TG drop exposed to CX EtOH. First, the physical properties, such as density and viscosity of both EtOH and TG are affected by the amount of $CO_2$ ($x_{CO2}$) dissolved. For both TG and EtOH, the viscosity decreases substantially with $x_{CO2}$ while the density increases by about 5% in the pressure range of this

study (< 6 MPa) [30-33]. Second, the dissolution of $CO_2$ into TG and EtOH is accompanied by exothermic or endothermic effects depending on pressure, temperature and mole fraction $x_{CO2}$ [34-36], which affects the temperature at the interface potentially leading to IFT gradients. The excess enthalpies for mixtures of $CO_2$+olive oil were reported to be exothermic at 35 and 80°C for a $CO_2$ pressure of 9 MPa [34]. Likewise, exothermic effects were reported for the dissolution of $CO_2$ into EtOH at 35°C and 7.5 MPa [35]. It seems therefore likely that exothermic effects could occur at the interface between TG and CX EtOH. Third, mutual solubility between TG and CX EtOH is enhanced at elevated $CO_2$ pressures [37], and therefore mass transfer of EtOH into the TG drop and *vice versa* can be expected. Thus, it can be anticipated that dissolution of EtOH into the TG drop phase leads to a local decrease in density and thus a density gradient. Finally, IFT is affected by the amount of $CO_2$ adsorbed at the interface, which is related to the concentration of $CO_2$ in the adjacent fluids [38]. Both phases can dissolve relatively large amounts of $CO_2$, with EtOH and fish oil TG reaching $CO_2$ mole fractions of $x_{CO2} > 0.25$ [39, 40] and $x_{CO2} > 0.75$ [41], respectively, at 40°C and pressures of up to about 5 MPa. Therefore, when CX EtOH enters the TG drop the solubility of $CO_2$ inside the TG drop may be substantially reduced, leading to the formation of bubbles of $CO_2$. Such bubble formation was observed inside an aged drop as described previously in Chapter 6 [29].

Interfacial turbulence in the system TG+CX EtOH rendered the drop interface to appear rough almost instantaneously after a drop was pressed out of the capillary, as illustrated in Fig. 7-1 for a freshly formed pendant drop at 40°C and 4.83 MPa showing images taken at 1 s intervals immediately after drop formation up to 7 s. The effects mentioned above may lead to local gradients in IFT at the interface inducing fluid movements at the interface and fluid convection adjacent to the interface. The rough appearance of the freshly formed interface was observed throughout drop formation and afterwards for up to several seconds, as illustrated in images 1 to 5 of Fig. 7-1. Furthermore, after aging of the drop, the TG phase inside the pendant drop often circulated

vigorously at increased pressure of $CO_2$, which may be caused by gradients in IFT causing interfacial convection.

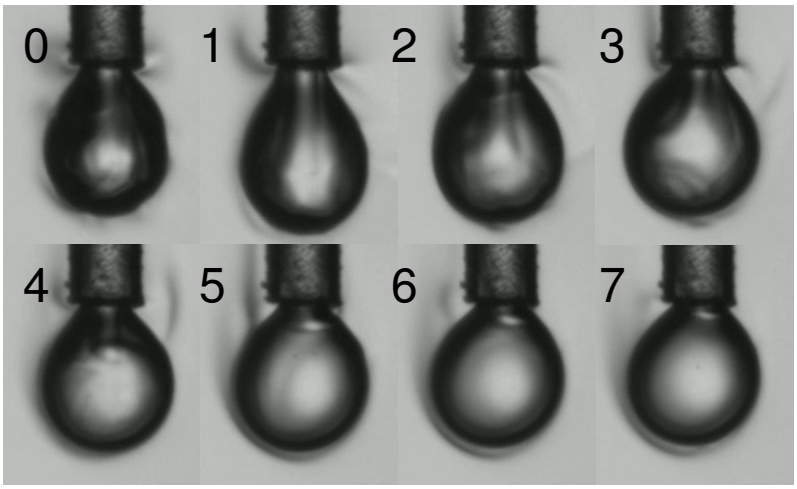


**Figure 7-1.** Images for a pendant drop of fish oil TG in contact with CX EtOH at 40°C and 4.8 MPa recorded 1 s apart showing interfacial turbulence at the drop interface (0-5 s), a kicking motion to the left side (6 s), as well as change of the drop shape observed during the first 7 s after drop formation.

### 7.4.2 Auto-oscillating pendant drop

In the system fish oil TG+CX EtOH, vigorous internal mixing of pendant drops could be frequently observed in this study accompanied by formation of gas bubbles inside the drop. Furthermore, some drops developed a kicking motion usually sideways. The drop illustrated in Fig. 7-1 was kicking sideways at 6 s. A kicking or oscillating drop is a known phenomenon [13], which may occur if mass transfer is locally enhanced at one side of the drop thus leading to a local concentration gradient at the interface thereby inducing spontaneous drop motion towards that side. For example, in the case of the drop shown in Fig. 7-1, enhanced mass transfer at the left side of the drop, as evidenced by the darker schlieren on that side, potentially led to a local decrease in IFT at the left hemisphere of the drop. This local decrease in IFT caused the interface to be pulled towards regions of higher IFT on the right hemisphere of the drop. However, this spontaneous interfacial motion generated tangential shear stress acting on the adjoining bulk liquid so that the drop was pushed to the left. The

drop motion could further enhance mass transfer at the left hemisphere, thereby reinforcing the Marangoni effect leading to an oscillating kicking motion [42].

A similar kicking motion was reported previously for water drops surrounded by dense $CO_2$ containing 9 wt% of EtOH [5]. Sutjiadi-Sia *et al.* [5] indicated that IFT was lowered by the solute inducing a local decrease in pressure across the meniscus due to the IFT gradient. They [5] further explained that this asymmetrical pressure distribution over the drop surface resulted in fluid flow (of water) inside the drop into that region causing the kicking movement in that direction. However, assuming the interface is not rigid it seems that a sudden local decrease in internal pressure at the interface of the drop would cause a fluid motion from both the water phase and from the surrounding continuous phase since pressure acts in all directions. It was described earlier [43] in relation to IFT gradients generated by means of a temperature gradient that the flow in the interface is in the direction of the tangential stress. Thus, because liquid is flowing in the tangential direction along the interface liquid from the bulk is drawn to the interface due to continuity. Tangential flow adjacent to the interface naturally occurs on both sides of the interface. Thus, it appears that for drops surrounded by a dense fluid an impulse potentially caused inside the drop by bulk liquid flowing rapidly to the interface and that caused outside the drop by the surrounding liquid flowing to the interface may cancel each other especially if both liquids have comparable densities and viscosities. However, in case of a thin liquid layer in contact with air a local depression of the surface was observed when a thermally induced IFT gradient due to a hot spot was generated [44]. In that case [44], the liquid inside the thin liquid layer was pulled away from the hot spot by interfacial movement and no bulk liquid was available to compensate for that fluid motion leading to the local depression. The situation in a drop appears to be different to that in a thin liquid layer since a sudden local decrease in IFT leading to interfacial movement and tangential fluid motion away from a spot with a local IFT minimum can be compensated by the bulk drop liquid, which can flow into that region. Instead of a local depression it seems more reasonable that a sudden local decrease of IFT at the interface of a pendant drop could lead to local bulging

of the interface. The overall internal pressure of the drop must remain constant at the moment when the sudden local IFT decrease occurs since for the rest of the drop the IFT is not affected immediately by the local IFT gradient. Therefore, because the interface is locally 'weaker' the bulk liquid of the drop could push the interface outwards until the local balance between the IFT and pressure difference across the interface is established. The pressure difference across the interface, which is dictated by the IFT and pressure of the bulk drop liquid, is closely related to the local curvature of the drop ($\Delta P \approx 2\gamma/R$). At the same time the local IFT gradient causes the interface to spread over the entire drop compensating for the IFT gradient and thus lowering the internal pressure of the drop.

The above sequence of events could happen within fractions of a second, which makes it probably impossible to observe experimentally considering the tiny length scales. In this context, it seems noteworthy that in 1958 Haydon [45] explained the kicking drop phenomenon based on an incorrect assumption that a decrease of IFT leads to an increase in the internal pressure of the drop thus leading to a kick towards the exterior phase. However, later Sørensen [46] described more convincingly that a local increase in surfactant concentration at one drop hemisphere resulting in the decrease of IFT would give rise to a decrease in Laplace overpressure ($2\gamma/R$) just behind that part of the interface. However, as described above, it appears that neither the assumption of Sørensen (i.e. local decrease in Laplace overpressure) nor that of Haydon (local increase in pressure) are convincing, but rather that the local pressure drop across the interface dictated by the bulk drop liquid remains initially fairly constant and that a sudden local decrease in IFT is compensated by a change of interfacial curvature in that region, which subsequently leads to a decrease in pressure and fluid flow into that region, which coincides with the tangential motion of the interface to regions of higher IFT until it is equilibrated and lowered for the entire drop so that the Laplace overpressure of the entire drop is decreased. According to Sørensen [46] the streaming inside the drop takes place from the surfactant-poor to the surfactant-rich hemisphere of the drop, which appears to be correct for the bulk of the drop. However, as described in more detail below related to our observations of the

auto-oscillating pendant drop, it was observed that first a rapid movement at the interface away from the solute-rich zone took place, which concomitantly generated shear stress to the adjacent fluids inside and outside of the drop resulting in fast drop movement and forced convection inside and outside of the drop. Therefore, close to the interface the tangential fluid motion was away from the region of decreased IFT, whereas the bulk liquid from the center of the drop is forced to flow into that region for continuity reasons.

A pendant drop developing an auto-oscillating up and down motion was observed as well. The periodic motion is illustrated in Fig. 7-2, showing the vertical drop apex position relative to an arbitrary reference point below the drop versus time along with images and symbolic drawings of drops (labeled a to i). The drop symbols demonstrate both the movement of the drop apex (block arrows) and the observed flow patterns (line arrows). The pendant drop of fish oil in CX EtOH at 4.83 MPa and 40°C with a diameter of about 0.22 mm and a volume of approximately 0.005 μL was generated slowly in about 6 s (Fig. 7-2). As indicated by the arrows and photo inserts pointing at the line in Fig. 7-2 during drop formation (apex position decreasing) the drop exhibited several downward kicking movements at t = 2, 3.5 and 5.6 s. Then, when the formation of the drop was completed and the apex reached its final position (t = 6.5 s) the drop started to oscillate spontaneously in a periodic manner (t = 7 s) with a cycle duration of about 1.5 s. A sequence of drop images taken during the cycle starting at t = 8.5 s together with the symbolic drawings of drops at the top of the chart (labeled a to i) illustrate the convective pattern and mechanism leading to the oscillating movement. First, a sudden tangential movement of the interface away from the apex of the drop was observed, indicated by the arrows in the symbolic drop (a) in Fig. 7-2.

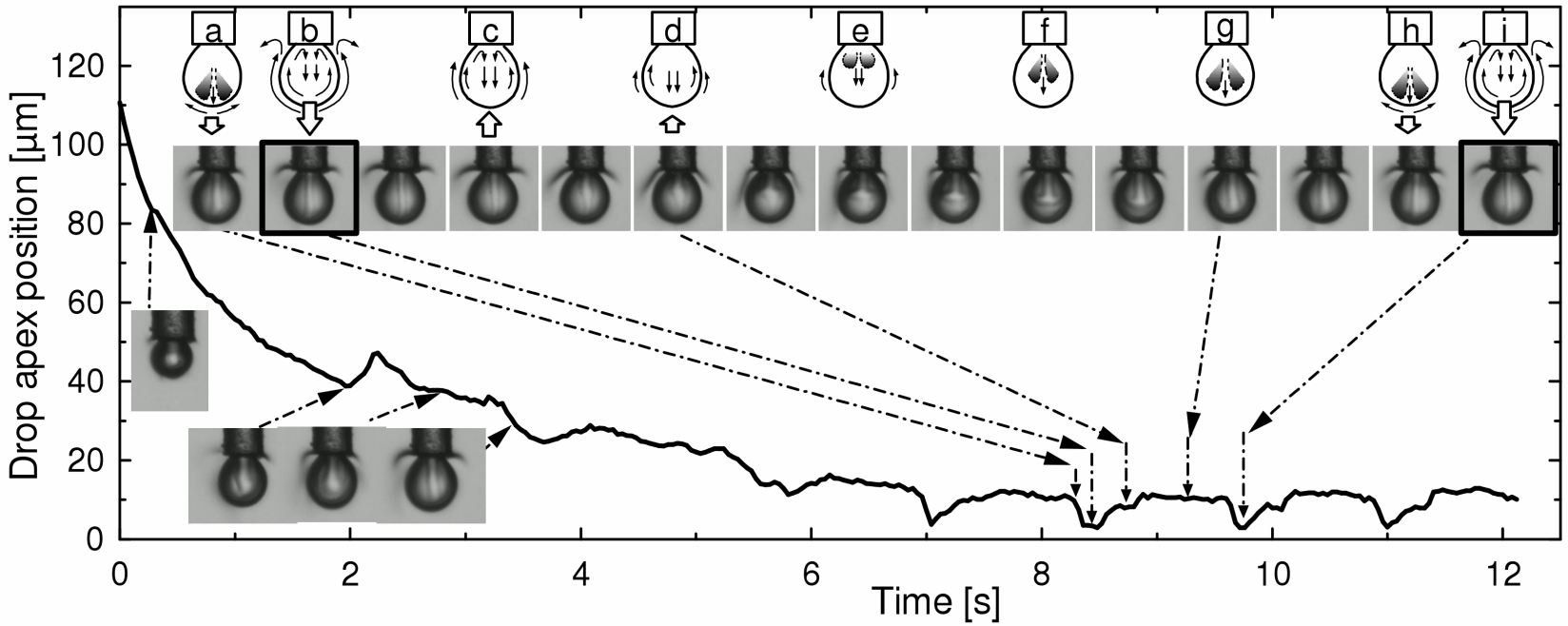


**Figure 7-2.** Vertical apex position of an auto-oscillating pendant drop of fish oil TG in CX EtOH at 4.83 MPa and 40°C over time and the observed flow patterns inside and around the drop.

The sudden movement of the interface was caused by an IFT gradient, which appeared to originate from a local concentration gradient of EtOH at the interface in the apex of the drop. A higher interfacial concentration of EtOH could originate from enhanced mass transfer at the tip of the drop due to convection during drop formation and longer exposure time than the freshly formed interface at the sides of the drop. Concurrently, with the rapid interfacial convection directed from the bottom of the drop towards the capillary, a sudden downwards motion of the drop along with a flow upwards on both sides of the interface outside and inside of the drop were observed. The schlieren visible next to the capillary tip and above the drop moved upwards as the drop moved down resembling the shape of an opening umbrella. Once the drop apex reached the lowest point it bounced back upwards to the original position (Fig. 7-2). The movement upwards was considerably slower than the downwards kicking motion. As the drop moved back upwards the schlieren outside of the drop moved downwards potentially due to density driven convection thereby resembling an umbrella being closed (Fig. 7-2, c to f).

A convection pattern was observed inside of the drop illustrated by the line arrows inside of the symbolic drops in Fig. 7-2. While the fluid inside the drop close to the interface moved upwards, a downwards flow developed at the center of the drop. Furthermore, once the drop apex returned to its original level (Fig. 7-2, symbolic drop e) the fluid inside the top of the drop close to the interface, which was rapidly forced upwards due to interfacial convection, appeared darker, indicating a change in density or composition due to EtOH uptake. This fluid region is also illustrated by the shaded area inside the symbolic drops (Fig. 7-2, e to h). The fluid at the top of the drop enriched in EtOH resembled a plume, which was subsequently forced downwards at the center of the drop. A circulation pattern was visible inside the drop, with the plume slowly moving towards the bottom tip of the drop. When the darker plume enriched in EtOH reached the inside interface at the bottom of the drop, the cycle started again causing a rapid downward movement of the drop. Since the drop was followed only up to 12 s it is unknown how long the oscillation lasted. However,

it appears that the cycle time decreased from about 1.5 s to about 1.2 s during the first three cycles meaning that the process accelerated, possibly due to the viscosity of the drop phase being decreased by EtOH dissolution. The rapid convection inside the drop was clearly driven by interfacial convection; therefore, the size of the pendant drop seemed relevant for the development of the internal flow pattern and periodic motion as well. In systems with small drops or where the densities of the drop and the surrounding fluid are similar, gravitational effects are small compared to interfacial tension effects [47]. Furthermore, it was shown that the elasticity of the drop interface and viscosities of the drop and the surrounding fluid affect drop oscillation as well [47]. Based on the observations of the TG+CX EtOH system, the small droplet size seemed further advantageous because the plume enriched in EtOH, which was forced towards the bottom interface of the drop by the established convective flow pattern, reached the interface before being diluted and reinitiated the cycle. In larger drops, the plume rich in EtOH could get diluted by the bulk fluid before reaching the interface at the bottom. Thus, in larger drops, the mechanism observed in Fig. 7-2 may not be possible.

It is known that autonomous self-sustained translational motion and even levitation of drops are possible for drops surrounded by a media with an imposed thermal gradient [43], leading to interfacial tension gradients and fluid flow inside and outside of the drop due to Marangoni effects [42]. IFT gradients along the interface of a drop can also be caused by compositional variations along the interface [42] thereby leading to translational motion. The flow pattern illustrated in Fig. 7-2 originated at the apex of the drop where a local IFT gradient induced interfacial movement towards the capillary, which led to shear stress in the adjacent fluid causing ‘forced‘ convection in an upward direction at the drop interface and in a downward direction at the center of the drop due to continuity reasons. However, a flow pattern in the opposite direction was described for both a water drop in a $CO_2$ surrounding as well as for a water drop in toluene with acetone transfer into the drop [2]. The observed pattern in the water drops [2] was apparently driven by acetone dissolving into the water drop at the phase boundary

and bottom of the drop first, thereby leading to a local decrease in density and subsequently to a density gradient. The lighter parts ascended from the center of the drop and forced liquid to descend close to the interface [2]. It seems that the direction of the flow pattern depends strongly on the mechanism initiating the circulation. Natural convection due to density gradients may cause the liquid in the drop to ascend in the center of the drop, whereas for IFT induced circulation the liquid descends in the center of the drop as observed in Fig. 7-2. Therefore, if the solute transfer from the continuous phase into the drop leads to a decrease in both drop density and IFT the size of the drop may influence which of the two mechanisms prevails. In smaller drops shear stress caused by sudden interfacial movements can lead to fluid movement in the drop that affects a larger portion of the drop volume compared to large drops, where viscous effects and density driven convection compensate the interfacial shear stress.

### 7.4.3 Jet formation of fish oil TG into CX EtOH

At elevated pressures, pendant drop formation became challenging due to the very low IFT (< 0.1 mN/m) and the reduced viscosities of both the drop and continuous phases. The energy input required to generate a jet is greatly reduced under those conditions. Thus, even though very low flow rates were employed to generate a pendant drop the liquid coming out of the capillary often immediately formed elongated drops or even a jet rather than a pendant drop.

Jet formation of fish oil TG into CX EtOH was observed at 40°C from atmospheric pressure up to 10.4 MPa. The formation of a jet of fish oil TG into CX EtOH at atmospheric pressure is shown in Fig. 7-3.

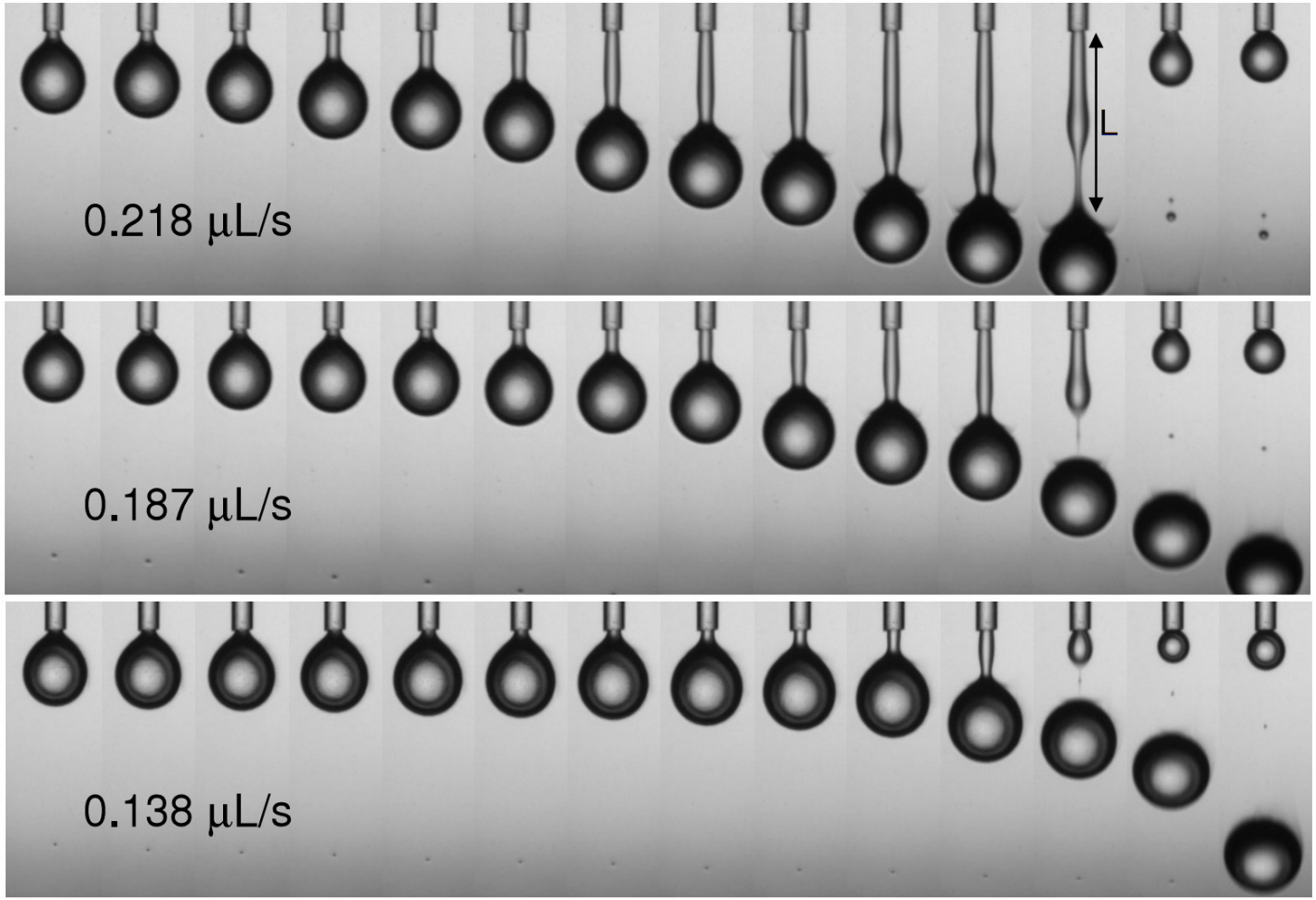


**Figure 7-3.** Images of jet formation of fish oil TG into CX EtOH at 0.1 MPa and 40°C taken at 0.05 s intervals, showing flow rates, drop pinch-off and satellite drops. The ID of the capillary is 100 µm.

Since the drops and jets were generated manually in this study by using a micrometering valve it was not possible to set a certain flow rate for each experiment. However, for jets involving drop growth the flow rates were estimated by analyzing the change in drop volume using the images of the growing pendant drop taken at 40 fps (Fig. 7-3). Thus, the increase in pendant drop volume over time was used to quantify the flow rate (Fig. 7-4).

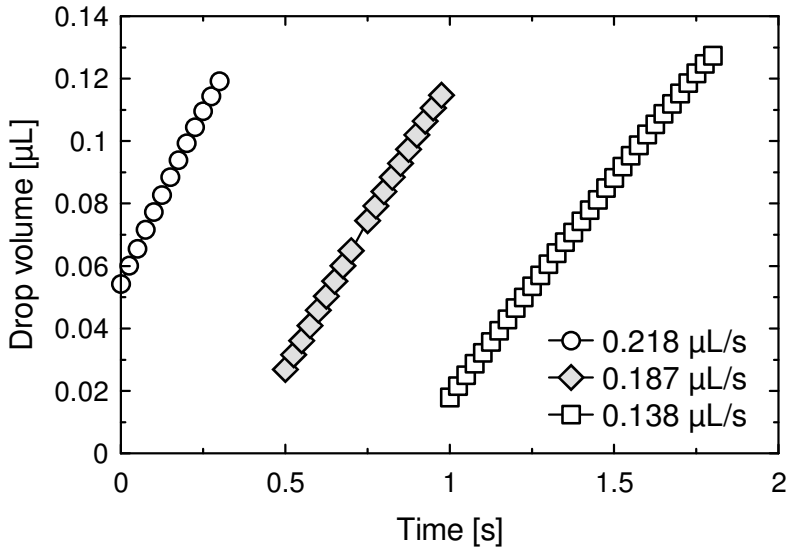


**Figure 7-4.** Change in drop volume over time for the jets shown in Fig. 7-3 to estimate flow rate.

The Reynolds numbers ($Re_j = v_j * d_c * \rho_j / \mu_j$) of the jets shown in Fig. 7-3 were all < 0.1, which were calculated using the capillary inner diameter $d_c$, density of fish oil TG $\rho_j$ [33], viscosity $\mu_j$ [30] and the estimated jet velocity $v_j$ obtained from flow rate $Q$ using $d_c$ to calculate the jet cross sectional area. In the laminar regime at the low pressure conditions, the relative jet breakup length ($L/d_c$) increased linearly with flow rate $Q$ (Fig. 7-5).

A similar trend was found by Badens *et al.* [48] for low flow velocities in the laminar regime for jet breakup length of water and ethanol injected into high pressure $CO_2$ below their mixture critical point (MCP). Badens *et al.* [48] reported that depending on $CO_2$ pressure, at the same flow rates methylene chloride formed an axisymmetrical jet, an asymmetrical jet and an atomizing jet at 6, 7 and

8 MPa, respectively. The atomizing jet of methylene chloride disintegrated into gaseous plumes rather than drops at conditions above the MCP [48], indicating that miscibility and mutual solubility between the jet and surrounding phase are of great importance.

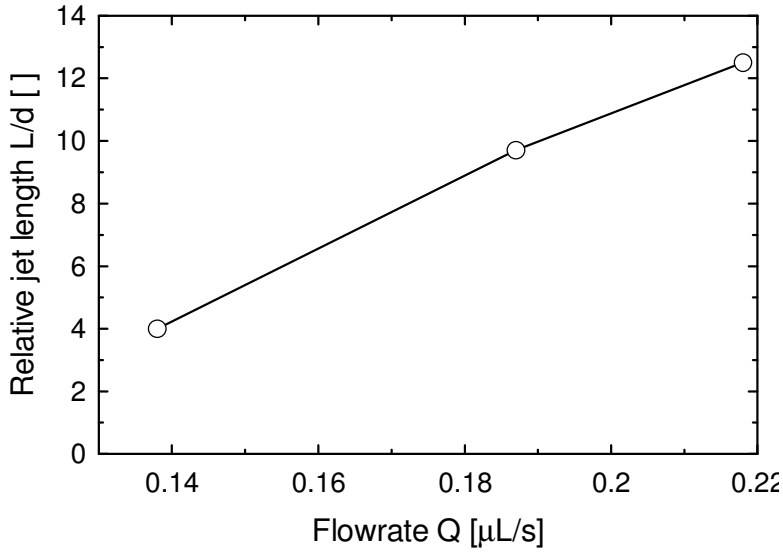


**Figure 7-5.** Relative jet length (L/d) versus flow rate Q for the jets shown in Fig. 7-3.

The jet images (Fig. 7-3) further show the pinch-off of the drop from the jet and formation of satellite drops, with two satellite drops visible at the higher flow rate. The ligaments between the falling drop and the jet recoil and form one or two satellite drops (Fig. 7-3).

At elevated pressures where IFT vanished or reached ultra low values, jet formation was observed at flow rates much lower than those illustrated in Fig. 7-3. Unfortunately, due to the manual method of generating the jets the flow rate could not be quantified by the method of analyzing the growing pendant drop volume as described above. However, several phenomena could be observed in these low-velocity jets. A whipping jet was observed at 40°C and 6.21 MPa as illustrated in Fig. 7-6, which shows images taken every 0.5 s of the jet, exhibiting lateral movements swinging from one side to the other. The drop forming at the tip of the jet seemed to ascend before it was released in a spherical shape.

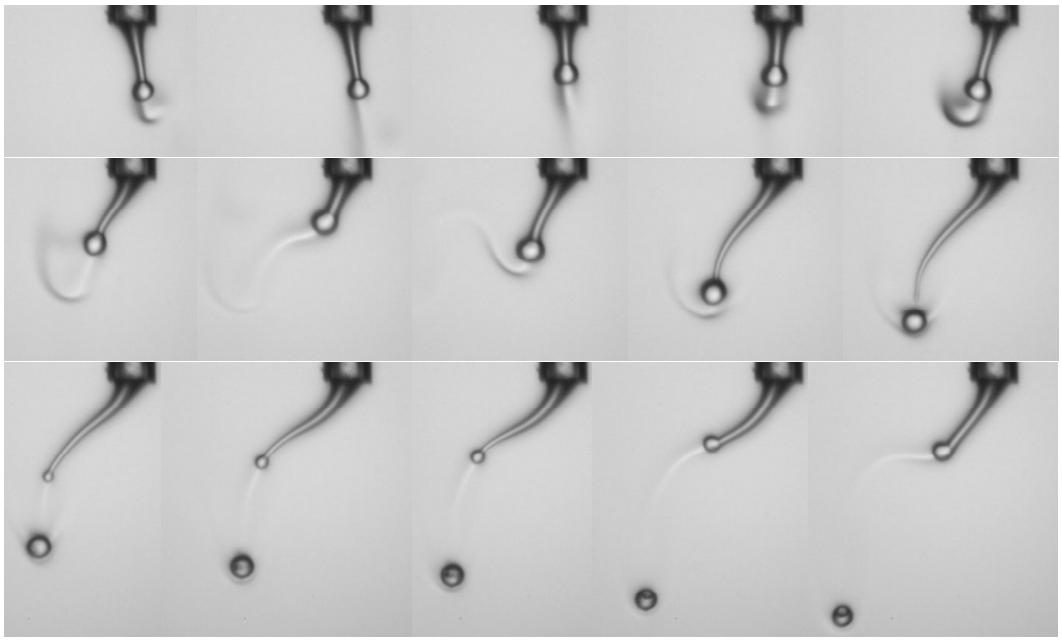

**Figure 7-6.** Images of a slowly whipping jet of fish oil TG into CX EtOH at 6.21 MPa and 40°C taken at 0.5 s intervals showing the formation of a tiny gas bubble inside the detached drop.

Furthermore, as soon as the drop was released from the jet, a tiny gas bubble formed inside the drop indicating stranding of $CO_2$ (Fig. 7-6). The gas bubble inside the drop may impact the settling velocity of the drop due to the increased buoyancy. The jet illustrated in Fig. 7-7, having a slightly higher flow rate at 40°C and 6.21 MPa released the drops much faster according to the images taken every 0.1 s and did not swing from side to side while releasing spherical drops. However, a tiny gas bubble could also be observed inside the drop in the last image (Fig. 7-7). The jet illustrated in Fig. 7-8 recorded at 40°C and 6.9 MPa at 0.12 s intervals shows a straight jet with rapidly forming drops, which are decreasing in size as soon as they are released potentially due to dissolution of TG into CX EtOH.

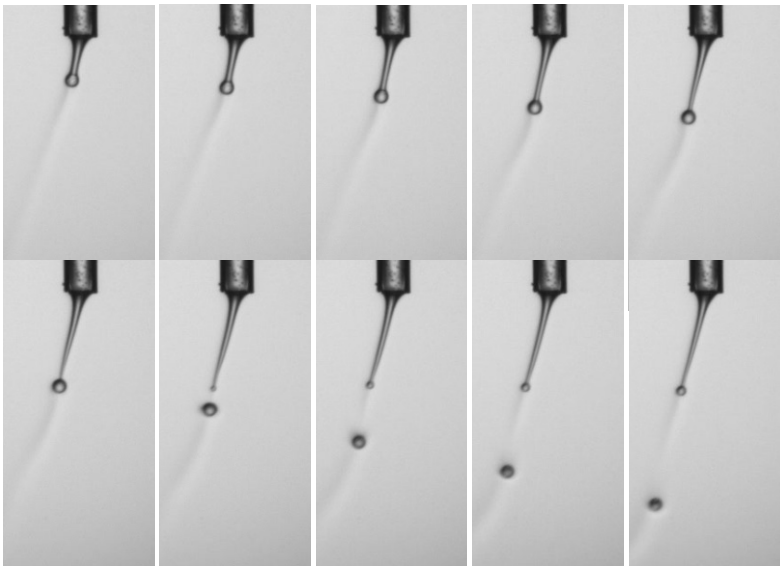

**Figure 7-7.** Images of a jet of fish oil TG into CX EtOH at 6.21 MPa and 40°C taken at 0.1 s intervals showing the formation of a tiny gas bubble inside the detached drop.

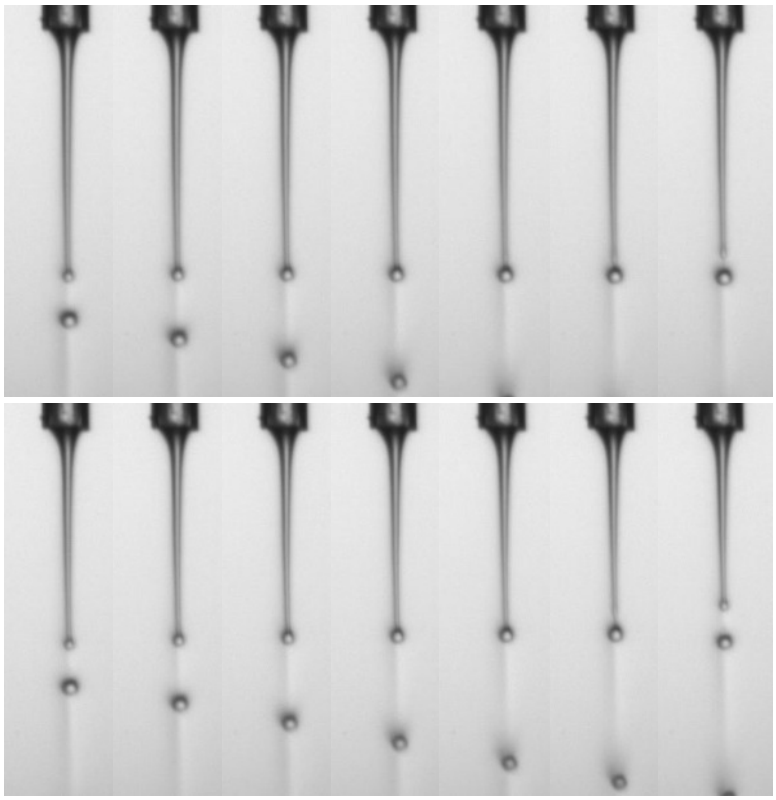

**Figure 7-8.** Images of a jet of fish oil TG into CX EtOH at 6.9 MPa and 40°C taken at 0.12 s intervals showing that the drops decrease in size after detachment.

Increasing the pressure further to 7.65 MPa in the vicinity of the MCP of $CO_2$+EtOH the contact angle and wettability between the fish oil TG and silica capillary was greatly affected. As illustrated in Fig. 7-9, the liquid climbed up the outside of the capillary tip and formed a large drop, which could not be held at the tip of the capillary. Additionally, the mass transfer of TG in CX EtOH was enhanced as manifested by the schlieren visible around the drop (Fig. 7-9).

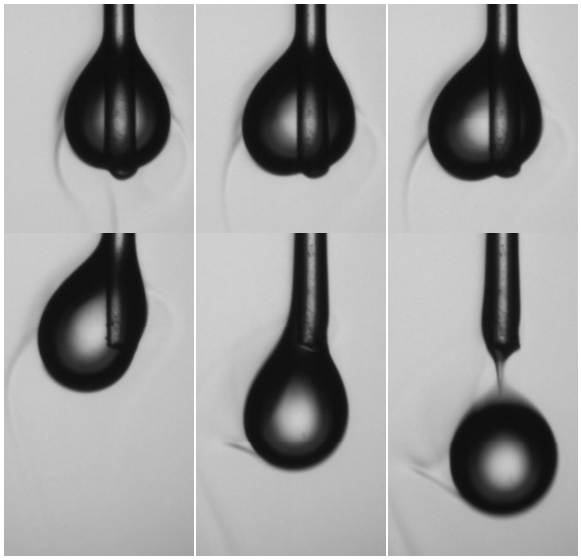

**Figure 7-9.** Wetting behavior of fish oil TG drop on a silica capillary submersed in CX EtOH at 7.65 MPa and 40°C.

The jet in Fig. 7-10 at 40°C and 10.4 MPa was formed at higher flow rates and drop formation occurred rapidly, as shown by the images taken in 0.04 s intervals (25 fps). Furthermore, the drops detaching from the jet were much larger than those observed at lower pressures (Figs. 7-6 to 7-8) potentially due to rapid uptake of EtOH leading to a lower density and swelling of the drop. For the sequence of images shown in the lower section of Fig. 7-10, the flow rate was suddenly increased leading to the increasing jet diameter with time. The jet shown in Fig. 7-11 was generated under the same conditions as that in Fig. 7-10, showing images at 0.04 s intervals. The drops forming at the tip of the jet were again larger than those obtained at pressures below the MCP. Furthermore, the drop falling from the jet shown in the bottom sequence appeared with a clean

interface at the lower hemisphere whereas the zone closer to the neck of the jet was darker potentially caused by interfacial turbulence due to mass transfer into the freshly formed interface.

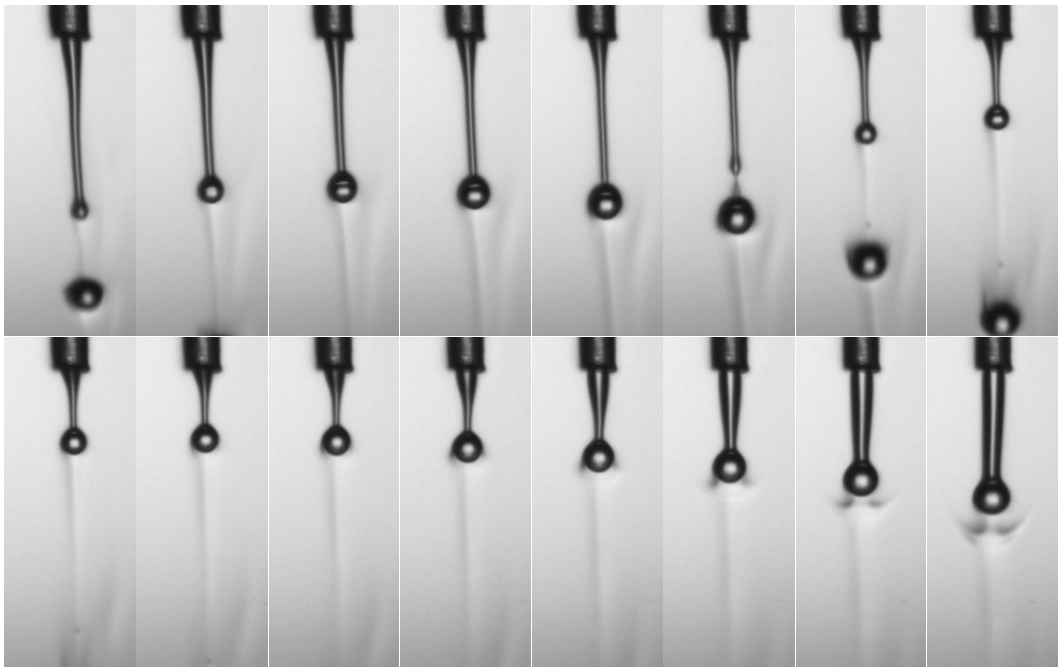

**Figure 7-10.** Images of a jet of fish oil TG into CX EtOH above the MCP of $CO_2$+EtOH at 10.34 MPa and 40°C taken at 0.04 s intervals showing the drop diameter being larger than the ID of the capillary (100 μm).

As the drop was pinched off the jet (Fig. 7-11), the interface of the drop seemed to contract rapidly towards the upper hemisphere where the IFT was probably higher. Therefore, the IFT gradient between the leading hemisphere and the zone closer to the neck of the jet appeared to cause interfacial movement that pushed the drop faster downwards.

Kerst *et al.* [49] studied disintegration of free jets and liquid falling films of methyl myristate under high pressure $CO_2$ showing that jet disintegration was strongly affected by elevated $CO_2$ pressures observing that it occurred at lower Reynolds numbers compared to atmospheric conditions. Furthermore, Kerst *et al.* [49] developed a correlation for the jet disintegration length at elevated pressures

based on Reynolds number, Weber number and ratios of both viscosities and densities of gas and liquid phases, respectively.

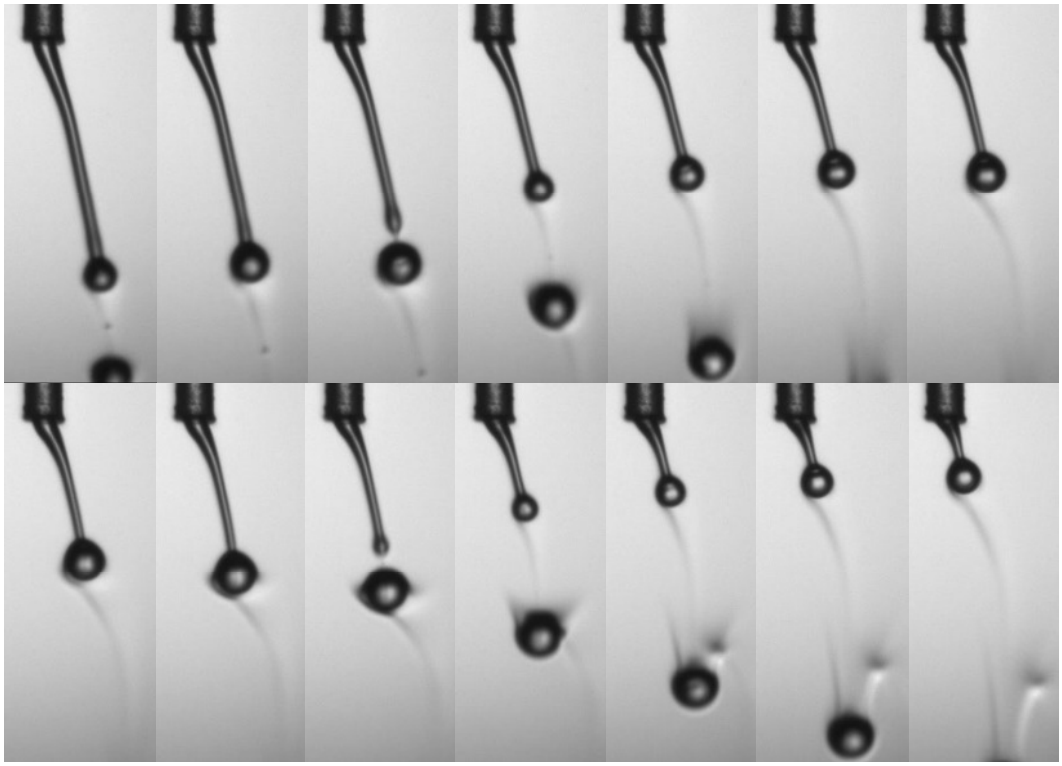

**Figure 7-11.** Images of a jet of fish oil TG into CX EtOH above the MCP of $CO_2$+EtOH at 10.34 MPa and 40°C taken at a 0.04 s interval showing interfacial activity at the interface of the detaching drop.

Jet disintegration in high pressure conditions was further studied by Czerwonatis and Eggers [50] who developed a new dimensionless number taking into account the Ohnesorge number, Weber number and ratio of liquid to gas viscosity to predict the transition zones for Rayleigh breakup, sinuous wave breakup and atomization after injecting water (polar) and vegetable oil (non-polar) into pressurized $CO_2$ and nitrogen, respectively. Investigation of the hydrodynamic behavior of ethanol injected into dense $CO_2$ below and above the MCP of the system by Dukhin *et al.* [51] revealed that jet breakup modes observed at lower pressures (Rayleigh, sinuous wave breakup, atomization) were also possible at pressures slightly below or near the MCP where equilibrium IFT

were very small or vanished. Equilibrium IFT could not be established rapidly during jet formation so that the two phases present were stabilized during jetting by a dynamic interfacial tension [51]. However, at pressures far above the MCP the ethanol jet did not behave like a spray or atomizing jet but rather as a gas jet where no drop formation or interface was observed [51]. Badens *et al.* [48] studied jet atomization of water, methylene chloride and ethyl alcohol into pressurized $CO_2$. Methylene chloride was injected into $CO_2$ at various pressures below and above the MCP, where an interface was clearly visible for the jet and the drops after jet disintegration at pressures below the MCP whereas above the MCP the interface was only observed for the plain jet before the breakup zone [48]. Jet breakup in the near-critical regime of the system $CO_2$+dichloromethane were investigated by Lee *et al.* [52] suggesting that for particle formation of polylactic acid (PLA) based on the supercritical antisolvent (SAS) process, the particles obtained in the dripping and Rayleigh disintegration modes at low flow rates were more uniform in size than those obtained at higher flow rates leading to wavy disintegration and turbulent jet breakup.

## 7.5 Conclusions

Drop phenomena related to interfacial turbulence and Marangoni effects were observed in the system of fish oil TG in contact with CX EtOH. Furthermore, the factors and mechanisms leading to an auto-oscillating drop at elevated pressures were described. The observed flow patterns inside and outside of the auto-oscillating drop were illustrated. Jet formation of fish oil TG injected into CX EtOH at atmospheric pressure as well as elevated pressures below and above the MCP of $CO_2$+EtOH were presented, where it was found that the formation of jets and drops was possible at pressures above the MCP of $CO_2$+EtOH where IFT was found vanish. The detached drops from jets at pressures above the MCP appeared larger than those obtained at pressures slightly below the MCP. These findings may be beneficial for development of processes involving jet and drop formation of lipids such as fish oil TG in contact with CX EtOH. Further investigations are required to better quantify the flow rates leading to jet formation, to predict jet

characteristics, such as jet-breakup length and describing the transition between flow regimes in such systems.

## 7.6 References


1. M. Hozawa, N. Komatsu, N. Imaishi, K. Fujinawa, Interfacial turbulence during the physical absorption of carbon dioxide into non-aqueous solvents. J. Chem. Eng. Jpn. 17 (1984) 173-179.

2. B. Arendt, R. Eggers, Interaction of Marangoni convection with mass transfer effects at droplets. Int. J. Heat Mass Transfer 50 (2007) 2805-2815.

3. M. Wegener, A.R. Paschedag, M. Kraume, Mass transfer enhancement through Marangoni instabilities during single drop formation. Int. J. Heat Mass Transfer 52 (2009) 2673-2677.

4. B. Arendt, D. Dittmar, R. Eggers, Interaction of interfacial convection and mass transfer effects in the system $CO_2$-water. Int. J. Heat Mass Transfer 47 (2004) 3649-3657.

5. Y. Sutjiadi-Sia, P. Jaeger, R. Eggers, Interfacial phenomena of aqueous systems in dense carbon dioxide. J. Supercrit. Fluids 46 (2008) 272-279.

6. P.A. Lyford, H.R.C. Pratt, F. Grieser, D.C. Shallcross, The Marangoni effect and enhanced oil recovery: Part 1. Porous media studies. Can. J. Chem. Eng. 76 (1998) 167-174.

7. P.A. Lyford, D.C. Shallcross, F. Grieser, H.R.C. Pratt, The Marangoni effect and enhanced oil recovery: Part 2. Interfacial tension and drop instability. Can. J. Chem. Eng. 76 (1998) 175-181.

8. S.C. Ayirala, W. Xu, D.N. Rao, Interfacial behaviour of complex hydrocarbon fluids at elevated pressures and temperatures. Can. J. Chem. Eng. 84 (2006) 22-32.

9. C.Y. Sun, G.J. Chen, Measurement of interfacial tension for the $CO_2$ injected crude oil plus reservoir water system. J. Chem. Eng. Data 50 (2005) 936-938.

10. P. Jaeger, R. Eggers, Liquid-liquid interphases at high pressures in presence of compressible fluids. Thermochim. Acta 438 (2005) 16-21.

11. C.V. Sternling, L.E. Scriven, Interfacial turbulence - Hydrodynamic instability and the Marangoni effect. AIChE J 5 (1959) 514-523.

12. T.S. Sørensen, Marangoni instability at a spherical interface. Breakdown of fluid drops at low surface tension and cytokinetic phenomena in the living cell. J. Chem. Soc., Faraday Trans. 2 76 (1980) 1170-1195.

13. J.B. Lewis, H.R.C. Pratt, Oscillating droplets. Nature 171 (1953) 1155-1156.

14. J. Temos, H.R.C. Pratt, G.W. Stevens, Mass transfer to freely-moving drops. Chem. Eng. Sci. 51 (1996) 27-36.

15. N.M. Kovalchuk, D. Vollhardt, Marangoni instability and spontaneous non-linear oscillations produced at liquid interfaces by surfactant transfer. Adv. Colloid Interface Sci. 120 (2006) 1-31.

16. L. Rayleigh, On convection currents in a horizontal layer of fluid, when the higher temperature is on the under side. Philos. Mag. Series 6 32 (1916) 529-546.

17. E.S. Perez de Ortiz, H. Sawistowski, Interfacial stability of binary liquid-liquid systems-I. Stability analysis. Chem. Eng. Sci. 28 (1973) 2051-2061.

18. E.S. Perez de Ortiz, H. Sawistowski, Interfacial stability of binary liquid-liquid systems-II. Stability behaviour of selected systems. Chem. Eng. Sci. 28 (1973) 2063-2069.

19. S. Slavtchev, M.A. Mendes, Marangoni instability in binary liquid-liquid systems. Int. J. Heat Mass Transfer 47 (2004) 3269-3278.

20. J.R.A. Pearson, On convection cells induced by surface tension. J. Fluid Mech. Digital Archive 4 (1958) 489-500.

21. E.S. Perez de Ortiz, H. Sawistowski, Stability analysis of liquid-liquid systems under conditions of simultaneous heat and mass transfer. Chem. Eng. Sci. 30 (1975) 1527-1528.

22. M. Hennenberg, T.S. Sørensen, A. Sanfeld, Deformational instability of a plane interface with transfer of matter. Part 1. - Non-oscillatory critical states with a linear concentration profile. J. Chem. Soc., Faraday Trans. 2 73 (1977) 48-66.

23. T.S. Sørensen, F.Y. Hansen, J. Nielsen, M. Hennenberg, Deformational instability of a plane interface with transfer of matter. Part 2. - Non-oscillatory and oscillatory modes with linear and exponential concentration profiles. J. Chem. Soc., Faraday Trans. 2 73 (1977) 1589-1601.

24. T.S. Sørensen, M. Hennenberg, F.Y. Hansen, Deformational instability of a plane interface with transfer of matter. Part 3. - Effects of thickness of

diffusion zone and of low surface tension. J. Chem. Soc., Faraday Trans. 2 74 (1978) 1005-1018.

25. M. Hennenberg, P.M. Bisch, M. Vignes-Adler, A. Sanfeld, Mass transfer, marangoni effect, and instability of interfacial longitudinal waves. I. Diffusional exchanges. J. Colloid Interface Sci. 69 (1979) 128-137.

26. M. Hennenberg, A. Sanfeld, P.M. Bisch, Adsorption-desorption barrier, diffusional exchanges and surface instabilities of longitudinal waves for aperiodic regimes. AIChE J 27 (1981) 1002-1008.

27. M.A. Mendes-Tatsis, E.S. Perez De Ortiz, Marangoni instabilities in systems with an interfacial chemical reaction. Chem. Eng. Sci. 51 (1996) 3755-3761.

28. A. Javadi, D. Bastani, J. Kragel, R. Miller, Interfacial instability of growing drop: Experimental study and conceptual analysis. Colloids Surf., A 347 (2009) 167-174.

29. B. Seifried, F. Temelli, Interfacial tension of fish oil triglycerides in contact with gas-expanded ethanol. Part 1: Measurement and correlation. J. Supercrit. Fluids (2010) (submitted).

30. B. Seifried, F. Temelli. Viscosity of marine lipids in equilibrium with high pressure carbon dioxide. in Proceedings: 9th International Symposium on Supercritical Fluids (ISSF). 2009. Arcachon, France.

31. R. Sih, M. Armenti, R. Mammucari, F. Dehghani, N.R. Foster, Viscosity measurements on saturated gas-expanded liquid systems - Ethanol and carbon dioxide. J. Supercrit. Fluids 43 (2008) 460-468.

32. B. Seifried, F. Temelli, Density of carbon dioxide-expanded ethanol at (313.2, 328.2 and 343.2) K. J. Chem. Eng. Data (2010) (published online March 29, 2010; DOI: 10.1021/je900830s).

33. B. Seifried, F. Temelli, Density of marine lipids in equilibrium with carbon dioxide. J. Supercrit. Fluids 50 (2009) 97-104.

34. D. Mock, A. Cabanas, J.A.R. Renuncio, C. Pando, Excess enthalpies of mixtures of olive oil and supercritical carbon dioxide. J. Supercrit. Fluids 14 (1999) 173-180.

35. R.A. Hauser, J.P. Zhao, P.R. Tremaine, A.E. Mather, Excess molar enthalpies of six (carbon dioxide + a polar solvent) mixtures at the temperatures 298.15 K and 308.15 K and pressures from 7.5 MPa to 12.6 MPa. J. Chem. Thermodyn. 28 (1996) 1303-1317.

36. D.R. Cordray, R.M. Izatt, J.J. Christensen, J.L. Oscarson, The excess enthalpies of (carbon dioxide + ethanol) at 308.15, 325.15, 373.15, 413.15, and 473.15 K from 5.00 to 14.91 MPa. J. Chem. Thermodyn. 20 (1988) 655-663.

37. E.J. Hernandez, G.D. Mabe, F.J. Senorans, G. Reglero, T. Fornari, High-pressure phase equilibria of the pseudoternary mixture sunflower oil plus ethanol plus carbon dioxide. J. Chem. Eng. Data 53 (2008) 2632-2636.

38. B. Seifried, F. Temelli, Interfacial tension of marine lipids in contact with high pressure carbon dioxide. J. Supercrit. Fluids 52 (2010) 203-214.

39. I. Tsivintzelis, D. Missopolinou, K. Kalogiannis, C. Panayiotou, Phase compositions and saturated densities for the binary systems of carbon dioxide with ethanol and dichloromethane. Fluid Phase Equilib. 224 (2004) 89-96.

40. Z. Knez, M. Skerget, L. Ilic, C. Lutge, Vapor-liquid equilibrium of binary $CO_2$-organic solvent systems (ethanol, tetrahydrofuran, ortho-xylene, meta-xylene, para-xylene). J. Supercrit. Fluids 43 (2008) 383-389.

41. C. Borch-Jensen, J. Mollerup, Phase equilibria of fish oil in sub- and supercritical carbon dioxide. Fluid Phase Equilib. 138 (1997) 179-211.

42. M.G. Velarde, A.Y. Rednikov, Y.S. Ryazantsev, Drop motions and interfacial instability. J. Phys. Condens. Matter 8 (1996) 9233-9247.

43. N.O. Young, J.S. Goldstein, M.J. Block, The motion of bubbles in a vertical temperature gradient. J. Fluid Mech. 6 (1959) 350-356.

44. A.V. Hershey, Ridges in a liquid surface due to the temperature dependence of surface tension. Phys. Rev. 56 (1939) 204-204.

45. D.A. Haydon, An investigation of droplet oscillation during mass transfer. 1. The conditions necessary, and the source of the energy for the oscillations. Proc. R. Soc. London, Ser. A 243 (1958) 483-491.

46. T. Sørensen, M. Hennenberg, Instability of a spherical drop with surface chemical reactions and transfer of surfactants, in Lecture notes in physics: Dynamics and instability of fluid interfaces. 1979, Springer Berlin / Heidelberg. p. 276-315.

47. C.A. Miller, L.E. Scriven, The oscillations of a fluid droplet immersed in another fluid. J. Fluid Mech. 32 (1968) 417-435.

48. E. Badens, O. Boutin, G. Charbit, Laminar jet dispersion and jet atomization in pressurized carbon dioxide. J. Supercrit. Fluids 36 (2005) 81-90.

49. A.W. Kerst, B. Judat, E.U. Schlünder, Flow regimes of free jets and falling films at high ambient pressure. Chem. Eng. Sci. 55 (2000) 4189-4208.

50. N. Czerwonatis, R. Eggers, Disintegration of liquid jets and drop drag coefficients in pressurized nitrogen and carbon dioxide. Chem. Eng. Technol. 24 (2001) 619-624.

51. S.S. Dukhin, C. Zhu, R. Dave, R. Pfeffer, J.J. Luo, F. Chavez, Y. Shen, Dynamic interfacial tension near critical point of a solvent-antisolvent mixture and laminar jet stabilization. Colloids Surf., A 229 (2003) 181-199.

52. L.Y. Lee, L.K. Lim, J. Hua, C.H. Wang, Jet breakup and droplet formation in near-critical regime of carbon dioxide-dichloromethane system. Chem. Eng. Sci. 63 (2008) 3366-3378.

# 8 Viscosity of Fish Oil Triglycerides in Equilibrium with High Pressure Carbon Dioxide[1]

## 8.1 Introduction

Lipids when saturated and expanded with $CO_2$ under pressure undergo significant changes in their physical and transport properties, including density (Chapter 3) [1], interfacial tension (Chapter 4) [2] and viscosity [3]. Viscosity affects a wide variety of processes through its impact on mass, heat and momentum transfer. Optimal design of processing equipment involving high pressure $CO_2$ requires viscosity data, due to its impact on jet formation [4], flow behavior of falling films [5-7], reactions and membrane separations [8], as well as gas-assisted mechanical oilseed pressing [9, 10].

Peter and coworkers [3, 11] used a capillary viscometer to determine the viscosity and rheological behavior of soybean oil [3] and various fatty acids [11] saturated with $CO_2$, ethane or propane and reported that the decrease in viscosity with pressure was more pronounced for systems equilibrated with ethane and especially with propane. Lockemann *et al.* [12] determined the liquid phase viscosities of the systems $CO_2$+oleic acid, $CO_2$+methyl myristate, and $CO_2$+methyl palmitate at 40, 50, and 60°C and pressures of up to 12.6 MPa by visually observing the rising or sinking velocity of small saturated gas bubbles and of glass beads, respectively, in the liquid within a high-pressure view cell. The authors [12] found that the viscosity decreased by about an order of magnitude for both the fatty acid esters and fatty acid to fairly constant levels at elevated pressures independent of temperature. Furthermore, the viscosity of fatty acid ethyl esters was about an order of magnitude lower than that of the fatty acid [12]. The viscosities of oleic and linoleic acid and their methyl esters as well as anhydrous milk fat saturated with dense $CO_2$ were determined with a closed loop capillary viscometer and Newtonian flow behavior of these mixtures was demonstrated [13]. Viscosity of $CO_2$-saturated cocoa butter measured with a high pressure quartz viscometer at several temperatures [14] decreased with $CO_2$

[1] A version of this chapter has been submitted to J. Supercrit. Fluids (2010) for consideration for publication.

pressure to constant levels depending on temperature, which is contrary to findings for other systems such as corn oil [15]. At $CO_2$ pressures above 15 MPa, the viscosity of $CO_2$-saturated cocoa butter reached a higher constant value (4 mPa.s) at 40°C than at 80 or 100°C (both about 2.5 mPa.s) [14]. On the other hand, the viscosity of $CO_2$-saturated corn oil [9, 15, 16] measured with a rolling ball viscometer decreased with $CO_2$ pressure to a practically temperature-independent value of around 2.5 mPa.s at pressures above 15 MPa and remained constant up to 30 MPa. The viscosity of $CO_2$-saturated mixtures of sunflower oil/methyl laureate [8] and castor oil/methyl oleate [8] were reported to decrease substantially with $CO_2$ pressure also reaching relatively constant levels of about 11 and 4 mPa.s, respectively. Even though several studies have reported liquid phase viscosity of $CO_2$-expanded lipids there is lack of viscosity and rheological data for $CO_2$-expanded fish oil in the literature. Therefore, the objective of this study was to determine the viscosity and rheological behavior of fish oil triglycerides in equilibrium with $CO_2$ at 40, 55 and 70°C and pressures of up to about 12 MPa.

## 8.2 Experimental

### 8.2.1 Materials

Refined fish oil extracted from anchovy and sardine was obtained from Ocean Nutrition Canada (ONC, Halifax, NS, Canada) in the form of triglycerides (TG), as described in Section 3.2.1. Certified standard calibration oils of various viscosities were used to check the calibration and performance of the rheometer (oils S3, S6, N10, Cannon Instrument Company, State College, PA, USA). All other material specifications and handling protocols were similar to those described in Section 3.2.1.

### 8.2.2 Viscosity measurements

#### 8.2.2.1 Apparatus to determine viscosity

The apparatus to determine viscosity and rheological properties of fish oil in equilibrium with $CO_2$ at 40, 55 and 70°C at pressures of up to 12.4 MPa consisted of a computer controlled rotational rheometer (UDS200, Anton Paar, Graz, Austria) equipped with a bob and cup setup (CC 23Pr/Q0, Anton Paar, Graz, Austria) in a thermostated pressure cell (TEZ 150P, Anton Paar, Graz, Austria) with Peltier temperature control (Fig. 8-1). The bob and cup had a radius of 11.52 and 12.5 mm, respectively, with an active length of 83.5 mm. The pressure cell with a sample volume of 11.5 mL rated up to 15 MPa was equipped with a magnetic coupling pressure head. The system was pressurized using a $CO_2$ cylinder with a helium headspace at 12.4 MPa (Praxair, Edmonton, AB, Canada) together with a pressure reducing regulator (Swagelok KPP series, Swagelok, Edmonton, AB, Canada). The pressure in the system was monitored by means of a Bourdon type pressure gauge.

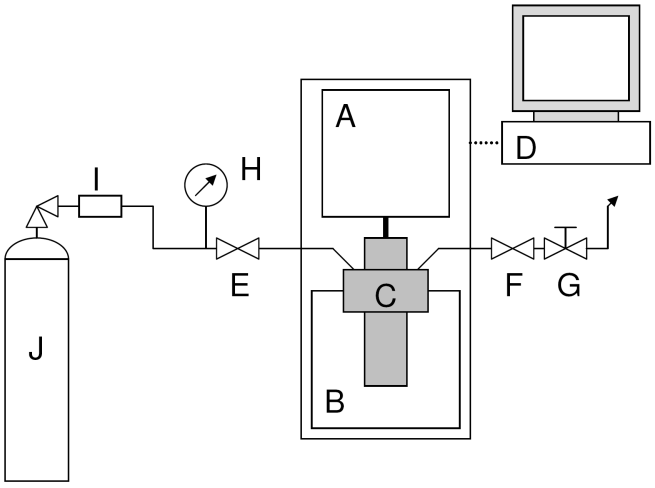


**Figure 8-1.** Rheometer setup: A) rheometer, B) thermostat, C) high pressure cell, D) computer, E) inlet valve, F) outlet valve, G) metering valve, H) pressure indicator, I) pressure reducing regulator, J) $CO_2$ cylinder.

#### 8.2.2.2 Calibration and performance

The performance of the system was first tested at atmospheric pressure with certified standard calibration oils of various viscosities (Cannon Instrument Company, State College, PA, USA). During preliminary tests with high pressure $CO_2$ it was observed that after several experiments the internal friction of the pressure head increased contributing to the torque required to turn the bob thereby leading to inflated viscosity values. The increase in friction could be caused by extraction of lubricant from the ball bearings by dense $CO_2$ or by deposits of viscous lipids introduced during experiments. Therefore, before experiments the ball bearings inside the magnetic coupling head needed to be cleaned with acetone and lubricated using a few drops of low viscosity mineral oil (S3 standard oil, Cannon Instrument Company, State College, PA, USA). By cleaning and lubricating the bearings frequently friction was kept at a minimum so that the performance of the system was acceptable resulting in reproducible results. To verify the system performance at elevated pressures the viscosity of corn oil saturated with pressurized $CO_2$ was determined at a shear rate of 300 $s^{-1}$ at 40°C and pressures of up to 5.5 MPa, which compared well to available literature data [15] as illustrated in Fig. 8-2.

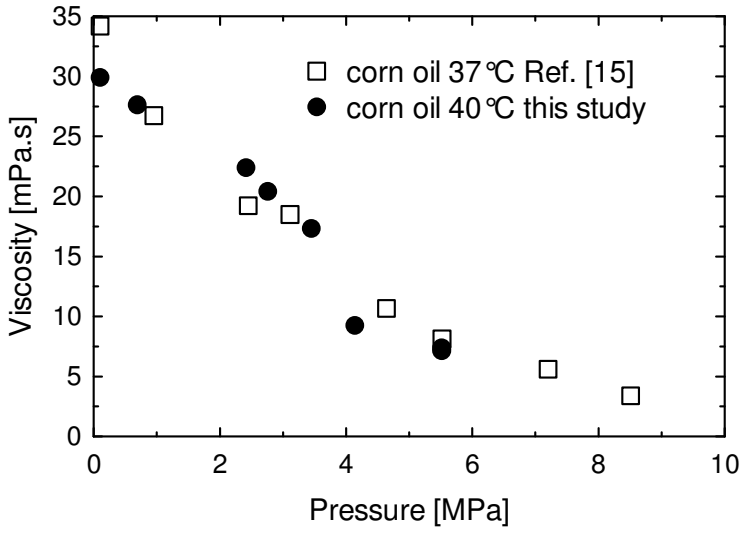


**Figure 8-2.** Viscosity of corn oil saturated with $CO_2$ at 40°C and various pressures determined in this study at a shear rate of 300 $s^{-1}$ compared to literature data at 37°C determined with a rolling ball viscometer [15].

#### 8.2.2.3 Determination of viscosity

The high pressure cell was flushed with $CO_2$ and preheated to the desired temperature prior to experiments. In order to fill the high pressure cell, the oulet tubing was disconnected and a known amount of fish oil (11.5 mL) was filled into the cell. The system was then slowly filled with $CO_2$ to the desired pressure level by adjusting the pressure reducing regulator. Since there was no mechanical mixing, equilibration and saturation of fish oil with $CO_2$ at elevated pressures inside the pressure cell took up to about 12 h for each pressure setting as indicated by a constant viscosity value measured by means of the rheometer. In a previous study reported in Chapter 3 [1], it was found that fish oil expanded up to about 40% by volume when equilibrated with $CO_2$ at pressures of up to 15 MPa at 40°C. The expansion of oil could lead to errors in case the ball bearings located inside the top of the pressure head get submersed in expanded fish oil. Therefore, $CO_2$ was carefully bubbled through the headspace of the high pressure cell every 1-2 h and prior to measurements to purge out expanded excess fish oil. For the first set of measurements, fish oil viscosity was determined at a constant shear rate of 300 $s^{-1}$ at all pressure and temperature levels. Then, the rheological properties were evaluated at each pressure level by measuring shear stress $\tau$ in [Pa] at different shear rates $\gamma$ in [$s^{-1}$] ranging from 100 to 500 $s^{-1}$. The consistency index $K$ in [Pa.$s^n$] and the dimensionless flow behavior index n were determined according to the power law:

$$\tau = K * \gamma^n \qquad (8\text{-}1)$$

All measurements were performed in triplicate under each condition.

## 8.3 Results and discussion

### 8.3.1 Viscosity

Viscosity of fish oil saturated with $CO_2$ is reported in Table 8-1 at a shear rate of 300 $s^{-1}$ at 40, 55, and 70°C and pressures of 0.1 to 12.4 MPa. Temperature and $CO_2$ pressure had a substantial effect on the viscosity of $CO_2$-expanded fish oil (Fig. 8-3). At atmospheric pressure, the viscosity of fish oil decreased

exponentially with temperature, which is consistent with findings reported for other vegetable oils [17].

**Table 8-1.** Viscosity of fish oil saturated with $CO_2$ at various pressures measured at 40, 55 and 70°C.

| T [°C] | P [MPa] | $\eta_{exp}$±SD[a] [mPa.s] |
|---|---|---|
| 40 | 0.1 | 24.98±0.41 |
| | 1.38 | 15.66±0.46 |
| | 2.76 | 10.57±0.36 |
| | 3.79 | 8.13±n/a |
| | 4.04 | 7.47±0.43 |
| | 5.86 | 4.95±0.3 |
| | 6.78 | 3.91±0.37 |
| | 9.65 | 2.63±0.17 |
| | 12.2 | 2.65±0.07 |
| 55 | 0.1 | 16.34±0.5 |
| | 3.1 | 8.77±0.28 |
| | 4.41 | 6.88±0.03 |
| | 6.02 | 5.37±0.21 |
| | 6.89 | 4.67±0.18 |
| | 9.65 | 3.63±0.09 |
| | 12.24 | 3.19±0.17 |
| 70 | 0.1 | 11.6±0.19 |
| | 2.76 | 7.08±0.5 |
| | 3.78 | 6.42±0.55 |
| | 6.19 | 4.92±0.22 |
| | 6.79 | 4.75±0.13 |
| | 9.62 | 3.98±0.17 |
| | 12.21 | 3.38±0.23 |

[a] Mean±standard deviation (SD) based on triplicate measurements.

With increasing saturation pressure of $CO_2$ the viscosity of $CO_2$-saturated fish oil decreased considerably. At 40°C, the viscosity decreased with $CO_2$ pressure by an order of magnitude from about 25 to 2.5 mPa.s by increasing the pressure from 0.1 to 12.4 MPa. These results are similar to those reported for corn oil saturated with $CO_2$, which also reached a fairly constant level of about 2.5 mPa.s at elevated pressures [15]. The effect of pressure on viscosity was more pronounced at lower temperatures due to a higher solubility of $CO_2$ in fish oil.

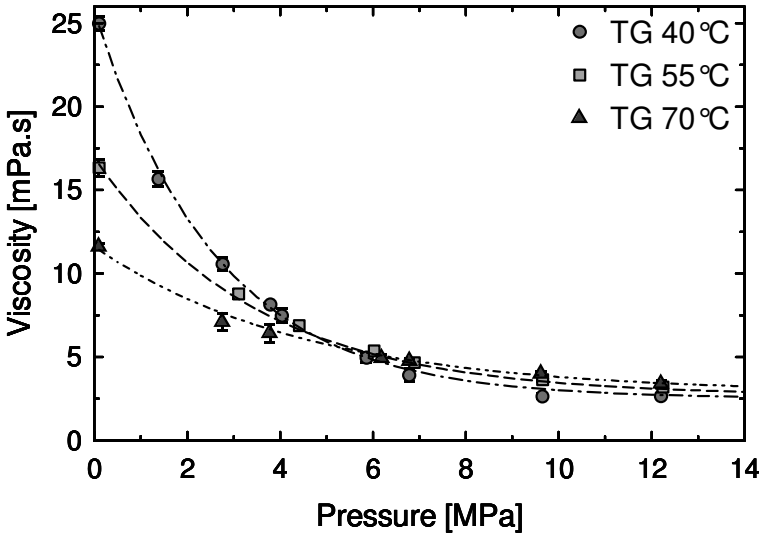


**Figure 8-3.** Viscosity of fish oil in equilibrium with $CO_2$ as a function of pressure at various temperatures at a shear rate of 300 $s^{-1}$. Lines were calculated using the correlation given in Eq. (8-2). Error bars represent standard deviation based on triplicate measurements.

At elevated pressures up to 12 MPa all isotherms approached viscosity levels of around 2.5 mPa.s with a slightly lower value for the lower temperatures. At about 5 MPa, a crossover of isotherms could be observed where the influence of temperature on viscosity was reversed. At pressures above 5 MPa, an increase in temperature caused a slight increase in viscosity due to the reduced solubility of $CO_2$ in fish oil at higher temperatures [18].

The following model correlates the measured viscosity data to pressure and temperature:

$$\eta(P,T) = \eta_{\infty}(T) + \left[(\eta_0(T) - \eta_{\infty}(T)\right] * e^{(-k(T)*(P-0.1))} \quad (8\text{-}2)$$

The first term $\eta_{\infty}(T)$ describes the asymptotically reached level of viscosity at elevated pressure as a function of temperature:

$$\eta_{\infty}(T) = A_1 + A_2 * T \quad (8\text{-}3)$$

The term $\eta_0(T)$ represents the viscosity at atmospheric pressure as a function of temperature according to the equation presented by Andrade [19]:

$$\eta_0(T) = A_3 * e^{\left(\frac{A_4}{T}\right)} \quad (8\text{-}4)$$

The temperature dependent exponential decline of viscosity with pressure is described by the last term with the exponent $k(T)$:

$$k(T) = A_5 * e^{-A_6 * T} \tag{8-5}$$

The model given in Eq. (8-2) with the calculated parameters presented in Table 8-2 described the experimental data well (Fig. 8-3) within the temperature and pressure range investigated in this study, with pressure $P$ in [MPa], temperature $T$ in [K] and viscosity $\eta$ in [mPa.s].

**Table 8-2.** Model parameters for correlation of viscosity of $CO_2$-expanded fish oil using Eq. (8-2).

| Model parameters | |
|---|---|
| $A_1$ | $-9.8413 \times 10^{-1}$ |
| $A_2$ | $1.1127 \times 10^{-2}$ |
| $A_3$ | $3.3975 \times 10^{-3}$ |
| $A_4$ | $2.7860 \times 10^{+3}$ |
| $A_5$ | $1.2583 \times 10^{+2}$ |
| $A_6$ | $1.8502 \times 10^{-2}$ |

### 8.3.2 Rheological behavior

Rheological behavior of fish oil saturated with $CO_2$ was evaluated at shear rates ranging from 100 to 500 $s^{-1}$ at 40, 55, and 70°C and pressures up to 12.4 MPa (Table 8-3). Fish oil saturated with pressurized $CO_2$ exhibited shear thickening (i.e. dilatant) flow behavior at elevated $CO_2$ pressures, which is demonstrated in Fig. 8-4 showing the increase of reduced viscosity at 40°C and various pressures as a function of shear rate. The reduced viscosity ($\eta_{red}$) was calculated according to Eq. (8-6):

$$\eta_{red}(P,T) = \frac{\eta(P,T)}{\eta_{250}(P,T)} \tag{8-6}$$

where $\eta(P,T)$ denotes the viscosity at various shear rates and $\eta_{250}(P,T)$ the viscosity determined at a shear rate of 250 $s^{-1}$ for the same pressure and temperature conditions. The viscosity was nearly independent of shear rate at atmospheric pressure indicating almost Newtonian behavior, whereas at elevated

pressures the value for viscosity at a shear rate of 500 $s^{-1}$ increased by up to 40% relative to that measured at a shear rate of 250 $s^{-1}$ (Fig. 8-4).

**Table 8-3.** Flow behavior index *n* and common logarithm of consistency index *K* for fish oil saturated with $CO_2$ at 40, 55 and 70°C.

| T [°C] | P [MPa] | n±SD[a] [] | $\log_{10}$ K±SD[a] $\log_{10}$ [Pa.s$^n$] |
|---|---|---|---|
| 40 | 0.10 | 1.02±0.02 | -1.64±0.047 |
| | 1.38 | 1.10±0.02 | -2.04±0.046 |
| | 2.76 | 1.15±0.02 | -2.35±0.047 |
| | 4.00 | 1.17±0.00 | -2.54±0.017 |
| | 5.57 | 1.34±0.04 | -3.16±0.104 |
| | 6.84 | 1.55±0.06 | -3.83±0.171 |
| | 9.65 | 1.41±0.07 | -3.49±0.202 |
| | 12.41 | 1.55±0.02 | -3.90±0.058 |
| 55 | 0.10 | 1.05±0.03 | -1.92±0.078 |
| | 3.10 | 1.10±0.01 | -2.29±0.024 |
| | 4.41 | 1.11±0.01 | -2.47±0.031 |
| | 6.00 | 1.13±0.02 | -2.61±0.078 |
| | 6.89 | 1.21±0.08 | -2.86±0.241 |
| | 9.65 | 1.20±0.02 | -2.94±0.118 |
| | 12.24 | 1.37±0.11 | -3.41±0.343 |
| 70 | 0.10 | 1.07±0.01 | -2.12±0.026 |
| | 2.76 | 1.10±0.03 | -2.40±0.063 |
| | 3.49 | 1.11±0.01 | -2.44±0.046 |
| | 4.14 | 1.13±0.06 | -2.57±0.159 |
| | 5.65 | 1.09±0.01 | -2.58±0.026 |
| | 6.19 | 1.16±0.03 | -2.71±0.119 |
| | 6.81 | 1.21±0.03 | -2.86±0.112 |
| | 9.65 | 1.22±0.03 | -2.97±0.097 |
| | 12.24 | 1.42±0.07 | -3.58±0.190 |

[a] Mean±standard deviation (SD) based on triplicate measurements.

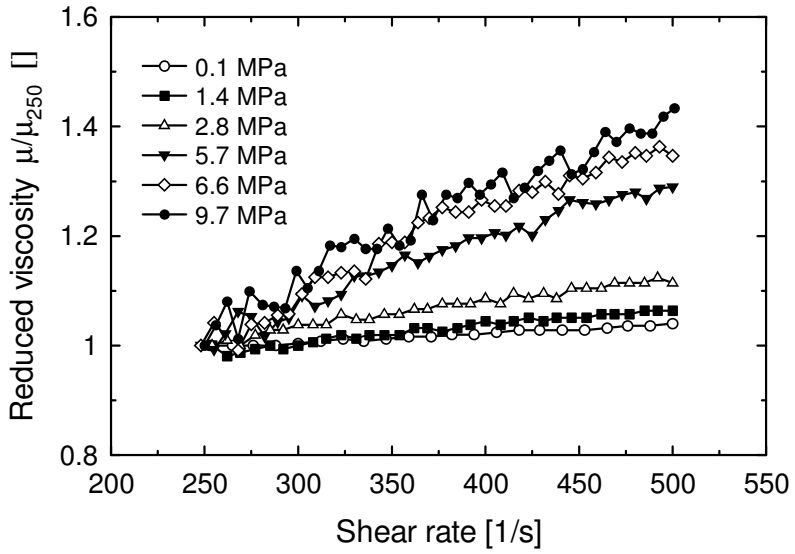


**Figure 8-4.** Shear thickening behavior of fish oil saturated with $CO_2$ at 40°C and various pressures showing the reduced viscosity ($\eta/\eta_{250}$) according to Eq. (8-6) versus shear rate ranging from 250 to 500 $s^{-1}$.

The relative fluctuations in the measured data increased with increasing pressure, since viscosity reached lower levels thereby increasing experimental uncertainty. Nevertheless, a pronounced increase in viscosity with shear rate could be observed at elevated pressures (Fig. 8-4). Furthermore, it is demonstrated in Fig. 8-4 that an increase in pressure from 2.8 to 5.7 MPa strongly affected the shear thickening behavior, while the effect of a further increase in pressure to 6.6 and 9.7 MPa was comparably less pronounced.

The rheological flow behavior was analyzed according to the power law given in Eq. (8-1). The flow behavior index *n* and consistency index *K* could be obtained by plotting the flow curves for the shear stress versus shear rate on a log-log scale resulting in straight lines, as illustrated in Fig. 8-5 for fish oil saturated at 40°C. By fitting a linear equation to the data the slope and the intercept of the flow curves corresponding to the flow behavior index *n* and common logarithm of the consistency index *K*, respectively, can be obtained.

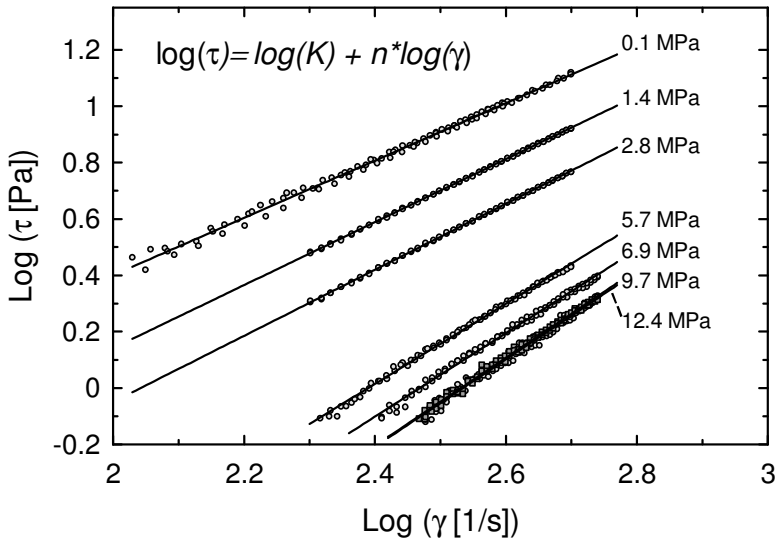


**Figure 8-5.** Flow curves according to the power law given in Eq. (8-1) for fish oil saturated with $CO_2$ at 40°C and various pressures measured at shear rates ranging from 100 to 500 $s^{-1}$.

As evidenced by the flow curves, the flow behavior index or slope of the flow curves increased with pressure, while the consistency index or intercept decreased (Fig. 8-5). However, at pressures above 6.9 MPa the flow curves in Fig. 8-5 had nearly the same slope, indicating that the flow behavior index and thus dilatant behavior seemed to approach a fairly constant level once a certain degree of saturation in the liquid phase was achieved. In this context, it should be mentioned that at 40°C, the viscosity decreased substantially up to about 6.9 MPa, whereas a further increase in pressure caused little change in viscosity (Fig. 8-3). Likewise, the flow behavior index increased from initially around $n$=1 at atmospheric conditions demonstrating Newtonian flow behavior to about $n$=1.55 at 6.9 MPa indicating dilatant flow behavior. Further increase in pressure to 12.4 MPa did not affect the flow behavior index $n$ strongly. Furthermore, the flow curves at pressures of 9.7 and 12.4 MPa appeared to be almost identical (Fig. 8-5) indicating that viscosity as well as dilatant flow behavior reached a plateau.

Previous evaluation of the volumetric expansion of fish oil TG in equilibrium with $CO_2$ at 40°C (Chapter 3) showed that the expansion reached a

plateau as well at pressures of 8 to 10 MPa. Thus, it can be speculated that viscosity and rheological behavior are related to volumetric expansion.

The impact of pressure and temperature on the flow behavior index *n* and consistency index *K* are illustrated in Figs. 8-6 and 8-7, respectively. For the flow behavior indices at 55 and 70°C a somewhat similar trend could be observed (Fig. 8-6). At all temperatures, the flow behavior index *n* was close to 1 at atmospheric conditions and increased with pressure (Fig. 8-6). On the other hand, the consistency index K (shown as log *K* in Fig. 8-7) decreased with pressure to very low values . The consistency index (*K*) approached values close to zero at high pressures (Fig. 8-7). Dilatant flow behavior was also observed for the systems pelargonic acid+$CO_2$ and pelargonic acid+ethane, whereas oleic, linoleic and valeric acids did not show dilatant flow behavior when saturated with the same gases [11]. Furthermore, dilatant flow behavior was also reported for a 4:1 mixture of oleic acid+stearic acid saturated with $CO_2$ at elevated pressures [3].

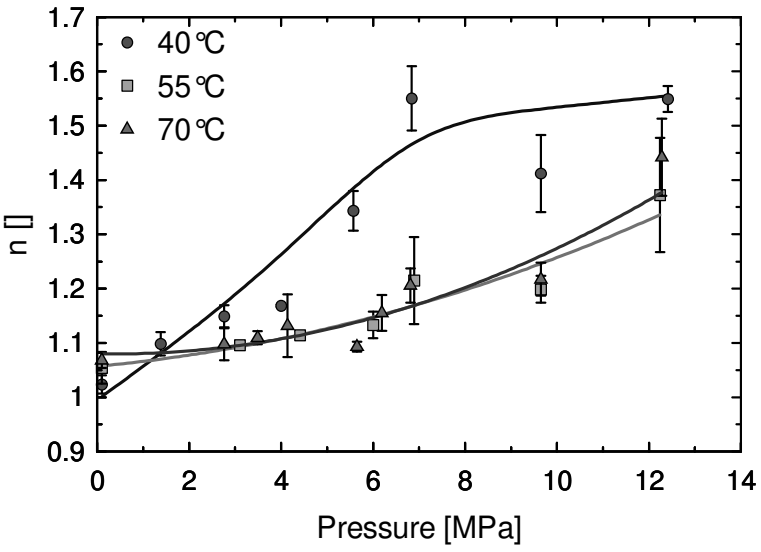


**Figure 8-6.** Flow behavior index n of $CO_2$-expanded fish oil versus pressure at different temperatures. Error bars represent standard deviation based on triplicate measurements.

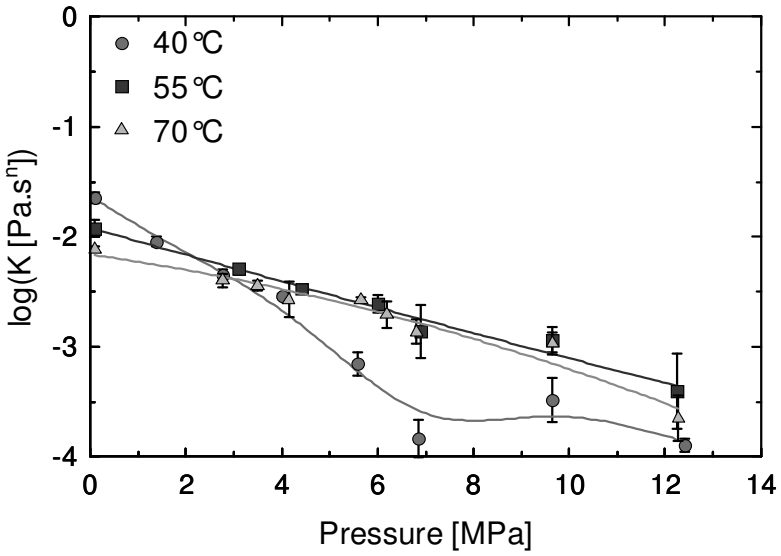


**Figure 8-7.** Consistency index K of $CO_2$-expanded fish oil versus pressure at different temperatures. Error bars represent standard deviation based on triplicate measurements.

## 8.4 Conclusions

Viscosity of fish oil in equilibrium with $CO_2$ was determined at 40, 55 and 70°C and pressures of up to 12 MPa. The viscosity decreased substantially with increasing pressure. At 40°C, the viscosity decreased by about an order of magnitude due to the high solubility of $CO_2$ in fish oil. At elevated pressures, fish oil expanded with $CO_2$ exhibited pronounced shear thickening behavior, which seemed to reach a plateau at pressures where viscosity approached a constant value as well. The decrease in liquid phase viscosity and change in rheological behavior appeared to be linked to volumetric expansion caused by uptake of $CO_2$. Knowledge of rheological properties of lipids, such as fish oil triglycerides, is fundamental to understand and optimize processing equipment for existing and novel technologies under development using high pressure $CO_2$. Fundamental viscosity data will help to better understand flooding behavior of packed columns operated at high pressure or to optimize spray nozzle design. New process development as well as optimization and modeling of existing processes will benefit from the viscosity data.

## 8.5 References


1. B. Seifried, F. Temelli, Density of marine lipids in equilibrium with carbon dioxide. J. Supercrit. Fluids 50 (2009) 97-104.

2. B. Seifried, F. Temelli, Interfacial tension of marine lipids in contact with high pressure carbon dioxide. J. Supercrit. Fluids 52 (2010) 203-214.

3. S. Peter, E. Weidner, H. Jakob, Die Viskosität koexistierender Phasen bei der überkritischen Fluidextraktion. Chem. Ing. Tech. 59 (1987) 59-62.

4. N. Czerwonatis, R. Eggers, Disintegration of liquid jets and drop drag coefficients in pressurized nitrogen and carbon dioxide. Chem. Eng. Technol. 24 (2001) 619-624.

5. A. Blaha-Schnabel, A. Beyer, B. Czech, H. Jakob, H. Schiemann, E. Weidner, S. Peter, Influence of interfacial tension and viscosity on the behavior of a packed column in near-critical fluid extraction. Chem. Eng. Commun. 146 (1996) 13-31.

6. M. Moser, C. Trepp, Investigating the stability of falling films at round vertical film carriers under high pressure. Chem. Eng. Technol. 20 (1997) 612-616.

7. R. Stockfleth, G. Brunner, Film thickness, flow regimes, and flooding in countercurrent annular flow of a falling film at high pressures. Ind. Eng. Chem. Res. 40 (2001) 6014-6020.

8. E. Pomier, N. Delebecque, D. Paolucci-Jeanjean, M. Pina, S. Sarrade, G.M. Rios, Effect of working conditions on vegetable oil transformation in an enzymatic reactor combining membrane and supercritical $CO_2$. J. Supercrit. Fluids 41 (2007) 380-385.

9. S. Voges, R. Eggers, A. Pietsch, Gas assisted oilseed pressing. Sep. Purif. Technol. 63 (2008) 1-14.

10. P. Willems, N.J.M. Kuipers, A.B. de Haan, Gas assisted mechanical expression of oilseeds: Influence of process parameters on oil yield. J. Supercrit. Fluids 45 (2008) 298-305.

11. S. Peter, H. Jakob, The rheological behavior of coexisting phases in systems containing fatty acids and dense gases. J. Supercrit. Fluids 4 (1991) 166-172.

12. C.A. Lockemann, E.U. Schlünder, Liquid-phase viscosities of the binary systems carbon dioxide-oleic acid, carbon dioxide-methyl myristate, and carbon dioxide-methyl palmitate at high pressures. Chem. Eng. Process. 34 (1995) 487-493.

13. P. Kashulines, S.S.H. Rizvil, P. Harriott, J.A. Zollweg, Viscosities of fatty acids and methylated fatty acids saturated with supercritical carbon dioxide. J. Am. Oil Chem. Soc. 68 (1991) 912-921.

14. M.J. Venter, P. Willems, S. Kareth, E. Weidner, N.J.M. Kuipers, A.B. de Haan, Phase equilibria and physical properties of $CO_2$-saturated cocoa butter mixtures at elevated pressures. J. Supercrit. Fluids 41 (2007) 195-203.

15. M. Hobbie, Ph.D. Thesis: Bildung von Tropfen in verdichteten Gasen und stationäre Umströmung fluider Partikel bei Drücken bis zu 50 MPa. 2006, TU Hamburg-Harburg: Hamburg, Germany.

16. P.T. Jaeger, Ph.D. Thesis: Grenzflächen und Stofftransport in verfahrenstechnischen Prozessen am Beispiel der Hochdruck-Gegenstrom-fraktionierung mit überkritischem Kohlendioxid. 1998, TU Hamburg-Harburg: Hamburg, Germany.

17. H. Noureddini, B. Teoh, L. Davis Clements, Viscosities of vegetable oils and fatty acids. J. Am. Oil Chem. Soc. 69 (1992) 1189-1191.

18. C. Borch-Jensen, J. Mollerup, Phase equilibria of fish oil in sub- and supercritical carbon dioxide. Fluid Phase Equilib. 138 (1997) 179-211.

19. E. Andrade, The viscosity of liquids. Nature 125 (1930) 309-310.

# 9 Viscosity of Fish Oil Fatty Acid Ethyl Esters in Equilibrium with High Pressure Carbon Dioxide[1]

## 9.1 Introduction

Processing of lipids using supercritical fluids, especially supercritical carbon dioxide (SC-$CO_2$), has been studied for many decades and still offers potential for novel process development [1]. In separation processes, the knowledge of phase equilibrium data is as important as the understanding of transport properties, such as viscosity. Viscosity of liquids saturated and expanded with $CO_2$ greatly influences the performance of processing equipment due to its effects on mass, heat and momentum transfer. The viscosity of $CO_2$-expanded lipids is much lower than that of pure lipids under pressure, which plays a key role in a wide variety of processes such as jet formation [2], the flowing behavior of falling films [3-5], reactions and membrane separations [6], as well as gas-assisted mechanical oilseed pressing [7, 8]. In general, the liquid phase viscosities decreased substantially with increasing $CO_2$ pressure in all lipid+$CO_2$ systems reported, whereas the viscosity of the gas phase containing $CO_2$+lipids increased [9]. For example, for the system $CO_2$+methyl oleate in the dense gas phase a linear increase in viscosity with mass fraction of methyl oleate was reported, resulting in a viscosity rise of about 20% for a lipid content of 5 wt% compared to pure SC-$CO_2$ under the same conditions [10].

The liquid phase viscosity of lipids in dense gas systems has been studied for many decades applying numerous experimental techniques. Viscosity and rheological flow behavior were determined for soybean oil and various fatty acids saturated with $CO_2$, ethane or propane using a high pressure capillary viscometer [9, 11]. Viscosity of fatty acids and methyl esters saturated with $CO_2$ were determined by visually observing the rising or sinking velocity of small saturated gas bubbles or of glass beads, respectively [12]. The viscosities of oleic and linoleic acid, their methyl esters as well as anhydrous milk fat saturated with

[1] A version of this chapter has been submitted to J. Supercrit. Fluids (2010) for consideration for publication.

dense $CO_2$ were determined with a closed loop capillary viscometer [13]. Viscosity of $CO_2$-saturated cocoa butter was measured with a high pressure quartz viscometer [14] and that of $CO_2$-saturated corn oil measured with a rolling ball viscometer [7, 15, 16]. A vibrating rod viscometer was used to measure the viscosity of $CO_2$-saturated mixtures of sunflower oil/methyl laureate [6] and castor oil/methyl oleate [6]. The liquid phase viscosities of gas-expanded methanol, ethanol and acetone were determined with a falling weight viscometer [17-19]. Other techniques employed for measuring viscosities of gases and liquids under high pressure such as pressurized $CO_2$ include a torsionally rotating quartz crystal [20], vibrating wire viscometer [21, 22] or oscillating disc [23].

The use of oscillating quartz crystals oscillating in thickness-shear mode, such as a quartz crystal microbalance (QCM), for measuring viscosities at elevated pressures has not been employed extensively. A QCM was used to study the viscosity of a supercritical electrolyte solution [24], consisting of quaternary ammonium salts in supercritical difluoromethane (SC-$CH_2F_2$) up to pressures of 30 MPa. Furthermore, the effects of various solutes, such as salicylic acid, naphthalene, and p-methylbenzoic acid on the viscosity of SC-$CH_2F_2$ were investigated using a QCM [25]. However, both studies [24, 25] did not seem to take into account the influence of pressure on the resonant frequency of the QCM. Investigations [26-28] on the behavior of a QCM under high pressure $CO_2$ have shown that the resonance frequency of a QCM is affected by mass loading, the surrounding fluid properties (viscosity, density), adsorption at the surface, hydrostatic pressure, temperature, and surface roughness of the QCM. The basic QCM theory and numerous applications were reviewed previously [29]. Further high pressure QCM applications include solubility measurements of metal chelates [30], the detection of the vapor-liquid critical point of multi-component mixtures [31], measuring dissolution of polymer films into SC-$CO_2$ [32] or monitoring high pressure phase behavior of binary mixtures to map the phase diagram [33].

The objectives of this study were to determine the viscosity and rheological behavior of fish oil fatty acid ethyl esters (FAEE) in equilibrium with

$CO_2$ at 40, 55 and 70°C and pressures of up to about 12 MPa using a rotational viscometer furnished with a high pressure cell and to assess the potential of a QCM to determine the viscosity of CX liquids at elevated pressures.

## 9.2 Experimental

### 9.2.1 Materials

All materials used in this study, such as refined fish oil FAEE, anhydrous ethanol, bone dry $CO_2$ and nitrogen were similar to those described in Section 3.2.1. Furthermore, acetone (HPLC grade, Fisher Scientific Canada, Ottawa, ON, Canada) was used for cleaning and calibration purposes of the rotational viscosimeter and QCM.

### 9.2.2 Apparatus

#### 9.2.2.1 Rotational rheometer

The apparatus to determine viscosity and rheological properties of FAEE in equilibrium with $CO_2$ at 40, 55 and 70°C and pressures of up to 12.4 MPa consisted of a computer controlled rotational rheometer (UDS200, Anton Paar, Graz, Austria) equipped with a bob and cup setup in a thermostated pressure cell with Peltier temperature control. The apparatus was described in detail in Section 8.2.2.1. Prior to experiments the ball bearings of the magnetic coupling inside the pressure head were cleaned with acetone and lubricated with low viscosity mineral oil (S3 standard oil, Cannon Instrument Company, State College, PA, USA) to keep friction at a minimum. The friction in the system was determined prior to experiments and the motor of the rheometer adjusted accordingly. By cleaning and lubricating the bearings frequently friction was kept at a minimum so that the performance of the system was acceptable resulting in fairly reproducible results.

#### 9.2.2.2 Quartz crystal microbalance

The main setup of the apparatus for evaluating the performance of the QCM for viscosity measurements consisted mainly of a syringe pump (ISCO Model 250D,

Isco Inc., Lincoln, NE, USA), a circulating pump, and a high-pressure view cell equipped with electric heaters and placed in a temperature controlled insulated air bath, which has been described in detail in Section 3.2.3 [34]. However, some modifications were undertaken to accommodate an additional high pressure cell equipped with the QCM between the view cell and the circulation pump, as illustrated in Fig. 9-1.

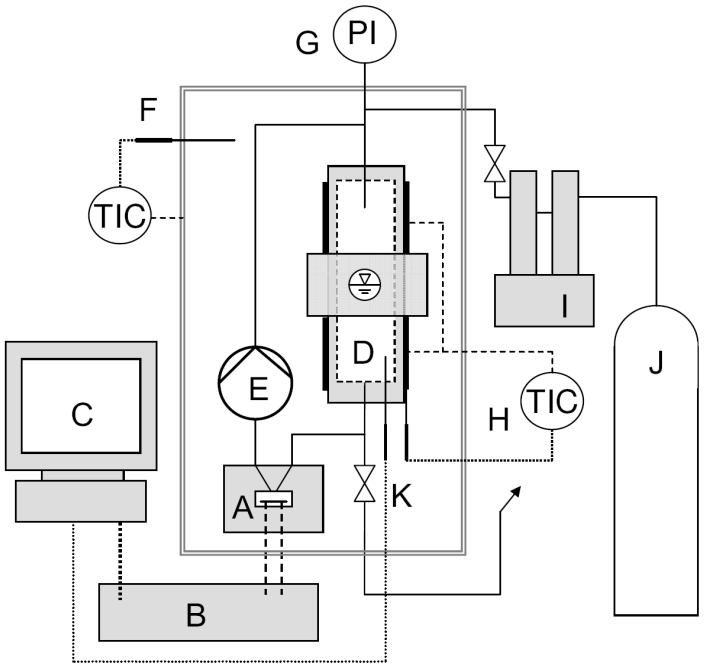


**Figure 9-1.** Quartz Crystal Microbalance (QCM) setup: A) QCM cell, B) resonator/frequency counter (RQCM), C) computer, D) high pressure view cell, E) circulation pump, F) thermostated circulating airbath, G) pressure indicator, H) temperature controlled electric heaters, I) syringe pump, J) $CO_2$ cylinder, K) thermistor.

A magnetically-driven piston pump, which is described in the Appendix, was employed to convey the liquid from the bottom of the view cell through the QCM cell to the top of the view cell, spraying it into the upper $CO_2$-rich phase facilitating equilibration. The change in viscosity was monitored by means of a QCM placed in a custom made high pressure cell (Fig. 9-2), which was connected in line between the view cell and the circulation pump by means of polyether ether ketone (PEEK) tubing (OD 1/16 in) to electrically insulate the QCM from

the rest of the system to minimize interference and noise in the frequency signal. The sensor crystal used in this study was a 9 MHz AT-cut quartz crystal with polished wrap-around gold plated electrodes (ICM, Oklahoma City, OK, USA).

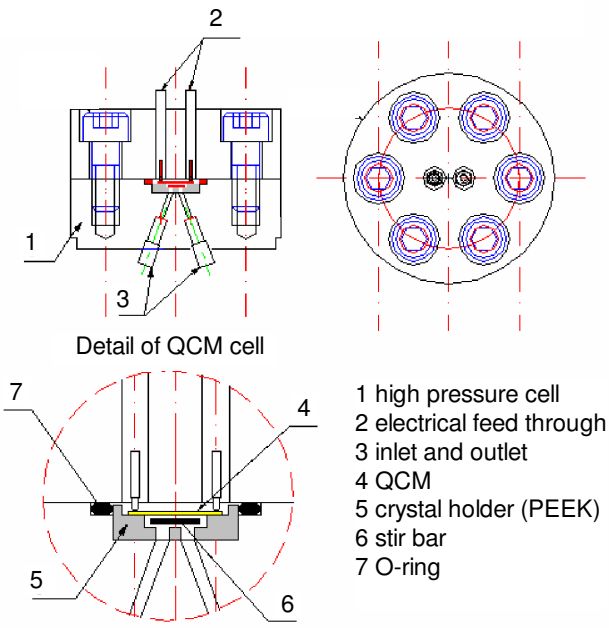


**Figure 9-2.** Details of the high pressure QCM cell.

The quartz crystal and electrodes had a diameter of 14 and 6.5 mm, respectively, with quartz having a stiffness of $29.01 \times 10^9$ N/m$^2$ and a density of 2649 kg/m$^3$. The resonant frequency of the QCM was determined by means of an integrated Research Quartz Crystal Microbalance (RQCM, Maxtek, Santa Fe Springs, CA, USA) hooked up to a computer with RQCM software to record frequency shifts of the crystal. The RQCM allowed capacitance adjustments over a wide range so that the QCM can be operated in liquid environments. The resonant frequency readings were taken after minimizing the resistance of the QCM by means of fine adjustment of the capacitance of the RQCM so that a stable frequency locked by the RQCM was achieved. To determine the frequency response of the QCM in pure ethanol at elevated hydrostatic pressures the system was completely filled with ethanol and pressurized using an HPLC pump (Beckman Model 110A, Fullerton, CA, USA).

### 9.2.3 Determination of viscosity and rheological behavior with the rotational rheometer

The viscosity and rheological flow behavior of fish oil FAEE saturated with $CO_2$ up to 11.8 MPa at 40, 55, 70°C were determined in triplicate using the rotational rheometer. The procedure applied for determining the viscosity and rheological behavior has been described previously for fish oil TG saturated with $CO_2$ in Chapter 8 [35]. FAEE can expand substantially up to about 60% by volume when saturated with pressurized $CO_2$ as described in Chapter 3 [34]. The expansion of FAEE may lead to additional friction and errors if the ball bearings of the magnetic coupling inside the pressure head come in contact with the expanded FAEE. Therefore, $CO_2$ was carefully bubbled through the headspace of the high pressure cell every 1-2 h and prior to measurements to keep the liquid level in the cup constant by purging out expanded excess FAEE. For the first set of measurements, FAEE viscosity was determined at constant shear rates of 300 $s^{-1}$ and 500 $s^{-1}$ at all pressure and temperature levels. Then the rheological flow behavior was determined in triplicate at all pressure and temperature conditions. The shear stress $\tau$ [Pa] was determined with the rheometer at shear rates $\gamma$ [$s^{-1}$] ranging from 300 to 600 $s^{-1}$. The consistency index $K$ in [Pa.$s^n$] and the dimensionless flow behavior index $n$ were evaluated according to the power law:

$$\tau = K * \gamma^n \qquad (9\text{-}1)$$

### 9.2.4 Determination of viscosity with the QCM

#### 9.2.4.1 Theory and calibration of the QCM

The resonant frequency of an AT-cut quartz crystal submersed in a fluid depends on numerous factors, including the thickness of the crystal, mass loading on the crystal, pressure, temperature, surface roughness as well as viscosity and density of the surrounding fluid [27, 36, 37]. By keeping the temperature constant during all experiments, avoiding mass loading on the electrode surface and using a crystal with an optically polished surface to minimize the influence of surface roughness the factors affecting the resonant frequency of the QCM submersed in a

liquid are reduced down to pressure $P$, density $\rho$ and viscosity $\eta$. In that case, the total frequency shift due to changes in pressure, density and viscosity are described by:

$$\Delta f = \Delta f_P + \Delta f_{\rho\eta} \tag{9-2}$$

The first term $\Delta f_P$ describes the frequency shift due to hydrostatic pressure [38]:

$$\Delta f_p = f_0 \cdot \alpha \cdot (P - P_0) \tag{9-3}$$

where $f_0$ is the fundamental crystal frequency at a reference pressure $P_0$ and $\alpha$ is a constant quantifying the effect of pressure on the resonant frequency [38]. The second term $\Delta f_{\rho\eta}$ represents the shift in crystal frequency due to a change in density ($\rho$) and viscosity ($\eta$) of the surrounding fluid compared to a reference fluid with $\rho_0$ and $\eta_0$. A simple relationship was proposed by Kanazawa and Gordon [37] showing that the frequency shift of a QCM submersed in liquid was linearly correlated to the square root of the product $\rho \cdot \eta$:

$$\Delta f_{\rho\eta} = -c \cdot n \cdot f_0^{3/2} \cdot \left(\sqrt{\rho \cdot \eta} - \sqrt{\rho_0 \cdot \eta_0}\right) \tag{9-4}$$

In Eq. (9-4), $c$ is a coefficient depending on the quartz crystal's shear modulus and density, and $n$ is the number of crystal faces immersed in the liquid ($n$=2 in this study). Therefore, the overall frequency shift of a QCM exposed to a pressurized liquid relative to that in a reference fluid at the same temperature can be calculated by combining Eqs. (9-3) and (9-4) as follows:

$$\Delta f = C_1 \cdot \Delta P + C_2 \cdot \Delta\sqrt{\rho \cdot \eta} \tag{9-5}$$

where $\Delta P = (P - P_0)$ is the pressure increase relative to atmospheric pressure $P_0$ and $\Delta\sqrt{\rho \cdot \eta}$ relates to the change in the square root of the product density times viscosity relative to that of the reference fluid. In this study, the frequency shift was calculated relative to the frequency of the blank crystal in air at atmospheric pressure and 40°C. In order to calibrate the QCM and to determine the constants $C_1$ and $C_2$ for the crystal used in this study, the resonant frequency of the QCM at a constant temperature of 40°C was recorded in various liquids of known density and viscosity. It is necessary to separate the effect of pressure from that of density and viscosity on crystal frequency in order to obtain $C_1$ and $C_2$. Therefore, the

calibration of the QCM was carried out in two steps. The first calibration step was performed at constant atmospheric pressure by varying density and viscosity using various standard calibration oils and acetone. The second calibration step was done using a liquid up to high hydrostatic pressures for which density and viscosity values vary only little with pressure and data are available. The liquid chosen for elevated pressures was ethanol for which density and viscosity data at elevated hydrostatic pressures are available [39, 40]. Thereby, it was possible to generate two different frequency response curves nearly orthogonal to each other, which are used to derive the QCM response surface and then determine the constants $C_1$ and $C_2$ according to Eq. (9-5).

For the calibration at atmospheric pressure the QCM was installed in the high pressure QCM cell (Fig. 9-2), which was located in the thermostated circulating air bath. The resonance frequency of the clean QCM in air at 40°C was recorded. The test liquid was then injected into the QCM cell by using a syringe ensuring that any trapped air bubbles were removed from the cell. The QCM cell was installed upside down in the apparatus, so that the inlet and outlet were located at the top facilitating removal of gas bubbles. After thermal equilibration for several hours the frequency of the QCM was recorded. In case of the standard oils the density and viscosity were provided by the manufacturer and taken from literature for acetone [41, 42]. Between each calibration measurement the crystal was thoroughly cleaned by flushing the cell with acetone and pushing air through the cell until the resonant frequency was the same as that recorded before for the clean QCM in air. The frequency response of the QCM versus the square root of the product $\rho \cdot \eta$ for the standard oils and acetone was plotted resulting in a straight line for the calibration curve (Fig. 9-3). After obtaining the calibration curve at atmospheric pressure the viscosity of anhydrous ethanol was determined to check the QCM performance. Using the calibration curve with density data for ethanol from literature [42] the viscosity of anhydrous ethanol was determined at 40°C. The measured viscosity of anhydrous ethanol at 40°C and atmospheric pressure obtained with the QCM was 0.829 mPa.s, whereas literature data ranged from 0.824 to 0.833 mPa.s [40, 41, 43]. Thus, the deviation for the measured ethanol

viscosity from literature data was less than about 0.5%, which was considered acceptable. Thus, the influence of density and viscosity on resonance frequency was ascertained yielding the constant $C_2$ in Eq. (9-5).

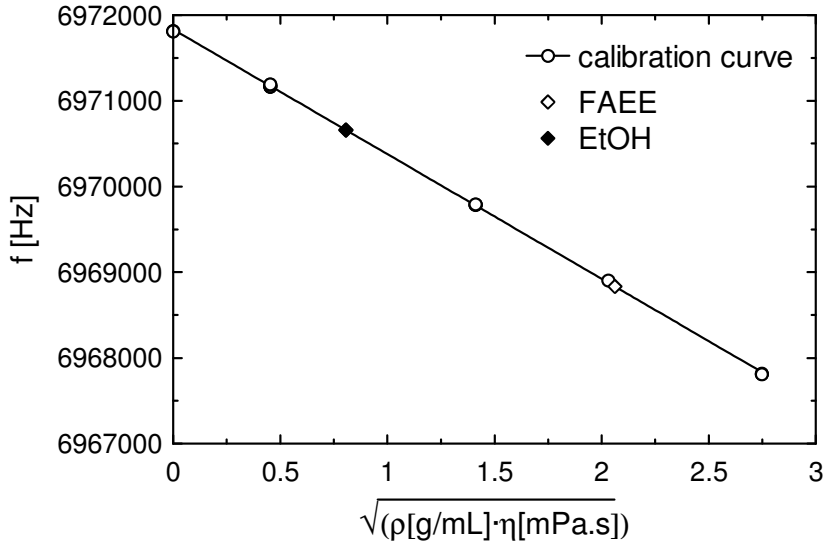


**Figure 9-3.** Calibration curve for the QCM at atmospheric pressure with various calibration oils and acetone.

The QCM was then calibrated up to elevated pressures using anhydrous ethanol at 40°C by recording the QCM frequency response at pressures ranging from 0.1 MPa up to about 8 MPa in order to assess the pressure effect (i.e. constant $C_1$ in Eq. (9-5)). For this purpose the QCM cell was connected to the apparatus as illustrated in Fig. 9-1. The apparatus was filled entirely with ethanol, which was circulated through the QCM cell using the circulation pump and warmed up to 40°C. The system was then pressurized to the desired pressure level by pushing ethanol into the view cell by means of an HPLC pump (Beckman Model 110A, Fullerton, CA, USA) connected to the bottom outlet of the view cell. After pressurization and thermal equilibration the frequency response of the QCM was recorded. Using available literature data for viscosity and density of ethanol at elevated pressures [39, 44] the calibration surface could be plotted as illustrated in Fig. 9-4.

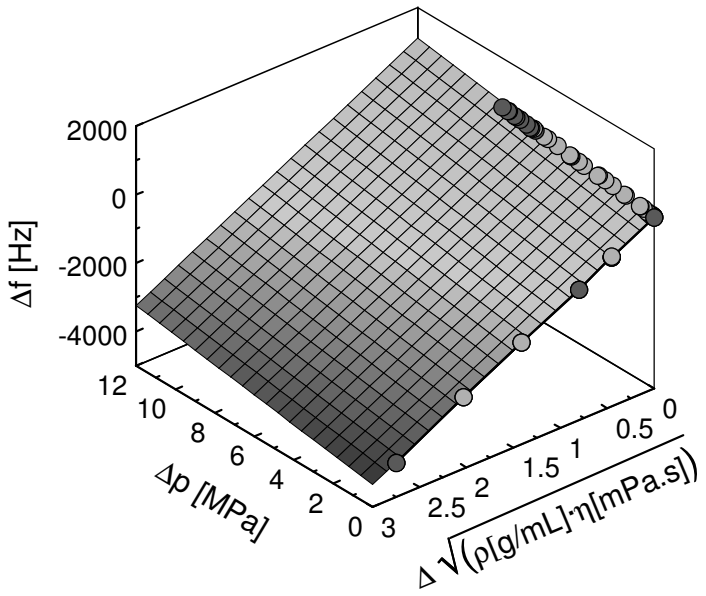


**Figure 9-4.** Calibration surface for the QCM using anhydrous ethanol at elevated pressures and calibration oils and acetone at atmospheric pressure.

Thus, by fitting the Eq. (9-5) to the frequency responses measured at atmospheric and elevated pressures the calibration constants $C_1$ and $C_2$ were obtained. The values calculated for the QCM system used in this study were $C_1$= 92.13 Hz/MPa and $C_2$=-1447.97 Hz/(mPa.s·g/mL)$^{1/2}$. The value for the constant $C_1$ translates into an α value defined as [27]:

$$\alpha = \frac{1}{f_o} * \frac{df(Hz)}{dP(MPa)} \tag{9-6}$$

of 1.024x10$^{-5}$ MPa$^{-1}$ for the QCM with $f_0$= 9 MHz used in this study, which agrees well with the α values of 1.045x10$^{-5}$ MPa$^{-1}$ at 25°C reported by Stockbridge [38] and 1.015x10$^{-5}$ MPa$^{-1}$ at 40°C obtained using a correlation given by Park *et al.* [27], for 5 MHz AT-cut crystals.

In order to obtain the viscosity of a liquid at elevated pressures from the measured frequency shift of the quartz crystal submersed in the liquid Eq. (9-5) with its constants $C_1$ and $C_2$ and the density of the surrounding liquid are required. It should be noted that due to differences in surface roughness or slight variations in crystal properties the constants $C_1$ and $C_2$ can vary to a certain extent between different quartz crystals and therefore need to be determined for each crystal

individually. Furthermore, the crystal should not be removed from the QCM cell after calibration or between measurements, because mounting effects can alter the crystal response as well.

#### 9.2.4.2 Measurement of the viscosity of $CO_2$-expanded liquids

The performance of the QCM to measure the viscosity at 40°C of FAEE and $CO_2$-expanded FAEE and ethanol was evaluated in this study. First, the viscosity of FAEE at atmospheric pressure was determined by filling the QCM cell with a syringe removing any air bubbles and warming up to 40°C in the thermostated circulating air bath. Then after thermal equilibration of 6 h, the frequency of the QCM was recorded. Using the calibration constants and the density of FAEE as determined previously in Chapter 3 [34], the viscosity of FAEE could be ascertained. After that, the QCM cell was connected to the system, which had been flushed with $CO_2$ prior to the experiment (Fig. 9-1). As soon as the QCM cell was connected, the system was filled up to the window level of the view cell with FAEE. The circulation pump was activated and FAEE circulated until the system reached a constant temperature of 40°C and a stable frequency of the QCM could be recorded. The frequency was considered stable when it did not change by more than about 5-10 Hz within 10 min indicating equilibrium. During frequency readings the circulation pump was stopped to avoid interference with the crystal response. After reaching a constant frequency at atmospheric pressure the system was pressurized with $CO_2$ using the syringe pump to the next pressure level. The system was allowed to equilibrate for up to 10 h before a stable QCM frequency was recorded.

In order to compare the performance of the QCM for the determination of viscosity of CX liquids to available literature data, the viscosity of $CO_2$-expanded ethanol was determined as well using the density of CX ethanol as reported previously in Chapter 5 [45]. After thoroughly flushing and cleaning the apparatus with anhydrous ethanol the viscosity of CX ethanol was determined according to the same protocol as described for FAEE. FAEE and ethanol [46] expand substantially when saturated with pressurized $CO_2$. Therefore, the liquid level was

kept constant at the level of the window in the view cell by bleeding out small amounts of liquid at the bottom of the view cell during the experiments so that enough space was available for the liquids to expand.

## 9.3 Results and discussion

### 9.3.1 Viscosity determined by a rotational rheometer

Viscosity of fish oil FAEE saturated with $CO_2$ was determined at 40, 55, and 70°C and pressures of 0.1 to 12.4 MPa using a rotational rheometer at shear rates of 300 and 500 $s^{-1}$ (Table 9-1). The viscosity decreased with increasing pressure at both shear rates and all temperatures as illustrated in Fig. 9-5 and 9-6 at 500 and 300 $s^{-1}$, respectively. However, at elevated temperatures the drop in viscosity was less pronounced, which can be attributed to a lower solubility of $CO_2$ in the lipid phase at higher temperatures in the pressure range studied [13].

**Table 9-1.** Viscosity of fish oil FAEE saturated with $CO_2$ measured with the rotational rheometer at shear rates of 300 and 500 $s^{-1}$ at 40, 55 and 70°C and various pressures.

| T | P | $\eta_{exp}$ ±SD[a] [mPa.s] | |
|---|---|---|---|
| [°C] | [MPa] | 300 $s^{-1}$ | 500 $s^{-1}$ |
| 40 | 0.10 | 3.21 ±0.35 | 3.56 ±0.16 |
| | 3.28 | 2.05 ±0.26 | 3.01 ±0.11 |
| | 6.14 | 1.52 ±0.08 | 2.32 ±0.14 |
| | 7.38 | 1.35 ±0.00 | 2.02 ±0.02 |
| | 9.65 | 1.11 ±0.13 | 1.63 ±0.24 |
| | 11.79 | 1.06 ±0.12 | 1.59 ±0.19 |
| 55 | 0.10 | 2.42 ±0.02 | 3.10 ±0.10 |
| | 3.45 | 1.69 ±0.11 | 2.62 ±0.11 |
| | 6.14 | 1.49 ±0.15 | 2.28 ±0.08 |
| | 7.24 | 1.24 ±0.00 | 1.90 ±0.00 |
| | 9.65 | 1.23 ±0.20 | 1.70 ±0.21 |
| | 11.79 | 1.03 ±0.25 | 1.48 ±0.14 |
| 70 | 0.10 | 2.03 ±0.07 | 2.93 ±0.12 |
| | 3.45 | 1.95 ±0.20 | 2.83 ±0.17 |
| | 6.14 | 1.57 ±0.09 | 2.42 ±0.07 |
| | 9.65 | 1.47 ±0.07 | 2.03 ±0.06 |
| | 11.72 | 1.33 ±0.10 | 1.81 ±0.02 |

[a] Mean±standard deviation (SD) based on triplicate measurements.

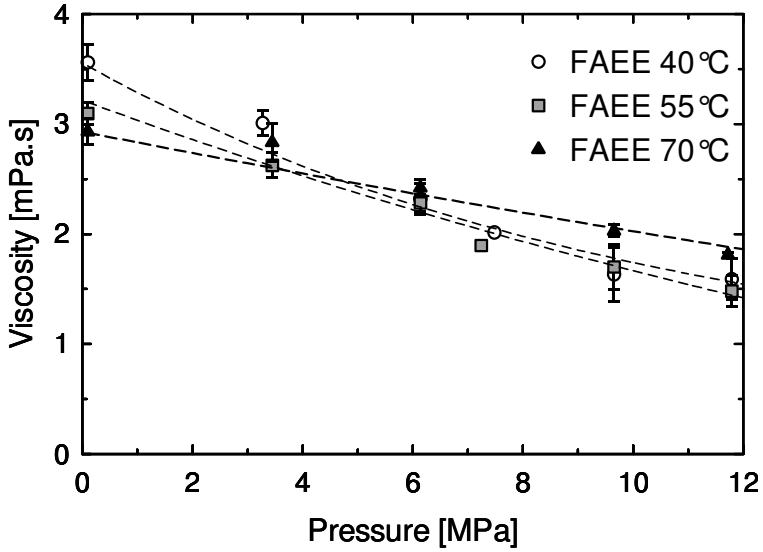


**Figure 9-5.** Viscosity of fish oil FAEE in equilibrium with $CO_2$ as a function of pressure at various temperatures determined with the rheometer at a shear rate of 500 $s^{-1}$. Dashed lines were calculated using the correlation given in Eq. (9-7). Error bars represent standard deviation based on triplicate measurements.

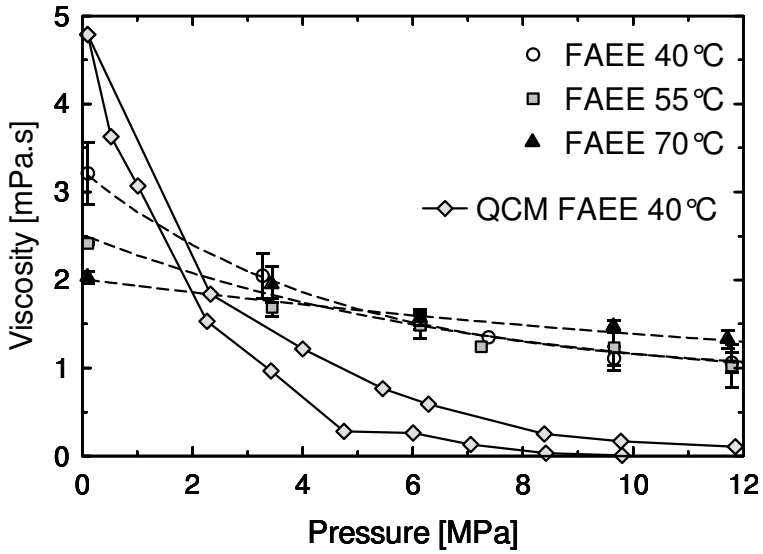


**Figure 9-6.** Viscosity of fish oil FAEE in equilibrium with $CO_2$ as a function of pressure at various temperatures determined with the rheometer at a shear rate of 300 $s^{-1}$. Viscosity values obtained with the QCM are illustrated by the diamonds and solid line. Dashed lines were calculated using the correlation given in Eq. (9-7). Error bars represent standard deviation based on triplicate measurements.

At atmospheric pressure, the viscosity of FAEE decreased with temperature, whereas at elevated pressures the viscosity increased with increasing temperature. At 40°C, the viscosity of CX FAEE measured at a shear rate of 300 $s^{-1}$ decreased with increasing $CO_2$ pressure from about 3.2 to 1.1 mPa.s by increasing the pressure from 0.1 to 11.8 MPa. Due to the effect of temperature on $CO_2$ solubility a crossover point could be observed at about 5 MPa where the influence of temperature on viscosity was reversed. Thus, at pressures above 5 MPa an increase in temperature up to 70°C caused an increase in viscosity compared to 40 and 55°C.

The following model was used to correlate the measured viscosity $\eta$ [mPa.s] to pressure $P$ [MPa] and temperature $T$ [K] at shear rates of 300 and 500 $s^{-1}$:

$$\eta(P,T) = \eta_\infty(T) + \left[(\eta_0(T) - \eta_\infty(T)\right] * e^{(-k(T)*(P-0.1))} \quad (9\text{-}7)$$

The first term $\eta_\infty(T)$ describes the level of viscosity at elevated saturation pressure as a function of temperature:

$$\eta_\infty(T) = A_1 + A_2 * T \quad (9\text{-}8)$$

The term $\eta_0(T)$ represents the viscosity at atmospheric pressure as a function of temperature according to the equation presented by Andrade [47]:

$$\eta_0(T) = A_3 * e^{\left(\frac{A_4}{T}\right)} \quad (9\text{-}9)$$

The temperature dependent exponential decline of viscosity with pressure is described by the last term with the exponent $k(T)$:

$$k(T) = A_5 + A_6 * T \quad (9\text{-}10)$$

The model given in Eq. (9-7) with the parameters presented in Table 9-2 is valid for the temperature and pressure ranges investigated in this study and corresponds reasonably well to the experimental data as shown by the dashed lines in Figs. 9-5 and 9-6.

**Table 9-2.** Model parameters for the correlation of viscosity of $CO_2$-expanded fish oil FAEE using Eq. (9-7).

| | Shear rate | |
|---|---|---|
| | **300 $s^{-1}$** | **500 $s^{-1}$** |
| $A_1$ | 5.143 | 10.95 |
| $A_2$ | $-1.350 \times 10^{-2}$ | $-3.298 \times 10^{-2}$ |
| $A_3$ | $1.423 \times 10^{-2}$ | $3.541 \times 10^{-1}$ |
| $A_4$ | $1.695 \times 10^{+3}$ | $7.198 \times 10^{+2}$ |
| $A_5$ | $2.036 \times 10^{0}$ | $7.662 \times 10^{-1}$ |
| $A_6$ | $-5.782 \times 10^{-3}$ | $-2.139 \times 10^{-3}$ |

The results for CX FAEE found in this study are comparable to those reported for methyl myristate and methyl palmitate saturated with $CO_2$ determined by observing the rising velocity of gas bubbles [12]. The viscosity of methyl palmitate decreased from 3.7 to 0.6 mPa.s at 40°C by increasing the saturation pressure from atmospheric to 8.8 MPa [12]. Furthermore, a decrease in viscosity with pressure was also reported for methyl oleate and methyl linoleate saturated with $CO_2$ determined with a high-pressure capillary viscometer [13]. However, due to the shorter fatty acid chain length the viscosities for methyl oleate and linoleate were found to be about 0.425 and 0.36 mPa.s at 40°C and 12 MPa, which are lower than that for the longer chain FAEE in this study. In addition, the viscosity of methyl linoleate was lower than that of methyl oleate at 40°C at both atmospheric pressure and elevated pressure [13], showing that the degree of saturation greatly impacts the viscosity of the $CO_2$-expanded esters as well. The viscosities of fatty acid methyl and ethyl esters increase with chain length but decrease with increasing degree of unsaturation in the fatty acid chain [48, 49]. In this study, the lowest viscosities observed for the CX FAEE were about 1 mPa.s. However, at elevated pressures the sensitivity of the rotational rheometer could be affected by mechanical friction in the ball bearings inside the magnetic coupling of the measurement cell potentially leading to slightly increased viscosity values. The lower detection limit of the rheometer with the

high pressure bob and cup attachment at the shear rates applied in this study seemed to be in the range of 0.5 to 1 mPa.s.

### 9.3.2 Rheological behavior of FAEE based on rotational rheometer measurements

Rheological behavior of fish oil FAEE saturated with $CO_2$ was determined using the rotational rheometer at shear rates ranging from 300 to 600 $s^{-1}$ at 40, 55, and 70°C and pressures up to about 12 MPa (Table 9-3).

**Table 9-3.** Flow behavior index *n* and common logarithm of consistency index *K* for fish oil FAEE saturated with $CO_2$ at 40, 55 and 70°C.

| T [°C] | P [MPa] | n ± SD[a] [] | $\log_{10}$ K ± SD[a] $\log_{10}$ [Pa.s$^n$] |
|---|---|---|---|
| 40 | 0.10 | 1.10 ±0.13 | -2.74 ±0.38 |
| | 3.28 | 1.49 ±0.07 | -3.88 ±0.20 |
| | 6.14 | 1.52 ±0.28 | -4.05 ±0.72 |
| | 9.65 | 1.42 ±0.20 | -3.83 ±0.62 |
| | 11.79 | 1.59 ±0.38 | -4.39 ±1.02 |
| 55 | 0.10 | 1.44 ±0.07 | -3.67 ±0.30 |
| | 3.45 | 1.43 ±0.05 | -3.79 ±0.13 |
| | 6.14 | 1.34 ±0.16 | -3.58 ±0.44 |
| | 9.65 | 1.11 ±0.16 | -3.12 ±0.46 |
| | 11.79 | 1.18 ±0.26 | -3.37 ±0.74 |
| 70 | 0.10 | 1.35 ±0.05 | -3.54 ±0.17 |
| | 3.45 | 1.28 ±0.05 | -3.33 ±0.15 |
| | 6.14 | 1.19 ±0.11 | -3.19 ±0.30 |
| | 9.65 | 0.96 ±0.08 | -2.63 ±0.21 |
| | 11.72 | 1.01 ±0.02 | -2.84 ±0.08 |

[a] Mean±standard deviation (SD) based on triplicate measurements.

The rheological flow behavior was analyzed according to the power law (Eq. 9-1). Fish oil FAEE saturated with pressurized $CO_2$ exhibited shear thickening (i.e.

dilatant) flow behavior at atmospheric and at elevated $CO_2$ pressures. The impact of pressure and temperature on the flow behavior index *n* and consistency index *K* are illustrated in Figs. 9-7 and 9-8, respectively.

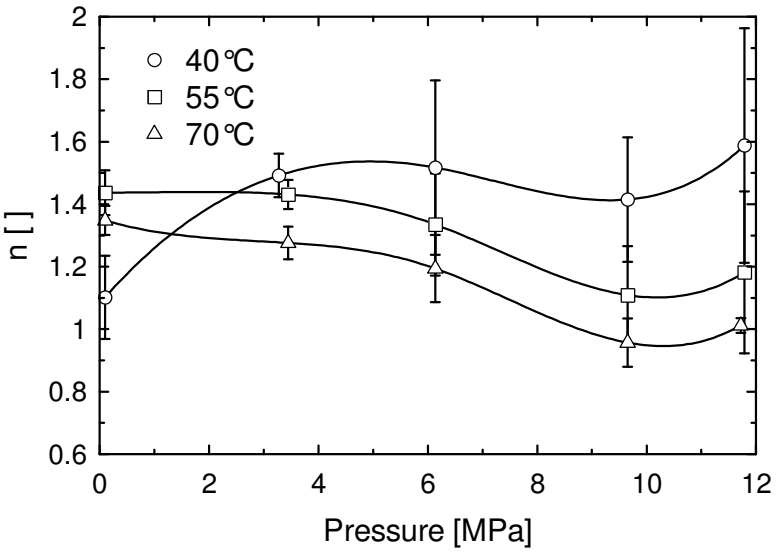


**Figure 9-7.** Flow behavior index *n* of $CO_2$-expanded fish oil FAEE versus pressure. Error bars represent standard deviation based on triplicate measurements.

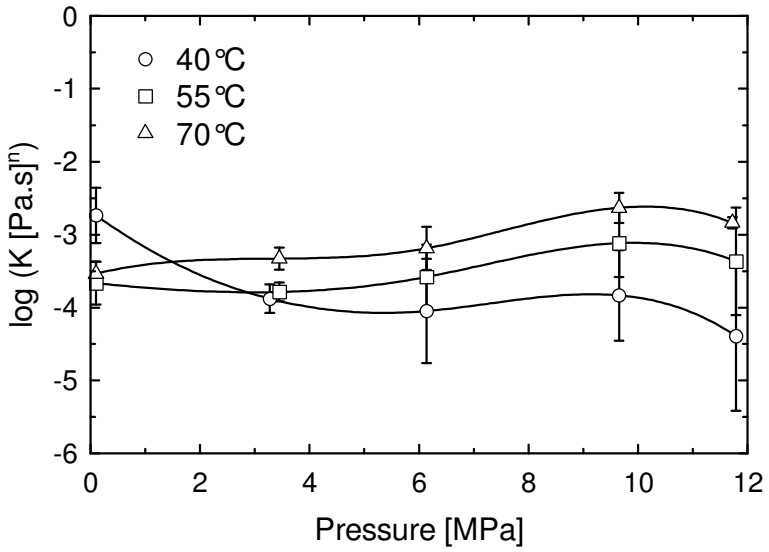


**Figure 9-8. C**onsistency index *K* of $CO_2$-expanded fish oil FAEE versus pressure. Error bars represent standard deviation based on triplicate measurements.

While the flow behavior index *n* at 40°C was close to 1 at atmospheric pressure indicating Newtonian flow behavior it increased up to about 1.6 at elevated pressure corresponding to shear thickening behavior. On the other hand, a flow behavior index of about 1.4 was obtained at atmospheric pressure at both 55 and 70°C, which decreased with increasing $CO_2$ pressure to a value closer to one. This seems surprising; therefore, the possibility of friction affecting the results must be considered. The higher volatility of FAEE at the higher temperatures may have contributed to this. It appeared that due to friction in the rheometer as described above, the experimental error was relatively high as evidenced by the large standard deviations at the higher pressures (Figs. 9-7 and 9-8). Nevertheless, a shear thickening behavior was also reported for pelargonic acid+$CO_2$ [11], and for a 4:1 mixture of oleic acid and stearic acid saturated with $CO_2$ [9]. As described in Chapter 3 [34], fish oil FAEE in equilibrium with $CO_2$ at 40°C expanded up to about 67% by volume reaching a constant level above 8 to 10 MPa, which corresponded to the constant levels of both viscosity (Fig. 9-6) and flow behavior index *n* (Fig. 9-7). It can be assumed that dissolution of $CO_2$ into the liquid phase causing volumetric expansion affects the viscosity as well as rheological

behavior. The consistency index ($K$) was nearly constant at a level between $10^{-3}$ and $10^{-4}$ considering the relatively large experimental error.

### 9.3.3 Viscosity determined by QCM

The potential of a QCM for measuring viscosities of gas-expanded liquids up to elevated pressures was evaluated in this study. After calibration of the QCM with known test liquids at atmospheric and elevated pressures as described above, the viscosity of FAEE at atmospheric pressure and 40°C was determined using the QCM based on previously reported density data for FAEE in Chapter 3 [34]. The viscosity of FAEE at 40°C obtained with the QCM was 4.79 mPa.s, which was higher than that found with the rheometer, namely 3.21 mPa.s and 3.56 mPa.s at 300 and 500 $s^{-1}$, respectively. Because the shear rates for a QCM were estimated to be much higher ($10^6$ $s^{-1}$) [50] a viscosity value larger than that found with the rheometer seems valid considering the dilatant behavior of FAEE based on the rheometer results. The Kanazawa equation (Eq. (9-4)) describes the response of the QCM to a Newtonian liquid, and thus the dilatant behavior of FAEE may lead to deviations as well. Nevertheless, the response of the QCM for the CX FAEE was recorded and evaluated up to pressures of about 12 MPa. Two measurements were carried out, which are illustrated in Fig. 9-6 together with the results obtained by the rotational rheometer. It can be seen that the viscosity values obtained by the QCM method was higher at atmospheric pressure, while it approached zero at elevated pressures. The response of the QCM indicating a viscosity of close to zero indicates that the liquid surrounding the QCM did not adhere to the surface of the QCM. Therefore, the no-slip boundary condition was not fulfilled and the QCM shear waves were not transmitted into the liquid.

The QCM response was also tested in contact with CX ethanol, resulting in a lower viscosity as well, as illustrated in Fig. 9-9.

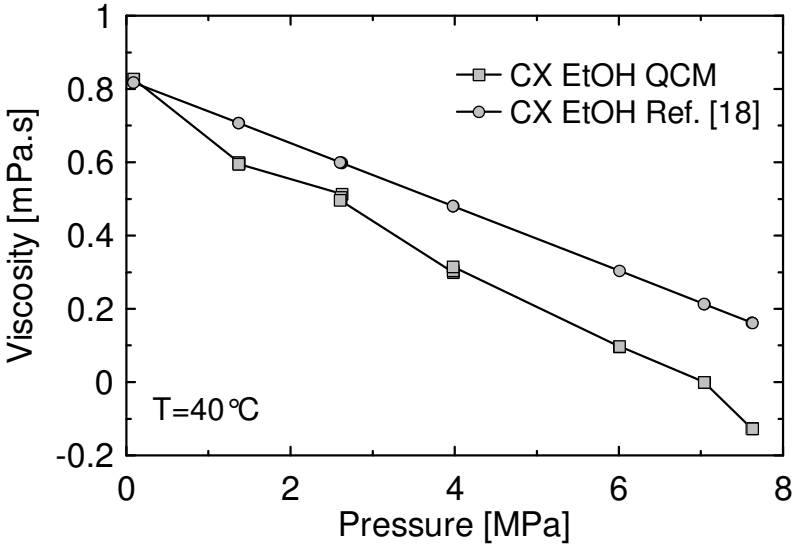


**Figure 9-9.** Viscosity of CX EtOH determined with the QCM compared to literature [18].

While the QCM was accurate in determining the viscosity of the gas-free ethanol at atmospheric pressure the response to gas-expanded ethanol indicated that the viscosity was underestimated, which was very likely due to the slip at the QCM surface. It has been reported that with the very high shear rates generated at the surface of the QCM the no slip boundary condition is often not fulfilled [51]. Furthermore, the generation of nano-bubbles at the surface of the QCM can lead to slip [52, 53] between the QCM and the liquid, which is related to the gas content of the liquid. Therefore, it can be concluded that the formation of gas bubbles in the gas-saturated liquids at the surface of the QCM in case of CX FAEE and ethanol is very likely, which led to the slip and eventually lower viscosity values obtained by using the QCM. Besides gas bubbles, the wettability of the surface and surface roughness [54] can affect the slip between the liquid and QCM surface as well [55]. It has been further suggested that the interaction between the surface and liquid is very important with slip being larger for a hydrophilic liquid on a hydrophobic surface than for a hydrophobic liquid on a hydrophobic surface [55]. Decoupling of a superhydrophobic QCM from the surrounding liquid water has been reported recently [56]. Since the wettability and

wetting angle of liquids in equilibrium with dense $CO_2$ on solid surfaces change with pressure [57-59] it is difficult to predict the behavior of the CX FAEE and ethanol system on the gold surface in terms of wettability. Finally, it was found that it is more likely for slip to occur with liquids of relatively low viscosity such as water compared to liquids of a higher viscosity comparable to glycerol [60].

It can be concluded that, while a QCM seems to have potential for viscosity measurements of pure liquids up to relatively high elevated hydrostatic pressures, the application of a QCM for viscosity measurements of CX liquids seems challenging mainly due to slip at the QCM surface. However, further research is required to evaluate the QCM performance for liquid systems under elevated hydrostatic pressure.

## 9.4 Conclusions

Viscosity of fish oil FAEE in equilibrium with $CO_2$ was determined at 40, 55 and 70°C and pressures of up to 12 MPa using a rotational rheometer at shear rates of 300 and 500 $s^{-1}$. The viscosity decreased with increasing $CO_2$ pressure at all temperatures. At 40°C, the viscosity decreased by about 67% from 3.21 to 1.06 mPa.s by increasing the $CO_2$ pressure from 0.1 to 11.8 MPa due to the high solubility of $CO_2$ in fish oil. FAEE showed pronounced shear-thickening behavior at atmospheric and elevated pressures, which was affected by temperature. The performance of a QCM sensor to measure viscosity of gas-expanded liquids was evaluated. The QCM seemed to perform well with Newtonian liquids at atmospheric and elevated pressures. However, the QCM response to CX liquids led to an underestimation of viscosity, which indicates that slippage between the QCM surface and the CX liquid occurred. Potential reasons for the slip are bubble formation and change in wettability. Furthermore, due to the non-Newtonian behavior of the CX FAEE, the application of the Kanazawa equation may not be valid. Nevertheless, the QCM did detect a decrease in viscosity, which might be useful for some applications, such as the detection of phase changes or in-situ monitoring of reactions. The understanding of viscosity and rheological behavior

of $CO_2$-expanded lipids is fundamental for optimizing processing equipment and novel process developments using high pressure $CO_2$.

## 9.5 References


1. F. Temelli, Perspectives on supercritical fluid processing of fats and oils. J. Supercrit. Fluids 47 (2009) 583-590.

2. N. Czerwonatis, R. Eggers, Disintegration of liquid jets and drop drag coefficients in pressurized nitrogen and carbon dioxide. Chem. Eng. Technol. 24 (2001) 619-624.

3. A. Blaha-Schnabel, A. Beyer, B. Czech, H. Jakob, H. Schiemann, E. Weidner, S. Peter, Influence of interfacial tension and viscosity on the behavior of a packed column in near-critical fluid extraction. Chem. Eng. Commun. 146 (1996) 13-31.

4. M. Moser, C. Trepp, Investigating the stability of falling films at round vertical film carriers under high pressure. Chem. Eng. Technol. 20 (1997) 612-616.

5. R. Stockfleth, G. Brunner, Film thickness, flow regimes, and flooding in countercurrent annular flow of a falling film at high pressures. Ind. Eng. Chem. Res. 40 (2001) 6014-6020.

6. E. Pomier, N. Delebecque, D. Paolucci-Jeanjean, M. Pina, S. Sarrade, G.M. Rios, Effect of working conditions on vegetable oil transformation in an enzymatic reactor combining membrane and supercritical $CO_2$. J. Supercrit. Fluids 41 (2007) 380-385.

7. S. Voges, R. Eggers, A. Pietsch, Gas assisted oilseed pressing. Sep. Purif. Technol. 63 (2008) 1-14.

8. P. Willems, N.J.M. Kuipers, A.B. de Haan, Gas assisted mechanical expression of oilseeds: Influence of process parameters on oil yield. J. Supercrit. Fluids 45 (2008) 298-305.

9. S. Peter, E. Weidner, H. Jakob, Die Viskosität koexistierender Phasen bei der überkritischen Fluidextraktion. Chem. Ing. Tech. 59 (1987) 59-62.

10. M.E. Yener, P. Kashulines, S.S.H. Rizvi, P. Harriott, Viscosity measurement and modeling of lipid-supercritical carbon dioxide mixtures. J. Supercrit. Fluids 11 (1998) 151-162.

11. S. Peter, H. Jakob, The rheological behavior of coexisting phases in systems containing fatty acids and dense gases. J. Supercrit. Fluids 4 (1991) 166-172.

12. C.A. Lockemann, E.U. Schlünder, Liquid-phase viscosities of the binary systems carbon dioxide-oleic acid, carbon dioxide-methyl myristate, and carbon dioxide-methyl palmitate at high pressures. Chem. Eng. Process. 34 (1995) 487-493.

13. P. Kashulines, S.S.H. Rizvil, P. Harriott, J.A. Zollweg, Viscosities of fatty acids and methylated fatty acids saturated with supercritical carbon dioxide. J. Am. Oil Chem. Soc. 68 (1991) 912-921.

14. M.J. Venter, P. Willems, S. Kareth, E. Weidner, N.J.M. Kuipers, A.B. de Haan, Phase equilibria and physical properties of $CO_2$-saturated cocoa butter mixtures at elevated pressures. J. Supercrit. Fluids 41 (2007) 195-203.

15. P.T. Jaeger, Ph.D. Thesis: Grenzflächen und Stofftransport in verfahrenstechnischen Prozessen am Beispiel der Hochdruck-Gegenstrom-fraktionierung mit überkritischem Kohlendioxid. 1998, TU Hamburg-Harburg: Hamburg, Germany.

16. M. Hobbie, Ph.D. Thesis: Bildung von Tropfen in verdichteten Gasen und stationäre Umströmung fluider Partikel bei Drücken bis zu 50 MPa. 2006, TU Hamburg-Harburg: Hamburg, Germany.

17. R. Sih, F. Dehghani, N.R. Foster, Viscosity measurements on gas expanded liquid systems-Methanol and carbon dioxide. J. Supercrit. Fluids 41 (2007) 148-157.

18. R. Sih, M. Armenti, R. Mammucari, F. Dehghani, N.R. Foster, Viscosity measurements on saturated gas-expanded liquid systems-Ethanol and carbon dioxide. J. Supercrit. Fluids 43 (2008) 460-468.

19. R. Sih, N.R. Foster, Viscosity measurements on saturated gas expanded liquid systems-Acetone and carbon dioxide. J. Supercrit. Fluids 47 (2008) 233-239.

20. W. Herreman, W. Grevendonk, A. De Bock, Shear viscosity measurements of liquid carbon dioxide. J. Chem. Phys. 53 (1970) 185-189.

21. A. Padua, W.A. Wakeham, J. Wilhelm, The viscosity of liquid carbon dioxide. Int. J. Thermophys. 15 (1994) 767-777.

22. P.S. Van Der Gulik, Viscosity of carbon dioxide in the liquid phase. Physica A 238 (1997) 81-112.

23. H. Iwasaki, M. Takahashi, Viscosity of carbon dioxide and ethane. J. Chem. Phys. 74 (1980) 1930-1943.

24. A.P. Abbott, E.G. Hope, D.J. Palmer, Effect of electrolyte concentration on the viscosity and voltammetry of supercritical solutions. Anal. Chem. 77 (2005) 6702-6708.

25. A.P. Abbott, E.G. Hope, D.J. Palmer, Effect of solutes on the viscosity of supercritical solutions. J. Phys. Chem. B 111 (2007) 8114-8118.

26. K. Otake, S. Kurosawa, T. Sako, T. Sugeta, M. Hongo, M. Sato, Frequency change of a quartz crystal microbalance at the supercritical condition of carbon dioxide. J. Supercrit. Fluids 7 (1994) 289-292.

27. K. Park, M. Koh, C. Yoon, H. Kim, H. Kim, The behavior of quartz crystal microbalance in high pressure $CO_2$. J. Supercrit. Fluids 29 (2004) 203-212.

28. Y.T. Wu, P.J. Akoto-Ampaw, M. Elbaccouch, M.L. Hurrey, S.L. Wallen, C.S. Grant, Quartz crystal microbalance (QCM) in high-pressure carbon dioxide ($CO_2$): Experimental aspects of QCM theory and $CO_2$ adsorption. Langmuir 20 (2004) 3665-3673.

29. C.K. O'Sullivan, G.G. Guilbault, Commercial quartz crystal microbalances - Theory and applications. Biosens. Bioelectron. 14 (1999) 663-670.

30. S.E. Guigard, G.L. Hayward, R.G. Zytner, W.H. Stiver, Measurement of solubilities in supercritical fluids using a piezoelectric quartz crystal. Fluid Phase Equilib. 187-188 (2001) 233-246.

31. J. Ke, P.J. King, M.W. George, M. Poliakoff, Method for locating the vapor-liquid critical point of multicomponent fluid mixtures using a shear mode piezoelectric sensor. Anal. Chem. 77 (2005) 85-92.

32. Y. Hussain, Y.T. Wu, P.J. Ampaw, C.S. Grant, Dissolution of polymer films in supercritical carbon dioxide using a quartz crystal microbalance. J. Supercrit. Fluids 42 (2007) 255-264.

33. J. Ke, K.E. Reid, M. Poliakoff, The application of a shear mode piezoelectric sensor to monitoring the high-pressure phase behaviour of asymmetric binary systems. J. Supercrit. Fluids 40 (2007) 27-39.

34. B. Seifried, F. Temelli, Density of marine lipids in equilibrium with carbon dioxide. J. Supercrit. Fluids 50 (2009) 97-104.

35. B. Seifried, F. Temelli, Viscosity of fish oil triglycerides in equilibrium with high pressure carbon dioxide. J. Supercrit. Fluids (2010) (submitted).

36. G. Sauerbrey, Verwendung von Schwingquarzen zur Wägung dünner Schichten und zur Mikrowägung. Z. Phys. A - Hadron Nucl. 155 (1959) 206-222.

37. K. Keiji Kanazawa, J.G. Gordon II, The oscillation frequency of a quartz resonator in contact with liquid. Anal. Chim. Acta 175 (1985) 99-105.

38. C.D. Stockbridge, Effect of hydrostatic pressure on rotated Y-cut quartz crystal resonators. Vacuum Microbalance Techniques 5 (1966) 179-192.

39. D. Pecar, V. Dolecek, Volumetric properties of ethanol-water mixtures under high temperatures and pressures. Fluid Phase Equilib. 230 (2005) 36-44.

40. M.J. Assael, S.K. Polimatidou, Measurements of the viscosity of alcohols in the temperature range 290-340 K at pressures up to 30 MPa. Int. J. Thermophys. 15 (1994) 95-107.

41. D.S. Viswanath, T.K. Ghosh, D.H.L. Prasad, N.V.K. Dutt, K.Y. Rani, Viscosity of Liquids. 2007: Springer Netherlands.

42. R.H. Perry, D.W. Green, J.O. Maloney, Perry's Chemical Engineers' Handbook. 7th ed. McGraw-Hill Chem. Eng. Series. 1997, New York: McGraw-Hill.

43. T.W. Phillips, K.P. Murphy, Liquid viscosity of halocarbons. J. Chem. Eng. Data 15 (1970) 304-307.

44. Y. Tanaka, Y. Matsuda, H. Fujiwara, H. Kubota, T. Makita, Viscosity of (water + alcohol) mixtures under high pressure. Int. J. Thermophys. 8 (1987) 147-163.

45. B. Seifried, F. Temelli, Density of carbon dioxide-expanded ethanol at (313.2, 328.2 and 343.2) K. J. Chem. Eng. Data (2009) (published online March 29, 2010; DOI: 10.1021/je900830s).

46. A. Kordikowski, A.P. Schenk, R.M. Van Nielen, C.J. Peters, Volume expansions and vapor-liquid equilibria of binary mixtures of a variety of polar solvents and certain near-critical solvents. J. Supercrit. Fluids 8 (1995) 205-216.

47. E. Andrade, The viscosity of liquids. Nature 125 (1930) 309-310.

48. C.A.W. Allen, K.C. Watts, R.G. Ackman, M.J. Pegg, Predicting the viscosity of biodiesel fuels from their fatty acid ester composition. Fuel 78 (1999) 1319-1326.

49. G. Knothe, K.R. Steidley, Kinematic viscosity of biodiesel fuel components and related compounds. Influence of compound structure and comparison to petrodiesel fuel components. Fuel 84 (2005) 1059-1065.

50. R. Thalhammer, S. Braun, B. Devoiokuhar, M. Groschl, F. Trampler, E. Benes, H. Nowotny, M. Kostal, Viscosity sensor utilizing a piezoelectric thickness shear sandwich resonator. IEEE Trans. Ultrason. Ferroelectr. Freq. Control 45 (1998) 1331-1340.

51. J.S. Ellis, G.L. Hayward, Interfacial slip on a transverse-shear mode acoustic wave device. J. Appl. Phys. 94 (2003) 7856-7867.

52. C. Neto, D.R. Evans, E. Bonaccurso, H.J. Butt, V.S.J. Craig, Boundary slip in Newtonian liquids: A review of experimental studies. Rep. Prog. Phys. 68 (2005) 2859-2897.

53. X.H. Zhang, Quartz crystal microbalance study of the interfacial nanobubbles. Phys. Chem. Chem. Phys. 10 (2008) 6842-6848.

54. G. McHale, M.I. Newton, Surface roughness and interfacial slip boundary condition for quartz crystal microbalances. J. Appl. Phys. 95 (2004) 373-380.

55. B. Du, I. Goubaidoulline, D. Johannsmann, Effects of laterally heterogeneous slip on the resonance properties of quartz crystals immersed in liquids. Langmuir 20 (2004) 10617-10624.

56. P. Roach, G. McHale, C.R. Evans, N.J. Shirtcliffe, M.I. Newton, Decoupling of the liquid response of a superhydrophobic quartz crystal microbalance. Langmuir 23 (2007) 9823-9830.

57. Y. Sutjiadi-Sia, H. Marckmann, R. Eggers, C. Holzknecht, S. Kabelac, The effect of in liquids dissolved dense gases on interfacial and wetting characteristics. Forsch. Ingenieurwes.- Eng. Res. 71 (2007) 29-45.

58. J.L. Dickson, G. Gupta, T.S. Horozov, B.P. Binks, K.P. Johnston, Wetting phenomena at the $CO_2$/water/glass interface. Langmuir 22 (2006) 2161-2170.

59. P.T. Jaeger, R. Eggers, Wetting of contact surfaces with fluid phases under elevated pressures. Chem. Ing. Tech. 66 (1994) 390-393.

60. F. Ferrante, A.L. Kipling, M. Thompson, Molecular slip at the solid-liquid interface of an acoustic-wave sensor. J. Appl. Phys. 76 (1994) 3448-3462.

# 10 Particle Formation and Microencapsulation of Fish Oil Applying Supercritical Fluid Drying[1]

## 10.1 Introduction

Particle formation using supercritical fluids has been researched for many decades, which resulted in the development of numerous processes using the supercritical fluid (SCF) either as solvent, such as in the 'rapid expansion of supercritical solutions' (RESS) process or as antisolvent as in the 'gas antisolvent' (GAS) process. Numerous variations and further developments of particle formation processes emerged as previously reviewed elsewhere [1-4]; however, many of those require organic solvents to dissolve the solute to be precipitated. For example, a novel approach to form β-carotene nanoparticles was presented by Cocero her coworkers [5], which is based on the 'supercritical fluid extraction of emulsions' (SFEE) process related to the GAS process. In the SFEE process [5], a nanoemulsion where an organic solvent (dichloromethane) carrying the solute is dispersed in water to form an oil-in-water emulsion, which is dried using supercritical $CO_2$ (SC-$CO_2$). Each droplet resembles a small GAS precipitator, where upon expansion with $CO_2$ and extraction of the organic solvent ultrasmall particles suspended in water are formed with a final organic solvent concentration of about 1 ppm [5].

More recently, particle formation processes using aqueous solutions containing the solute to be sprayed into a high pressure precipitation chamber together with pressurized $CO_2$ usually enriched with ethanol have been developed. This approach is often referred to as the supercritical fluid drying process, which has been applied to precipitate proteins [6], enzymes [7], lactose, maltose, trehalose, raffinose, cyclodextrin, low-molecular-weight dextrans and inulin [8] forming free-flowing powders. The effect of spraying conditions and nozzle design as well as the influence of various modifiers added to $CO_2$ on the shape and size distribution of particles obtained with supercritical fluid drying has

[1] A version of this chapter has been filed as a US provisional patent application on April 1, 2010 ( application #: 61320182).

been studied by Bouchard *et al.* [9, 10]. It was found that methanol and ethanol used as modifier in the SCF drying process acted as antisolvent in the precipitation of glycine, phenylalanine and lysozyme, besides their role in enhancement of water in SC-$CO_2$ and evaporative water removal, whereas 2-propanol and acetone did not act as an antisolvent and affected mainly the evaporative water removal [10]. Various nozzle configurations were tested as well in the SCF drying process, including a simple T-mixer with small inner diameter or coaxial converging nozzles, with and without mixing chamber, as well as with ultrasonic wave generator [9], which showed that the nozzle design, processing pressure and flow rates had a pronounced effect on particle size, whereas morphology was found to be more likely linked to the precipitation mechanism rather than the atomization process [9]. A mathematical model for the mass transfer from an aqueous drop to SC-$CO_2$+ethanol was developed to study the drying of aqueous solutions of lysozyme with $CO_2$+ethanol mixtures [11].

Another approach was applied using SC-$CO_2$ for drying of aqueous green tea extracts, employing a variation of the 'particles from gas-saturated solutions' (PGSS) process, using only pressurized $CO_2$ as the drying medium in a spray chamber at a mild temperature ranging from 30 to 60°C and 20 MPa to obtain free-flowing powders, containing the intact active ingredients, such as antioxidant polyphenols. Kluge *et al.* [12, 13] applied the SFEE process to obtain composite nanoparticles of an anti-inflammatory drug (Ketoprofen) and amorphous biodegradable polymer poly-lactic-co-glycolic acid (PLGA), finding that the PLGA concentration in the emulsion affected particle size and particle size distribution. A modified RESS process was applied to encapsulate essential oil into liposomes, using a mixture of $CO_2$+ethanol to dissolve both the liposome material and essential oil, which was mixed with a phosphate buffer and subsequently sprayed into a precipitation chamber, where a liposomal suspension was formed, which was freeze dried in a separate processing step [14]. A process for the encapsulation of lavandin essential oil in a matrix of n-octenyl succinic anhydride (OSAN)-modified starch by spraying an aqueous emulsion of the oil with SC-$CO_2$ applying a PGSS drying technique was reported [15]. The oil was

also encapsulated in polyethylene glycol (PEG) applying a PGSS technique, where the PEG was used in a molten form containing pressurized $CO_2$ forming a gas-saturated solution, which was mixed with the lavandin oil and sprayed into a precipitation chamber [15]. However, the microencapsulation of fish oil using a SCF drying technique has not been reported in the literature.

Therefore, the objective of this study was to investigate the potential of a SCF spray drying technique for particle formation using gum arabic and a long-chain carbohydrate, such as β-glucan. Furthermore, a novel approach to microencapsulate fish oil using a continuous injection process to form an emulsion coupled with the SCF spray drying process using a coaxial nozzle is evaluated, by assessing the effect of various process parameters, such as nozzle design, flow rate, solids concentration, and pressure on particle morphology, particle size distribution and finally oil content in the fish oil microcapsules.

## 10.2 Experimental

### 10.2.1 Materials

Gum arabic (GA) was used as purchased without any further treatment (ACROS Organic, Fisher Scientific, Canada). β-Glucan (BG) powder (moisture content of 8.7% and BG content of 75% dry weight basis) previously extracted from barley in our lab according to the protocols described by Ghotra *et al.* [16] was used in the spray experiments as well. Refined fish oil extracted from anchovy and sardine was obtained from Ocean Nutrition Canada (ONC, Halifax, NS, Canada) with the specifications described in Section 3.2.1. Food grade anhydrous ethanol (Commercial Alcohol, Winnipeg, MB, Canada) with a stated purity and water content of 99.99% and 0.008% by volume, respectively, was used without further purification. Hexane of analytical grade (Fisher Scientific, Canada) was used for determining the lipid content of fish oil microcapsules. Bone dry $CO_2$ with a purity of 99.9% and nitrogen with a purity of 99.998% were purchased from Praxair (Edmonton, AB, Canada).

### 10.2.2 Apparatus

The apparatus used for particle formation and microencapsulation consisted of a 200 mL view cell with an ID of 40 mm (Nova-Swiss, Effretikon, Switzerland) equipped with a coaxial-nozzle, temperature-controlled heaters and circulating air bath (Fig. 10-1). The system was pressurized with $CO_2$ by means of a syringe pump (O) (Isco Model 250D, Isco Inc., Lincoln, NE, USA). $CO_2$ was preheated to 45°C using temperature-controlled electric heaters and mixed with ethanol, which was pumped into the system with an HPLC pump (T) (Gilson 305, HPLC pump, Gilson Inc., Middleton, WI, USA).

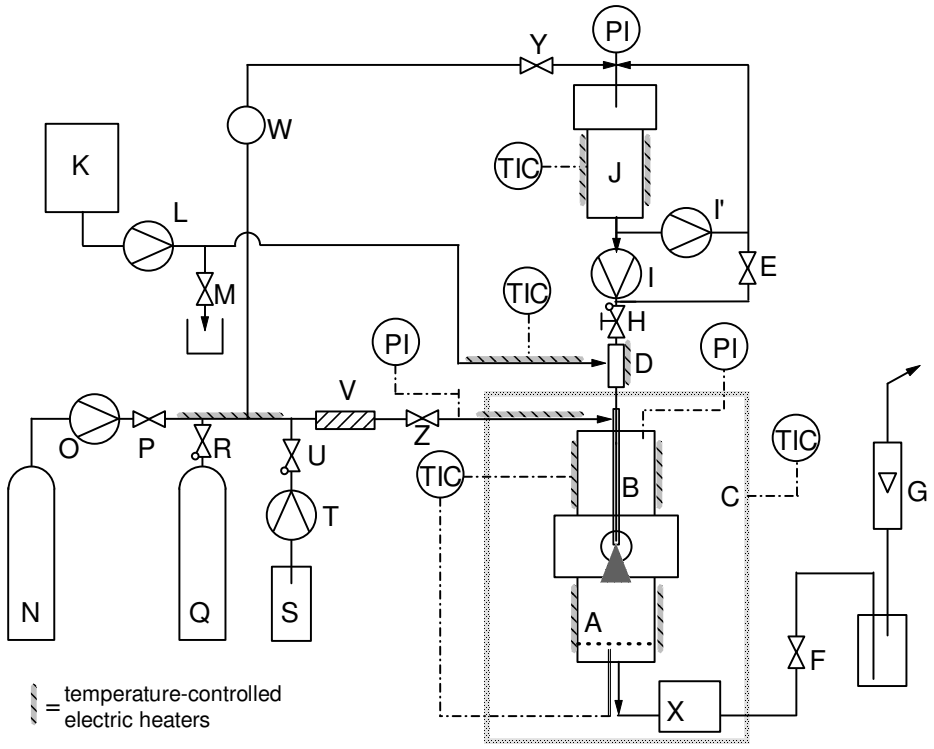


**Figure 10-1.** Apparatus for particle formation and microencapsulation: A) view cell equipped with filter; B) coaxial nozzle; C) thermostated circulating air bath; D) emulsifying device; E) needle valve; F) heated micrometering valve; G) rotameter; H) check valve and shut-off valve; I and I') piston pump; J) top reservoir; K) syringe with aqueous solution; L) piston pump; M) needle valve; N) $CO_2$ cylinder; O) syringe pump; P) shut-off valve; Q) $N_2$ cylinder; R) shut off valve; S) beaker with ethanol; T) HPLC pump; U) check valve; V) static mixer; W) pressure regulator; X) UV/VIS cell; Y, Z) shut-off valve.

Abbreviations: PI - pressure indicator; TIC - temperature indicator and controller.

The mixture of $CO_2$+ethanol passed through a double-helix static mixer prior to injection into the view cell flowing in the outer channel of the coaxial nozzle (B). The flow rate of $CO_2$ was adjusted using a heated metering valve (F) at the outlet of the view cell, and monitored by means of a rotameter (G), which was located after a sealed collection bottle trapping ethanol. The flow rate of $CO_2$ delivered into the system was displayed by the ISCO syringe pump controllers, which were set to constant pressure mode.

An aqueous solution containing the solid components to be precipitated was pumped by means of a metering piston pump (L) (LEWA GmbH, Leonberg, Germany) into the inner tube of the coaxial nozzle and sprayed into the view cell (A). Due to the high viscosity of the aqueous solutions containing BG the metering piston pump was equipped with additional spring-loaded poppet check valves (Swagelok Inc., Edmonton, AB, Canada) at the inlet and outlet of the pump. Three different arrangements were tested for the coaxial nozzle consisting of two seamless stainless steel tubings, as illustrated in Fig. 10-2.

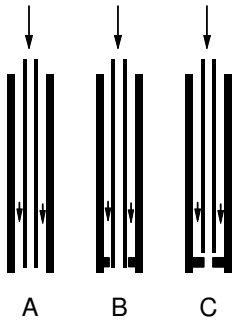


**Figure 10-2.** Coaxial nozzle configurations tested in the supercritical drying process.

The outer tubing of the coaxial nozzle had an OD and ID of 6.35 and 3.05 mm, while those of the inner tubing were 1.59 and 1.08 mm, respectively. Modified set-screw style threaded orifice inserts (ZM-35-M4-5-SS, O'Keefe Controls, Trumbull, CT, USA) were fitted into the outer tubing at the nozzle tip (Fig. 10-2B and C). The orifice diameter for nozzle B was 1.75 mm, while for nozzle C two orifice diameters, namely 0.51 and 0.89 mm, were tested. For design

C, the orifice length and the gap between the tip of the inner tubing and the nozzle orifice were both about 1 mm. The jet emerging from the nozzle tip could be observed through the window in the middle of the view cell allowing the observation of jet breakup, atomization, particle precipitation and nozzle clogging. The distance from the nozzle tip to the filter plate at the bottom of the view cell was about 7 cm. The filter to collect the particles consisted of a sintered metal frit with pore size of 10 μm, which was covered with a 0.1 μm nylon filter for each experiment to collect the particles.

In order to continuously generate an emulsion of fish oil in the aqueous solution two different custom-designed emulsifying devices (EMD) were assembled, as illustrated in Fig. 10-3.

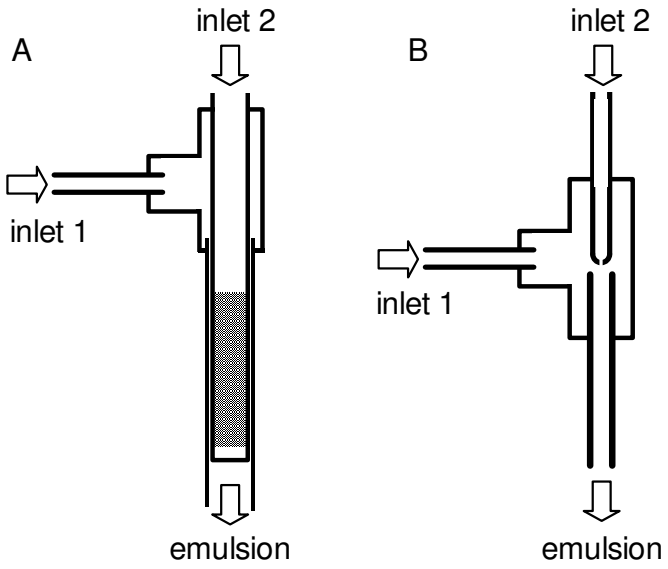


**Figure 10-3.** Two types of emulsifying device used to continuously inject fish oil into the aqueous solution of shell matrix.

For all experiments the aqueous solution with the shell material was pumped into inlet 1 of the EMD. As well, in case of the microencapsulation experiments, a mixture of fish oil+$CO_2$-expanded ethanol (CX EtOH) was injected through inlet 2 of the EMD (Fig. 10-3) to disperse the oil in the aqueous solution. The first design (Fig. 10-3A) consisted of a sintered stainless steel

sparging element (Mott Corp., Farmington, CT, USA) with an OD of 6.35 mm and average pore size ranging from 0.2 to 5 μm placed inside a stainless steel tubing with an ID of 7.04 mm, thereby leaving only a very narrow annulus between the sparger element and housing tube in order to generate high shear rates facilitating membrane emulsification. The second design (Fig. 10-3B), consisted of a stainless steel union-Tee (Swagelok Inc., Edmonton, AB, Canada) with a custom-made nozzle having a round cap and orifice diameter of 50 μm (Lenox Laser Inc., Glen Arm, MD, USA) pointing at the entrance of the outlet tube (OD and ID of 6.35 and 2 mm, respectively), leaving only a narrow gap between the nozzle tip and the outlet tube (0.5 mm) to generate high shear rates at the point of oil injection to facilitate emulsification.

For the microencapsulation experiments, the top reservoir of the apparatus was used to prepare a mixture of fish oil+CX EtOH. The top reservoir (60 mL) connected to a dual head piston pump (Minipump, Milton Roy, Ivyland, PA, USA), where one pump head was used to circulate the fish oil+CX EtOH mixture at a flow rate of 9.2 mL/min from the bottom to the top of the reservoir to facilitate equilibration, while the other pump head set to a flow rate ranging from 0.4 to 0.8 mL/min was used to inject that fish oil mixture into the emulsifying device at inlet 2 (Fig. 10-3). Since the performance of the check valves of that pump was found to be unpredictable at elevated pressures, additional external spring-loaded check valves (Swagelok Inc., Edmonton, AB, Canada) were installed at the pump head used to inject the fish oil mixture into the EMD. A high pressure UV/VIS detector (X) (Milton Roy, Ivyland, PA, USA) set to a wavelength of 290 nm was used at the outlet of the view cell to monitor the concentration of ethanol in the outlet stream of the view cell, allowing to observe *in situ* when steady state was reached.

### 10.2.3 Particle formation and microencapsulation experiments

All particle formation experiments were carried out with the view cell preheated to 40°C, while the $CO_2$+EtOH mixture was preheated to 45°C in the tubing leading to the nozzle. The slightly higher temperature in the pre-heater was

chosen to compensate for the cooling due to the Joule-Thomson effect during the expansion in the nozzle. The temperature in the spray chamber decreased during spraying from 40°C to a constant value of about 38°C. For the particle formation experiments, various process parameters and conditions were evaluated during preliminary tests, including pressure, flow rates, nozzle setup, emulsifying device setup and concentration of solids in the aqueous solution as listed in Table 10-1. An overview of the experimental conditions studied is provided in Table 10-2.

**Table 10-1.** List of parameters tested for particle formation and microencapsulation.

| Process parameter | | Range | Unit |
|---|---|---|---|
| Temperature | | 40 | °C |
| Pressure | | 24 | MPa |
| | | 10 | MPa |
| Nozzle setup | | A,B,C | |
| Orifice diameter | | 0.89 | mm |
| | | 0.51 | mm |
| $CO_2$ flow rate | | 21 | mL/min |
| | | 25 | mL/min |
| | | 32 | mL/min |
| EtOH flow rate | | 12 | mL/min |
| | | 24 | mL/min |
| Flow rate of aqueous solution | | 0.45 | mL/min |
| | | 0.9 | mL/min |
| | | 1.9 | mL/min |
| | | 2.8 | mL/min |
| Solid concentration[#] | BG | 0.84 | wt% |
| (wt%, as is basis) | | 0.95 | wt% |
| | | 1.67 | wt% |
| | GA | 21.8 | wt% |
| | | 10 | wt% |
| | GA+BG | 10+0.5 | wt% |
| Emulsifying device setup | | FRIT | |
| | | NOZZLE | |

[#]GA: gum arabic, BG: β-glucan.

**Table 10-2.** Experimental conditions for particle formation and encapsulation.

| Experiment[#] | P [MPa] | Flow rate [mL/min] | | | | Spray solution | | | Emulsifier setup[$] |
|---|---|---|---|---|---|---|---|---|---|
| | | Fish oil | $CO_2$ | EtOH | Solution | Solute | [wt%] | [mL] | |
| GA_1 | 24 | | 25 | 24 | 0.45 | GA | 10 | 5 | FRIT |
| GA_2 | 24 | | 25 | 24 | 0.45 | GA | 10 | 4.5 | FRIT |
| GA_3 | 24 | | 23 | 12 | 0.45 | GA | 10 | 5 | FRIT |
| BG_1 | 24 | | 25 | 24 | 0.73 | BG | 0.84 | 4.5 | no FRIT/cap |
| BG_2 | 24 | | 25 | 24 | 0.785 | BG | 0.84 | 21.5 | no FRIT/cap |
| BG_3 | 24 | | 25 | 24 | 0.73 | BG | 1.67 | 18 | no FRIT/cap |
| GA_BG_1 | 24 | | 25 | 24 | | GA | 10 | 5 | no FRIT/cap |
| | | | | | | BG | 0.5 | 5 | |
| GA_BG_2 | 24 | | 25 | 24 | 1.9 | GA | 9.8 | 1.5 | no FRIT/cap |
| | | | | | | BG | 0.5 | 1.5 | |
| GA_BG_3 | 24 | | 25 | 24 | 1.9 | GA | 9.93 | 7 | NOZZLE |
| | | | | | | BG | 0.5 | 7 | |
| GA_BG_4 | 10 | | 25 | 24 | 1.88 | GA | 9.87 | 7.5 | NOZZLE |
| | | | | | | BG | 0.52 | 7.5 | |
| GA_BG_FO_1 | 24 | 0.3 | 25 | 24 | 1.9 | GA | 9.93 | 8.5 | NOZZLE |
| | | | | | | BG | 0.5 | 8.5 | |
| GA_BG_FO_2 | 10 | 0.3 | 25 | 24 | 1.88 | GA | 9.87 | 7 | NOZZLE |
| | | | | | | BG | 0.52 | 7 | |
| GA_BG_FO_3 | 10 | 0.8 | 25 | 24 | 1.42 | GA | 9.87 | 10 | NOZZLE |
| | | | | | | BG | 0.52 | 10 | |

[#] GA: gum arabic; BG: β-glucan; FO: fish oil.
[$] FRIT: EMD type A; no FRIT/cap: replaced sparging element with a cap; NOZZLE: EMD type B.

#### 10.2.3.1 Particle formation protocol

For the particle formation experiments, the system was heated to 40°C and pressurized with $CO_2$ to the experimental pressure. A continuous flow rate of $CO_2$ was established by adjusting the heated metering valve at the outlet of the view cell. The cosolvent pump (T) was started to continuously deliver EtOH to the system at the desired flow rate. After about 10 min steady state was reached as evidenced by the constant absorption indicated by the UV/VIS detector, as well as a constant temperature in the view cell. The spray process was started by switching on pump (L) to deliver the aqueous solution of solids into the coaxial nozzle.

Spraying of the aqueous solution could be observed through the window of the view cell so that if clogging of the nozzle occurred, a pressure impulse was generated by closing the shut-off valve (Z) at the inlet of the nozzle for a few seconds so that the flow of the incoming $CO_2$+EtOH mixture could be interrupted and a pressure pulse was generated, which generally freed the nozzle orifice from a plug. Spraying of the aqueous solution was carried out for about 5 to 10 min until the spray chamber seemed to be full of particles, which were swirling around inside the spray chamber. However, due to fine particles depositing in the cavity of the window of the cell the view of the nozzle was blocked after several minutes. However, due to the pressure indicators installed before and after the nozzle the occurrence of blocking in the nozzle could be detected by monitoring the pressure drop across the nozzle.

At the end of the experiment, the tubing between the nozzle and pump (L) was back-flushed carefully by opening the needle valve (M) so that the remaining aqueous solution was pushed out of the line, to avoid drops from falling out of the nozzle onto the dried particles during the depressurization step. After the spraying was stopped, the ethanol pump was stopped and the view cell was flushed with pure $CO_2$ at the same pressure and temperature conditions until no more ethanol was collected in the collection flask at the outlet of the view cell. Then the $CO_2$ inlet valve (P) was closed and the valve of the nitrogen cylinder (R) opened,

which gradually led to a change of pressure inside of the view cell to that of the pressure level of the nitrogen cylinder, which was about 16 MPa. Then, nitrogen was flushed through the view cell until all $CO_2$ was replaced, as monitored by the UV/VIS detector. Thereby, no liquid $CO_2$ was formed inside the view cell and all remaining ethanol potentially dissolved in $CO_2$ was pushed out of the cell, prior to depressurization. As soon as all $CO_2$ was removed from the cell, the view cell was depressurized slowly to atmospheric pressure and particles precipitated onto the filter paper inside the view cell were collected.

#### 10.2.3.2 Microencapsulation protocol

Microencapsulation experiments were carried out similar to the particle formation experiments, except that prior to the experiments 5 mL of fish oil and 20 mL of EtOH were filled into the top reservoir, which was preheated to 40°C. The top reservoir was then pressurized to 9 MPa using the pressure regulator (W). The valve (Y) was closed and the circulation pump (I and I') set to a flow rate of 18 mL/min was started, while valve (E) was open, to achieve equilibration of the EtOH+fish oil+$CO_2$ mixture. The circulation was started about 40 min prior to starting the particle formation experiments, as described above. In the microencapsulation process the aqueous solution was pumped into the high pressure cell and then as soon as the first solids precipitated in the view cell, the oil injection was started by opening valve (H) and closing valve (E), after the pump head (I) was set to the desired flow rate. The flow rates of aqueous solution and fish oil+ethanol+$CO_2$ mixture were chosen to result in a theoretical oil load in the particles of about 15-20% by weight. Similar to the particle formation protocols, the spraying was carried out until the view cell seemed to be filled with particles, which usually amounted to about 1 g of solids, at which moment the oil injection from the top reservoir was interrupted by closing valve (H) and stopping the pump (I and I') immediately. At the same time, the injection of aqueous solution was stopped by switching off pump (L). In addition, as soon as spraying was finished the ethanol cosolvent pump was stopped and the particle formation protocol was followed to depressurize and collect the dry powder.

### 10.2.4 Particle characterization

Particle size and morphology were evaluated using scanning electron microscopy (SEM). For this purpose, the particles were placed on an adhesive sample stub and coated with a thin conductive layer (150 Å) of gold using a Nanotek SEMprep II sputter coater (Prestwich, Manchester, UK). The samples were analyzed with a SEM equipped with a Bruker Silicon Drift (BSD) detector and $LaB_6$ crystal source capable of providing images from 20x to 100,000x with a resolution of about 5 to 10 nm (Zeiss EVO MA 15, Carl Zeiss, Oberkochen, Germany).

Particle size distribution for the dry powder was determined in triplicate for each sample using a laser diffraction particle size analyzer (CILAS 1180, Cilas, Orleans, France) with a measurement range from 0.04 to 2500 μm.

The approximate bulk density was estimated by weighing the particles directly after collecting them from the view cell and by determining their volume in a graduated cylinder.

In order to determine the lipid content in the microcapsules, the powder was dissolved in 20 mL of water at 75°C and then thoroughly mixed with 40 mL of hexane in a separation funnel. The organic phase containing hexane and fish oil was transferred into a beaker and hexane was evaporated under the fume hood using a hot air blower at about 50°C. The remaining fish oil was determined gravimetrically.

## 10.3 Results and discussion

An overview of the results obtained for various experimental conditions, such as visual appearance, bulk density, mass of powder collected and index to the SEM images for particle morphology is presented in Table 10-3.

**Table 10-3.** Summary of experimental outcomes for particle formation and encapsulation.

| Experiment | Particles collected [g] | Particle bulk density [g/mL] | Appearance of precipitate | SEM images |
|---|---|---|---|---|
| GA_1 | 0.500 | 0.035 | fine voluminous powder | Fig. 10-7 A,B, D-I |
| GA_2 | 0.120 | 0.017 | fine voluminous powder | similar to GA_1 |
| GA_3 | 0.083 | 0.042 | fine voluminous powder | Fig. 10-7 C |
| BG_1 | 0.029 | 0.006 | voluminous fibrils cobweb | no SEM |
| BG_2 | 0.157 | 0.006 | voluminous fibrils cobweb | Fig. 10-8 A-I |
| BG_3 | 0.188 | | thicker fibrils | no SEM |
| GA_BG_1 | 0.270 | | fine voluminous powder | Fig. 10-9 A-G, Fig. 10-11 |
| GA_BG_2 | 0.055 | | fine voluminous powder | no SEM |
| GA_BG_3 | 0.965 | 0.038 | fine voluminous powder | no SEM |
| GA_BG_4 | 0.791 | | fine voluminous powder | Fig. 10-9 H,I |
| GA_BG_FO_1 | 0.942 | | fine voluminous powder | Fig. 10-10 D-G,I |
| GA_BG_FO_2 | 0.716 | 0.023 | fine voluminous powder | Fig. 10-10 A,C |
| GA_BG_FO_3 | 0.951 | | fine voluminous powder | Fig. 10-10 B,H |

### 10.3.1 Screening of processing parameters

During preliminary tests it was found that the maximum flow rate of the syringe pump (O) resulting in a constant continuous flow was about 25 mL/min. With that $CO_2$ flow rate and the upper limit of the HPLC pump (T) capable of delivering 24 mL/min of ethanol it was found that the best flow rate for the relatively viscous aqueous solution was in the range of 0.9 to 1.9 mL/min. With those flow rates, the best results in terms of jet breakup, atomization and particle precipitation were achieved with the nozzle design C. Precipitates obtained by using the nozzle configurations Fig. 10-2A and B are shown in Fig. 10-4. These precipitates were

rod-like structures far from a powder, which was a direct result of the highly viscous solution being injected at low flow rates, thereby not forming fine droplets. Higher flow rates would be required for the precipitation of fine particles.

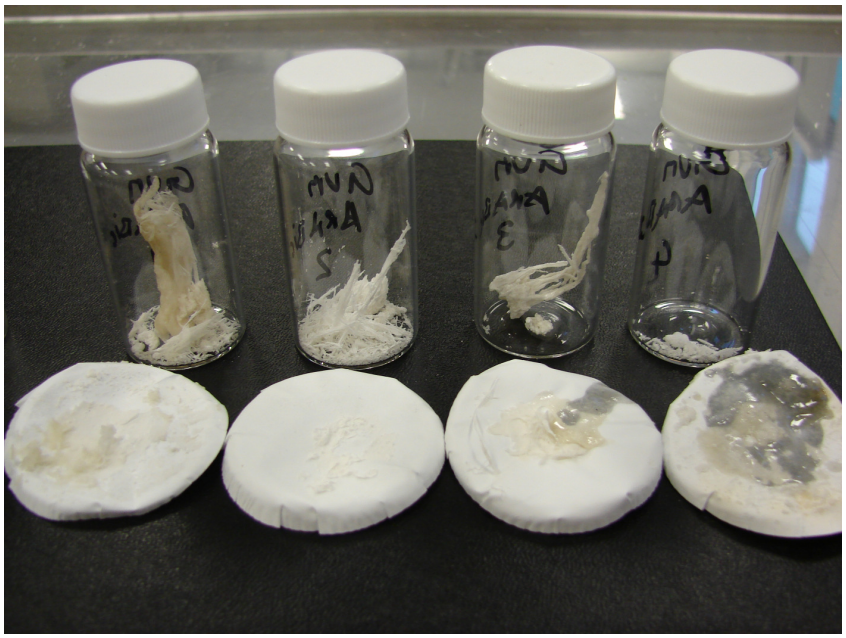

**Figure 10-4.** Gum arabic precipitates with nozzle configuration A and B.

Due to the relatively high viscosity of the aqueous solutions used (for example, an aqueous solution of 0.5 wt% BG concentrate as is had a viscosity of about 19 mPa.s at 40°C and a shear rate of 129 $s^{-1}$), it was impossible to generate a jet breakup and fine dispersion with nozzles A and B at the very low flow rates achievable with the available pumps. Therefore, all subsequent experiments were carried out with the nozzle setup C with an orifice diameter of 0.89 mm. Furthermore, during preliminary tests, the emulsifier device consisting of the sparging element (Fig. 10-3A) did not prove to work well at the very low flow rates; it also caused problems during the depressurization step, since liquid was pressed out through the porous tubing, which fell onto the dry particles and destroyed the samples. Consequently, the device illustrated in Fig. 10-3B employing a nozzle was used for all subsequent runs.

### 10.3.2 Particle characterization

#### 10.3.2.1 Visual appearance

The particles obtained in successful experiments were mostly free-flowing fluffy particles as illustrated in Fig. 10-5, except when pure BG solutions were sprayed, which resulted in fine fibrils and cobweb-like structures (Fig. 10-6).

**Figure 10-5.** Powder of gum arabic obtained by SCF drying.

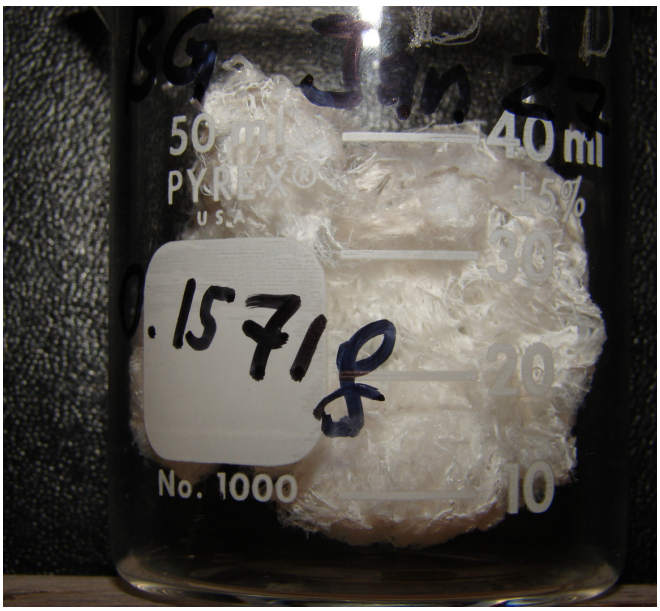


**Figure 10-6.** Cobweb-like structure of β-glucan obtained by SCF drying.

#### 10.3.2.2 Bulk density

The bulk density of the obtained particles was very low, which ranged from 0.017 to 0.042 g/mL for GA and was about 0.006 g/mL for BG fibrils (Fig. 10-6)..

#### 10.3.2.3 Particle morphology

The morphologies observed under the SEM were very diverse ranging from perfectly spherical particles, porous asymmetrical particles and amorphous structures in the case of GA (Fig. 10-7) to ultra-thin (<100 nm) fibrils and nano-porous sheets in the case of BG (Fig. 10-8). The morphology of particles obtained by co-precipitation of GA+BG resembled a mixture of fine particles both spherical and amorphous intertwined with fibrous structures (Fig. 10-9). The most striking particles with agglomerates of nano-spheres were obtained by the microencapsulation protocol, which may be attributed to the increased ethanol content of the total mixture prior to atomization (Fig. 10-10). Therefore, the anti-solvent effect of ethanol on BG may have triggered local nuclei formation prior to atomization. The morphology of particles depend on the mechanism of precipitation, which can be either due to the anti-solvent effect or due to spray drying effect, as was found for lysozyme precipitation in a PGSS process [17], where nitrogen-assisted atomization resulted in spherical particles, but $CO_2$-assisted atomization depended on the conditions of the pre-mixer, where spherical particles were formed at elevated temperatures but fibrils were formed at lower temperatures. It was reported that the anti-solvent effect due to higher $CO_2$ solubility in the solvent was more pronounced [17]. Thus, if the anti-solvent effect is strong enough to induce precipitation before the atomization can take place, it is less likely to obtain spherical particles. In the case of BG, the ethanol present in the $CO_2$ phase caused a very rapid precipitation due to the anti-solvent effect, which may be the reason why BG formed mainly fibrils and sheets, whereas GA formed spheres and amorphous structures as well.

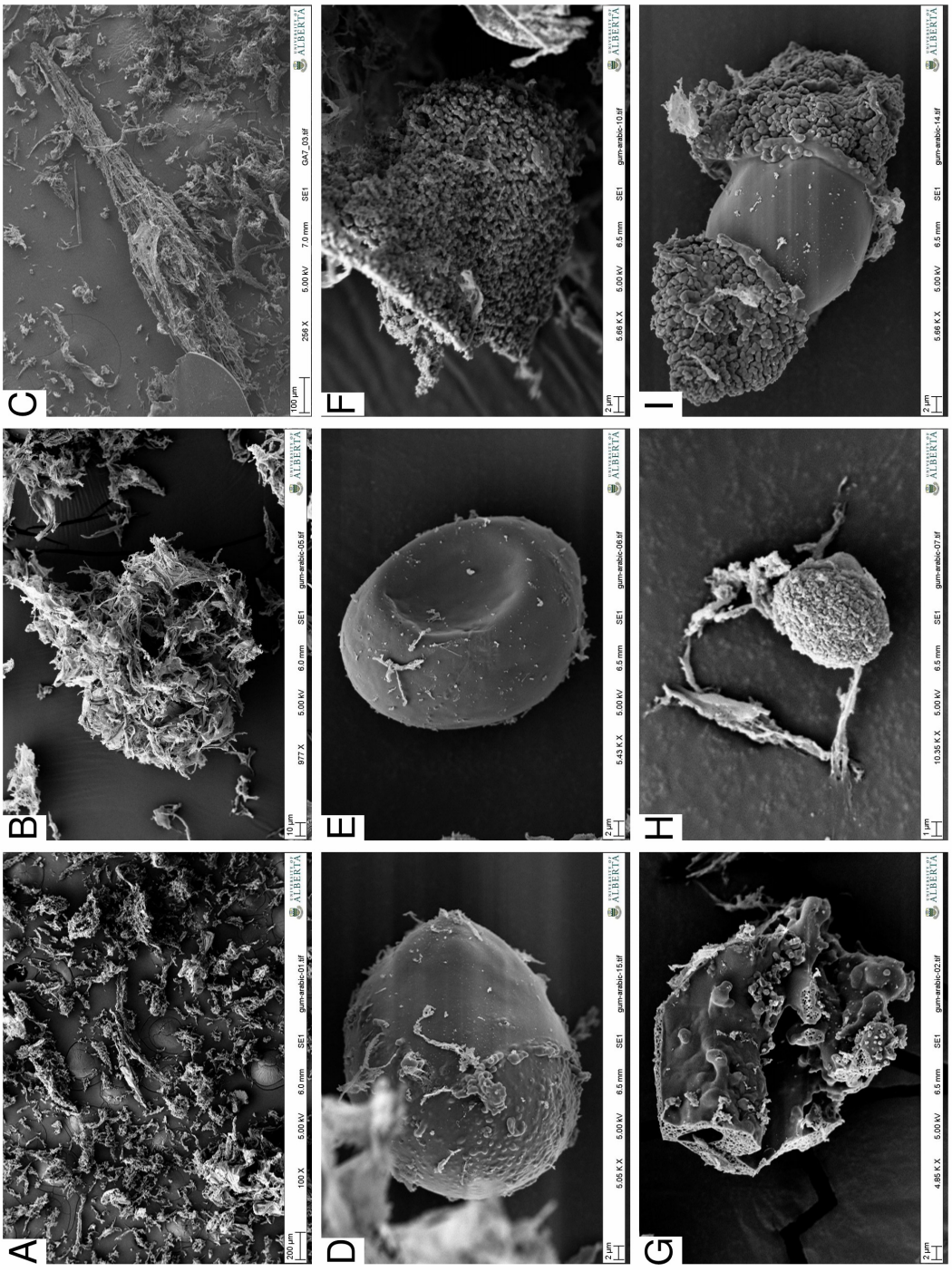


**Figure 10-7.** Morphologies of gum arabic (GA) particles obtained by SCF drying process.

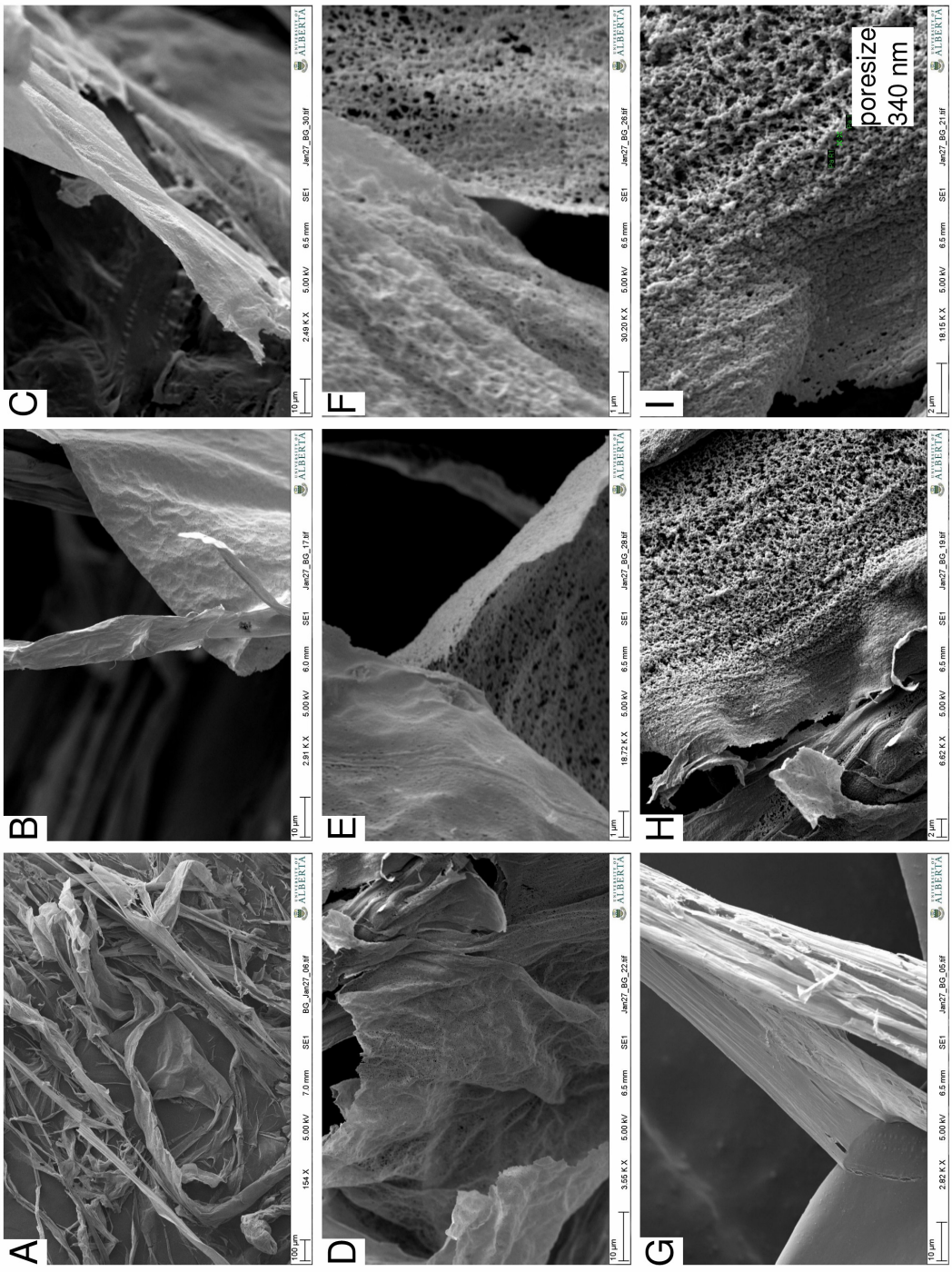


**Figure 10-8.** Morphologies of β-glucan (BG) particles obtained by SCF drying process.

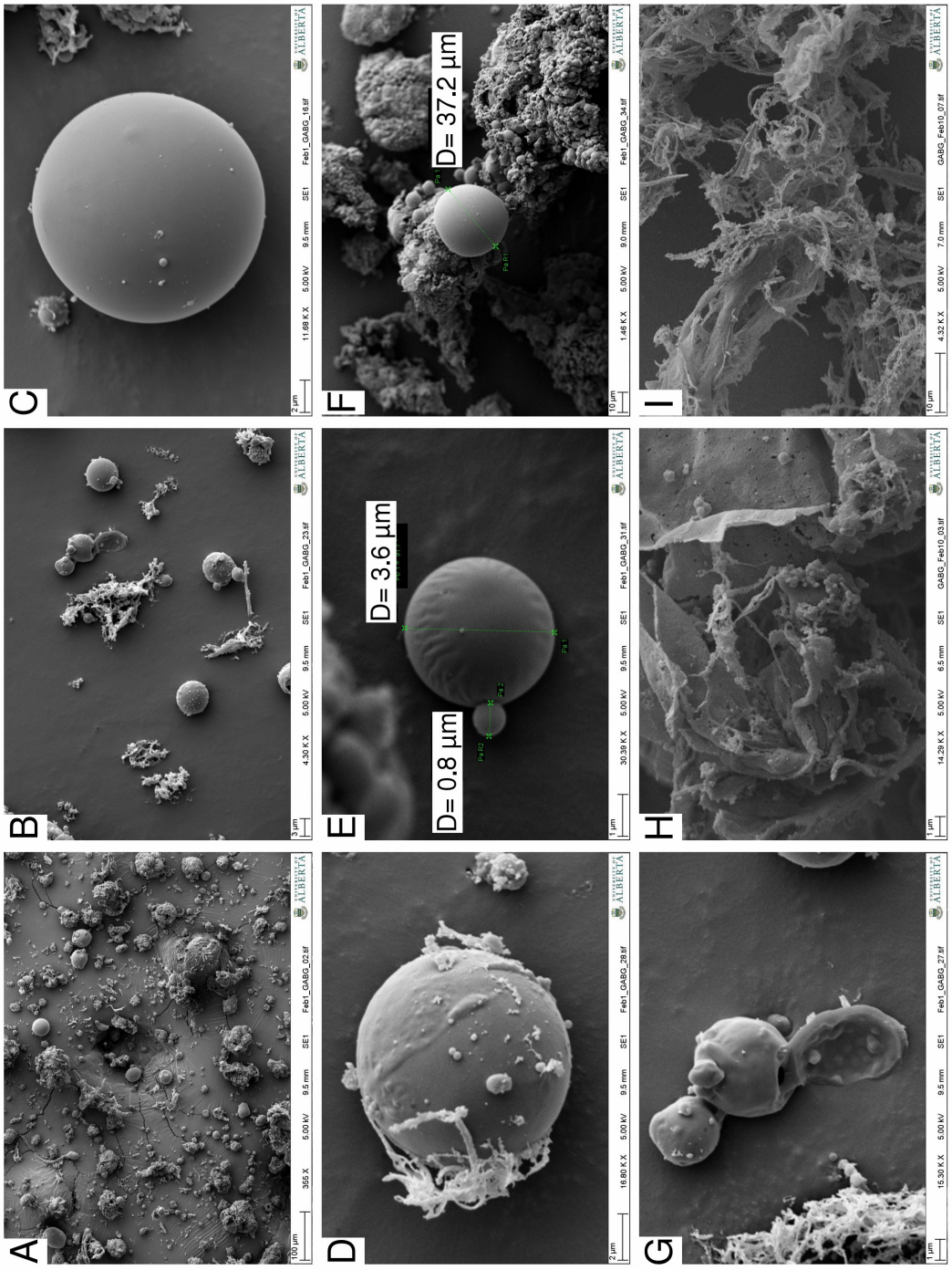


**Figure 10-9.** Morphologies of particles of gum arabic with β-glucan (GA_BG) obtained by SCF drying process.

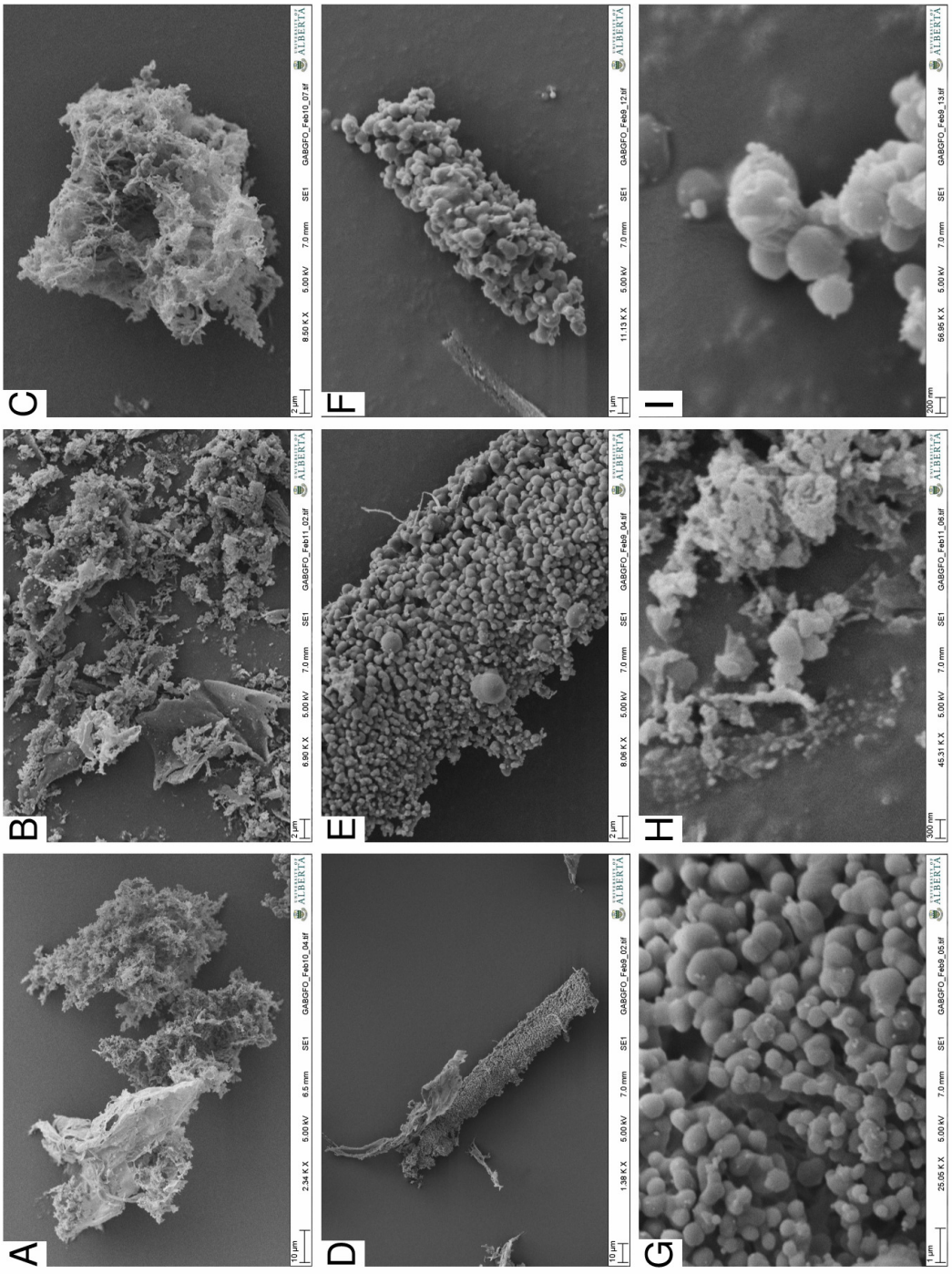


**Figure 10-10.** Morphologies of particles of gum arabic and β-glucan with co-injection of fish oil+EtOH+$CO_2$ (GA_BG_FO) in the SCF drying process.

More research is required to clarify the mechanism of precipitation for GA, which may depend on hydrodynamics in the coaxial nozzle prior to atomization and on the ethanol concentration in the $CO_2$ phase as well, because increased ethanol content would enhance water solubility and thus speed-up the drying process.

For the experiments with fish oil+ethanol+$CO_2$ injection, the $CO_2$ injected with the fish oil may act like a "spray enhancer" and may facilitate atomization, especially of the viscous solution and cause internal instabilities in the jet due to gas bubble formation, which leads to finer droplet formation in the coaxial nozzle and improved atomization. Agglomerates of nano-spheres were obtained in spherical and rod-like structures.

As well, some of the spheres seemed to burst and produced hollow spheres and tiny globules in experiments using a mixture of GA and BG (GA_BG) (Fig. 10-11).

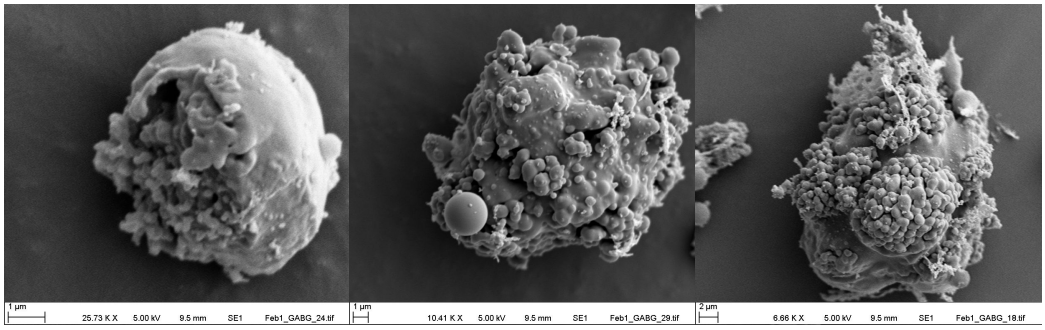


**Figure 10-11**. Bursting spheres with nano-globules of gum arabic and β-glucan (GA_BG).

### 10.3.2.4 Particle size distribution

The particle size distribution (PSD) was determined based on volume ($Q_3$) for the particles precipitated at 10 and 24 MPa with and without co-injection of fish oil+ethanol+$CO_2$ as illustrated in Figs. 10-12 and 10-13. The PSD at 10 MPa showed that the particles agglomerated to larger particles in the range between 500 to 1000 µm in the case of GA_BG, while there was also a peak in the distribution in the submicron range.

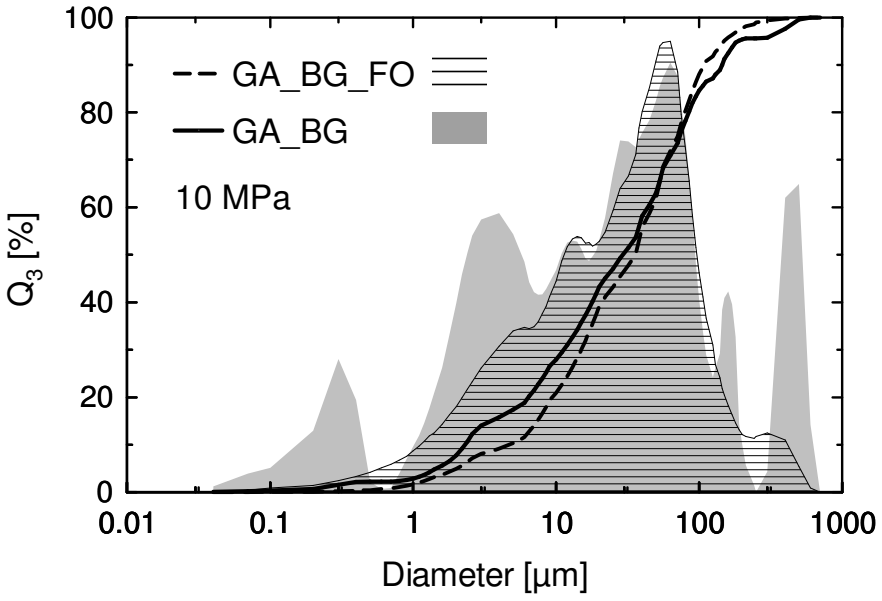


**Figure 10-12.** Particle size distribution for particles obtained at 10 MPa.

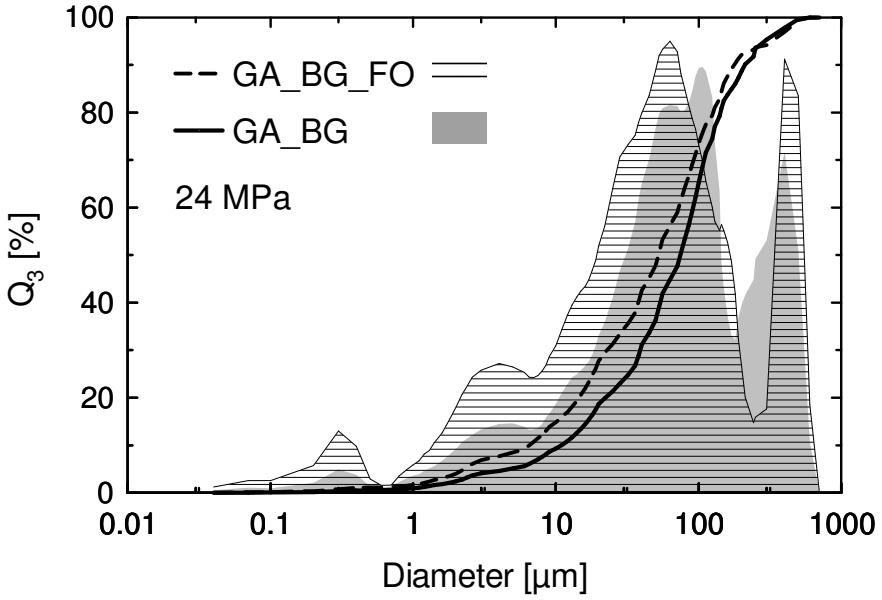


**Figure 10-13.** Particle size distribution for particles obtained at 24 MPa.

It must be highlighted that between the experiments carried out at 10 MPa and those carried out at 24 MPa, an additional check valve was installed in the injection pump head (I) for the fish oil mixture, because it appeared that the internal check valves of the pump did not work properly. However, it can be clearly seen for the GA_BG powder obtained at 10 MPa, that the PSD was multi-modal, supporting the observations in the SEM images that the particles were very diverse non-uniform in size and agglomerated. On the other hand, the experiment at 10 MPa with co-injection of fish oil mixture resulted in a more uniform PSD. The mean particle diameter of the powders obtained at 10 MPa were substantially smaller than those obtained at 24 MPa (Table 10-4).

**Table 10-4.** Mean particle diameter for selected experimental conditions.

| **Pressure [MPa]** | **Experimental conditions[$]** | **Median diameter at 50% $Q_3$ [μm]** | **Mean particle diameter [μm]** |
|---|---|---|---|
| 24 | GA_BG_3 | 73.2 | 117.8 |
| | GA_BG_FO_1 | 52.9 | 105.1 |
| 10 | GA_BG_4 | 29.4 | 69.6 |
| | GA_BG_FO_2 | 34.2 | 47.5 |

[$] refer to Table 10-2.

#### 10.3.2.5 Lipid content in the microcapsules

The lipid content of the particles was determined by dissolving the powder (0.5 g) in 20 mL water first. It should be noted that the powder dissolved readily in water, without forming clumps and that the solution released a smell of fish oil. However, the particles did not have that distinct fish odor, which could indicate that the encapsulation was complete. Nevertheless, it appeared that very small amount of oil was present in the sample (GA_BG_FO_3), since no fish oil appeared visible at the top of the solution. After dissolution, the lipid content of the powder was determined to be about 1% for the sample generated by

experiment GA_BG_FO_3. This oil content was much lower than expected. According to the estimated oil to solid ratio injected into the system, the powder should contain around 15 to 20 wt% of fish oil. Therefore, it can be assumed that most of the oil was extracted by the $CO_2$+ethanol mixture under the conditions in the spray chamber. It would therefore be necessary to optimize the $CO_2$ pressure, and potentially reduce the ethanol content to a much lower level. Ethanol has been shown to increase triglyceride solubility in SC-$CO_2$ substantially [18], which can reach about 5 wt% in $CO_2$ at 50°C and 10 MPa if 10 wt% of ethanol is present in $CO_2$. On the other hand, the removal of surface oil from the microcapsules due to the solvent power of $CO_2$+ethanol, thereby producing clean microcapsules can be an advantage in terms of the oxidative stability of the fish oil powder.

## 10.4 Conclusions

Particle formation of gum arabic and β-glucan from an aqueous solution was demonstrated applying supercritical drying at a mild temperature of 40°C and pressures of 10 and 24 MPa using ethanol as co-solvent to enhance water solubility in SC-$CO_2$ and as an anti-solvent to precipitate the polysaccharides. The morphology of the obtained β-glucan precipitate from the SCF drying process was different from that of GA. While GA formed spherical and amorphous particles, BG formed fibrils and sheet-like structures only. The bulk density of the precipitates was very low ranging from about 0.006 g/mL for the BG cobweb structure to about 0.04 g/mL for GA particles. Encapsulation of fish oil was attempted targeting about 20% oil content in the microspheres. When the mixture of fish oil+ethanol+$CO_2$ was injected into the aqueous solution prior to atomization nano-particles and nano-globular agglomerates formed.

The oil content in the microcapsules was only about 1%. Two potential reasons for this low oil content could be anticipated. First, the selected injection flow rate on the pump (I) was set to very low levels based on the performance of this pump for non-compressible liquids. However, the mixture of fish oil+ethanol+$CO_2$ is compressible; therefore, the amount of mixture injected was probably much lower than intended, which could be the main reason for the low

oil load in the particles. Second, part of the fish oil could have been extracted from the particles after precipitation, due to the relatively high solubility of fish oil in the SC-$CO_2$+ethanol mixture. Therefore, this process needs to be further studied in order to find optimum processing conditions to increase the oil load in the particles and to minimize the amount of oil extracted from the capsules. Another potential improvement could be to inject only a small amount of ethanol in combination with the fish oil into the aqueous solution and then spray the charged solution into a larger precipitation chamber with warm nitrogen as drying medium instead of $CO_2$, to avoid oil extraction from the particles after precipitation.

## 10.5 References


1. A. Shariati, C.J. Peters, Recent developments in particle design using supercritical fluids. Curr. Opin. Solid State Mater. Sci. 7 (2003) 371-383.

2. Z. Knez, E. Weidner, Particles formation and particle design using supercritical fluids. Curr. Opin. Solid State Mater. Sci. 7 (2003) 353-361.

3. J. Jung, M. Perrut, Particle design using supercritical fluids: Literature and patent survey. J. Supercrit. Fluids 20 (2001) 179-219.

4. P. York, Strategies for particle design using supercritical fluid technologies. Pharm. Sci. Technol. Today 2 (1999) 430-440.

5. F. Mattea, A. Martin, A. Matias-Gago, M.J. Cocero, Supercritical antisolvent precipitation from an emulsion: beta-Carotene nanoparticle formation. J. Supercrit. Fluids 51 (2009) 238-247.

6. N. Jovanović, A. Bouchard, G.W. Hofland, G.J. Witkamp, D.J.A. Crommelin, W. Jiskoot, Stabilization of proteins in dry powder formulations using supercritical fluid technology. Pharm. Res. 21 (2004) 1955-1969.

7. A. Bouchard, N. Jovanović, W. Jiskoot, E. Mendes, G.J. Witkamp, D.J.A. Crommelin, G.W. Hofland, Lysozyme particle formation during supercritical fluid drying: Particle morphology and molecular integrity. J. Supercrit. Fluids 40 (2007) 293-307.

8. A. Bouchard, N. Jovanović, G.W. Hofland, W. Jiskoot, E. Mendes, D.J.A. Crommelin, G.J. Witkamp, Supercritical fluid drying of carbohydrates: Selection of suitable excipients and process conditions. Eur. J. Pharm. Biopharm. 68 (2008) 781-794.

9. A. Bouchard, N. Jovanović, A.H. de Boer, A. Martin, W. Jiskoot, D.J.A. Crommelin, G.W. Hofland, G.J. Witkamp, Effect of the spraying conditions and nozzle design on the shape and size distribution of particles obtained with supercritical fluid drying. Eur. J. Pharm. Biopharm. 70 (2008) 389-401.

10. A. Bouchard, N. Jovanović, A. Martin, G.W. Hofland, D.J.A. Crommelin, W. Jiskoot, G.J. Witkamp, Effect of the modifier on the particle formation and crystallisation behaviour during precipitation from aqueous solutions. J. Supercrit. Fluids 44 (2008) 409-421.

11. A. Martin, A. Bouchard, G.W. Hofland, G.J. Witkamp, M.J. Cocero, Mathematical modeling of the mass transfer from aqueous solutions in a supercritical fluid during particle formation. J. Supercrit. Fluids 41 (2007) 126-137.

12. J. Kluge, F. Fusaro, N. Casas, M. Mazzotti, G. Muhrer, Production of PLGA micro- and nanocomposites by supercritical fluid extraction of emulsions: I. Encapsulation of lysozyme. J. Supercrit. Fluids 50 (2009) 327-335.

13. J. Kluge, F. Fusaro, M. Mazzotti, G. Muhrer, Production of PLGA micro- and nanocomposites by supercritical fluid extraction of emulsions: II. Encapsulation of Ketoprofen. J. Supercrit. Fluids 50 (2009) 336-343.

14. Z. Wen, B. Liu, Z. Zheng, X. You, Y. Pu, Q. Li, Preparation of liposomes entrapping essential oil from *Atractylodes macrocephala Koidz* by modified RESS technique. Chem. Eng. Res. Des. (2010) (in press).

15. S. Varona, S. Kareth, M.J. Cocero. Encapsulation of essentials oils using biopolymers for their use in ecological agriculture. in 9th International symposium on supercritical fluids 2009. Arcachon, France.

16. B.S. Ghotra, T. Vasanthan, F. Temelli, Rheological properties of aqueous blends of high purity barley β-glucan with high purity commercial food gums. Food Chemistry 117 (2009) 417-425.

17. M.A. Rodrigues, J. Li, L. Padrela, A. Almeida, H.A. Matos, E.G. de Azevedo, Anti-solvent effect in the production of lysozyme nanoparticles by supercritical fluid-assisted atomization processes. J. Supercrit. Fluids 48 (2009) 253-260.

18. G. Brunner, S. Peter, On the solubility of glycerides and fatty acids in compressed gases in the presence of an entrainer. Sep. Sci. Technol. 17 (1982) 199-214.

# 11 Conclusions and Recommendations

Fish oil has proven health benefits due its high content of polyunsaturated fatty acids (PUFA) such as eicosapentaenoic acid (C20:5 ω-3, EPA) and docosahexaenoic acid (C22:6 ω-3, DHA) [1]. However, due to the high level of PUFA, fish oil is susceptible to oxidative deterioration [2] and must be protected before being incorporated into food systems. One possibility to protect the oil from contact with air is to microencapsulate the fish oil, to create a physical barrier between the oil and its environment. Fish oil in the form of microcapsules or microspheres has been produced in the industry and research labs by means of spray drying, complex coacervation, freeze drying techniques and others. However, some of the conventional techniques suffer from shortcomings such as high processing temperatures, contact with air, or the need for organic solvents or cross-linking agents.

Supercritical fluid technology may offer the potential to overcome the need for high processing temperatures, contact with air, and potentially hazardous chemicals. Carbon dioxide ($CO_2$) with its critical point at moderate temperature and pressure ($T_c$=31.1°C, $P_c$=7.4 MPa) could be a suitable processing medium for the preparation of microencapsulated fish oil. Particle formation using supercritical carbon dioxide (SC-$CO_2$) technology has been studied for many decades [3, 4], with recent developments applied to SCF drying of aqueous solutions carrying sensitive nutraceuticals, proteins or carbohydrates [5, 6]. However, since there was no evidence in the literature that microencapsulation of fish oil has been performed using SCF drying techniques, there was a need to develop and evaluate the potential for such an approach to microencapsulate fish oil in a matrix consisting of biopolymers, including gum arabic and β-glucan, which has numerous health benefits [7]. The basic idea was to combine the health benefits of fish oil with those of soluble fibre, by developing a continuous process for emulsification and encapsulation of fish oil into the shell material, applying SC-$CO_2$ and ethanol as co-solvent as well as anti-solvent. Ethanol can enhance

the solubility of water in SC-$CO_2$ (co-solvent), while at the same time it decreases the solubility of polysaccharides in water (antisolvent) causing precipitation.

Therefore, in order to develop such a process, some physical properties and behavior of fish oil in contact with pressurized $CO_2$ and $CO_2$-expanded ethanol were evaluated first, including the density, interfacial tension and viscosity. For these studies mixtures of ethyl esters and natural fish oils were used rather than pure triglycerides or ethyl esters, in order to reflect what is used by the industry. Therefore, minor variations between different batches and sources of fish oils can be expected. However, the batch to batch variations in data are estimated to be in the order of about 5 to 10% so that the main trends found should still be valid. These investigations were described in detail in Chapters 3 to 9 of this thesis, whereas the process development and evaluation of the SCF drying process for particle formation and microencapsulation was presented in Chapter 10. The main findings of the studies are summarized below.

The density of marine lipids, such as fish oil in the form of triglycerides (TG) and fatty acid ethyl esters (FAEE), in equilibrium with pressurized $CO_2$ was determined at 40, 55 and 70°C and pressures of up to about 25 MPa (Chapter 3). For this purpose a novel device, consisting of a spring loaded balance with a sinker and an optical measuring system was designed and built to determine density under high pressure conditions. The density of both TG and FAEE increased with $CO_2$ pressure by about 5% up to 25 MPa. In addition, the volumetric expansion of fish oil TG and FAEE was determined at 40°C, which reached about 67 and 38% by volume, respectively, with increasing $CO_2$ pressure up to 15 MPa.

The interfacial tension (IFT) of marine lipids in contact with pressurized $CO_2$ was determined at 40, 55 and 70°C and pressures of up to about 25 MPa (Chapter 4). The IFT of both fish oil TG and FAEE decreased substantially with $CO_2$ pressure by more than an order of magnitude. In the case of FAEE, IFT reached ultra low levels and eventually vanished above 15 MPa, whereas for TG it approached a fairly constant level at elevated pressure of about 2 mN/m.

The density of $CO_2$-expanded (CX) ethanol was determined using the spring balance system at 40, 55 and 70°C and pressures of up to about 12 MPa (Chapter 5). For that purpose, a seal-less magnetically coupled piston pump was designed and built to facilitate equilibration in the view cell (Appendix). The density of CX ethanol increased up to a maximum value by about 3.7 to 6.3% in the temperature range of 40 to 70$^{o}$C and pressures from 6 to 9 MPa, respectively. However, as the mixture critical point of $CO_2$+ethanol was approached and a single homogeneous phase was formed the density decreased substantially.

The interfacial tension (IFT) of fish oil in contact with CX ethanol was determined at 40, 55 and 70°C and pressures of up to about 6 MPa (Chapter 6). The IFT of fish oil TG decreased substantially with pressure to ultra low values at moderate pressures of 6, 4.3 and 0.2 MPa at 40, 55, and 70°C, respectively. Furthermore, interfacial phenomena and Marangoni effects were observed in the system fish oil+CX ethanol, including interfacial turbulence, oscillating and kicking drops, as well as rapid internal mixing in pendant drops (Chapter 7).

The viscosity and rheological behavior of fish oil TG in equilibrium and expanded with pressurized $CO_2$ (CX TG) was determined at 40, 55 and 70°C and pressures of up to about 12 MPa using a rotational viscometer (Chapter 8). The viscosity of fish oil TG determined at a shear rate of 300 $s^{-1}$ decreased substantially with pressure and reached nearly constant levels of about 2.5 mPa.s at pressures above 10 MPa. Furthermore, fish oil in equilibrium and expanded with $CO_2$ exhibited shear-thickening (dilatant) behaviour, which was determined under similar conditions using a rotational viscometer and applying shear rates from 100 to 500 $s^{-1}$. At 40°C, the flow behavior index n increased from about 1 at atmospheric conditions corresponding to Newtonian behaviour to a level of 1.5 at 12 MPa, demonstrating dilatant behavior.

The viscosity and rheological behavior of fish oil FAEE in equilibrium and expanded with pressurized $CO_2$ (CX FAEE) was determined at 40, 55 and 70°C and pressures of up to about 12 MPa using a rotational viscometer (Chapter 9). At 40°C, the viscosity of CX FAEE decreased with $CO_2$ pressure to about one third of its initial value from 3.2 mPa.s to 1.1 mPa.s by increasing the $CO_2$

pressure from 0.1 to 11.8 MPa, respectively. Furthermore, a novel measuring technique, employing a quartz crystal microbalance (QCM) was evaluated for determination of viscosity of CX liquids. It was shown that the frequency response of a QCM when submersed in pure gas-free Newtonian liquids could be used to accurately determine liquid phase viscosity at atmospheric and elevated pressures. However, it was found that the QCM could not be used for measuring viscosity of CX liquids, due to the non-Newtonian behavior of most CX liquids and the potential formation of gas bubbles at the oscillating interface between the QCM and the CX liquid, leading to slip and thus underestimation of the viscosity.

The findings of the above studies (Chapters 3 to 9), focusing on the determination of physicochemical properties led to a better understanding of the behavior of the complex systems under investigation. The initial concept of the microencapsulation process was then modified to establish the final concept to design the emulsification step for the SCF drying process to produce microencapsulated fish oil. The aim was to produce finely dispersed fish oil in an aqueous solution of the shell material (gum arabic and β-glucan). For this reason, it seemed advantageous to first equilibrate the fish oil with a mixture of ethanol+$CO_2$ at a temperature of 40°C and a pressure of 9 MPa, to generate a mixture of fish oil+ethanol+$CO_2$. Under those conditions, the $CO_2$+ethanol mixture is above the mixture critical point of ethanol+$CO_2$, where the IFT was found to vanish and the solubility of fish oil in the ethanol+$CO_2$ phase is greatly enhanced, leading to a homogeneous mixture. It was envisioned that the injection of such a mixture into an aqueous solution would lead to stranding of the oil into fine droplets, so that subsequent SCF drying would result in the oil engulfed in the shell matrix.

Therefore, in order to develop such a process, the particle formation was tested first with aqueous solutions of gum arabic and β-glucan with various nozzle configurations and process parameters, such as pressure, flow rates and solids concentration (Chapter 10). The particle formation at 40$^{o}$C and pressures of 24 and 10 MPa was successful and resulted in particles having very diverse morphologies and diameters ranging from several hundred nanometers to about

500 μm. The precipitation of β-glucan alone resulted in the formation of fibrils and very thin sheet like structures, appearing like a cobweb with an extremely low bulk density, whereas precipitation of gum arabic and mixtures of gum arabic with β-glucan resulted in the formation of free flowing, voluminous powder.

Microencapsulation of fish oil was tested by injecting the fish oil+ethanol+$CO_2$ mixture prior to spraying and precipitation in the SCF drying process. The injection caused formation of nanoparticles and agglomerates consisting of very small globules as well as amorphous structures, which resulted in a very light free flowing powder of low bulk density. The obtained microcapsules have a water-soluble shell material, which would limit their application in aqueous products such as beverages. However, the powder can potentially be incorporated into dry powder mix applications, where the powder would be stored under dry conditions until usage, such as infant formula. However, in order to extend the range of applications, the shell material of the microcapsules may be modified further.

The oil content of the microcapsules obtained was relatively low at 1 wt%, due to the low flow rate setting of the piston pump used for injecting the fish oil+ethanol+$CO_2$ mixture and due to the relatively high solubility of oil in the SCF used for the drying process potentially leading to extraction of the fish oil from the microcapsules. The process can be optimized further in order to maximize the oil content in the microcapsules and to reduce the amount of oil extracted from the microcapsules during the dryng step. This optimization can include minimizing the ethanol load in the SCF and adjusting pressure and temperature conditions. Furthermore, it seems that a different drying medium, such as nitrogen instead of SC-$CO_2$+ethanol could eliminate the problem altogether. However, changing the drying medium will change the mechanism of precipitation from an antisolvent mechanism to a spray drying mechanism, which is expected to influence particle morphology. Nevertheless, the initial step of injecting the fish oil dispersed in CX ethanol or at elevated pressures in the form of a homogeneous phase consisting of fish oil+$CO_2$+ethanol into an aqueous solution of GA+BG may still lead to a local antisolvent effect by ethanol, causing

the first precipitation around the injected droplets. Thereby, the first layer of the encapsulation shell could form, which may be beneficial for the subsequent spraying and atomization into a nitrogen atmosphere. Furthermore, in order to better understand the mechanisms of particle formation, leading to either spherical or amorphous particles, it is necessary to study interfacial properties, such as interfacial tension of the aqueous biopolymer mixtures in contact with pressurized $CO_2$+ethanol mixtures, as well as the interfacial viscosity. In addition, the emulsification step, where a mixture of fish oil+ethanol+$CO_2$ is injected into the aqueous biopolymer solution, should be studied in a view cell in order to better understand the stranding and dispersion of fish oil under high pressure conditions leading to emulsification and initial shell formation. Interfacial activity and phenomena such as the Marangoni effect could influence the mass transfer and therefore the performance of the emulsification step as the oil is dispersed into the aqueous solution, as well as the atomization step for the injection of the emulsion into the SCF in the spray chamber. Nozzle design and flow rates have a great influence on particle size, shape and morphology besides affecting the potential for nozzle clogging, which need to be studied as well.

This thesis presents fundamental data as well as applied research in the area of supercritical fluid processing of lipids, particle formation and microencapsulation. The findings for the fundamental data, including density, viscosity and interfacial tension and enhanced understanding of the behavior of the systems evaluated should be useful for other process development and applications as well. In addition, the basic concept for the development of a novel process for particle formation and microencapsulation has been evaluated. Particle formation using a SCF drying technique was successfully applied to produce fibrils, spherical and amorphous particles, which may find applications not only in the food industry but other sectors as well, including the pharmaceutical or cosmetic industry. As well, the results obtained in the study of the novel approach for microencapsulation of fish oil evaluated in this thesis may inspire further research and be the first stepping stone for continued development considering the suggestions provided above.

## 11.1 References


1. F. Sahena, I.S.M. Zaidul, S. Jinap, N. Saari, H.A. Jahurul, K.A. Abbas, N.A. Norulaini, PUFAs in fish: Extraction, fractionation, importance in health. Compr. Rev. Food Sci. Food Safety 8 (2009) 59-74.

2. J.B. Rossell, Fish Oils. 2009, Leatherhead, Surrey; Chichester, West Sussex, U.K.: Leatherhead Food International; Wiley-Blackwell.

3. J. Jung, M. Perrut, Particle design using supercritical fluids: Literature and patent survey. J. Supercrit. Fluids 20 (2001) 179-219.

4. A. Shariati, C.J. Peters, Recent developments in particle design using supercritical fluids. Curr. Opin. Solid State Mater. Sci. 7 (2003) 371-383.

5. D. Meterc, M. Petermann, E. Weidner, Drying of aqueous green tea extracts using a supercritical fluid spray process. J. Supercrit. Fluids 45 (2008) 253-259.

6. A. Bouchard, N. Jovanović, G.W. Hofland, W. Jiskoot, E. Mendes, D.J.A. Crommelin, G.J. Witkamp, Supercritical fluid drying of carbohydrates: Selection of suitable excipients and process conditions. Eur. J. Pharm. Biopharm. 68 (2008) 781-794.

7. C.S. Brennan, L.J. Cleary, The potential use of cereal (1-->3,1-->4)-β-D-glucans as functional food ingredients. J. Cereal Sci. 42 (2005) 1-13.

# APPENDIX

# 12 APPENDIX: Design of a high-pressure circulating pump for viscous liquids[1]

## 12.1 Introduction

In phase equilibria studies, one can significantly shorten the time needed for equilibration by using a circulating pump. Seal-less magnetically coupled pumps offer the advantage of avoiding the use of elastomeric seals or lubricants, thereby minimizing the occurrence of leaks, down-time and the need for maintenance. Furthermore, with a seal-less magnetically coupled pump all wetted parts can be made of stainless steel, which is particularly attractive for applications where the fluid is under high pressure, toxic or corrosive. A review of the scientific literature reveals numerous innovative designs for magnetically coupled pumps, with the majority of the published work describing reciprocating positive displacement pumps [1-23]. Commercially available magnetically coupled pumps are often centrifugal or gear pumps (HMD/Kontro, Micropump) rated up to about 34 MPa (5000 psi), whereas only a few of the magnetically coupled pump designs reported in the literature apply rotary action [4, 15, 20]. Those non-reciprocating pumps, incorporate rotors shaped like a turbine [4], an Archimedean screw [20], a simple magnetic stirbar [8], or other rotary type pump impeller [15]. Among those rotary-type magnetically coupled pumps, the Archimedean screw pump [20] was designed for circulating liquids under high pressure. This rather interesting design of a screw pump consists of a helical screw shaped rotor inside a high pressure cylindrical autoclave, which is driven by an externally wound stator functioning similar to a synchronous motor [20]. The advantage of this isochoric working Archimedean screw pump is that it avoids pulsation in the circulated fluid, which may be favorable in a supercritical fluid phase equilibria apparatus, where volume and pressure changes may lead to solute precipitation inside the pump. However, the Archimedean screw pump suffers from a very complex design and low pump efficiency.

---

[1] A version of this chapter has been published in Rev. Sci. Instr. 80 (2009) art. no. 075104. Reprinted with permission from Seifried and Temelli, Rev. Sci. Instr. 80 (2009) art. no. 075104. Copyright © 2009, American Institute of Physics.

Magnetically coupled reciprocating piston pumps have been successfully used for circulating both liquids and gases in applications involving high and low pressures and temperatures. Magnetically coupled reciprocating pumps described in the literature use either solenoids [1-3, 5-7, 10, 13, 17, 18] or permanent magnets [9, 12, 14, 16, 19, 21-23] to drive the piston inside the pump cylinder. In some cases, the piston or parts of it are made from permanent magnets or magnetic stainless steel. The magnetically coupled pump reported by Torre *et al.* [14] incorporates a permanent magnet attached to bellows instead of a piston. Both approaches using either solenoids or permanent magnets used for driving the piston have advantages and disadvantages depending on the application of the pump. Permanent magnets have the great advantage that they do not generate heat during operation. This heat generation encountered in electromagnetically driven pumps depends on the type of solenoid, the power rating, and duty cycle. Heat generation may be of concern in situations where the heat can not be dissipated efficiently; thereby leading to challenges in phase equilibria measurements. However, a pump using permanent magnets requires an additional drive assembly involving externally moving parts to achieve linear motion. This drive assembly can consist either of a pneumatic actuator [23] or an electric motor equipped with a mechanical transmission to convert circular to linear motion by use of either a mechanical disc-and-arm [9] or disc-and-cable linkage [21, 22], a two crank assembly or a crank slot drive [9, 12, 19]. An external drive assembly and custom shaped magnets, often made from rare earth material to resist elevated temperatures over extended periods of time, can be costly. Additionally, pumps with permanent magnets and moving parts may not be suitable for an experimental setup where space is limited. Furthermore, to accommodate such a pump in a temperature-controlled environment may require the motor to be outside of the temperature-controlled environment to avoid damage to the motor and facilitate temperature control.

Considering the shortcomings of the pumps described above, the objective of the pump design presented in this study was to create a compact seal-less circulating pump for pumping viscous fluids at pressures of up to 34 MPa (5000

psi) and temperatures up to about 80 ºC. Having no external moving parts and due to its small size as well as reasonably low heat generation, the pump can be placed in a temperature-controlled circulating air bath for applications where constant temperature is important. Furthermore, using solely off-the-shelf parts to build the pump facilitates straightforward assembly without the need for a machine shop.

## 12.2 Pump description

The pump presented here consists of three main parts, namely the pump body, the controller and a 12 V direct current (DC) power supply. The design of this high pressure pump is similar to previously reported pumps, such as the all glass circulating pump described by Watson [1], the electromagnetic pump presented by Sterner [2] and the magnetic pump designed more recently by Peleties *et al.* [23]. However, the main difference is that the pump presented here (Figs. 12-1 and 12-2) is suitable to circulate viscous fluids at pressures of up to 34 MPa (5000 psi) and is made entirely of commercially available parts.

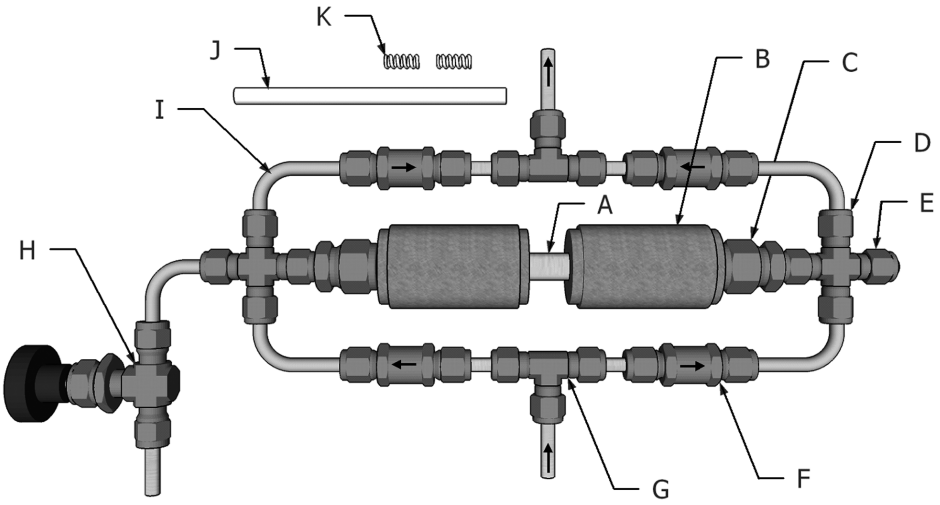


**Figure 12-1.** Circulating pump body parts: (A) pump cylinder, (B) solenoids (S1 and S2), (C) reducing union, (D) union cross, (E) plug, (F) check valve, (G) union-tee, (H) needle valve, (I) ¼" tubing, (J) piston, (K) compression spring.

The pump body consists of a stainless steel (SS316) high pressure cylindrical tube, containing a magnetic stainless steel (SS416) piston. The piston is driven by

two alternatively energized solenoids placed at both ends of the cylinder. This piston movement causes the fluid to be drawn in on one side of the cylinder and pushed out the other side.

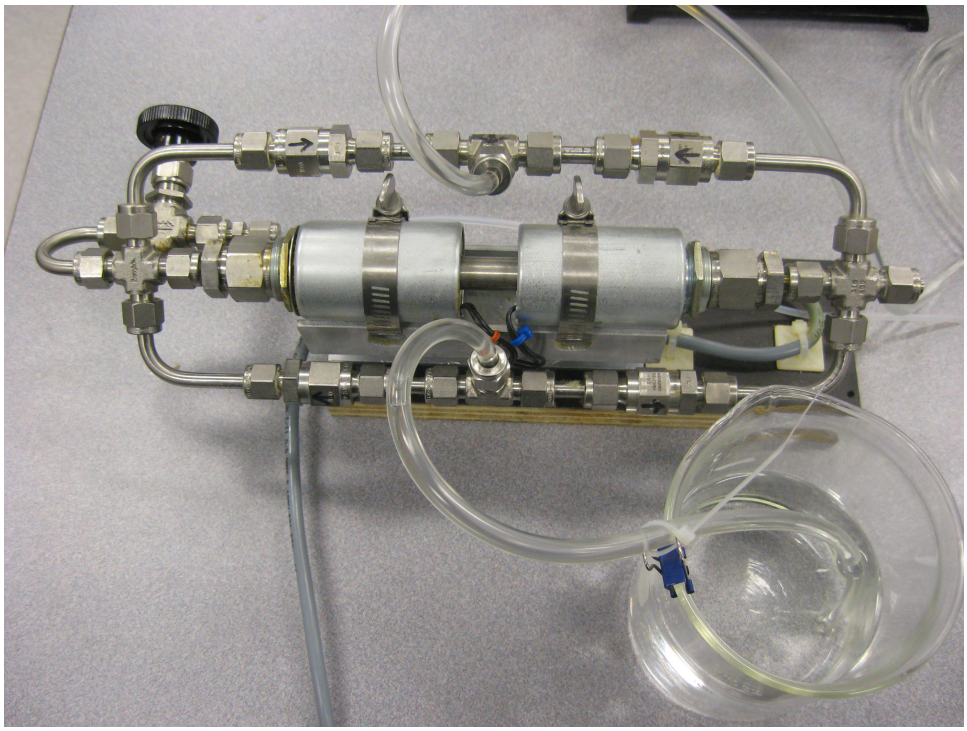

**Figure 12-2.** Photograph of circulating pump.

Both ends of the cylinder connect to a check-valve bridge made from standard high pressure fittings and check valves. The check-valve bridge rectifies the flow, resulting in a dual acting pump. The solenoids are alternatively activated through current from the 12 V DC power supply. Switching the current alternatively between the two solenoids is accomplished by two solid-state relays hooked up to the electronic controller, which is essentially a square wave generator based on a 555-timer integrated circuit (Fig. 12-3). The potentiometers (Pot1, Pot2 in Fig. 12-3) of the electronic controller allow continuous adjustment of the reciprocation frequency in the range from 20 to 120 cycles per minute, corresponding to a frequency of 0.33 to 2 Hz. The controller circuit design (Fig. 12-3) is quite simple and can be assembled on a prototyping breadboard, thereby reducing the need for

soldering components to a minimum. The construction of the pump body and electronic circuit is described in more detail in the subsequent sections.

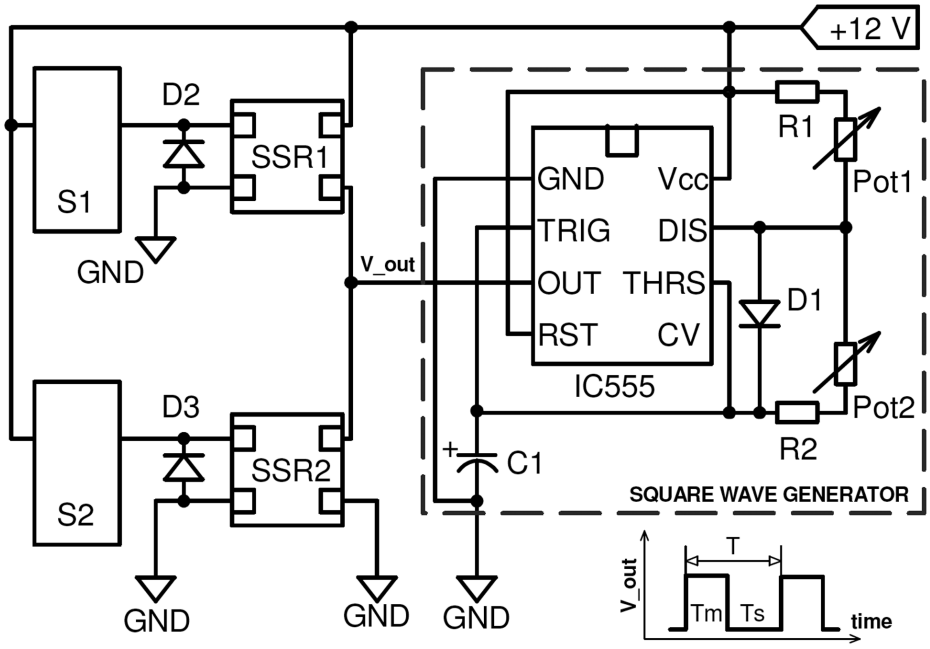


**Figure 12-3.** Electronic circuit of pump controller with electronic components used: (IC555) timer integrated circuit, (R1 and R2) 12 kΩ resistors, (Pot1 and Pot2) 100 kΩ linear variable potentiometers , (C1) electrolytic capacitor 22 μF, (D1) signal diode 1N4148, (SSR1 and SSR2) solid state solenoids, (D2 and D3) rectifier diodes 1N4001, (S1 and S2) linear pull 12 V DC solenoids.

### 12.2.1 Construction of the pump body

The pump body and internal parts are constructed using commercially available high pressure tubing, parts and fittings, all made from stainless steel (Fig. 12-1). The parts used to make this pump together with a list of suppliers and estimated costs are given in Table 12-1. Most of the parts listed can be purchased from local stores or from other suppliers as well. The pump is normally operated horizontally as illustrated in Fig. 12-2 but can also be operated in a vertical configuration. In order to assemble the pump body one needs the following tools: a drilling machine, wrenches to tighten the fittings, a tube bender and a hacksaw to cut the tubes and the piston rod to an appropriate length.

**Table 12-1.** Parts for pump body.

| Part | # of units | Description | Supplier<br>Part #<br>Unit price in US$ |
|---|---|---|---|
| | | **Smooth bore seamless tubing** | www.mcmaster.com |
| **A** | 1 | Material: SS316 | 89785K149 |
| | | ½" OD, .334" ID, .083" wall | 20 per ft. |
| | | **Sealed linear solenoid** | www.mcmaster.com |
| **B** | 2 | Manufacturer: Guardian Electric | 69905K851 |
| | | TP8X16-C-12V-DC, continuous, pull, 1" stroke, 60 oz force | 25 |
| | | **Reducer:** | www.swagelok.com |
| **C** | 2 | Material: SS316 | SS-810-R-4 |
| | | ½" OD X ¼" OD | 19 |
| | | **Union cross:** | www.swagelok.com |
| **D** | 2 | Material: SS316 | SS-400-4 |
| | | ¼" OD | 41 |
| | | **Plug:** | www.swagelok.com |
| **E** | 1 | Material: SS316 | SS-400-P |
| | | ¼" OD | 5 |
| | | **Poppet check valve:** | www.swagelok.com |
| **F** | 4 | Material: SS316, ¼" OD | SS-CHS4-1/3 |
| | | cracking pressure 1/3 psig | 60 |
| | | **Union Tee:** | www.swagelok.com |
| **G** | 2 | Material: SS316 | SS-400-3 |
| | | ¼" OD | 23 |
| | | **Integral bonnet needle valve:** | www.swagelok.com |
| **H** | 1 | Material: SS316 | SS-1VS4 |
| | | 0.37 Cv, ¼" OD, Vee Stem | 72 |
| | | **Tubing:** | www.swagelok.com |
| **I** | | Material: SS316 | SS-T4-S-049-20 |
| | | ¼" OD, .049" wall | 47 per 20ft. |
| | | **Piston,** precision ground rod**:** | www.mcmaster.com |
| **J** | 1 | Material: SS416 magnetic (!) | 88955K262 |
| | | 5/16" OD, | 20 per 3 ft. |
| | | **Compression spring:** | www.mcmaster.com |
| **K** | 2 | Material: SS302 | 9002T23 |
| | | 11/16" length, .3" OD, .022" wire | 3 |

The pump cylinder (Part A) fabricated from a smooth bore seamless stainless steel (SS316) tubing with an outer diameter (OD) of 1.27 cm (0.5 in) and inner diameter (ID) of 0.848 cm (0.334 in) is cut to a length of 20 cm (7.9 in). The piston is made from a magnetic stainless steel (SS416) precision ground rod, with a diameter of 0.794 cm (5/16 in), cut to a length of 13 cm (5.11 in) and both ends chamfered. Both the tube and rod used to fabricate the pump cylinder and piston, respectively, have matching standard diameters readily available off-the-shelf, resulting in a reasonably small annular gap without the need for extra honing or machining. The commercially available pull-type solenoids used for driving the

piston are manufactured usually with one end closed. Therefore, a hole at the end of the solenoid needs to be drilled to accommodate the pump cylinder. When assembling the pump, one has to place the solenoids on the pump cylinder tube and swage the reducing union fittings on with the solenoids in place. The piston is placed inside the pump cylinder together with compression springs on each side. The compression springs prevent wear, which could be caused by impact of the piston onto the reducer in case of overshooting. The check-valve bridge is assembled according to Fig. 12-1 using standard high pressure stainless steel (SS316) tubing rated up to at least 34 MPa (5000 psi) with an OD of 0.635 cm (0.25 in) as well as check valves and compression fittings. The check valves have a cracking pressure of 2.3 kPa (1/3 psi) and must be installed in the flow direction specified in Fig. 12-1. By means of two worm-drive hose and tube clamps (Fig. 12-2) the solenoids and pump body are clamped to a U-shaped aluminum channel, which is screwed onto a platform. A valve (Part H) placed at one end of the pump facilitates priming and cleaning of the pump.

### 12.2.2 Construction of the electronic pump controller

The pump is controlled by an electronic circuit as illustrated in Fig. 12-3. The main part of this controller is a square wave generator. The output of this square wave generator is connected to two solid state relays (SSR1 and SSR2), which direct the current from the 12 V DC power supply alternatively to solenoids S1 and S2, respectively. The heart of the square wave generator is a 555-timer integrated circuit. The output signal ($V_{out}$) of the square wave generator depends on the value of resistors R1 and R2, as well as the capacitance C1 and the settings of the potentiometers Pot1 and Pot2. The frequency and duty cycle of this square wave generator can be adjusted by changing the resistance of the potentiometers Pot1 and Pot2, respectively. Space time ($T_s$) and mark time ($T_m$) as illustrated in Fig. 12-3, can be tuned individually by adjusting potentiometers Pot1 and Pot2, respectively. Using the values given in Fig. 12-3 for resistors and capacitance, the reciprocation frequency ($f = (T_s + T_m)^{-1}$) of the pump can be adjusted from approximately 0.33 Hz up to 2 Hz. Setting both potentiometers to about the same

resistance results in a square wave with a 50% duty cycle (i.e. $T_s = T_m$), which yields the best performance when the pump is operated horizontally. All electronic components are available at an affordable price and can be easily installed on a prototyping breadboard, which does not require soldering skills. The parts required for the construction of this controller, including electronic parts for the square wave controller circuit, together with a box, solid-state relays and cooling fan to avoid overheating of the relays are listed in Table 12-2, together with a list of suppliers and estimated costs. However, most parts can be found in local electronic component stores.

**Table 12-2.** Parts for pump controller.

| Part | # of units | Description | Supplier<br>Part #<br>Unit price in US$ |
|---|---|---|---|
| **SSR1**<br>**SSR2** | 2 | **Solid state relay:**<br>Manufacturer: Crydom<br>0 to 100 V DC; 12 A to 20 mA | www.alliedelec.com<br>682-0068<br>45 |
| **n/a** | 2 | **Heatsink:**<br>Manufacturer: Crydom<br>Aluminum, 8-32 threaded | www.alliedelec.com<br>682-0063<br>8 |
| **n/a** | 1 | **Metal box:**<br>Manufacturer: Hammond<br>Aluminum; 3“x 6“x 6“ | www.alliedelec.com<br>806-1886<br>33 |
| **n/a** | 1 | **12 V DC cooling fan:**<br>Globe Motors;<br>2.36"sq x 1.00", CFM 17 | www.alliedelec.com<br>965-0286<br>18 |
| **n/a** | 1 | **Breadboard:**<br>solderless | www.alliedelec.com<br>237-0015<br>8 |
| **IC** | 1 | **555 timer IC:**<br>LM555CN, supply: +18 V max.<br>output current: 200 mA | www.thesource.ca<br>2761723X<br>5 |
| **R1**<br>**R2** | 2 | **Carbon resistors:**<br>12 kΩ, (brown red orange gold )<br>¼ W, 5% | www.thesource.ca<br>288-0605<br><1 |
| **Pot1**<br>**Pot2** | 2 | **Linear taper potentiometer:**<br>100 kΩ, | www.thesource.ca<br>2710092<br>6 |
| **D1** | 1 | **Signal diode:**<br>1N4148 | www.thesource.ca<br>2761620<br>2 |
| **C1** | 1 | **Electrolytic capacitor:**<br>22 µF, 35 V | www.thesource.ca<br>2720802<br>1 |
| **D2**<br>**D3** | 2 | **Rectifier diodes:**<br>1N4001 MIC | www.thesource.ca<br>2761101<br>1.50 |

## 12.3 Performance of the pump

The performance of the pump was tested by pumping liquids with low and moderately high viscosities at various pumping heights and settings for the reciprocation frequency. The liquids used for the performance tests were anhydrous ethanol and corn oil, for the low- and high-viscosity liquids, respectively. For the experimental setup, flexible Tygon™ tubings with an ID of 0.4 cm and length of 40 and 200 cm were connected to the inlet and outlet of the pump, respectively. After priming the pump with the test liquid, the inlet tubing was placed in a 500 mL beaker filled with the test fluid and the outlet tubing was placed at a higher level discharging into an empty 100 mL graduated cylinder. The average flow rate was obtained by measuring the time required to fill the graduated cylinder for various frequency settings and pumping heights (H). The measurements were carried out at room temperature (22 °C) and repeated at least 3 times. During extended periods of operation solenoids tend to warm up. However, the solenoids selected for this pump are of a continuous duty type with a power rating of 10 watts. The continuous duty type solenoids can be energized indefinitely according to the manufacturer and are able to handle 100% 'on' time. These solenoids allow continuous operation without excessive heat generation. Using the pump in a temperature controlled air bath would further help to minimize the effect of heat generated by the solenoids. However, in order to assess the impact of heat generated in the coil of the solenoids during operation, the temperature at the solenoid surface as well the temperature of the corn oil before and after passing through the pump were monitored throughout the experiments. In these experiments the pump was operated at ambient conditions and not placed in a temperature controlled circulating air bath. The oil temperature was measured at the inlet and outlet using a digital thermometer equipped with a J-type thermocouple. Even though the solenoids warmed up to 38 °C, measured with the same thermocouple placed on the surface of the solenoid during aforementioned experiments over the duration of several hours of continuous operation, the temperature increase for the pumped liquid at the outlet was less than 0.2 °C. The pump has been designed to be placed in a temperature-

controlled circulating air bath for experiments carried out between 40 and 70 °C. Thus, the effect of heat generation in the solenoids on the circulated fluid is considered negligible. The circulating air bath aids in dissipating the heat away from the solenoids, thereby minimizing potential temperature fluctuations in the pumped liquid caused by the warm solenoids.

### 12.3.1 Flowrate vs. reciprocation frequency

The average pumping height from the start to the end of the frequency performance test with corn oil and ethanol was 23.5 and 20 cm, respectively. This pumping height difference corresponds to an actual setup of the experimental apparatus for which this pump was designed. For ethanol, a linear relationship between the flow rate and reciprocation frequency up to 2 Hz was ascertained (Fig. 12-4).

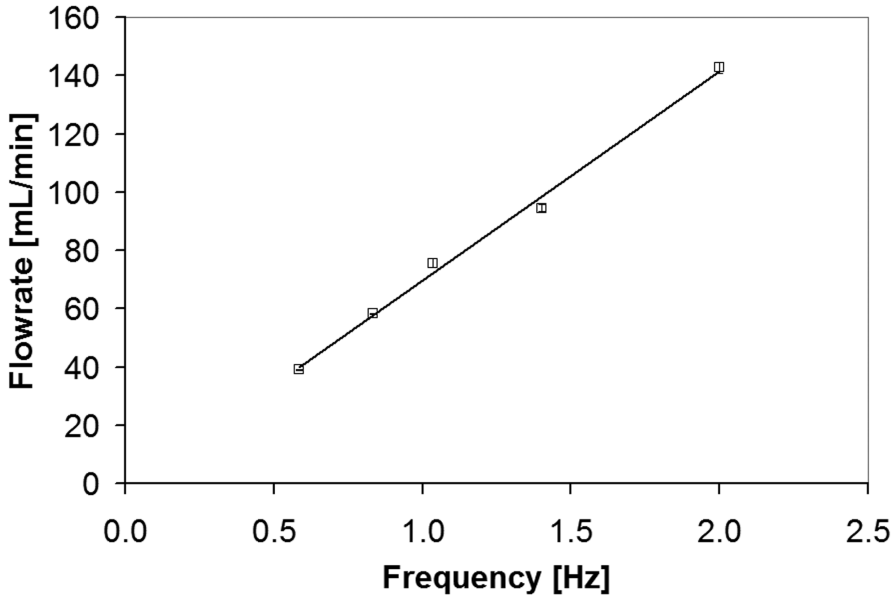


**Figure 12-4.** Flow rate of ethanol vs. reciprocation frequency. Data points represent mean ± standard deviation based on triplicate measurements.

However, for the more viscous corn oil there was a nonlinear relationship between reciprocation frequency and flow rate (Fig. 12-5). Increasing the frequency from the minimum setting, the flow rate increased and reached a

maximum value. Upon further increase of the reciprocation frequency, the flow rate decreased slightly (Fig. 12-5). This optimum frequency was found to be approximately 1 Hz for corn oil using the pump described here. This nonlinear behavior is caused by the higher viscosity of corn oil, which leads to increased flow resistance in the tubings, check valves and in the pump body. When the reciprocation frequency is increased beyond the optimum frequency while pumping a viscous fluid, the performance of the pump may be impaired due to a substantial lag in the check valves as well as between the piston and the alternating magnetic fields of the solenoids, leading to a decreased flowrate.

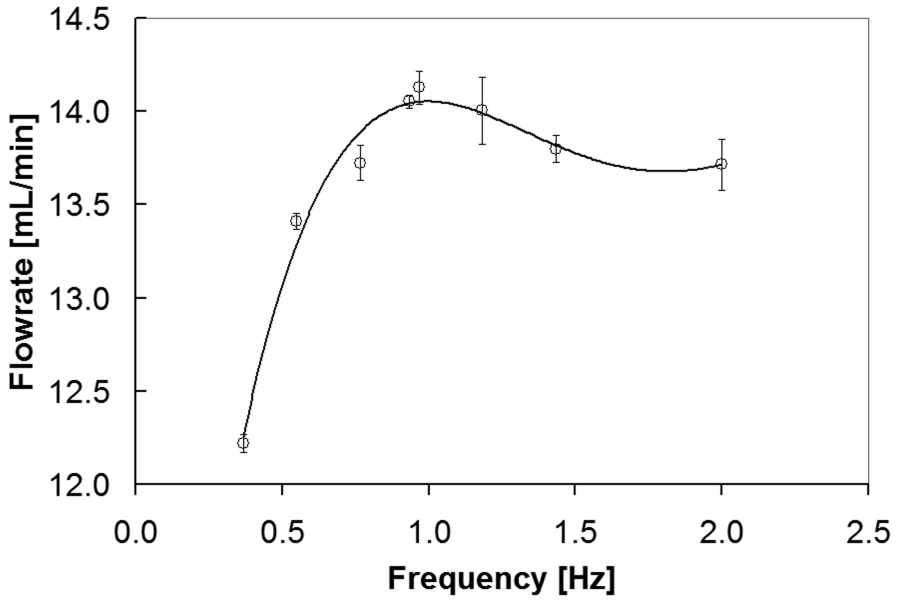


**Figure 12-5.** Flow rate of corn oil vs. reciprocation frequency. Data points represent mean ± standard deviation based on triplicate measurements.

### 12.3.2 Flow rate vs. pumping height

The performance of the pump set to a reciprocation frequency of 1 Hz was tested at various levels for the pumping height. For this test the same inlet and outlet tubing was used as in the frequency performance test. The results of this test (Fig. 12-6) showed clearly that the flow rate was strongly related to pumping height, for both ethanol and corn oil. Furthermore, the flow rate for ethanol was about 6-

fold higher than that for the more viscous corn oil. This difference is mainly caused by the friction head, which is related to viscosity. The viscosity at 22 ºC is about 56 mPa.s and 1.12 mPa.s for corn oil and ethanol, respectively [24, 25]. Additionally, the pump head is a function of liquid density, which is 0.919 g/cm$^3$ and 0.788 g/cm$^3$ for corn oil and ethanol at 22 ºC, respectively [25, 26].

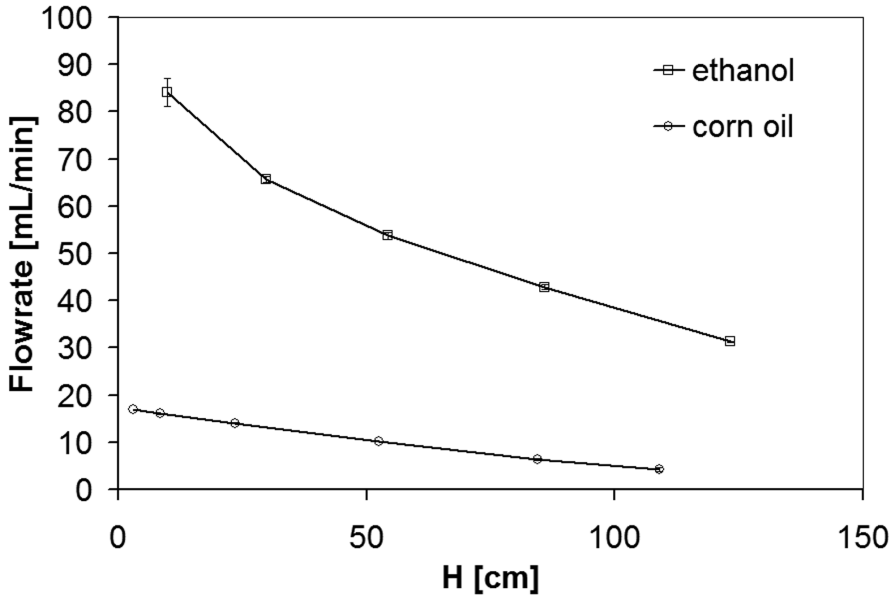


**Figure 12-6.** Flowrate vs. pumping height. Data points represent mean ± standard deviation based on triplicate measurements.

The higher viscosity and density of corn oil affects strongly the flow rate achievable by this pump. However, in the actual experimental apparatus for which this pump has been constructed, the length for the inlet and outlet tubing is about 30 cm for both the inlet and outlet tubing, which causes less friction head loss and better flow rates. Nevertheless, with the long Tygon™ tubings attached in the performance test and at a pumping height of about 10 cm the maximum flow rate achieved by this pump at a reciprocation frequency of 1 Hz was 17 cm$^3$/min and 85 cm$^3$/min for corn oil and ethanol, respectively. By doubling the reciprocation frequency to 2 Hz the pump was able to deliver a flow rate of about 170 cm$^3$/min for ethanol at a pumping height of 10 cm.

## 12.4 Conclusions

A simple circulating pump has been constructed using off-the-shelf parts that require little or no modifications, so that the pump body and electronic controller can be assembled easily using commonly available tools. The pump is capable of circulating liquids under atmospheric conditions as well as under pressures of up to 34 MPa (5000 psi) with rheological properties ranging from those of ethanol to corn oil. For liquids with higher viscosities, such as corn oil, the circulation frequency needs to be optimized, because of increased friction head in the pump, check valves and tubing. The higher viscosity can lead to a lag between the piston and magnetic field of the solenoids, which results in lower pump efficiency. The pump capacity can be improved by using a cylinder, piston and solenoids with larger diameters. Furthermore, the piston and pump cylinder could be manufactured using precisely machined and honed parts to improve pump efficiency for liquids without particulate matter. Small particles in the liquid, causing the piston to jam in the cylinder bore, could be of concern for precisely machined pumps [23]. Therefore, a relatively large tolerance between the piston and ID of the pump cylinder can prevent malfunction caused by small particles getting stuck between the piston and cylinder. The large tolerances between piston and cylinder combined with the reliability of standard parts used for our design render this pump very sturdy and practically maintenance-free. The pump is suitable to be operated at temperatures of up to about 80 ℃. The temperature rating for the solenoids is usually higher at around 130 ℃ or more depending on the insulation material used. However, increasing the temperature of the solenoids causes an increase in electrical resistance in the wires of the solenoid leading to a decrease in magnetic force, which may be detrimental to pump performance. Check valves used in this pump are spring loaded with a cracking pressure of 2.3 kPa (1/3 psi). There is potential for optimization of the flow rate for viscous fluids by modifying the spring force of the check valves. Increasing the spring force can lead to increased flow resistance in the check valves leading to a reduced flowrate. However, for viscous fluids an increased spring force may reduce the lag in check valves at higher reciprocating frequency thus improving the flow

rate. Therefore, depending on the viscosity of the fluid an optimum spring and cracking pressure could be determined. For non-viscous liquids, pump performance may be improved by using ball check valves in a vertical arrangement without springs thereby reducing flow resistance. However, the check valves used in our design are a trade-off between increased flow resistance and reduced lag, which allows horizontal and vertical operation of the pump as well as pumping of both viscous and non-viscous liquids.

Finally, the pump has been successfully used maintenance-free in our lab to circulate corn oil and other lipids in contact with supercritical carbon dioxide at pressures of up to 25 MPa (3600 psi) and temperatures ranging from 40 to 70 ºC for more than 2000 hours of operation.

## 12.5 References


1. J.S. Watson, An all glass circulating pump for gases. Can. J. Technol. 34 (1956) 373-375.

2. C.J. Sterner, Electromagnetic pump for circulating gases at low flow rates. Rev. Sci. Instrum. 31 (1960) 1159-1160.

3. T. Ellis, A demountable glass circulating pump. J. Sci. Instrum. 39 (1962) 234-235.

4. H.M. Papee, A. Montefinale, T.W. Zawidzki, A new laboratory all-glass circulation pump for gases. J. Sci. Instrum. 39 (1962) 394-396.

5. F.B. Canfield, J.K. Watson, A.L. Blancett, Electromagnetic gas pump for low temperature service. Rev. Sci. Instrum. 34 (1963) 1431-1433.

6. K.L. Erdman, J.R. MacDonald, G.A. Beer, D.A. Axen, Simple gas circulation pump. Rev. Sci. Instrum. 35 (1964) 241.

7. D. Kallo, I. Preszler, K. Payer, Circulating pump and flowmeter for kinetic reaction apparatus. J. Sci. Instrum. 41 (1964) 338-340.

8. G.L. Petriconi, A.C. Montefinale, H.M. Papee, A simple laboratory centrifugal glass circulation pump and gas saturator for liquids. J. Sci. Instrum. 42 (1965) 662-663.

9. S. Duncan, F. Lawson, A double-acting all-glass gas circulating pump. J. Sci. Instrum. 44 (1967) 388.

10. S. Arnold, B. Franklin, B. Hyde, N. Lacey, R. Merritt, G. Reece, An improved gas-circulating pump. J. Phys. E: Sci. Instrum. 2 (1969) 1137-1139.

11. M.J. Hiza, A.G. Duncan, A simple gas recirculation pump for low flow and high pressure applications. Rev. Sci. Instrum. 40 (1969) 513-514.

12. W.E.A. Ruska, L.J. Hurt, R. Kobayashi, Circulating pump for high pressure and -200 to +400°c application. Rev. Sci. Instrum. 41 (1970) 1444-1446.

13. H. Mansoorian, E.F. Capps, H.L. Gielen, Compact, magnetic recirculating pump for wide range temperature and pressure operation. Rev. Sci. Instrum. 46 (1975) 1350-1351.

14. F.J. Torre, D.M. Eshelman, M.W. Lee, Closed system gas circulating pump. Rev. Sci. Instrum. 47 (1976) 1142-1143.

15. K. Yukinari, N. Asada, Magnetic-coupled type circulating pump. Natl. Tech. Rep. (Matsushita Electr. Ind. Co.) 23 (1977) 448-456.

16. D.H. Ziger, C.A. Eckert, Simple high-pressure magnetic pump. Rev. Sci. Instrum. 53 (1982) 1296-1297.

17. W.J. Rogers, F. Fontalba, E.F. Capps, J.C. Holste, K.N. Marsh, K.R. Hall, Magnetic circulating pumps for use over wide ranges of temperature and pressure. Rev. Sci. Instrum. 59 (1988) 193-194.

18. M.W.M. Hisham, S.W. Benson, Simple high-speed circulating pump for gases. Rev. Sci. Instrum. 60 (1989) 1349-1350.

19. B.D. Drake, M.T. Dunbar, R.L. Smith Jr, An easy to construct, economical, safe, high-pressure magnetic pump for pressures to 140 MPa suitable for circulation of supercritical fluids. Rev. Sci. Instrum. 61 (1990) 2474-2475.

20. W. Pleass, E.H.A. Prescott, D. Steer, D. Steytler, A sealess pump to circulate supercritical fluids in high pressure systems. Rev. Sci. Instrum. 61 (1990) 1120-1122.

21. Y. Ding, M.D. LeVan, A high-capacity magnetic pump for gas circulation in closed systems. Rev. Sci. Instrum. 73 (2002) 230-231.

22. J. Van Doorn, A.E. Mather, High pressure circulating pump. Rev. Sci. Instrum. 73 (2002) 4037-4039.

23. F. Peleties, J.P.M. Trusler, A.R.H. Goodwin, G.C. Maitland, Circulating pump for high-pressure and high-temperature applications. Rev. Sci. Instrum. 76 (2005) art. no. 105103 p.1-3.

24. H. Noureddini, B.C. Teoh, L.D. Clements, Viscosities of vegetable oils and fatty acids. J. Am. Oil Chem. Soc. 69 (1992) 1189-1191.

25. D.R. Lide, CRC Handbook of Chemistry and Physics. 88 ed. CRC Handbook of Chemistry and Physics, ed. D.R. Lide. 2004, Boca Raton, FL CRC Press/Taylor and Francis.

26. H. Noureddini, B.C. Teoh, L.D. Clements, Densities of vegetable oils and fatty acids. J. Am. Oil Chem. Soc. 69 (1992) 1184-1188.